UNIVERSITY OF SOUTHAMPTON

FACULTY OF MEDICINE

Cancer Sciences

Volume 1 of 1

B-cell receptor signalling in malignant B cells: Analysis of BTK "by-pass" pathways and time-resolved, single-cell quantification of Ca^{2+} mobilisation

by

Rachael Arthur

Thesis for the degree of Doctor of Philosophy

March 2021

UNIVERSITY OF SOUTHAMPTON

ABSTRACT

FACULTY OF MEDICINE

Cancer Sciences

Thesis for the degree of Doctor of Philosophy

B-cell receptor signalling in malignant B cells: Analysis of BTK "by-pass" pathways and time-resolved, single-cell quantification of Ca^{2+} mobilisation

Rachael Arthur

The B-cell receptor (BCR) is the key functional unit of normal B cells and continues to exert an important influence post-transformation in various B-cell malignancies, including chronic lymphocytic leukaemia (CLL). BCR activation initiates formation of the signalosome, a multi-protein signalling complex which includes BTK, a kinase which is the target for drugs used to treat CLL and other B-cell malignancies, including ibrutinib and acalabrutinib. BTK phosphorylates PLCγ2 leading to intracellular calcium (iCa^{2+}) mobilisation and downstream pro-survival/proliferation responses. However, the ability of ibrutinib to interfere with anti-IgM-induced iCa^{2+} mobilisation in CLL cells varies between samples revealing the presence of alternate, BTK-independent signalling to iCa^{2+}. Identification of this alternate BTK "by-pass" signalling pathway may allow the development of new strategies to more effectively block BCR signalling in malignant B cells.

Flow cytometric analysis of iCa^{2+} release is widely used as a measure of BCR signalling capacity. Strong sIgM signalling capacity is associated with shorter survival and this assay may therefore have value as a biomarker to predict CLL patient outcomes. However, there are several limitations of flow cytometry, including the inability to study single-cells over time. This might mask intraclonal heterogeneity, whereby a potentially rare subset of cells might have 'atypical' signalling and/or inhibitor responses contributing to disease progression and/or treatment failure. Thus, new approaches to quantify iCa^{2+} release may improve the prognostic power of BCR signal analysis.

This project had two main aims both focused on the critical BTK→PLCγ2→iCa^{2+} signalling pathway. First, to identify the nature and importance of the BTK "by-pass" signal, and second, to determine whether the method of analysing iCa^{2+} mobilisation could be improved by using microwell arrays to study single-cell, time-resolved iCa^{2+} mobilisation.

Analysis of primary CLL samples demonstrated that BTK by-pass signalling was a drug class-effect as it was observed with both ibrutinib and acalabrutinib. It was most evident in samples with the strongest anti-IgM signalling capacities suggesting that acquisition of BTK "by-pass" signalling is responsible for stronger iCa^{2+} responses *per se*. Analysis using multi-inhibitor beads and target phosphorylation demonstrated that BTK "by-pass" occurred despite full occupancy of the BTK active site by inhibitor, and use of a BTK-targeting PROTAC revealed that "by-pass" signalling was not due to kinase-independent functions of BTK. Mapping of PLCγ2 phopshorylation sites demonstrated that retained anti-IgM-induced iCa^{2+} mobilisation was associated with BTK-independent activatory phosphorylation of PLCγ2 at Tyr^{753} and Tyr^{759} in both CLL samples and B-lymphoma cell lines. Since PLCγ2 Tyr^{753} and Tyr^{759} can be phosphorylated by SYK and a SYK inhibitor fully blocked anti-IgM-induced iCa^{2+} responses in all samples, direct SYK-mediated phosphorylation of PLCγ2 may be one potential pathway of BTK "by-pass" signalling.

Microwell arrays consist of thousands of wells designed to trap single-cells and, coupled with fluorescent microscopy, have the potential to be used to analyse time-resolved iCa^{2+} mobilisation. Microwell size is crucial for optimal trapping of single cells, and the device was fabricated and optimised to trap a high percentage of single CLL cells. Responses to ionomycin could be measured in primary CLL cells, and there was a variable reponse to anti-IgM in some samples, validated by effective inhibition of these responses following kinase inhibitor pretreatment. Despite substantial technical challenges that remain to be addressed, including increasing the sensitivity of the assay, the arrays hold promise for more in-depth analysis of iCa^{2+} mobilisation.

Overall, the results provide new insight into mechanisms of BTK "by-pass" signalling, and some evidence to tentatively support the hypothesis that microwell arrays may be an attractive approach to assess iCa^{2+} flux in malignant B cells.

Table of Contents

Table of Tables

Table of Figures

Table of Figures

List of Accompanying Materials

Video 1: CLL686 anti-IgM.avi

Video 2: CLL686 control antibody and ionomycin.avi

Video 3: CLL686 ionomycin.avi

Academic Thesis: Declaration Of Authorship

I, Rachael Arthur

declare that this thesis titled **'B-cell receptor signalling in malignant B cells: Analysis of BTK "by-pass" pathways and time-resolved, single-cell quantification of Ca^{2+} mobilisation'** and the work presented in it are my own and has been generated by me as the result of my own original research.

I confirm that:

1. This work was done wholly or mainly while in candidature for a research degree at this University;
2. Where any part of this thesis has previously been submitted for a degree or any other qualification at this University or any other institution, this has been clearly stated;
3. Where I have consulted the published work of others, this is always clearly attributed;
4. Where I have quoted from the work of others, the source is always given. With the exception of such quotations, this thesis is entirely my own work;
5. I have acknowledged all main sources of help;
6. Where the thesis is based on work done by myself jointly with others, I have made clear exactly what was done by others and what I have contributed myself;
7. Parts of this work have been published as:
   Arthur, R., Valle-Argos, B., Steele, A.J., and Packham, G. 2020. **Development of PRTACs to address clinical limitations associated with BTK-targeted kinase inhibitors.** *Exploration of Targeted Anti-tumor Therapy.* 1(3): 131-152.

Signed: .....

Date: .....

Acknowledgements

Firstly, I would like to thank my supervisor Professor Graham Packham for providing me with the opportunity to carry out this research in his laboratory, and for his constant support and guidance throughout my PhD. I would also like to thank my second supervisor Professor Hywel Morgan for allowing me to join his laboratory group and for his help and knowledge. I also thank the cleanroom facilities in the Zepler Institute, all the staff who trained me and especially Lukas Vojkuvka for always answering my questions and helping me with technical issues.

In addition, I would like to thank Dr Adam Linley (University of Liverpool, UK) for allowing me to visit their laboratories and learn how to carry out the multi-inhibitor beads (MIBs) assay, and for providing the MIBs. I also thank Professor Craig Crews (Yale University, USA) for his kind gift of the PROTAC MT-802.

I also thank all the members of the Graham Packham lab group, as well as the wider B-cell malignancy research group both past and present, and the members of the Centre for Hybrid Biodevices research group. I would like to especially thank Dr Beatriz Valle-Argos for all her help and guidance in the lab. I also especially thank Dr Anna Desalvo for providing teaching and training in fabrication of devices and imaging techniques, Dr Sumit Kalsi for his help in refining fabrication and Fernando Garcia for troubleshooting microscope hardware issues. I also thank Dr Francesco Forconi and the tumour bank staff for collecting, processing and storing samples. I thank all the patients who provided material for these studies.

I would also like to thank my parents and sister, and my friends for encouragement and support over the last 4 and a half years. I particularly thank John, for his continual patience and encouragement during this challenging time of writing my thesis during national lockdowns. I would not have been able to complete my PhD without these people.

Finally, I would like to thank Cancer Research UK and University of Southampton for funding this project.

Definitions and Abbreviations

ABC-DLBCL	Activated B-cell-like diffuse large B-cell lymphoma
AID	Activation-induced cytidine deaminase
AML	Acute myeloid leukaemia
APS	Ammonium persulfate
AUC	Area under the curve
BCR	B-cell receptor
BLNK	B-cell linker protein
BSA	Bovine serum albumin
BTK	Bruton's tyrosine kinase
BTKi	Bruton's tyrosine kinase inhibitor
CD	Cluster of differentiation
CDR	Complementarity determining region
CICR	Calcium-induced calcium-release
CIT	Chemoimmunotherapy
CLL	Chronic lymphocytic leukaemia
CRAC	Calcium-release activated channel
CRBN	Cereblon
DAG	Diacylglycerol
DTT	Dithiothreitol
DLBCL	Diffuse large B-cell lymphoma
DMSO	Dimethyl sulfoxide
EBV	Epstein-Barr virus
ECOG	Eastern Cooperative Oncology Group
EDTA	Ethylenediaminetetraacetic acid
EGFR	Epidermal growth factor receptor
EGTA	Ethylene glycol-bis(2-aminoethylether)-N,N,N',N'-tetraacetic acid
ER	Endoplasmic reticulum
ERK	Extracellular signal-related kinase
FBS	Foetal bovine serum

FDCs	Follicular dendritic cells
GC	Germinal centre
GCB-DLBCL	Germinal centre B-cell-like diffuse large B-cell lymphoma
HEL	Hen-egg lysozyme
HEPES	4-(2-hydroxyethyl)-1-piperazineethanesulfonic acid
HRP	Horseradish peroxidase
IAP	Inhibitor of apoptosis protein
iCa^{2+}	Intracellular calcium
$i[Ca^{2+}]$	Intracellular calcium concentration
IC	Isotype control
Ig	Immunoglobulin
IGHV	Immunoglobulin heavy chain variable region
IgM	Immunoglobulin M
IL	Interleukin
IMDM	Iscove's Modified Dulbecco's Medium
IP_3	Inositol trisphosphate
IPA	Isopropyl alcohol
IPI	International prognostic index
IP_3R	Inositol trisphosphate receptor
ITAMs	Immunoreceptor tyrosine-based activation motif
JNK	c-Jun NH2-terminal kinase
LDH	Lactase dehydrogenase
M-CLL	Mutated chronic lymphocytic leukaemia
MDM2	Mouse double minute 2 homolog
MFI	Mean fluorescence intensity
MHC	Major histocompatibility complex
MIBs	Multi-inhibitor beads
mRNA	Messenger RNA
NFAT	Nuclear factor of activated T cells
NF-κB	Nucelar factor κB
NHL	Non-Hodgkin's lymphoma

PBMCs	Peripheral blood mononuclear cells
PBS	Phosphate buffered saline
$PI(3,4,5)P_3$	Phosphatidylinositol (3,4,5)-trisphosphate
$PI(4,5)P_2$	Phosphatidylinositol 4,5-bisphosphate
PI3K	Phosphoinositide 3-kinase
PIP5K	Phosphatidylinositol-4-phosphate 5-kinase
PKC	Protein kinase C
PLCγ1	Phospholipase C gamma 1
PLCγ2	Phospholipase C gamma 2
PM	Plasma membrane
PMMA	Poly(methyl methacrylate)
PROTAC	Proteolysis targeting chimeras
RAG	Recombination-activating genes
RIPA	Radioimmunoprecipitation assay buffer
RPMI	Roswell Park Memorial Institute medium
RNA	Ribonucleic acid
RNAi	Ribonucleic acid interference
RSS	Recombination signal sequences
SAM	Sterile-alpha motif
SCF	Stem cell factor
SDS	Sodium dodecyl sulfate
SDS-PAGE	Sodium dodecyl sulfate – polyacrylamide gel electrophoresis
SH2	Src-homology 2
SH3	Src-homology 3
SHM	Somatic hypermutation
sIg	Surface immunoglobulin
sIgM	Surface immunoglobulin M
SLO	Secondary lymphoid organ
SOCE	Store-operated calcium entry
STIM	Stromal interaction molecule
SYK	Spleen tyrosine kinase

TBS-T	Tris-buffered saline with Tween®20
TC	Ternary complex
TEMED	N, N, N', N'-Tetramethyl ethylenediamine
U-CLL	Unmutated chronic lymphocytic leukaemia
VHL	Von Hippel-Lindau
XID	X-linked immunodeficiency
XLA	X-linked agammaglobulinemia

Chapter One

Introduction

1 Introduction

1.1 Overview

The overall goal of the experiments described in this thesis was to determine the nature of the BTK "by-pass" pathway leading to intracellular calcium (iCa^{2+}) mobilisation and investigate whether microwell arrays provided a useful approach for time-resolved analysis of iCa^{2+} flux at the single-cell level. Studies were performed with primary samples from chronic lymphocytic leukaemia (CLL) patients, where the BTK "by-pass" phenomenon was first observed, and established B-cell lymphoma cell lines. This introduction therefore provides the key background to the 3 main elements of the project; (i) B-cell receptor (BCR) function and associated signalling pathways, (ii) B-cell malignancies and the clinical significance of the BCR-associated signalling pathways, and (iii) the importance of time-resolved, single-cell iCa^{2+} flux analysis.

1.2 B-cell development

B cells are a vital component of the adaptive immune response which recognise antigen via their BCR (described in further detail in **Section 1.3**) and mediate the production of antigen-specific antibodies (Lebien and Tedder, 2008). They internalise and then present antigen to $CD4^+$ T-cells for help (Avalos and Ploegh, 2014). The BCR consists of a surface immunoglobulin (sIg), which mediates antigen-binding specificity, coupled to two transmembrane signal transduction molecules, CD79A and CD79B (also known as Ig-α and Ig-β, respectively) (Stevenson and Caligaris-Cappio, 2004; Burger and Chiorazzi, 2013) (**Figure 1-1**). Membrane-bound immunoglobulins are comprised of two identical heavy (H) and two identical light (L) chains, where the N-terminal region of both the H and L chains is highly variable and is responsible for antigen recognition and the C-terminal region is a 'constant' region that determines the signalling capacity of the BCR and the effector function of the resultant, secreted antibody (Alt et al., 1987). The variable regions contain hypervariable subregions, known as complementarity-determining regions (CDRs), that mediate antigen contact (Tonegawa, 1983). The BCR gains its diversity through immunoglobulin gene recombination, somatic hypermutation (SHM) and class switching enabling production of a large repertoire of antibodies with differing specificity and effector functions.

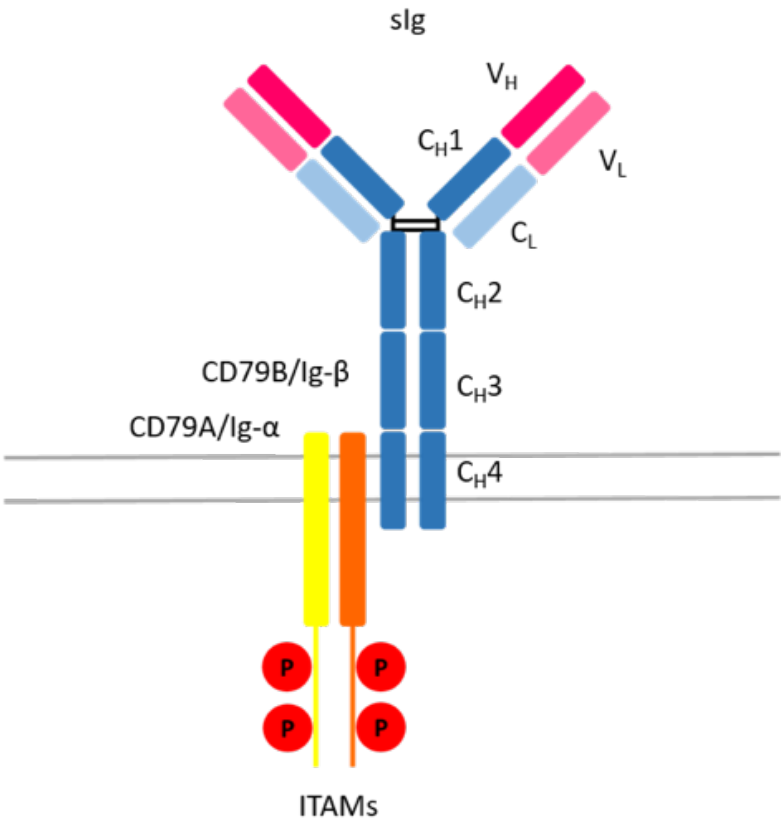

FIGURE 1-1: STRUCTURE OF THE B-CELL RECEPTOR (BCR).

The BCR comprises the surface immunoglobulin (sIg) molecule consisting of constant heavy (C_H) regions, variable heavy (V_H) regions, constant light (C_L) regions, and variable light (V_L) regions. This molecule couples with CD79A and CD79B, also known as Ig-α and –β, which contain immunoreceptor tyrosine-based activiation motifs (ITAMs) that are phosphorylated upon antigen engagement with the BCR, which initiates the intracellular signalling cascade. Adapted from (Burger and Chiorazzi, 2013).

B-cell development occurs in two main stages (summarised in **Figure 1-2**): the antigen-independent phase (occurring in the foetal liver and adult bone marrow) which is characterised by initial immunoglobulin gene rearrangements, and the antigen-dependent phase (occurring in the peripheral lymphoid organs), which requires interaction between mature naïve B cells and antigen to generate antibody secreting plasma cells and long-lived memory B cells (Kindt, Goldsby and Osborne, 2007).

The antigen-independent phase of B-cell development leads to the generation of mature, naive B cells. The earliest distinctive B-lineage cell, called the progenitor B cell (pro-B cell), is derived from the lymphoid precursor cell. Proliferation and differentiation of pro-B cells into precursor B cells (pre-B cells) requires microenvironmental stimuli provided by bone marrow stromal cells. This includes direct cell:cell interaction through molecules expressed on the surface of bone marrow stromal cells (including VCAM-1 and stem cell factor (SCF), binding VLA-4 and c-Kit on the B-cell, respectively), along with secretion of interleukin (IL)-7 from bone marrow stromal cells which binds the IL-7 receptor on the B-cell surface (Kindt, Goldsby and Osborne, 2007). These interactions drive the maturation process to form pre-B cells, and by this stage complete heavy chain gene rearrangement has occurred with the cells expressing membrane μ chain. The heavy chain (genes located on chromosome 14) comprises a constant (C_H) region, encoded by one of eight different genes termed μ, δ, γ1, γ2a, γ2b, γ3, ε, and α, which influences both the signalling capacity of the BCR and the effector function of the secreted antibody produced following plasma cell maturation (Kindt, Goldsby and Osborne, 2007). The C_H region is joined to the variable (V_H), diversity (D_H) and joining (J_H) regions. In the heavy chain, D_H and J_H are joined first, followed by V_H joining to the D_HJ_H sequence. The membrane μ chain associates with the surrogate light chain and couples with the CD79A/B heterodimer to form the pre-B-cell receptor (pre-BCR), which is essential for continued B-cell development.

Recombination signal sequences (RSSs) flank each germline V_H (located 3' to the gene), D_H (located both sides of the gene) and J_H (located 5' to the gene) gene region (Oettinger et al., 1990). These sequences function as signals for the recombination process during gene rearrangement. Each RSS contains a conserved palindromic heptamer (CACAGTG, or its complementary sequence) and a conserved nonamer (ACAAAAACC, or its complementary sequence) separated by a sequence of 12 or 23 base pairs (bp) (Tonegawa, 1983; Roth, 2014). For the heavy chain, all D spacers are 12 bp and all V and J spacers are 23 bp . Sequences with a 12 bp

spacer can only join sequences with a 23 bp spacer, ensuring that, for example, a V_H region cannot join another V_H region; this is known as the 12/23 rule (Alt et al., 1987; Roth, 2014).

Recombination-activating genes (RAG)-1 and RAG-2 are the enzymes that catalyse V(D)J recombination. RAG1/2 recognise the RSSs and cleave a single DNA strand between the RSS and the coding sequence producing a hairpin structure followed by a double strand break at the signal sequence (Kindt, Goldsby and Osborne, 2007 ; McBlane *et al*., 1995). Addition of nucleotides at the end of the cut strands can occur to increase overall variable region variation. Finally, the strands undergo repair to join the coding sequences, before transcription and translation continue.

Each pre-B-cell proliferates to generate as many as 256 descendants, which then undergo gene rearrangement of the light chain to increase overall diversity. The light chain comprises either the κ or λ constant (C_L) region which is joined to the variable (V_L) and joining (J_L) regions (located on chromosomes 2 or 22, respectively). After both rearrangement of the heavy chain and the light chain, the B-cell is classified as an immature B-cell which expresses an antigen-specific membrane-bound IgM (with either κ or λ light chains) on the cell surface, coupled with CD79A/B forming a fully functional BCR (Kindt, Goldsby and Osborne, 2007). At this stage, engagement of the BCR will elicit cell death or anergy (a state of cellular lethargy resulting from engagement of the BCR in the absence of sufficient $CD4^+$ T-cell help) (Yarkoni et al., 2010). These negative selection processes eliminate immature B cells that express auto-antibodies against self-antigens (clonal deletion). However, the B-cell has the opportunity to edit the light chain gene of its receptor to mutate specificity away from autoreactivity with the help of RAG-1 and RAG-2 enzymes.

The B cell is now a mature naïve B cell which, and upon its release into the periphery, will co-express sIgM and sIgD through a change in RNA splicing allowing the production of two mRNAs. sIgM/D is coexpressed with other cell surface markers including CD19 (present on all B cell lineages), CD21 and CD22 (Lebien and Tedder, 2008). Mature naïve B cells migrate to secondary lymphoid organs (SLO) (such as spleen and lymph nodes) where they can undergo activation, proliferation and differentiation in response to antigen; this is the antigen-dependent phase of B-cell development. Naïve B cells are nondividing cells in the G_0 phase of the cell cycle. Activation, by interaction with antigen and BCR crosslinking, drives the resting cell into the cell cycle. B-cell

responses to thymus-dependent antigens require direct contact with helper T (T_H) cells as well as exposure to cytokines.

Following initial exposure to antigen in SLO, germinal centres (GCs) are formed which are characterised by several differentiation events: SHM, affinity maturation and class switching, leading to the formation of plasma cells and memory cells (summarised in **Figure 1-3**). GCs have two histologically distinct zones, called the dark and light zones, which are associated with important functional differences (Kindt, Goldsby and Osborne, 2007). In the first stage of GC formation, activated B cells undergo intense proliferation (clonal expansion) forming a well-defined dark zone within the GC. At this stage the cells, termed centroblasts, are defined by their large size, extended cytoplasm and diffuse chromatin. Centroblasts differentiate into centrocytes, which are small nondividing B cells. The centrocytes migrate into the light zone of the GC where they can make contact with antigen presented on follicular dendritic cells (FDCs), and receive T-cell help. B-cells likely undergo multiple cycles of mutation and selection in the GC, migrating between the dark and light zones, to produce cells with high affinity antibodies (Oprea and Perelson, 1997). This is known as the cyclic re-entry model.

SHM takes place in B cells within the dark zone of the GC following response to antigen and it is extremely focussed with the majority of the mutations occurring within the CDRs. SHM occurs randomly (mediated by the enzyme activation-induced cytidine deaminase (AID)) and will therefore generate cells with receptors with a range of affinities for a particular antigen. Selection is required to derive a population with increased affinity, and this occurs within the light zone of the GC. Centrocytes must compete for the relatively small amount of antigen presented by FDCs, therefore centrocytes with high-affinity receptors are more likely to be successful in binding FDC-bound antigen. Those that fail to bind antigen or receive T cell help rapidly undergo apoptosis. This process is known as affinity maturation. A key differentiation signal occurs through interaction with $CD4^+$ T_H cells, expressing CD40L which binds CD40 expressed on the B-cell, signalling the differentiation of the centrocyte to a memory B-cell. CXCR4 expression is crucial for GC dark and light zone separation and migration of B cells within the GC. CXCR4 expression is higher on centroblasts than centrocytes, and SDF-1 (CXCL12), the primary ligand for CXCR4, is more highly expressed in the dark zone of the GC, suggesting that the interaction between CXCR4 and SDF-1 is required for centroblast localisation to the dark zone (Allen et al., 2004). The expression of CXCR5 directs cells to the light zone, where it's ligand CXCL13 is expressed.

Class-switching allows any given V_H-D_H-J_H domain to associate with the constant region of any isotype which is important for influencing signalling and enables antibody specificity to remain consistent but the biological effector activity to vary. For example, IgG is capable of crossing the placenta to protect the developing foetus as well as activating the complement system and mediating opsonisation through binding Fc receptors on phagocytic cells; IgA is the predominant immunoglobulin in secretions such as breast milk and saliva, with a role in passive immunity; and IgE is critical for the allergic reaction response (Kindt, Goldsby and Osborne, 2007). Although the exact mechanism remains unclear, the process of class switching requires switch regions located in the DNA, a switch recombinase enzyme(s), cytokines that dictate the isotype to which the B cell switches and AID. This is specifically important for plasma cells, the antibody-secreting cells, one of the two cell types that differentiate from centrocytes. Centrocytes receiving signals from FDCs, including interaction with CD23 and IL-1α, differentiate into plasma cells with the primary role of secreting antibodies upon infection to bind the target antigen and initiate its removal from the body. Centrocytes receiving stimulation from CD40 presented on T cells will differentiate into memory B cells which are long-lived cells that allow for a rapid antibody-mediated immune response upon reinfection.

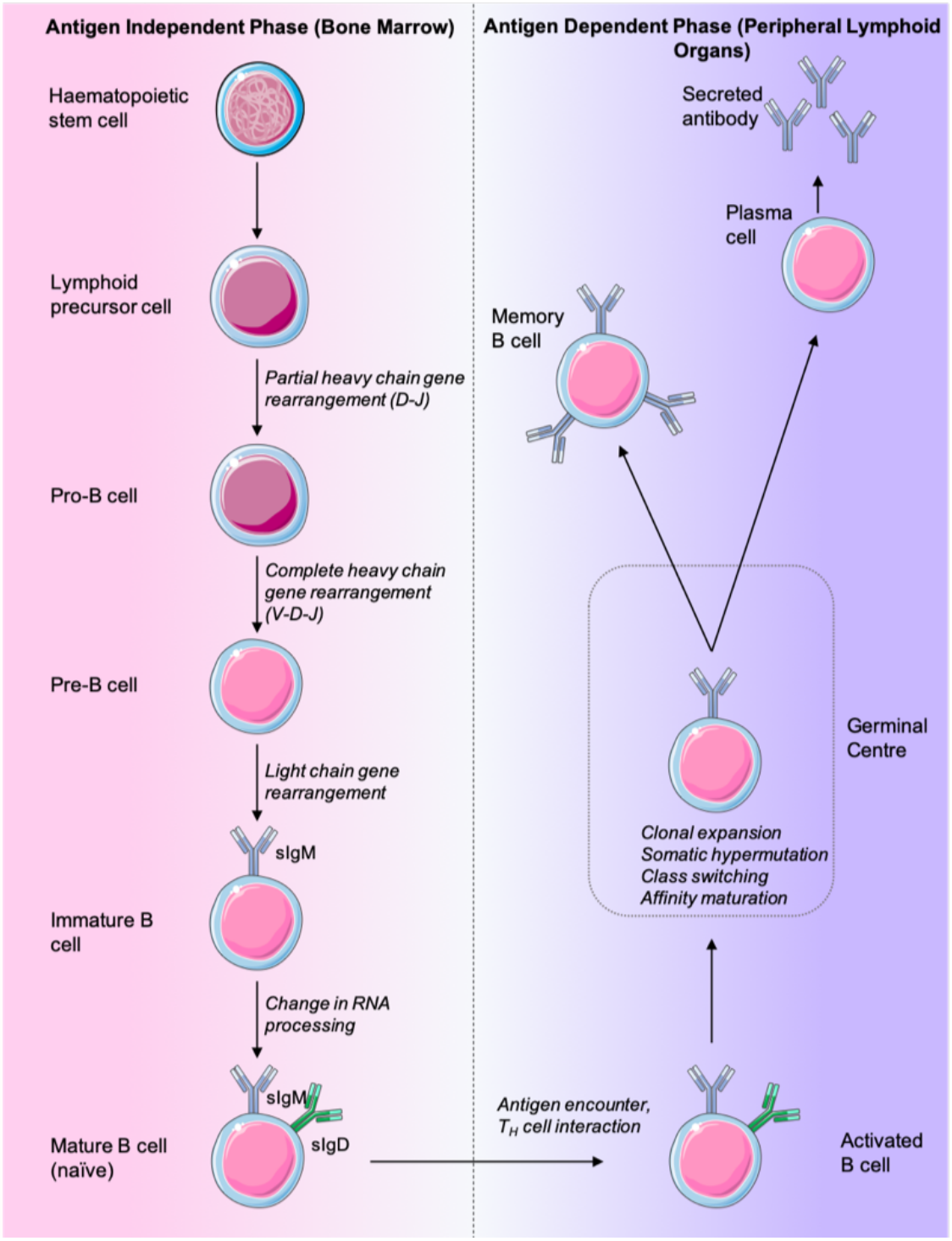

FIGURE 1-2: SUMMARY OF NORMAL B-CELL DEVELOPMENT.

B-cell development occurs in two main stages, the antigen independent phase (shown on the left hand side) occurring in the bone marrow, and the antigen dependent phase (shown on the right hand side) occurring in peripheral lymphoid organs. The antigen independent phase is characterised by sequential immunoglobulin gene rearrangement to produce a naïve B cell expressing sIgM and sIgD. Upon migration of these mature B cells to peripheral lymphoid organs, they can encounter antigen to become activated. Activated B cells form germinal centres characterized by clonal expansion, somatic hypermutation, class switching and affinity maturation (discussed in main text) to produce either antibody-secreting plasma cells or long-lived memory B cells. Figure adapted from Kindt, Goldsby and Osborne, 2007 and prepared using Servier Medical Art.

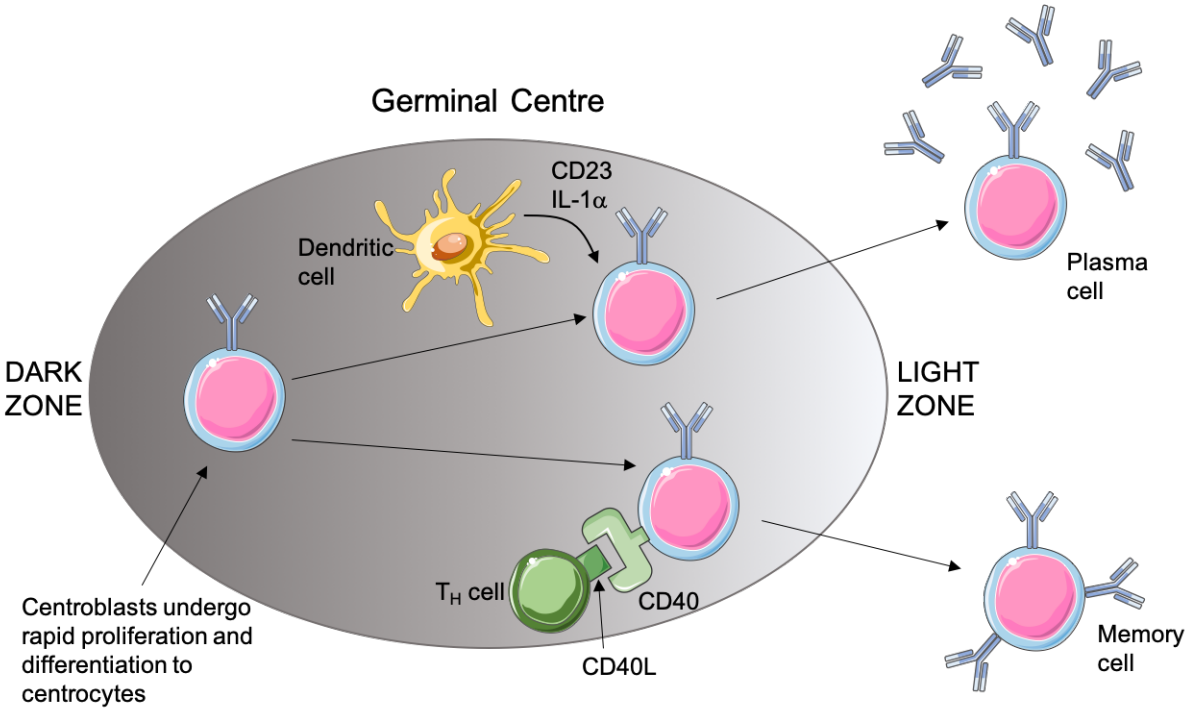

FIGURE 1-3: GERMINAL CENTRE (GC) REACTION.

Activated B cells that have encountered antigen form GCs where they undergo rapid proliferation and differentiation from centroblasts to centrocytes in the dark zone. Following division, B-cells migrate to the light zone where they interact with dendritic cells or T-helper cells to ensure their survival. B-cells compete to bind to dendritic cells ensuring that only B-cells with high antigen affinity progress, and interaction with cytokines, including CD23 and IL-1α, allow their differentiation into antibody-secreting plasma cells upon exit of the GC. Centrocytes that receive a signal from T-helper cells, through interaction of CD40 expressed on the centrocytes and CD40L expressed on T-helper cells, mature into long-lived memory B cells. B-cells in the GC that do not bind dendritic cells or receive signals from T-helper cells will die by apoptosis ensuring that only high-affinity B-cells complete the maturation process. Figure adapted from Kindt, Goldsby and Osborne, 2007 and prepared using Servier Medical Art.

1.3 The B-cell receptor and associated signalling pathways

1.3.1 The B-cell receptor

The BCR (**Figure 1-1**) is the key functional unit of normal B cells (Lam et al., 1997) and continues to play a major role post-transformation in determining the behaviour of malignant B cells (Young et al., 2019). Antigen engagement results in phosphorylation of conserved tyrosine residues within immunoreceptor tyrosine-based activation motifs (ITAMs) in the cytoplasmic domains of CD79A and CD79B by the kinase LYN (Yamanashi et al., 1991; Clark et al., 1992). This leads to recruitment (via its dual SH2 domains) and activation of a second kinase, SYK (Dai et al., 2006). This results in the assembly of a multiprotein complex termed the "signalosome" resulting in activation of protein and lipid kinases (e.g. BTK and phosphatidylinositol 3-kinase (PI3K)), adaptor molecules (BLNK) and other enzymes (e.g. phospholipase Cγ2 (PLCγ2)) (Fu et al., 1998; Marshall et al., 2000; Rickert, 2013). Furthermore, phosphorylation of CD19, a membrane protein functioning as a BCR coreceptor (Mette Buhl and Cambier, 1999), along with activated BLNK, recruits PI3K to the membrane (Marshall et al., 2000; Dai et al., 2006) where its substrate $PI(4,5)P_2$ is located.

The BCR "senses" the environment for molecules that bind with significant avidity and the strength and nature of the response following receptor engagement is varied (Packham et al., 2014). The level of stimulation and the context of antigen engagement determines whether antigen binding to normal B cells triggers signalling responses leading to survival/proliferation, apoptosis or anergy (Packham et al., 2014). The signals from the BCR drives the positive and negative selection of B cells establishing the balance between tolerance and immunity (Cornall and Goodnow, 1998). The BCR also mediates a low-level, antigen-independent "tonic'' signal, which is essential for B-cell survival (Lam et al., 1997).

1.3.2 B-cell receptor induced Ca^{2+} signalling

Although multiple pathways are activated downstream of the BCR, signalling via PLCγ2 leading to increased iCa^{2+} concentration ($i[Ca^{2+}]$) is particularly important for B-cell responses (Hikida et al., 2003). It is also the main focus of my studies. This section describes in detail the molecular events leading to increased $i[Ca^{2+}]$ via PLCγ2 and its functional consequences and is summarised in **Figure 1-4**.

The initial phase of increased i[Ca^{2+}] is mediated by IP_3 which triggers release of Ca^{2+} from endoplasmic reticulum (ER) stores (also see **Section 1.4.2**). Therefore, activation of PLCγ2 is the critical node downstream of the BCR in determining iCa^{2+} responses. PLCγ2 catalyses breakdown of the plasma membrane (PM)-associated inositol lipid, $PI(4,5)P_2$, to generate IP_3 and diacylglycerol (DAG) (**Figure 1-4**). DAG is retained within the PM whereas IP_3 is sufficiently water soluble to diffuse into the cytoplasm. Increased iCa^{2+}, triggered by IP_3, together with DAG accumulation leads to activation of protein kinase C isoforms which mediate activation of various MAPKs (ERK, c-JUN NH2-terminal kinase (JNK) and p38 MAPK), and nuclear translocation of the transcription factor Nuclear Factor-κB (NF-κB) (by inhibition of its inhibitor IKK) (Baba and Kurosaki, 2011; Scharenberg et al., 2007). Increased iCa^{2+} also activates calmodulin and calcineurin leading to nuclear translocation of Nuclear Factor of Activated T-cells (NFAT). NF-κB and NFAT in turn induce expression of target genes which promote B-cell survival (BCL2, BCL2A1), migration (CCR7) and proliferation (MYC, CCND1, CCND2) (Duyao et al., 1990; Pahl, 1999; Vogler, 2012; Iwanaga et al., 2008).

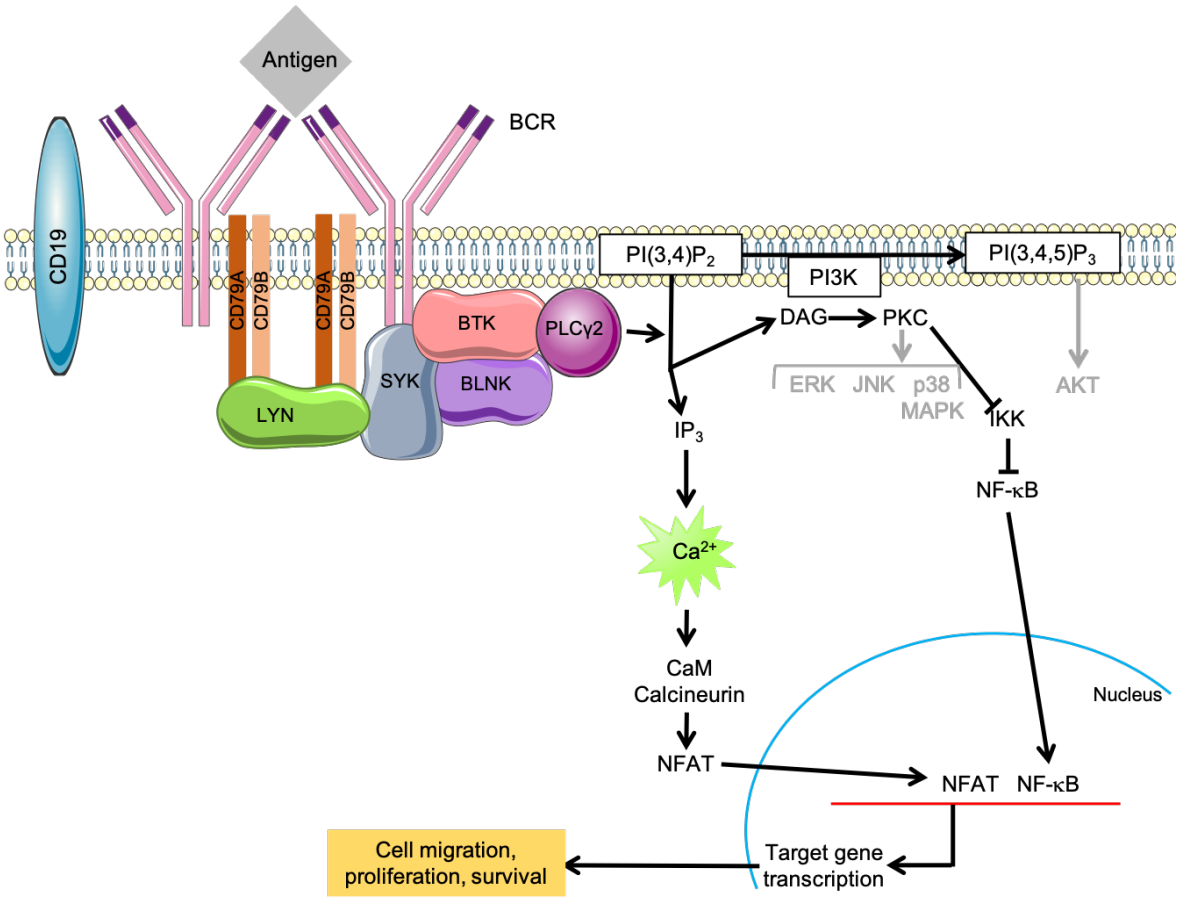

FIGURE 1-4: B-CELL RECEPTOR-ASSOCIATED INTRACELLULAR SIGNALLING PATHWAYS.

Engagement of the BCR initiates the formation of the signalosome, comprised of kinases, adapter molecules and other enzymes (e.g. LYN, SYK, BTK, BLNK and PLCγ2). The signalosome initiates many intracellular signalling pathways, including the production of IP_3 and DAG from $PI(4,5)P_2$, leading to the release of Ca^{2+} from intracellular stores. This illustration is simplified to show the most relevant pathways for this work. Adapted from (Stevenson et al., 2011) and prepared using Servier Medical Art.

1.3.3 Upstream pathways leading to PLCγ2 activation – the role of SYK, BTK, BLNK and PI3K

SYK is the main proximal kinase that initiates signalling downstream of the BCR leading to PLCγ2 activation. Thus, deletion of SYK in DT40 cells completely ablates anti-IgM-induced tyrosine phosphorylation of PLCγ2, accumulation of IP_3 and release of Ca^{2+} (Takata et al., 1994). (DT40 cells are derived from a chicken bursal lymphoma. They have a remarkably high rate of homologous recombination and are a commonly used model to investigate the effect of targeted gene ablation on BCR signalling responses (Winding and Berchtold, 2001)). Defective anti-IgM-induced iCa^{2+} release in SYK-deficient cells is rescued by enforced expression of wild type, but not kinase inactive SYK, demonstrating that it is the kinase activity of SYK that mediates anti-IgM-induced iCa^{2+} release.

Multiple studies have analysed the role of BTK, a Tec family non-receptor tyrosine kinase, in mediating BCR-induced iCa^{2+} responses downstream of SYK. Overall, these are consistant with the idea that BTK is an important mediator of BCR-induced iCa^{2+} mobilisation. However, these studies do reveal considerable complexities in this response, with evidence for both BTK-independent iCa^{2+} mobilisation, and an influence of BTK on the kinetics of the response. In addition to its role within the BCR-associated signalling pathway, BTK also contributes to other downstream signalling pathways initiated by other B-cell surface receptors including chemokine and toll-like receptors (de Gorter et al., 2007; Jefferies et al., 2003; Liu et al., 2011; Spaargaren et al., 2003). For example, BTK inhibition or deletion reduces CXCL12 (the major ligand for CXCR4)-mediated cell migration and adhesion, and homing of B cells to lymphoid organs *in vivo* (Guinamard et al., 1999). BTK also has important functions in non-B cells, for example it is important for FcγR-induced activation of pro-inflammatory cytokines in monocytes (Ren et al., 2016) and FcγRIIA-induced platelet activation (Goldmann et al., 2019).

The first study investigated phosphorylation-dependent activation of BTK kinase activity. SYK phosphorylates BTK on Tyr^{551}, located in the kinase domain of BTK, to increase BTK kinase activity (Kurosaki et al., 2000). This then results in autophosphorylation of BTK at Tyr^{223} (located in the SH3 domain) for full activation (Kurosaki and Kurosaki, 1997). A key property of Tec kinases distinct from other kinase families is their role in PLCγ2 activation and their ability to induce a sustained production of IP_3 required for iCa^{2+} mobilisation (discussed further in **Section 1.4**) (Scharenberg et al., 1998).

Deletion of BTK in DT40 cells completely abolishes anti-IgM-induced iCa^{2+} release and substantially (but not fully) reduces PLCγ2 tyrosine phosphorylation without effects on upstream phosphorylation of SYK or LYN (Takata and Kurosaki, 1996). In these experiments, reintroduction of wild type BTK expression restores anti-IgM-induced iCa^{2+} release confirming that the deficiency in BTK-depleted cells was due to the absence of BTK. Interestingly, reintroduction of a kinase inactive form of BTK partially restored iCa^{2+} release, although to a substantially lower level than the wild type protein. Thus, iCa^{2+} release is mainly mediated via BTK kinase activity but kinase-independent functions may also contribute. It is possible that kinase-independent activity is due to overexpression of non-physiological levels of BTK in these experiments, but this is one of several studies that point to a substantial kinase-independent function for BTK in iCa^{2+} release.

The function of BTK was also investigated by Fluckiger *et al*. in a series of experiments using B cells derived from X-linked agammaglobulinemia (XLA) patients (Fluckiger et al., 1998). XLA patients lack BTK expression due to loss-of-function germline mutations and this leads to absence of blood B cells and low levels of serum immunoglobulins (Tsukada et al., 1993; Vetrie et al., 1993). An analogous mutation of *Btk* in mice leads to the X-chromosome-linked immune-deficient (XID) phenotype which is characterised by a lack of antibody production to thymus-independent type 2 antigens, low levels of serum immunoglobulins, reduced numbers of B cells (B-cells are still present but respond abnormally and appear to be incapable of diversifying phenotypically and functionally due to disordered maturation), and an absence of proliferation in response to surface Ig cross-linking (Thomas et al., 1993; Rawlings et al., 1993). These findings suggest that the *xid* mutation causes a lack of essential signals for B cell activation and maturation (Rawlings et al., 1993).

B cells from normal donors and XLA patients were transformed with Epstein-Barr virus (EBV) resulting in immortalised BTK-replete and BTK-deficient B cell lines, respectively (Fluckiger et al., 1998). In these experiments, the transforming virus lacked LMP2 to avoid confounding effects of this viral membrane protein on signalling responses. In contrast to the experiments described above that were performed in DT40 cells (Takata and Kurosaki, 1996), iCa^{2+} release was substantially reduced, but not entirely absent in BTK-deficient cells. Therefore, in this system, BTK is important for anti-IgM-induced iCa^{2+} release but alternate pathways can also contribute. Anti-IgM-induced iCa^{2+} release could be rescued by overexpression of BTK, as well as other TEC-family

kinases (e.g. ITK and TEC), consistent with the idea that BTK is not obligate for iCa^{2+} release. When overexpressed in Ramos human lymphoma cells (which have endogenous BTK expression), BTK appeared to predominantly increase the duration, rather than the initial peak, of iCa^{2+} release. The mechanisms by which different phases of iCa^{2+} release and their biological importance are discussed in detail below (**Section 1.4**), but this observation suggests that the initial phase of iCa^{2+} release might not be absolutely dependent on BTK and that BTK mainly participates in subsequent phases that sustain iCa^{2+} levels. These different phases were linked to the initial IP_3-driven release of iCa^{2+} from the ER and subsequent influx of extracellular Ca^{2+}, respectively.

Tomlinson *et al*. also performed reconstitution experiments in BTK-deficient DT40 cells, but using an oestrogen-mediated inducible system to investigate whether BTK was sufficient to induce iCa^{2+} release in the absence of sIgM activation (Tomlinson et al., 2001). Activation of this conditional form of BTK alone induced low level, sustained iCa^{2+} release suggesting BTK is sufficient for the delayed but not initial phase of anti-IgM-induced iCa^{2+} release. This effect was dependent on the kinase activity of BTK since activation of a kinase-inactive form of BTK had no effect on iCa^{2+} in the absence of anti-IgM. Interestingly, like wild type BTK, this kinase-inactive form of BTK could reconstitute both the early and delayed phases of iCa^{2+} release in cells with anti-IgM co-stimulation again revealing kinase-independent BTK functions.

In addition to direct phosphorylation of BTK, SYK also phosphorylates and activates a non-catalytic, adapter protein call BLNK (Kurosaki and Tsukada, 2000). BLNK was initially demonstrated to bind to both SYK and PLCγ2 (as well as other signalling molecules including Vav, GRB2 and NCK) and overexpression of wild-type (but not non-phosphorylatable mutant) BLNK increases anti-IgM induced phosphorylation (Fluckiger et al., 1998) and iCa^{2+} release in Daudi human lymphoma cells (Fu et al., 1998). Subsequent experiments demonstrated that phosphorylated BLNK also bound BTK (Su et al., 1999; Hashimoto et al., 1999). The principal role of BLNK in iCa^{2+} signalling is to act as an adaptor to facilitate activating interactions between SYK/BTK and PLCγ2 (Fluckiger et al., 1998; Kurosaki and Tsukada, 2000).

An important issue to consider is the extent of linkage between BTK/PLCγ2 and PI3K pathways downstream of the BCR (Scharenberg and Kinet, 1998). Activated BLNK recruits PI3K to the membrane (Marshall et al., 2000; Dai et al., 2006) where its substrate $PI(4,5)P_2$ is located. PI3K phosphorylates $PI(4,5)P_2$ to generate $PI(3,4,5)P_3$, which acts as a docking site for the PH domains

of Tec family kinases (including BTK) (Salim et al., 1996), as well as AKT (Stokoe et al., 1997) (**Figure 1-4**). Thus, PI3K is thought to be required for the proper localisation of BTK, which is important for the activation of PLCγ2 (Mette Buhl and Cambier, 1999; Kim et al., 2004).

Several lines of evidence demonstrate that, at least in some systems, PI3K promotes anti-IgM-induced iCa^{2+} release. Chemical inhibition of PI3Kδ (i.e. with idelalisib) reduces BTK activation, BTK-dependent PLCγ2 phosphorylation and IP_3 production following anti-IgM activation (Hippen et al., 1997; Mette Buhl and Cambier, 1999; Kim et al., 2004). The influence of PI3K is likely mediated via accumulation of PIP_3 which promotes localisation of BTK (and PLCγ2) to the PM via their PH domains (Scharenberg et al., 1998). The contribution of PI3K to PLCγ2 activation appears to be modulatory rather than obligate since PI3K inhibitors only partially reduce IP_3 production and PLCγ2 phosphorylation, and to a lesser extent than PI3K inhibitors suppress AKT activation (Hippen et al., 1997; Mette Buhl and Cambier, 1999; Kim et al., 2004). This interface between PI3K and PLCγ2 activation provides a mechanism to explain how anti-IgM-induced iCa^{2+} release can be modulated by CD19 (which can play an important role in PI3K activation) and inhibitory receptors such as FcγRIIB which reduce PIP_3 levels by activation of the SHIP1 phosphatase (Hippen et al., 1997; Mette Buhl and Cambier, 1999; Scharenberg et al., 1998).

In addition to this upstream influence of PI3K, BTK may also be required for PI3K activity, independent of its kinase activity. Thus, BTK associates with phosphatidylinositol 4-phosphate 5-kinase (PIP5K), the enzyme that catalyses production of $PI(4,5)P_2$ and promotes recruitment of PIP5K to the PM following BCR stimulation to sustain $PI(4,5)P_2$ levels (Saito et al., 2003).

Joseph *et al.* probed the interdomain interactions within BTK (Joseph et al., 2017). They reported that unphosphorylated BTK exists in a dynamic equilibrium between multiple conformational states, with the predominant state in solution conforming to the autoinhibited state. The changes in BTK upon $PI(3,4,5)P_3$ binding are consistent with a conformational change from a closed autoinhibited conformation to that of an open active state providing further evidence that $PI(3,4,5)P_3$ is required for the continued activation of BTK allowing further downstream signalling events.

Overall, BTK is the core component upstream of PLCγ2, but studies point to variability, especially in regard to its impact on kinetics and potential non-kinase mediated functions, which will be critical to explore and understand further.

1.3.4 PLCγ2 phosphorylation

The main purpose of PLCγ2 in BCR signalling is to hydrolyse $PI(4,5)P_2$ to generate DAG and IP_3, which results in increased $i[Ca^{2+}]$. Although there is broad acceptance that PLCγ2 activation involves increased tyrosine phosphorylation, the role of individual phosphorylation sites and the role of BTK and other kinases in phosphorylating these sites remains incompletely understood. The domain structure of PLCγ2 (and PLCγ1) is shown in **Figure 1-5** and highlights the key phosphorylation sites. The main sites of PLCγ2 implicated downstream of the BCR are Tyr^{753} and Tyr^{759}, in the SH2-SH3 linker region of the catalytic domain, and Tyr^{1197} and Tyr^{1217} in the C-terminal region.

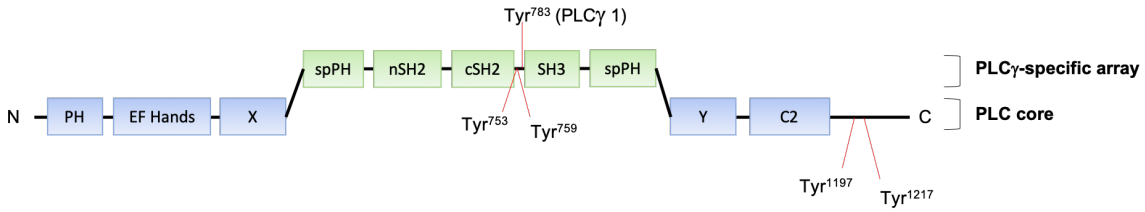

FIGURE 1-5: DOMAIN ORGANISATION OF PLCγ.

PLCγ1 and PLCγ2 share high sequence identity across their domain structure and are comprised of a core set of domains, referred to as the PLC core, and a PLCγ specific array that is involved with interaction with other proteins. The PLC core incorporates a pleckstrin homology (PH) domain, EF-hands, a TIM-barrel-like fold separated into two halves, termed X and Y, and a C2 domain. The PLCγ specific array contains a split PH (spPH) domain, two SH2 domains and an SH3 domain. The four canonical PLCγ2 tyrosine phosphorylation sites are indicated on the figure along with the key tyrosine phosphorylation site of PLCγ1. Figure drawn from information provided in (Koss et al., 2014; Rodriguez et al., 2001; Humphries et al., 2004).

Rodriguez *et al.* investigated the role of the Tyr^{753} and Tyr^{759} sites in reconstitution experiments in PLCγ2-deficient DT40 cells (Rodriguez et al., 2001). In contrast to wild type PLCγ2, enforced expression of PLCγ2 with substitutions of either Tyr^{753} or Tyr^{759} is unable to reconstitute anti-IgM-induced iCa^{2+} release. Mutation of both sites appears to completely ablate anti-IgM-induced PLCγ2 tyrosine phosphorylation suggesting that Tyr^{753} and Tyr^{759} are major sites of phosphorylation. However, the sensitivity of detection of total PLCγ2 tyrosine phosphorylation

was rather low in these experiments, so it was not clear that Tyr^{753} or Tyr^{759} were the only sites of PLCγ2 phosphorylation induced in these experiments, and the effect of mutations at Tyr^{1197} and Tyr^{1217} was not addressed. *In vitro* experiments demonstrated that Tyr^{753} and Tyr^{759} could be phosphorylated by BTK as well as various SRC-family kinases, including SRC, LCK and FYN. SYK could also phosphorylate PLCγ2 Tyr^{753} and Tyr^{759}, but its activity seemed relatively weak compared to the other kinases tested.

A similar analysis was performed by Watanabe *et al.*, but with extension to encompass the PLCγ2 C-terminal sites (Watanabe et al., 2001). These authors demonstrated using *in vitro* assays that BTK can phosphorylate all four of the major PLCγ2 phospho-acceptor sites and that, in DT40 cells, individual mutation of each site reduces, but does not ablate the ability of PLCγ2 to reconstitute anti-IgM-induced iCa^{2+} release. Simultaneous mutation of all four sites is required to ablate PLCγ2 activity.

Ozdener *et al.* demonstrated that, in addition to BTK, FCK, LCK and LYN kinases could also phosphorylate PLCγ2 *in vitro* (Ozdener *et al*., 2002). Mutation of Tyr^{753} and Tyr^{759} demonstrated that these sites are required for LCK-mediated phosphorylation and for the ability of LCK to increase PLCγ2 activity.

Kim *et al*. used mutations of PLCγ2 phosphorylation sites expressed in Ramos human lymphoma cells to probe the role of upstream kinases in regulating PLCγ2 phosphorylation (Kim et al., 2004). This study detected anti-IgM-induced phosphorylation of Tyr^{753}, Tyr^{759} and Tyr^{1217}, but not Tyr^{1197}. Given than anti-IgM-induced PLCγ2 Tyr^{1197} has been observed in other studies (Humphries et al., 2004; Watanabe et al., 2001), failure to detect phosphorylation at this site likely reflects a technical issue with the specific phospho-specific antibody used to detect modification of this site in this study. Depletion of SYK using RNA interference (RNAi) reduced phosphorylation of Tyr^{753}, Tyr^{759} and Tyr^{1217}, consistent with previous studies in DT40 cells (Takata et al., 1994) revealing an essential, initiating role for SYK upstream of PLCγ2. A chemical BTK inhibitor (BTKi) or RNAi to downregulate BTK expression, reduced Tyr^{753} and $Tryr^{759}$ phosphorylation, but had no effect of phosphorylation at Tyr^{1217}.

Humphries *et al*. investigated PLCγ2 phosphorylation in XLA cells (Humphries et al., 2004). In these experiments, lack of BTK in XLA cells was associated with reduced but not ablated iCa^{2+} release. It is not clear why the impact of BTK deficiency differs between the studies of Humphries *et al*. (partial) (Humphries et al., 2004) and Takata *et al*. (full block) (Takata et al., 1994), but this may relate to differences in the model systems used (human B-cell lines versus DT40 cell line, respectively) and therefore how the cells were cultured, stimulated and the levels of extracellular Ca^{2+}. Mutation of both Tyr^{753} and Tyr^{759} substantially reduced anti-IgM-induced iCa^{2+} release. Phosphorylation at these sites was substantially reduced in BTK-deficient cells but Tyr^{753} and Tyr^{759} phosphorylation in BTK-deficient cells could be rescued by overexpression of TEC or ITK, but not SYK. Finally, anti-IgM-induced phosphorylation of Tyr^{1197} and Tyr^{1217} was unaffected by the absence of BTK.

These findings led to an initial mechanistic model for anti-IgM-mediated PLCγ2 activation (Rawlings, 1999) (**Figure 1-6**). The first key step in this proposed model is activation of SYK which then phosphorylates BLNK to recruit PLCγ2 within the signalosome. In this initial phase, direct phosphorylation of PLCγ2 by SYK may initiate activation. SYK then phosphorylates BTK which, with BLNK, promotes further PLCγ2 activity. Such a model is consistent with observations that BTK is not essential for anti-IgM-induced iCa^{2+} release in some models and that the contribution of BTK may differ at different stages of the response (i.e. initial versus sustained). However, it is important to bear in mind that several lines of evidence point to additional, kinase independent roles for BTK, and that additional kinases may contribute. Moreover, current data do not provide a consensus on the identity of BTK-dependent and BTK-independent PLCγ2 phosphorylation sites. For example, Humphries *et al*. (Humphries et al., 2004) demonstrated a partial BTK-dependency, whereas Takata *et al*. (Takata et al., 1994) demonstrated a full BTK-dependency for PLCγ2 phosphorylation. Takata *et al*. (Takata et al., 1994) also demonstrated an important role for SYK in PLCγ2 phosphorylation whereas Rodriguez *et al*. (Rodriguez et al., 2001) concluded that SYK-induced phosphorylation of PLCγ2 was relatively weak, and Humphries *et al*. (Humphries et al., 2004) stated that there was no role for SYK. Therefore it is important that future work fully resolves which phosphorylation sites are important for initiating downstream pathways, as well as which kinases act on them, particularly in the setting of malignant B-cells which this pathway is a target for therapeutic intervention.

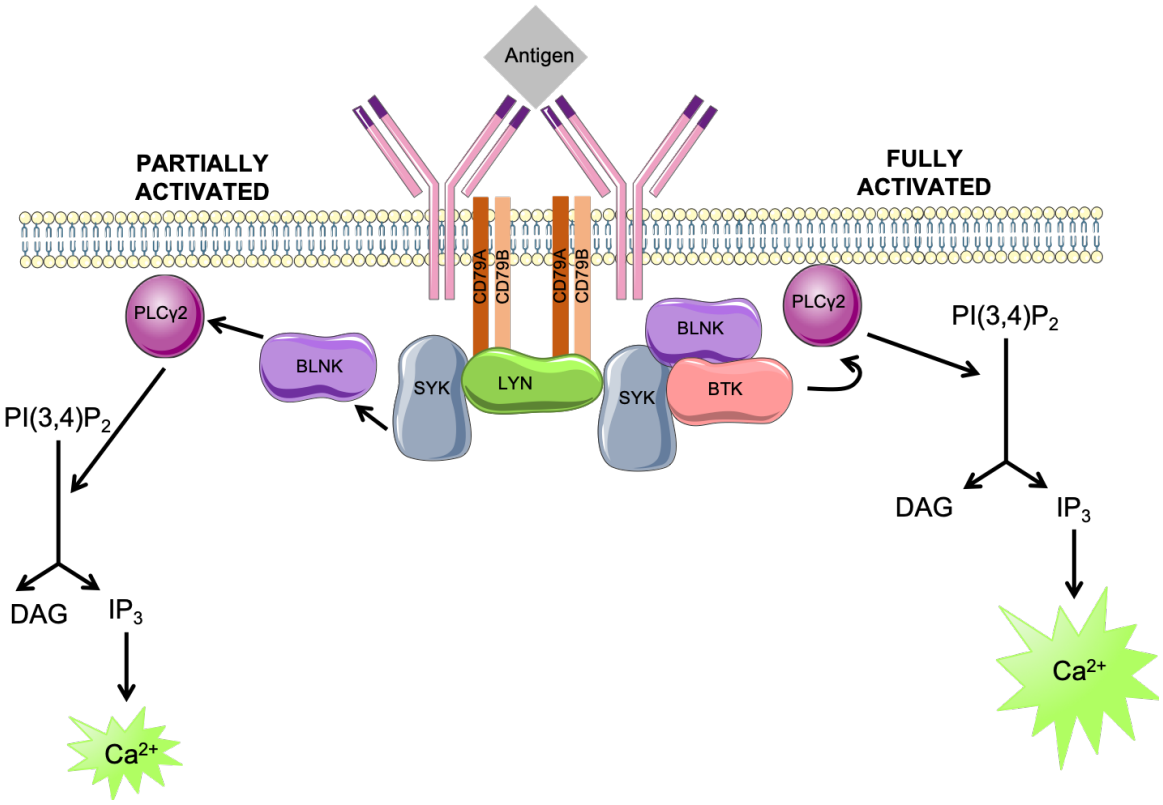

FIGURE 1-6: MECHANISTIC MODEL FOR ANTI-IGM MEDIATED PLCγ2 ACTIVATION.

Upon BCR engagement, activation of SYK is one of the first key steps, and it has been proposed that SYK can directly activate PLCγ2 with the help of BLNK (left hand pathway). This only allows for partial activation of PLCγ2 and therefore a smaller amount of Ca^{2+} is released from iCa^{2+} stores. In contrast, if SYK activates BTK and BTK subsequently activates PLCγ2, there is full activation and a greater mobilisation of iCa^{2+} (right hand pathway). Figure based on (Rawlings, 1999) and prepared using Servier Medical Art.

1.3.5 Activation of PLCγ1 following BCR stimulation

Although most studies have focused on PLCγ2 it is important to recognise that PLCγ1 is also expressed in at least some B cells and has the same catalytic activity as PLCγ2. *In vitro* studies have demonstrated that SYK can phosphorylate PLCγ1 at Tyr^{783}, a critical site for activation by PDGF or EGF (Law et al., 1996), located in the SH2-SH3 linker region of the catalytic domain (**Figure 1-5**). Moreover, anti-IgM induces BTK-dependent phosphorylation of PLCγ1 at Tyr^{783} in human B-cell lines (Humphries et al., 2004). Thus, in some settings PLCγ1 activation may contribute to anti-IgM-induced iCa^{2+} release in B cells.

1.3.6 Rac-mediated PLCγ2 activation

Walliser *et al.* demonstrated that interactions between Vav/Rac and PLCγ2 amplified BCR-induced Ca^{2+} responses and its associated effects e.g. translocation of NFAT to the nucleus (Walliser et al., 2015). Activated Rac, a small GTPase, can bind and activate PLCγ2 (Piechulek et al., 2005) through direct protein-protein interactions, which is phosphorylation-independent (Koss et al., 2014). Vav, a Rac activator, can physically interact with SYK, BTK and BLNK demonstrating that PLCγ2 activation through the Rac pathway can be initiated by BCR engagement (Walliser et al., 2015).

1.4 iCa^{2+} signalling

Ca^{2+} is a universal signalling molecule with a low cytosolic resting concentration (~10^{-7} M) and a high extracellular concentration (~10^{-3} M) (Uhlén and Fritz, 2010). Ca^{2+} signals can be classified as transient, sustained or oscillatory.

1.4.1 Transient Ca^{2+} signals

Transient Ca^{2+} signals occur when Ca^{2+} is released from ER stores. Due to the physical limitation of the Ca^{2+} store, this response will be short-lived (Scharenberg et al., 2007). Enzymatic activity of PM-tethered PLCγ2 increases following tyrosine phosphorylation allowing $PI(4,5)P_2$ to be hydrolysed producing the second messengers DAG and IP_3 (Junek et al., 2012). DAG activates the PKC pathway and IP_3 binds to its receptor (IP_3R), located on the ER membrane (Takata et al., 1994; Humphries et al., 2004), causing a conformational change in IP_3R (Uhlén and Fritz, 2010). The

conformational change opens Ca^{2+} channels allowing Ca^{2+} to move from the ER lumen to the cytosol (Uhlén and Fritz, 2010) increasing i[Ca^{2+}].

1.4.2 Sustained Ca^{2+} signals: store-operated Ca^{2+} entry

Sustained increases in i[Ca^{2+}] occur through a process known as store-operated Ca^{2+} entry (SOCE) and are required for many mechanisms including proliferation and differentiation of naïve B cells (Fluckiger et al., 1998). Regulation of i[Ca^{2+}] is vital since a lack of iCa^{2+} mobilisation, as seen in anergic cells, leads to cell death but sustained high levels of i[Ca^{2+}] becomes toxic to cells so also leads to cell death through necrosis and apoptosis (Fluckiger et al., 1998; Uhlén and Fritz, 2010).

Following internal Ca^{2+} store depletion, SOCE is activated, allowing extracellular Ca^{2+} to flow into the cells and ultimately allow the reuptake of Ca^{2+} ions into the ER lumen to replenish the stores (**Figure 1-7**). SOCE is mainly observed in non-excitable cells and is regulated by stromal interaction molecules (STIM) and Orai proteins (Uhlén and Fritz, 2010).

Members of the STIM family of single-transmembrane proteins sense reduced ER Ca^{2+} concentration (Scharenberg et al., 2007; Baba et al., 2014). There are two human STIM proteins and both are predominantly located in the ER (Hogan and Rao, 2015). STIMs have an N-terminal domain located in the ER lumen consisting of an EF-hand, which binds Ca^{2+}, and a sterile-α motif (SAM) (Smyth et al., 2010; Hogan and Rao, 2015). A single transmembrane segment connects the EF-hand to the C-terminal cytoplasmic tail, which interacts with $PI(4,5)P_2$ (Hogan and Rao, 2015). Following depletion of Ca^{2+} in the ER stores and dissociation of Ca^{2+} from the EF-hand, STIM moves within the ER membrane to ER-PM junctions where they then recruit Orai proteins (Smyth et al., 2010; Baba et al., 2014; Hogan and Rao, 2015). STIMs are thought to undergo a Ca^{2+}-dependent conformational change leading to a direct interaction with a PM Ca^{2+} release-activated channel (CRAC) encoded by multimers of Orai (Scharenberg et al., 2007). Orai proteins, consisting of 4 transmembrane helices (Hogan and Rao, 2015), function as pore-forming subunits of SOCE (also known as CRAC) channels (Smyth et al., 2010). Activated SOCE channels allow extracellular Ca^{2+} influx to the cytoplasm allowing Ca^{2+} signalling to continue beyond the point of ER-store depletion, as well as providing a source for refilling of the ER stores (Scharenberg et al., 2007).

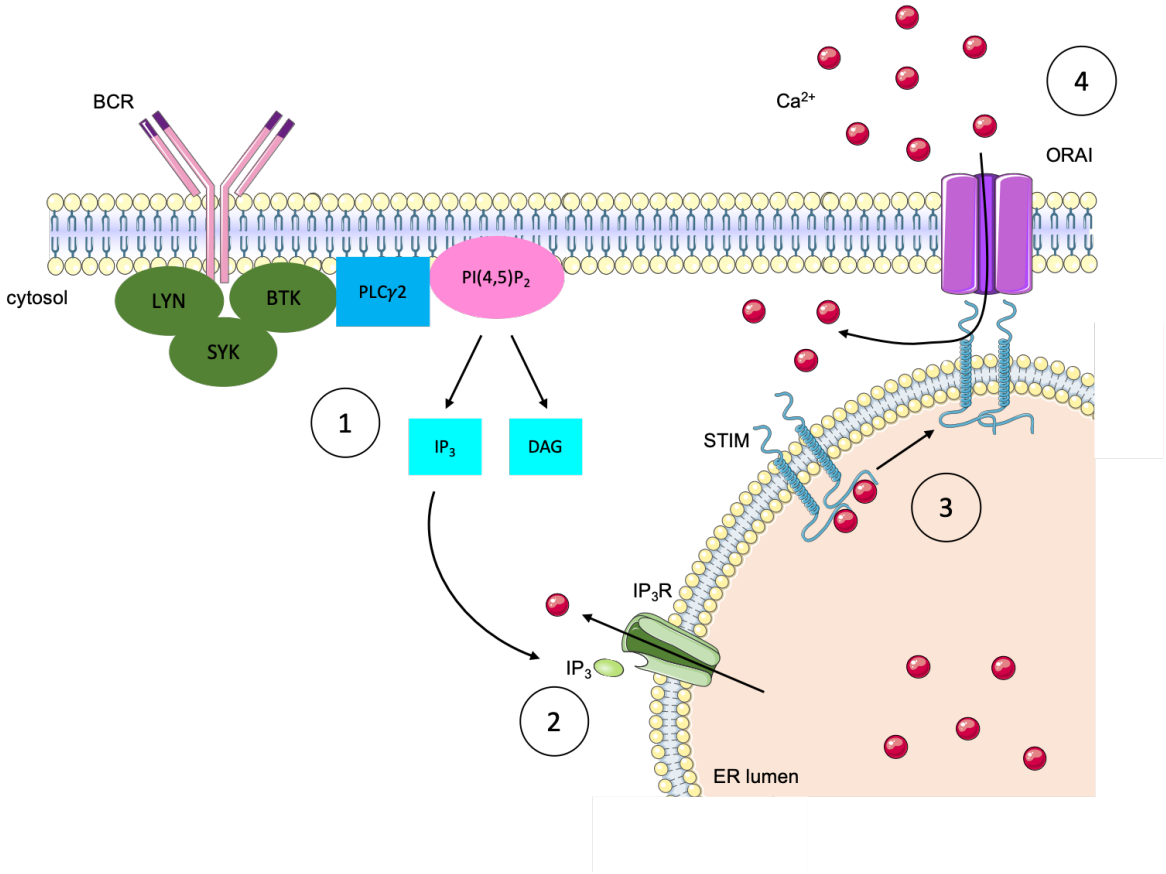

FIGURE 1-7: MECHANISM OF STORE-OPERATED CA^{2+} ENTRY (SOCE).

1) Activation of the B-cell receptor initiates an intracellular signalling cascade leading to the hydrolysis of $PI(4,5)P_2$ by PLCγ2, producing DAG and IP_3. 2) IP_3 binds to its receptor (IP_3R) on the endoplasmic reticulum (ER) membrane which causes a conformational change in the receptor allowing Ca^{2+} to move into the cytosol from the ER stores. 3) STIM contains an EF-hand domain which can sense Ca^{2+}; STIM is oriented in such a way that the EF-hand will be in the ER lumen. Following depletion of ER Ca^{2+}, and the subsequent dissociation of Ca^{2+} from the EF-hand domain, STIM will translocate to ER-plasma membrane junctions where it can recruit Orai proteins. 4) Orai proteins are pore-forming and following their activation will allow extracellular Ca^{2+} to enter the cell. Figure prepared using Servier Medical Art.

1.4.3 Oscillatory Ca^{2+} signals

Oscillatory Ca^{2+} signals can vary in frequency and amplitude, which correspond to different effector functions. These oscillatory responses cannot be tracked with flow cytometry, but do have important biological relevance and therefore highlight the importance of developing new approaches to quantify time-resolved, single-cell iCa^{2+} mobilisation. A key mechanism in the regulation of Ca^{2+} oscillations is a process called Ca^{2+}-induced Ca^{2+} release (CICR), which amplifies the signal and acts on the IP_3R (Uhlén and Fritz, 2010). When the i[Ca^{2+}] increases above 10^{-6} - 10^{-5} M, binding of Ca^{2+} ions to inhibitory sites within IP_3R prevents further release of Ca^{2+} (Uhlén and Fritz, 2010).

Early investigations into positive versus negative signalling responses in B cells and Ca^{2+} sensitivity and response dynamics of transcriptional regulators exploited the hen egg lysozyme (HEL) model. The HEL model is used to investigate anergy and uses transgenic mice expressing an immunoglobulin molecule specific against the HEL antigen (Cambier et al., 2007). B cells that express a BCR specific for the HEL antigen but mature in a mouse without being exposed to HEL antigen are naïve cells. B cells with the same BCR, but develop in mice where HEL antigen is chronically encountered as a self-antigen (i.e. lacking cognate T-cell help), will be tolerant, mature B cells; they have low-level, chronic signalling, but do not respond to further antigen addition.

Acute stimulation of naïve B cells with HEL and phorbol ester evoked a biphasic Ca^{2+} response, which consisted of an initial rapid and transient increase of i[Ca^{2+}] followed by a smaller persistent Ca^{2+} plateau (Dolmetsch et al., 1997; Healy et al., 1997). In contrast, i[Ca^{2+}] in tolerant B cells, which exhibit elevated basal i[Ca^{2+}], was not increased upon further BCR engagement (Healy et al., 1997). The single cell analysis of tolerant B cells revealed that the mean elevation of the basal i[Ca^{2+}] was a result of Ca^{2+} oscillations which could be rapidly quenched by chelation of extracellular Ca^{2+}; these oscillations are thought to arise from continued stimulation of the self-reactive BCR by HEL (Healy et al., 1997). Dolmetsch *et al.* showed that the Ca^{2+} spike could be generated in isolation by exposing the cells to ionomycin shortly before chelating extracellular Ca^{2+} using EGTA (Dolmetsch et al., 1997). This allowed them to determine that Ca^{2+} mobilisation produced by antigen engagement or ionomycin are attributable to Ca^{2+} release from internal stores (~25%) and to extracellular Ca^{2+} influx (~75%) (Dolmetsch et al., 1997).

The initial observations led the group to question whether the spike and plateau phases of the Ca^{2+} response activate distinct transcriptional pathways. Activation of NFAT was determined by its translocation to the nucleus. Western blot analysis detected dephosphorylated (activated) NFAT in the nuclei of freshly isolated tolerant B cells (Healy et al., 1997); complete activation occurred within 1 minute of exposure to HEL (Dolmetsch et al., 1997). In naïve B cells, dephosphorylated NFAT was only detected in the nucleus following stimulation suggesting that the circulating self-antigen induces low level Ca^{2+} oscillations which allow the translocation of NFAT to the nucleus despite there being no initial i[Ca^{2+}] peak (Healy et al., 1997). Healy *et al.* (1997) noted that the ERK pathway also requires continued exposure to self-antigen to remain activated. The authors showed approximately 15% of ERK2 was already phosphorylated in freshly isolated tolerant B cells but was only phosphorylated in naïve B cells following *in vitro* stimulation. The opposite was true of IκBα (cytoplasmic inhibitor of NF-κB) degradation. In naïve B cells, BCR stimulation induced IκBα degradation and the subsequent translocation of c-Rel and Rel-A (NF-κB subunits) within 15 minutes; this could be blocked by Ca^{2+} chelation (Healy et al., 1997). In freshly isolated tolerant B cells, IκBα degradation and nuclear translocation of c-Rel and Rel-A were not apparent and were not induced by *in vitro* stimulation with HEL antigen (Healy et al., 1997). This suggests a strong connection between the amount of BCR-induced protein tyrosine phosphorylation and Ca^{2+} signalling with the activation of different transcriptional pathways in tolerant B cells.

Cytosolic Ca^{2+} oscillations are a nearly universal mode of signalling in both excitable and non-excitable cells and whilst Ca^{2+} is known to mediate a diverse range of cell functions, it was not known whether the oscillations contribute to the signalling efficiency or specificity. Dolmetsch, Xu and Lewis (1998) suggested that oscillations in i[Ca^{2+}] might be beneficial for receptor-mediated signal transduction, e.g. by increasing the fidelity of low-level signalling, preventing desensitisation or increasing signalling specificity. Through development of a Ca^{2+} clamp technique, the authors investigated the role of oscillations with respect to the activation of several transcription factors including NFAT and NF-κB. They treated Jurkat T cells with thapsigargin, an inhibitor of ER Ca^{2+} ATPases that depletes internal Ca^{2+} stores and irreversibly activates store-operated CRAC channels in the plasma membrane (Dolmetsch et al., 1998; Debant et al., 2015). This allows elevation of i[Ca^{2+}] owing to Ca^{2+} influx through CRAC channels and removal of extracellular Ca^{2+} allows pumps in the membrane to return i[Ca^{2+}] to baseline levels and so by rapidly changing the concentration of extracellular Ca^{2+} it is possible to generate Ca^{2+} oscillations with a uniform frequency and amplitude (Dolmetsch et al., 1998). They report that oscillations reduce the effective Ca^{2+} threshold for activating transcription factors, which therefore increases signal detection at low levels of stimulation. Specificity of the signal is

encoded by the frequency of the oscillations with rapid oscillations stimulating all three transcription factors assessed (NFAT, NF-κB and Oct/OAP), whereas infrequent oscillations stimulated NF-κB alone (Dolmetsch et al., 1998). Whilst Dolmetsch, Xu and Lewis (1998) found that oscillation amplitude is unlikely to contribute significantly to selectivity between the pathways investigated, they did find that oscillation frequency determines which combination of transcription factors are active. Low oscillation frequencies activate NF-κB whereas higher frequencies activate NFAT, Oct/OAP and NF-κB. Dolmetsch, Xu and Lewis (1998) concluded that Ca^{2+} oscillations increase both the efficacy and specificity of the signals leading to gene expression and cell differentiation.

1.5 B-cell malignancies

B-cell malignancies encompass a broad range of cancer types ranging from indolent to aggressive disease. This section focusses on CLL, as primary CLL cells are used for most of the experiments described in this thesis. It also introduces diffuse large B-cell lymphoma (DLBCL), as established DLBCL-derived cell lines are also used as experimental models in some studies.

1.5.1 Chronic lymphocytic leukaemia

CLL is the most common leukaemia in the UK accounting for ~1% of all new cancer cases with ~3800 cases diagnosed every year (https://www.cancerresearchuk.org/about-cancer/chronic-lymphocytic-leukaemia-cll [accessed February 2021]). CLL more commonly affects people over the age of 60 (median age at diagnosis is ~70 years) (Kipps et al., 2017) and the disease is very rare in people ≤40 years old. It is more prevalent in men than women (at a 2:1 ratio), although it is not yet known why, and men may have a less favourable outcome (Catovsky, Fooks and Richards, 1989).

CLL is a low-grade B-cell malignancy characterised by the accumulation of mature $CD19^+$ $CD5^+$ B-cells in the blood, bone marrow and SLO, such as the lymph nodes and spleen (Kipps et al., 2017). CLL cells generally coexpress sIgM and sIgD, although at low levels compared with normal B cells. (Hamblin et al., 1999). The clinical course is highly heterogeneous with some patients requiring immediate treatment and others are managed by a “watch and wait” strategy where patients are generally not recommended for treatment unless the symptoms worsen or disease progression

becomes apparent. Patients often do not exhibit any symptoms and the disease may be diagnosed through routine blood tests. The symptoms associated with CLL are vague and can easily be the result of other illnesses. They tend to progress slowly but do get worse over time. Progressive disease course typically follows a response/relapse pattern whereby patients initially respond to treatment but then relapse and eventually succumb to the disease. The symptoms associated with CLL are the result of the accumulation of abnormal B-cells, which mean that patients cannot elicit adequate immune responses, therefore patients are more susceptible to infections. The accumulation of CLL cells in bone marrow can lead to bone pain, and lymph nodes or spleen lead to enlargement of lymph nodes/spleen. The accumulation of CLL cells in the bone marrow also interferes with other blood cell production. Red blood cell production decreases leading to anaemia, which makes patients feel breathless and tired, and platelet production decreases reducing the ability of blood to clot so patients become more susceptible to bleeding and bruising. Other common symptoms include weight loss and night sweats.

There are two main staging systems for CLL that are used by clinicians to assist with decision making for treatment strategies and care plans. The staging systems are called Binet (used primarily in the UK and Europe) (**Table 1-1**) and Rai (used primarily in the USA) (**Table 1-2**) (Binet *et al*., 1981; Rai *et al*., 1975). These staging systems often fail to accurately predict the clinical course of such a heterogeneous disease so other prognostic markers are a key area of research within the disease. Current prognostic markers include the presence or absence of somatic mutations in the *IGHV* genes, cell surface expression of molecules including CD38, CD49d, and CXCR4, intracellular expression of ZAP70, and other genetic risk factors. *IGHV* gene mutation status and the presence of del(17p) or mutated TP53 are the most important features directing therapy choices (discussed in more detail throughout this section).

CLL can be categorised into two major subgroups depending on the B-cell of origin from which the leukaemia is derived and this is determined by the mutational status of the expressed BCR-encoding *IGHV* gene; these are classified as unmutated (U)-CLL and mutated (M)-CLL (Damle et al., 1999; Hamblin et al., 1999). Unmutated cases are defined as those with >98% similarity to the germline sequence and mutated cases are defined as those with ≤98% similarity to the germline sequence (Damle et al., 1999). U-CLL, of poorer prognosis, is derived from B-cells prior to SHM, whereas M-CLL is derived from post-GC B-cells, which have undergone the process of SHM, and is associated with less aggressive disease (Stevenson and Caligaris-Cappio, 2004; Mockridge et al., 2007; Stevenson et al., 2011; Packham et al., 2014) (**Figure 1-8**). The 10-year survival for patients

diagnosed with U-CLL is around 30-35%, whilst for patients diagnosed with M-CLL, it is ~85% (Damle et al., 1999; Hamblin et al., 1999).

TABLE 1-1: BINET STAGING SYSTEM.

Stage	Clinical indication	Risk	Median survival (years)
A	<3 groups or enlarged lymph nodes, and high WBC count	Low	13
B	>3 groups of enlarged lymph nodes, and a high WBC count	Intermediate	8
C	Enlarged lymph nodes or spleen, high WBC count, anaemia and/or thrombocytopenia	High	2

(https://www.cancerresearchuk.org/about-cancer/chronic-lymphocytic-leukaemia-cll/staging [accessed February 2021]).

TABLE 1-2:RAI STAGING SYSTEM.

Stage	Clinical indication	Risk	Median survival (years)
0	Lymphocytosis only	Low	13
I	Lymphocytosis, enlarged lymph nodes	Low	13
II	Lymphocytosis, enlarged spleen and/or liver, lymph nodes may or may not be enlarged	Intermediate	8
III	Lymphocytosis, lymph nodes, spleen or liver may or may not be enlarged, anaemia	High	8
IV	Lymphocytosis, enlarged lymph nodes, liver or spleen, patient may or may not be anaemic, thrombocytopenia	High	2

(https://www.cancer.org/cancer/chronic-lymphocytic-leukemia/detection-diagnosis-staging/staging.html [accessed Febraury 2021]).

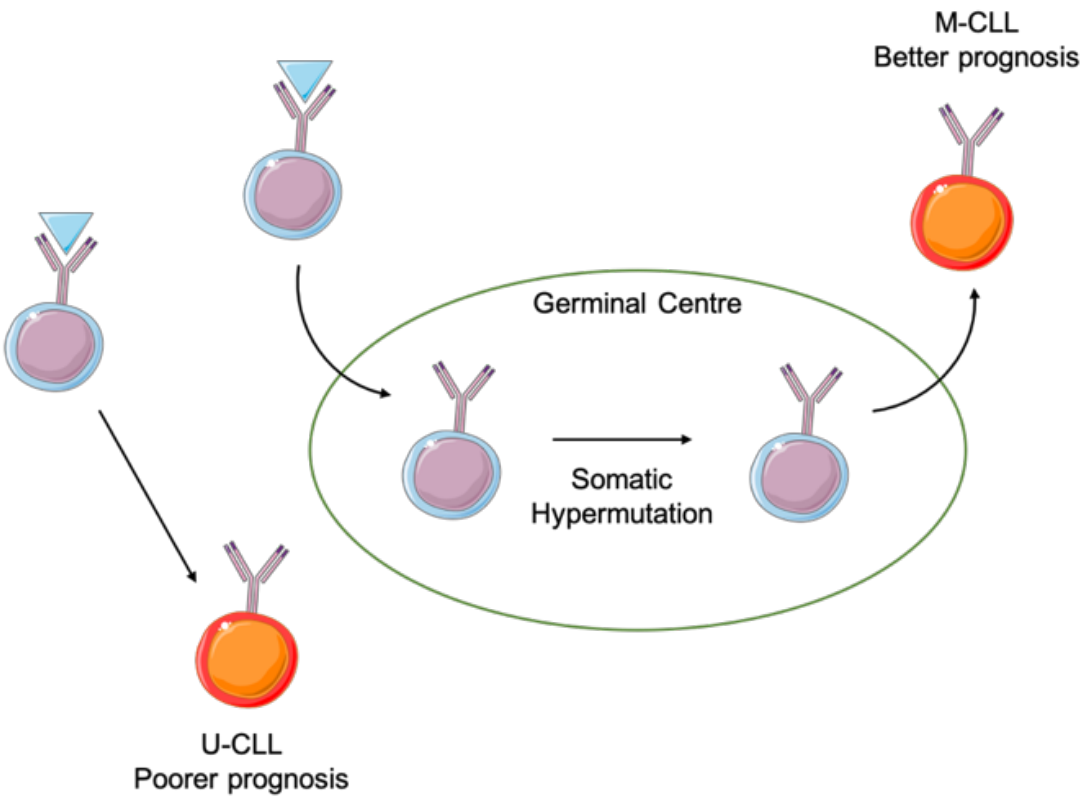

FIGURE 1-8: CELLULAR ORIGIN OF CHRONIC LYMPHOCYTIC LEUKAEMIA (CLL).

CLL can be divided into 2 major subgroups termed unmutated (U)-CLL and mutated (M)-CLL. U-CLL is derived from B cells prior to somatic hypermutation and has a poorer prognosis. M-CLL is derived from post-germinal centre B cells, which have undergone somatic hypermutation in the germinal centre and is associated with a less aggressive disease. Figure based on illustration provided by G. Packham and prepared using Servier Medical Art.

In addition to mutation status, the signalling capacity of the BCR on CLL cells has also been linked to outcome. Previous work has documented the use of iCa^{2+} mobilisation as a biomarker for assessing the signalling capacity of sIgM (using standard flow cytometry techniques to analyse samples labelled with a Ca^{2+}-sensitive fluorochrome) (Mockridge et al., 2007), which differs between U- and M-CLL and correlates with clinical outcome (D'Avola et al., 2016) (**Figure 1-9**). In general, the ability of sIgM to induce Ca^{2+} mobilisation is retained in U-CLL, but is variably down-modulated in M-CLL. Reduced sIgM signalling capacity in M-CLL is associated with a strong, reversible down-modulation of expression of sIgM, but not sIgD, and may reflect more pronounced induction of anergy in this subset. Interestingly, sIgM signalling capacity can also be influenced by microenvironmental factors. For example, IL-4 treatment *in vitro* leads to increased sIgM expression and anti-IgM-induced iCa^{2+} mobilisation (Aguilar-Hernandez et al., 2016).

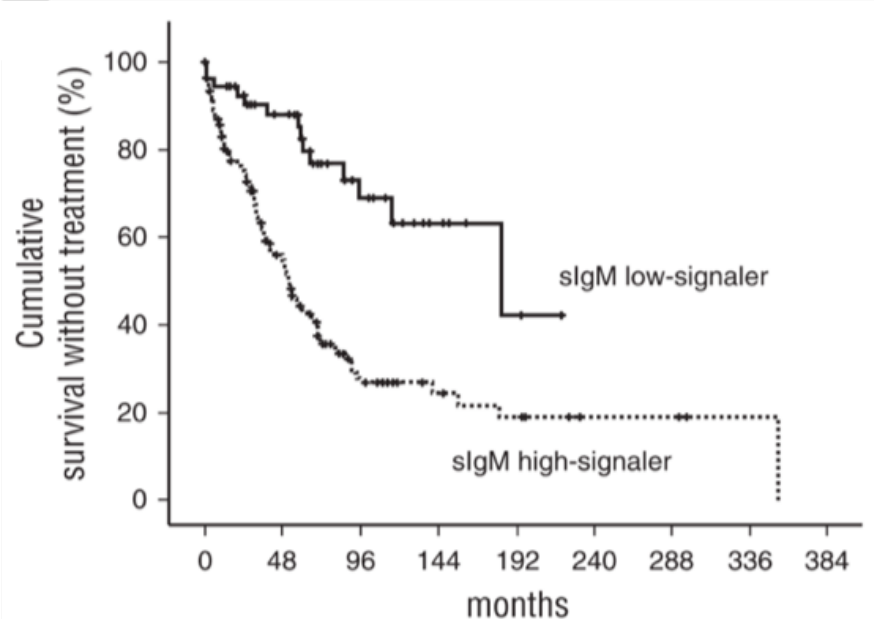

FIGURE 1-9: THE SIGNIFICANCE OF SIGM-INDUCED SIGNALLING FOR DISEASE PROGRESSION IN CLL.

Patients with high signalling cells (>5% cell population responds to anti-IgM stimulation), termed "sIgM high-signaller", is represented by the dotted line and have worse prognosis overall compared with patients with low signalling cells (≤5% cell population responds to anti-IgM stimulation), termed "sIgM low-signaller", which is represented by the solid line. Figure from (D'Avola et al., 2016).

Genetic alterations and a tumour-promoting microenvironment can both contribute to the accumulation of CLL cells. Around 80% of CLL patients have at least one of four common chromosomal changes: deletion of part of chromosome 13q (resulting in overexpression of the anti-apoptotic proteins BCL2 and MCL-1 due to loss of repressing miRNAs (*mir-15a* and *mir-16-1*, respectively) within this chromosomal region) (Calin et al., 2002), deletions of 17p or 11q (which result in defective DNA damage responses due to loss of genes encoding p53 or ATM), or trisomy 12 (the functional consequences of which are not well understood) (Pekarsky et al., 2018; te Raa and Kater, 2016; Autore et al., 2019). Next generation sequencing has also identified recurrent somatic mutations, the most common of which are loss-of-function mutations of p53 or ATM, activating mutations of NOTCH1 (leading to enhanced NOTCH1 signalling) and mutations of SF3B1 (splicing factor) and XPO1 (involved in nuclear export of proteins and RNAs) (Landau et al., 2015; Gaidano and Rossi, 2017). A complex karyotype and increased mutational burden is more commonly found within U-CLL and these patients have a worse prognosis compared with patients that have a normal karyotype or del(13q) as the sole genetic abnormality (Calin et al., 2002). The mutational burden also increases with treatment due to selection of drug resistant subclones. However, the overall burden of somatic mutations in CLL is relatively low compared to other B-cell malignancies (Alexandrov et al., 2013).

The tissue microenvironment also appears to have a key role in driving accumulation of CLL cells. CLL cell proliferation occurs within “proliferation centres”, which are microanatomical sites within SLOs where CLL cells can interact with an array of supporting cells, including stromal cells, nurse-like cells (a type of macrophage) and T cells (ten Hacken and Burger, 2016). These interactions promote CLL cell proliferation and survival via a range of factors, including CD40L, CXCL12, IL-4, BAFF and contact with integrins. CLL cells also secrete factors which influence the microenvironment, such as the T-cell attractants CCL3 and CCL4. Tissues are also the main site of antigen engagement of the BCR of CLL cells (Herishanu et al., 2011). As with normal B cells, there is an exchange of CLL cells between the blood and the tissue that is mediated by an array of chemokine receptors and integrins (Calissano et al., 2011; Redondo-Muñoz et al., 2019) which allow the CLL cells to enter the protective microenvironment of the SLOs.

The current treatment for CLL includes several chemoimmunotherapy (CIT) regimens that combine an anti-CD20 antibody (e.g. rituximab and obinutuzumab) with CHOP (cyclophosphamide, doxorubicin, vincristine, prednisolone), fludarabine, bendamustine, or

chlorambucil for less fit patients (Kipps et al., 2017). Occasionally radiotherapy, surgery and stem cell or bone marrow transplant are used. Whilst many patients respond well in the first instance, they will eventually relapse and require further rounds of therapy. There are alternative strategies for patients who do not respond well to these standard CIT regimens, particularly those with p53/ATM mutations. These include treatment with targeted agents such as BCL2 inhibitors (e.g. venetoclax) to reverse BCL2-mediated suppression of apoptosis (Schieber and Ma, 2019), or inhibitors targeted against BCR-associated signalling kinases (e.g. ibrutinib, discussed in detail in **Section 1.6** below) (Arnason and Brown, 2017). A subset of patients with M-CLL can experience a prolonged progression free survival hinting at a possible curative potential with CIT (Kipps et al., 2017), but CLL remains an incurable disease.

In summary, CLL is a common disease, which remains incurable. The BCR has an important role in this disease and determining the behaviour of the cells. The signalling capacity of the BCR can be used as a biomarker that correlates with clinical outcome and therefore, the BCR-associated signalling pathway is an attractive opportunity for therapeutic targets.

1.5.2 Diffuse large B-cell lymphoma

DLBCL is the most common type of non-Hodgkin's lymphoma (NHL) in adults with around 5500 people being diagnosed with DLBCL every year in the UK (this is approximately 40% of all NHL cases). DLBCL more commonly affects people ≥65 years of age and the incidence is higher in males than females (https://www.cancerresearchuk.org/about-cancer/non-hodgkin-lymphoma/types/diffuse-large-B-cell-lymphoma and https://lymphoma-action.org.uk/types-lymphoma-non-hodgkin-lymphoma/diffuse-large-b-cell-lymphoma [accessed February 2021]).

DLBCL is a high-grade lymphoma (Lenz et al., 2008) and, as the name would suggest, it is a neoplasm of large B-cells arranged in a diffuse pattern (Li et al., 2018). Patients most often present with a rapidly growing tumour mass in single or multiple, nodal or extranodal sites (Li et al., 2018) requiring immediate treatment. The tumour masses are typically painless and patients experience general "B symptoms" alongside the tumour growth, which include fever, night sweats and weight loss. Patients often report fatigue and loss of appetite as common general symptoms associated with DLBCL. Depending on the location of the lymphoma patients might also experience more specific symptoms, for example, if there is a tumour mass in the lung they might

experience breathlessness. Clinical biomarkers include serum lactase dehydrogenase (LDH) and beta-2-microglobulin being raised above normal (Li et al., 2018).

The current staging system for NHL is the Lugano staging system and prognosis is based on the international prognostic index (IPI) for DLBCL. IPI is based on age of the patient at diagnosis, stage of disease, Eastern Cooperative Oncology Group (ECOG) performance status, serum LDH level, and whether the patient has extranodal disease.

TABLE 1-3: LUGANO STAGING SYSTEM.

Stage	Description
I	Lymphoma is in only 1 lymph node area or lymphoid organ
IE	Lymphoma is in only 1 area of a single organ outside of the lymphatic system
II	Lymphoma is in 2 or more groups of lymph nodes on the same side of the diaphragm
IIE	Lymphoma is in a group of lymph nodes and in one area of a nearby organ
III	Lymphoma is in lymph node areas on both sides of the diaphragm or the lymphoma is in lymph nodes above the diaphragm and in the spleen
IV	Lymphoma has spread widely into at least one organ outside the lymph system

(https://www.ncbi.nlm.nih.gov/books/NBK66057/table/CDR0000062707__1075/ [accessed February 2021])

DLBCL is most commonly categorised into two subgroups termed germinal centre B-cell-like (GCB)-DLBCL and activated B-cell-like (ABC)-DLBCL depending on the cell of origin, however around 10-15% of cases are unclassifiable (Lenz et al., 2008; Dunleavy et al., 2018; Li et al., 2018) (**Figure 1-10**). GCB-DLBCL is derived from centrocytes within the GC, and ABC-DLBCL is derived from more differentiated plasmablasts after the cell has exited the GC (Koues et al., 2015). The subtypes are distinguished on the basis of their distinct gene expression patterns or by immunohistochemical analysis, but also differ with respect to the pattern of genetic mutations that they acquire. In general, GCB-DLBCL has more mutations associated with epigenetic control, apoptosis resistance (BCL2), PI3K pathway signalling, BCL6 and JAK-STAT signalling, whereas ABC-DLBCL has more mutations leading to BCR signalling activation, Toll-like receptor signalling activation, and NF-κB pathway activation (the NF-κB pathway is constitutively active in ABC-DLBCL) (Li et al., 2018). Patients with GCB-DLBCL generally have a better prognosis compared with patients with ABC-DLBCL, but the subgroups remain heterogeneous with a 5 year overall survival of 60-70% (Li et al., 2018).

The most common genetic alteration in GCB-DLBCL is the t(14,18) translocation involving BCL2, and also the amplification of mir-17-92 which results in less apoptosis than those overexpressing MYC alone (Lenz et al., 2008). Deletion of PTEN tumour suppressor is also seen in GCB-DLBCL and the inactivation of PTEN along with AKT pathway activation might contribute to disease pathogenesis (Lenz et al., 2008). Approximately 25% of ABC-DLBCL had trisomy 3, which was rarely found in GCB-DLBCL, and had frequent gain of 18q and loss of 6q and deletion of the INK4a/ARF tumour suppressor locus (Lenz et al., 2008). FOXP1, implicated as an oncogene, was found to be upregulated and activated in a subset of ABC-DLBCL and there was amplification of NFKBIZ, which enhances activation of some NF-κB targets such as IL-6, and BCL2 and NFATC1 were also found to be commonly overexpressed in ABC-DLBCL (Lenz et al., 2008). The more complex karyotypes are usually associated with more clinically aggressive disease or tumours that are treatment resistant (Li et al., 2018). A small percentage of DLBCL cases are categorised by rearrangements in MYC and BCL2 (or less commonly BCL6) and known as double-hit lymphoma (https://lymphoma-action.org.uk/types-lymphoma-non-hodgkin-lymphoma/diffuse-large-b-cell-lymphoma [accessed February 2021]). These tumours are much more aggressive and have a poorer prognosis.

Since DLBCL can advance quickly, treatment usually begins immediately. Current treatment for DLBCL is a CIT regimen combining rituximab (anti-CD20 monoclonal antibody) with CHOP chemotherapy, with or without radiotherapy. This treatment can succesffully achieve remission in a large number of patients (https://lymphoma.org/aboutlymphoma/nhl/dlbcl/dlbcltreatment/ [accessed March 2021]). For higher grade lymphomas, more advanced disease or more aggressive tumours (e.g. double-hit lymphoma), etoposide may also be included in the regimen resulting either in R-CHOEP or R-EPOCH, depending on the method of drug administration (https://lymphoma.org/aboutlymphoma/nhl/dlbcl/dlbcltreatment/ [accessed March 2021]). A phase II clinical trial of patients with relapsed or refractory disease showed that patients with ABC-DLBCL respond well to ibrutinib treatment, which is important since this subgroup has a poorer response to standard CIT compared with GCB-DLBCL (https://lymphoma.org/aboutlymphoma/nhl/dlbcl/dlbcltreatment/ [accessed March 2021]). Double-hit lymphoma has distinct prognostic features and requires a more standardised approach to care since there is currently no recognised standard available (Merron and Davies, 2018). Retrospective studies support the conclusion that dose adjusted R-EPOCH is a suitable regimen for first line treatment in these patients (Merron and Davies, 2018). Other drugs and targeted inhibitors, including lenolidamide and ibrutinib, are also under investigation in numerous clinical

trials showing some promise in improving outcomes in subsets of patients (Westin *et al*., 2019; Yoon *et al*., 2020; Younes *et al*., 2018).

ABC-DLBCL, of poorer prognosis, is more dependent on NF-κB signalling than BCR signalling pathways and is therefore expected to be less likely to respond to BCR-associated targeted therapies. However, Phelan *et al*. recently found a new complex in some cell lines and biopsies which shows enhanced BCR signalling and heightened ibrutinib-responsiveness most likely due to promoting dependence on BCR signalling within this subset (Phelan et al., 2018). The new supercomplex termed My-T-BCR is comprised of MYD88, TLR9 and the BCR and colocalises with mTOR on endolysosomes to drive pro-survival NF-kB and mTOR signalling (Phelan et al., 2018) opening up opportunities for better and more targeted therapies.

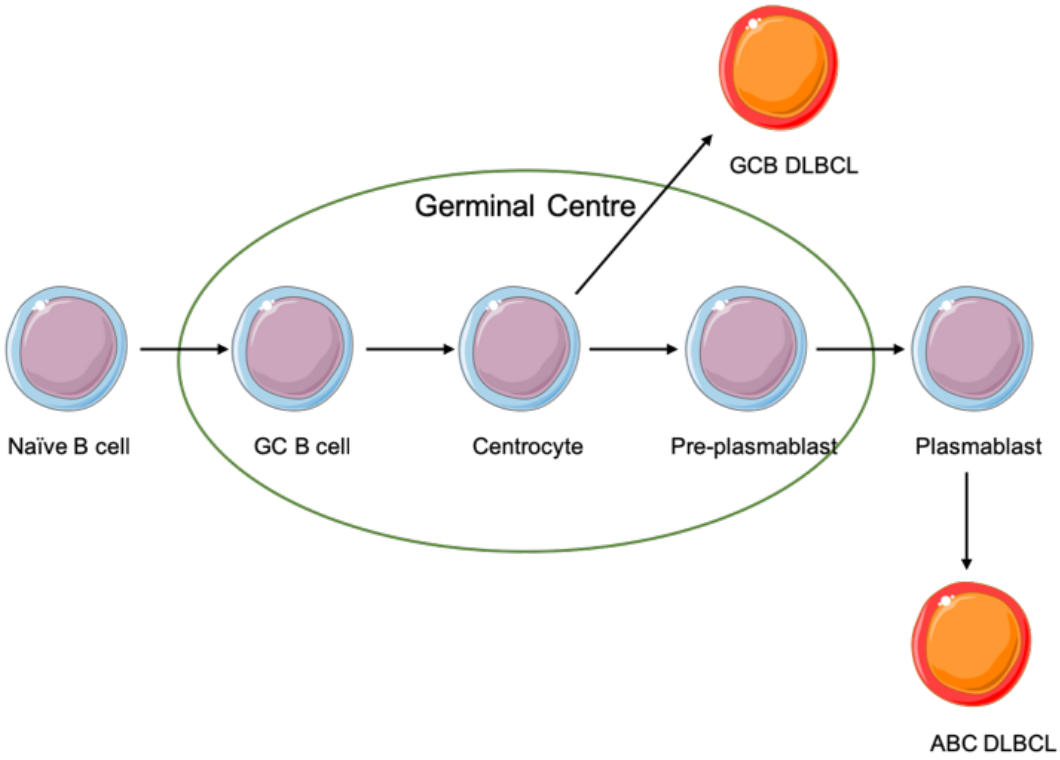

FIGURE 1-10: CELLULAR ORIGIN OF DIFFUSE LARGE B-CELL LYMPHOMA (DLBCL).

DLBCL can be divided into 2 subgroups termed germinal centre B-cell-like (GCB)-DLBCL and activated B-cell-like (ABC)-DLBCL. GCB-DLBCL is derived from centrocytes within the germinal centre (GC) and ABC-DLBCL is derived from more differentiated plasmablasts that have exited the GC. Figure adapted from (Koues et al., 2015) and prepared using Servier Medical Art.

1.6 BTK kinase inhibitor: ibrutinib

Ibrutinib (previously known as PCI-32765) is a clinically approved oral, once-daily BTK inhibitor used for the treatment of CLL and other B-cell malignancies. It covalently binds BTK at Cys^{481} (Byrd et al., 2013), located in the kinase domain of BTK, via a reaction between the cysteine thiol and the ibrutinib acrylamide group (**Figure 1-11**). This reaction prevents autophosphorylation of Tyr^{223} and thereby inhibits downstream activity, including phosphorylation of PLCγ2 (De Rooij et al., 2012) and ERK1/2 (Herman et al., 2014), and integrin-mediated adhesion to fibronectin or VCAM-1 and CXCL12/CXCL13/CCL19-induced adhesion, and migration (De Rooij et al., 2012). It is a potent BTK inhibitor (50% inhibition at ~0.5 nM in an *in vitro* kinase assay) (Honigberg et al., 2010). Ibrutinib can inhibit many other kinases including BLK and BMX (IC_{50} <1 nM) and TEC, EGFR, ERBB2, ITK and JAK3 (IC_{50} 1-20 nM) (Honigberg et al., 2010), only some of which contain an analogous cysteine residue to Cys^{481} in BTK.

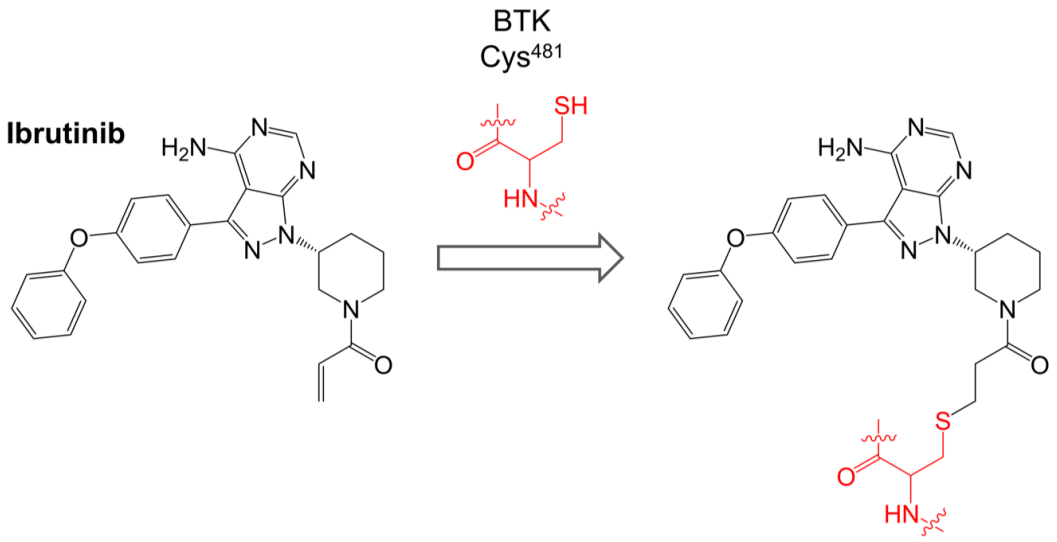

FIGURE 1-11: REACTION OF IBRUTINIB WITH CYS^{481} OF BTK.

Figure from (Arthur et al., 2020).

The effect of ibrutinib in primary CLL cells was first reported by Herman *et al*. (Herman et al., 2014) and confirmed that BTK tyrosine phosphorylation, downstream phosphorylation of AKT and ERK1/2, and activation of NF-κB was inhibited by ibrutinib. The effect of ibrutinib on CLL cell viability was relatively low (~10% cell killing at 1 μM ibrutinib treatment) but caspase-dependent apoptosis in both U- and M-CLL was observed. Ibrutinib-induced apoptosis was also observed in the presence of survival signals including CD40L, BAFF, fibronectin or co-culture with stromal cells. This study also showed that ibrutinib reduced the production of some cytokines (including IL-6, IL-10 and TNFα) from activated T cells, which do not express BTK, revealing potential off-target effects of ibrutinib.

Ponader *et al*. (Ponader et al., 2012) demonstrated that ibrutinib inhibited CLL cell survival induced by either anti-IgM or co-culture with nurse-like cells (NLC). CLL cell proliferation and secretion of CCL3/4 following NLC co-culture was reduced following ibrutinib treatment and interestingly, CCL3/4 concentrations were also reduced in the plasma of patients receiving ibrutinib suggesting that CCL3/4 could be used as a response biomarker. Ibrutinib also inhibited migration of CLL cells towards CXCL12/CXCL13 and inhibited AKT/ERK phosphorylation following stimulation with anti-IgM, CXCL12 or CXCL13. Of note, Ponader et al. also showed that the accumulation of leukemic cells was reduced post-ibrutinib treatment in the Eμ-TCL1 mouse model of CLL.

Ibrutinib can interfere with other downstream signalling responses, including induction of mRNA translation (Yeomans et al., 2016), and the potentiation of BCR signalling by IL-4 was shown to protect cells from the pro-apoptotic effects of ibrutinib (Aguilar-Hernandez et al., 2016).

As mentioned briefly already, potential off-target effects of ibrutinib have been revealed and it is important to consider these effects and how they can provide both benefits and drawbacks to the therapeutic potential of ibrutinib. For example, inhibition of ITK in T cells (one of the known kinases that ibrutinib can inhibit (Honigberg et al., 2010)) promotes beneficial Th1 immunity, and both BTK-dependent and -independent effects appear to contribute to enhanced T cell numbers and function in CLL patients (Dubovsky et al., 2013; Long et al., 2017) contributing to improved efficacy of the drug. More broadly, ibrutinib has been investigated in models of solid tumours, for example, EGFR/HER2-amplified breast cancer where cancer cell growth was inhibited by ibrutinib treatment (Chen et al., 2016).

Ibrutinib has radically improved outcomes for patients with CLL but there are limitations particularly with toxicity and development of resistance. The outcome of patients following ibrutinib discontinuation is poor, particularly for those who have experienced disease progression whilst on ibrutinib, and this highlights the need for alternative therapies (Maddocks et al., 2015; Jain and O'Brien, 2016).

Resistance is usually caused by disease progression or transformation to higher grade malignancy. Approximately 80% of patients experiencing disease progression have mutations of either BTK or PLCγ2 whereas the frequency of these mutations is lower (~40%) in cases that transform. The most common mutation found in BTK is a substitution at position 481, from a cysteine residue to a serine residue (C481S mutation), which only allows a weaker, non-covalent binding of ibrutinib to BTK (Buhimschi et al., 2018). C481S mutant BTK retains some enzymatic activity but is much less sensitive to inhibition by ibrutinib (Woyach et al., 2014) and it is suggestive that the mutant leads to progression of disease that retains BTK-dependence but reduced sensitivity to ibrutinib-mediated inhibition (Buhimschi et al., 2018).

Acquired mutations of PLCγ2, affecting a number of different amino acid residues, can also contribute to ibrutinib resistance by the hyperactivity or BTK-independent activation of PLCγ2 (e.g. via Vav/Rac) (Walliser et al., 2016). EHT-1864, a Rac1 and Rac2 inhibitor known to bind with high affinity, was used to investigate the role of Rac in the enhanced basal activity of PLCγ2^{R665W} and PLCγ2^{L845F}. A small decrease in IP_3 production was observed in wild type cells following treatment with EHT-1864, but a significant decrease in IP_3 production was observed in both the PLCγ2 mutants (Walliser et al., 2016) suggesting that they activate signalling pathways independently of BTK. Liu *et al.* sought to characterise the R665W and L845F mutants in PLCγ2 (which lead to ibrutinib resistance in CLL) further (Liu et al., 2015). The R665W mutation can exist without the C481S BTK mutation indicating that this mutation can lead to resistance without cooperating mutations in BTK. Wild type PLCγ2 or PLCγ2^{R665W} was introduced into PLCγ2-deficient DT40 cells and the mutant was found to augment Ca^{2+} flux and this effect was ibrutinib-resistant (Liu et al., 2015). Despite this preservation of signalling ability, the mutant lost the ability to retain Tyr^{1217} phosphorylation in the presence of ibrutinib and the enhanced BTK-independent Ca^{2+} release hints at potential BTK by-pass (Liu et al., 2015). Pharmacologically targeting SYK and LYN impeded Ca^{2+} release and downstream ERK activation in the PLCγ2 mutant cells suggesting a new

therapeutic potential for kinase inhibitors in ibrutinib-resistant patients with PLCγ2 mutation (Liu et al., 2015).

There are a wide range of side effects associated with ibrutinib treatment (including diarrhoea, nausea, fatigue, upper respiratory tract infections, rash, dyspnoea and oedema) with more severe toxicities including arthralgia, atrial fibrillation and rash in the front-line setting, and atrial fibrillation, infection, pneumonitis, bleeding and neutropenia in relapsed-refractory disease, which require immediate discontinuation of ibrutinib (Mato et al., 2016). The toxicities of ibrutinib can be explained, at least in part, by the off-target effects of ibrutinib (Patel et al., 2017). For example, SRC-family kinases (e.g. BLK) have a role in platelet activation (Levade et al., 2014; Senis et al., 2014) and platelet aggregation (Kamel et al., 2015). Platelets are crucial for the formation of thrombi to prevent excessive blood loss (Senis et al., 2014), so the inhibition of these platelet activating/aggregation-promoting kinases with ibrutinib likely accounts for the increased incidence of bleeding reported in patients treated with ibrutinib. Table 1-4 summarises the link between other off-target effects of ibrutinib and symptoms experienced by patients.

TABLE 1-4: OFF-TARGET EFFECTS OF IBRUTINIB CONTRIBUTING TO SIDE EFFECTS.

Off-target effect	Possible related symptoms	Reference(s)
EGFR inhibition	Rash and diarrhoea	(Gao et al., 2014)
BTK/TEC inhibition in cardiac tissue	Atrial fibrillation	(Brown et al., 2017; McMullen and Boey, 2014)
TEC (involved in collagen receptor glycoprotein VI signalling and platelet aggregation)	Bleeding	(Atkinson et al., 2003)

1.6.1 Alternative methods of BTK inhibition

Despite the dramatic clinical responses that can be induced by ibrutinib, toxicity and resistance are major limitations, therefore numerous new BTK inhibitors are being developed, including acalabrutinib and non-covalent inhibitors, such as vecabrutinib and ARQ-531 (Bond and Woyach, 2019). Acalabrutinib (**Figure 1-12**) is a second generation BTK inhibitor with improved pharmacologic features; it is more selective for BTK and has less non-specific irreversible binding to other kinases than ibrutinib (Byrd et al., 2016).

Table 1-5 provides summary information on the specificity of ibrutinib and acalabrutinib by comparing the IC_{50} values (the concentration required to inhibit the kinase function by 50%), and the binding affinity (indicated by the K_i values) for BTK and TEC.

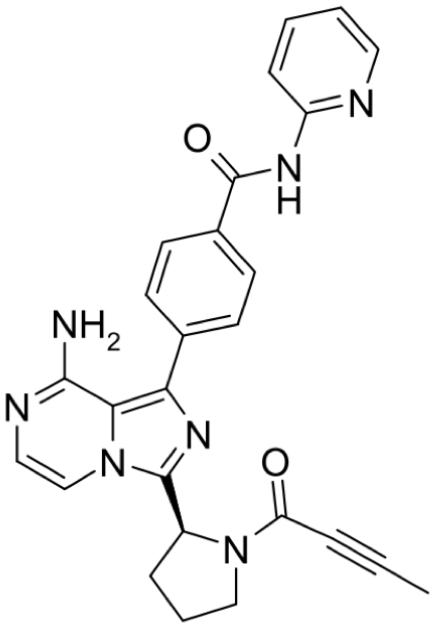

FIGURE 1-12: STRUCTURE OF ACALABRUTINIB.
Figure from (Barf et al., 2017).

TABLE 1-5:SUMMARY OF SPECIFICTY OF IBRUTINIB AND ACALABRUTINIB.

Drug	$IC_{50} \pm SD$		K_i (nM) $\pm$ SD	
	BTK	TEC	BTK	TEC
Ibrutinib	0.24 ± 0.2	0.24 ± 0.2	0.95 ± 0.009	1.8 ± 0.05
Acalabrutinib	2.3 ± 1.6	9.7 ± 2.6	8.7 ± 0.5	160 ± 37

Adapted from (Hopper et al., 2020).

An exciting alternative to conventional kinase inhibitors offers a new approach to targeted inhibition of BTK using proteolysis targeting chimeras (PROTACs) (Arthur et al., 2020). PROTACs comprise a warhead directed against the target of interest (in this case BTK) coupled to an E3 ligase-recruiting element via a linker region (**Figure 1-13**). This results in formation of a ternary complex (TC) comprising the target, PROTAC and an E3 ligase allowing ubiquitylation and the subsequent degradation of the target via the proteasome. Since the PROTAC is subsequently released from binding the target protein, they also act catalytically to inhibit target function. These compounds were developed to address some of the clinical limitations of ibrutinib by harnessing event-driven rather than occupancy-based pharmacology (Paiva and Crews, 2019; Konstantinidou et al., 2019; Bondeson et al., 2015) so only a transient binding is required for a biological effect. Moreover, they are used in my studies as a way to address potential non-kinase mediated functions of BTK.

Polyubiquitylation of the target protein is catalyzed by a family of enzymes termed E1, E2 and E3 (Dikic, 2017). E1 (ubiquitin-activating enzyme) activates ubiquitin and catalyses formation of a thioester linkage between the C-terminus of ubiquitin and a cysteine residue within the E1 protein. E1-bound ubiquitin is transferred to E2 (ubiquitin-conjugating enzyme), and is subsequently transferred to a lysine residue within the target protein via E3 (ubiquitin ligase). There are >500 E3 ligases which differ in their ability to recognize specific degradation signals within target proteins. E3 ligases commonly targeted by PROTACs include cereblon (CRBN), MDM2, VHL and IAP (Paiva and Crews, 2019; Konstantinidou et al., 2019). E1 continues to recruit and activate further ubiquitin molecules allowing E2 and E3 to form a polyubiquitin chain on the target protein. The C-terminus of each ubiquitin is linked to a lysine residue within the preceding ubiquitin molecule. It is this polyubiquitin chain that serves as a recognition signal for destruction via the proteasome. It is important to note that the choice of warhead, linker region and E3 ligase-recruiting element all have important influence on the effectiveness of the PROTAC and must be

optimised for the system of interest. The PROTAC mechanism of action is summarised in **Figure 1-13**.

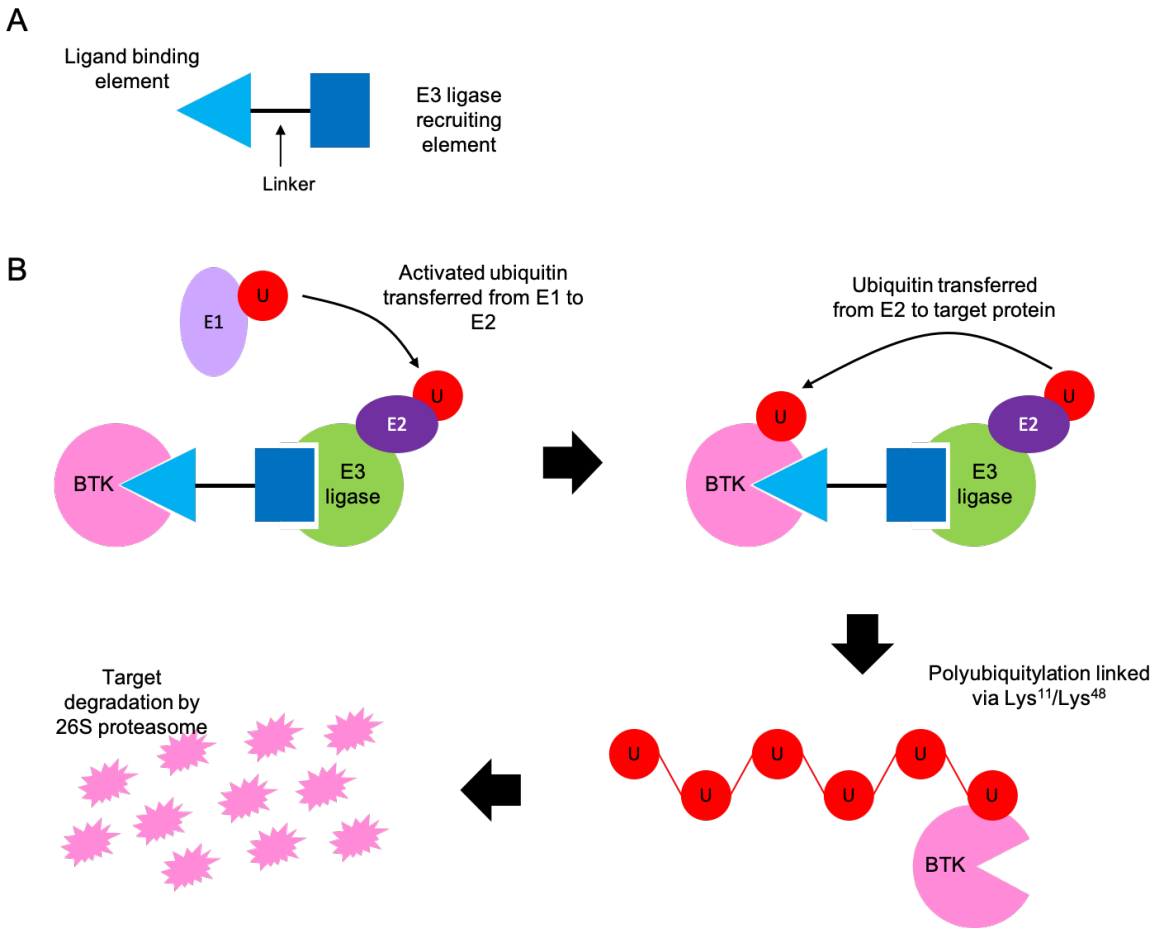

FIGURE 1-13: STRUCTURE AND MECHANISM OF PROTEOLYSIS TARGETING CHIMERAS (PROTACS).

A. The basic structure of a PROTAC comprises the ligand-binding element and the E3-ligase recruiting element, joined by a linker region. **B.** The mechanism of PROTAC-mediated degradation. The PROTAC recruits the target protein, e.g. BTK, and an E3 ligase, forming the ternary complex. The E3 ligase binds an E2 ligase which is ubiquitylated by transfer of ubiquitin from E1 ligase. Ubiquitin is transferred from E2 to the target protein. Multiple rounds of ubiquitylation occur and are linked through Lys^{11}/Lys^{48}. The target protein is then degraded by the 26S proteasome. The PROTAC and E3 ligase are released and available for further rounds of PROTAC-mediated target degradation. Figure based on (Arthur et al., 2020).

Huang *et al*. (Huang et al., 2018a) designed the first BTK-targeted PROTACs CJH-005-067 and DD-04-015 (**Figure 1-14**), which contain warheads derived from bosutinib (a non-covalent BTK inhibitor) and RN486, respectively and both contain pomalidomide-derived E3 ligase-recruiting elements (to recruit CRBN). Both compounds effectively reduced BTK expression with 4 hours in acute myeloid leukaemia (AML)-derived MOLM-14 cells. DD-04-015 exhibited an extreme "hook effect" at high concentrations, where effectiveness of BTK degradation is reduced. The "hook effect" is likely caused by extensive dimer formation of target:PROTAC and PROTAC:E3 ligase, rather than TC formation, which fails to elicit protein targeting to the proteasome at high concentrations of PROTAC. DD-04-015 and its parental inhibitor, RN486, both showed similar potencies when tested for growth inhibition in TMD8 cells. The potency of DD-04-015 was maintained following wash-out of drug for up to 6 hours and was suggested that this was caused by persistent effects following BTK degradation compared with reversible active site occupancy of RN486.

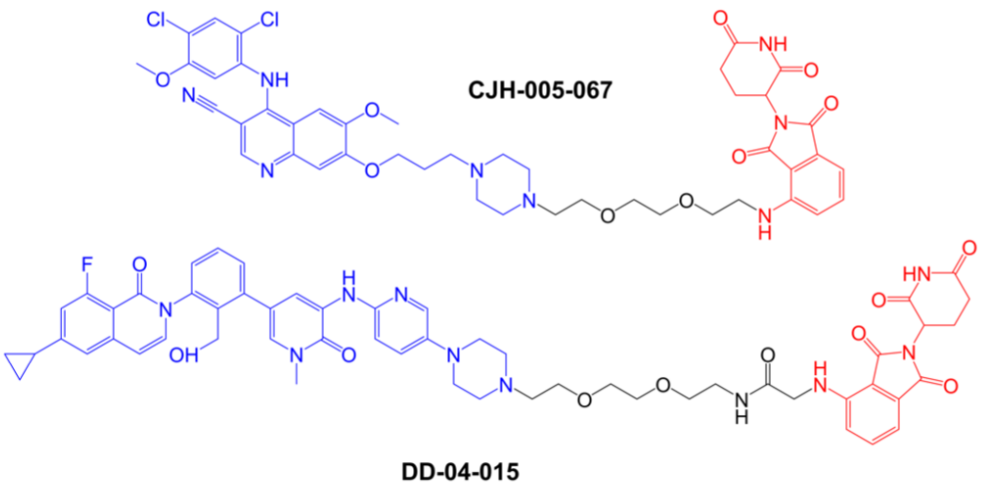

FIGURE 1-14: STRUCTURE OF CJH-005-067 AND DD-04-015 COMPOUNDS.

BTK-targeted warheads, derived from bosutinib in CJH-005-067 and RN486 in DD-04-015, are coloured blue and pomalidomide-derived CRBN-targeting moieties are coloured red. Figure adapted from (Huang et al., 2018a).

Buhimschi *et al*. (Buhimschi et al., 2018) described a series of BTK-targeted PROTACs utilizing a non-covalent BTK inhibitor warhead which was based on the ibrutinib scaffold but lacked the acrylamide group responsible for the covalent binding of ibrutinib to Cys^{481} of BTK. This warhead was coupled to various linkers and a pomalidomide-derived CRBN-recruiting element. The initial compounds had 12-atom linkers and very effectively reduced BTK expression in Namalwa cells (derived from Burkitt's lymphoma) but upon further exploration of the length of the linker regions Buhimschi *et al*. demonstrated that an 11-atom linker was most effective for BTK targeting with a DC_{50} (the concentration required to degrade 50% of the total BTK pool) of ~70 nM. Further reductions in linker length (to 8 or 5 atoms) completely abolished PROTAC activity.

My work has focussed on the PROTAC MT-802 which was synthesized using a different point on the E3 ligase-recruiting element for linker attachment (C5 of the phthalimide ring versus C4) (**Figure 1-15**). This allowed a shorter linker (8-atom linker) to be used whilst maintaining very potent activity (DC_{50} ~9 nM in 24 hour assay using Namalwa cells). MT-809, utilising a 12-atom linker attached at C5, also resulted in potent activity (DC_{50} ~12 nM). MT-802 and MT-809 very effectively induced BTK degradation (>99% maximal reduction at 250 nM) and did not show a hook effect at concentrations up to 2.5 µM.

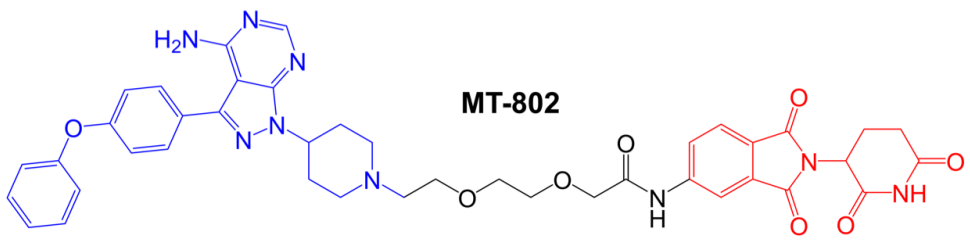

FIGURE 1-15: STRUCTURE OF MT-802.

The reversible BTK-targeting warhead based on ibrutinib is coloured blue and the CRBN-targeting moiety is coloured red. Figure based on (Buhimschi et al., 2018).

Further characterization focused on MT-802 and a related control compound SJF-6625, which is unable to bind CRBN due to methylation of the glutarimide ring of the pomalidomide moiety therefore rendering it incapable of BTK degradation. Time course experiments demonstrated that MT-802-induced BTK degradation occurred within 1 hour and was near maximal at 4 hours following treatment with 250 nM MT-802. BTK degradation following MT-802 treatment was blocked by the proteasome inhibitor epoxomicin or MLN-4924, an inhibitor of the NEDD8-activating enzyme that neddylates and activates the CRBN complex. BTK degradation was also prevented by an excess of either ibrutinib or pomalidomide confirming activity was dependent on formation of a TC.

Analysis of the specificity of MT-802 for kinase binding was performed using KINOMEscan (DiscoverX®), a competition based assay to measure binding of 468 kinases to an immobilized ligand. Kinases are prevented from binding immobilised ligand if their active site is already occupied (e.g. with ibrutinib or MT-802). The amount of kinase captured by immobilised ligand is compared between test and control samples, and qPCR is used to detect the specific kinases. This assay demonstrated that MT-802 also bound TEC, like ibrutinib, however a number of other ibrutinib-targeted kinases were only weakly bound by MT-802 (including ITK and JAK3). The increased specificity of MT-802 relative to ibrutinib is thought to be due to the non-covalent nature of the binding of the warhead to BTK.

The study by Buhimschi *et al*. is particularly interesting as it investigated the effects of BTK-targeted PROTACs on C481S mutant BTK, which is thought to be a major cause of ibrutinib resistance in CLL patients as previously mentioned. MT-802 was a less potent inhibitor of wild-type BTK than ibrutinib (IC_{50} for MT-802 was ~50 nM and ibrutinib was <0.05 nM) but it retained activity against C481S mutant BTK unlike ibrutinib (IC_{50} for MT-802 was ~20 nM and ibrutinib was ~2 nM). Arguably the most important finding was that MT-802 retained the ability to reduce the level of the active-autophosphorylated form of BTK in ibrutinib-resistant patient-derived CLL cells with C481S mutant BTK.

Zorba *et al*. (Zorba et al., 2018) investigated *in vivo* effects of subcutaneous administration of compound 10 (**Figure 1-16**) in rats where reduced BTK expression was seen in the spleen, but not in lung tissue, despite similar accumulation of the compound in both sites. Although the reasons

for this are unclear, it is suggested that this might reflect the tissue-specific variation in expression of components of the ubiquitin-proteasome system.

Tinworth *et al*. (Tinworth *et al*., 2019) addressed the impact of covalent modification of BTK by a BTK-targeted PROTAC through the comparison of PROTACs containing either irreversible or non-covalent ibrutinib-derived warheads coupled to an IAP-recruiting element (**Figure 1-17**). Both PROTACs inhibited BTK activity in *in vitro* assays, but only the non-covalent PROTAC resulted in reduced BTK expression in THP1 cells (derived from AML) with a DC_{50} ~200 nM at 16 hours. Tinworth et al. suggested that the covalently bound PROTAC, which could not induce BTK degradation, might block ubiquitin transfer or access to the proteasome. Further analysis in Ramos cells (stimulated with anti-IgM) showed the covalent PROTAC reduced BTK autophosphorylation (implying inhibition of kinase activity) but did not induce BTK degradation, whereas the reversible PROTAC weakly inhibited BTK autophosphorylation, but did induce BTK degradation.

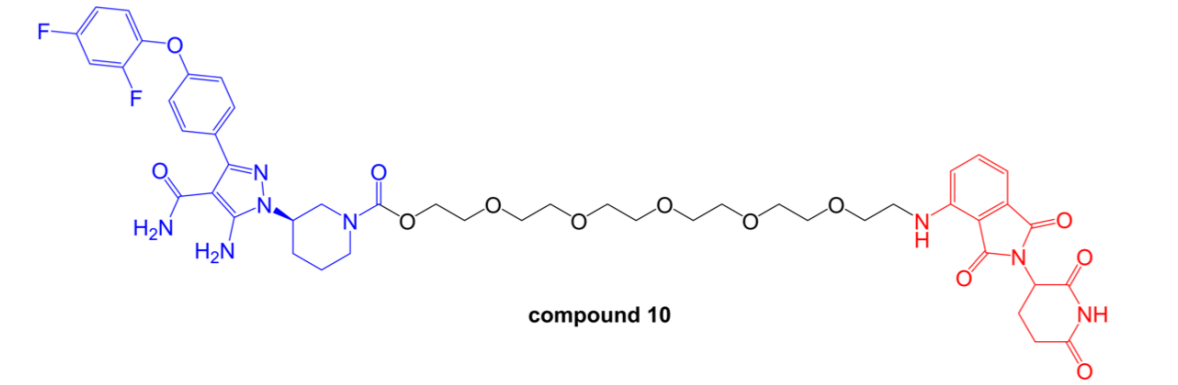

compound 10

FIGURE 1-16: STRUCTURE OF COMPOUND 10.

BTK-inhibiting warheads are coloured blue and pomalidomide-derived CRBN-targeting moieties are coloured red. Figure based on (Zorba et al., 2018).

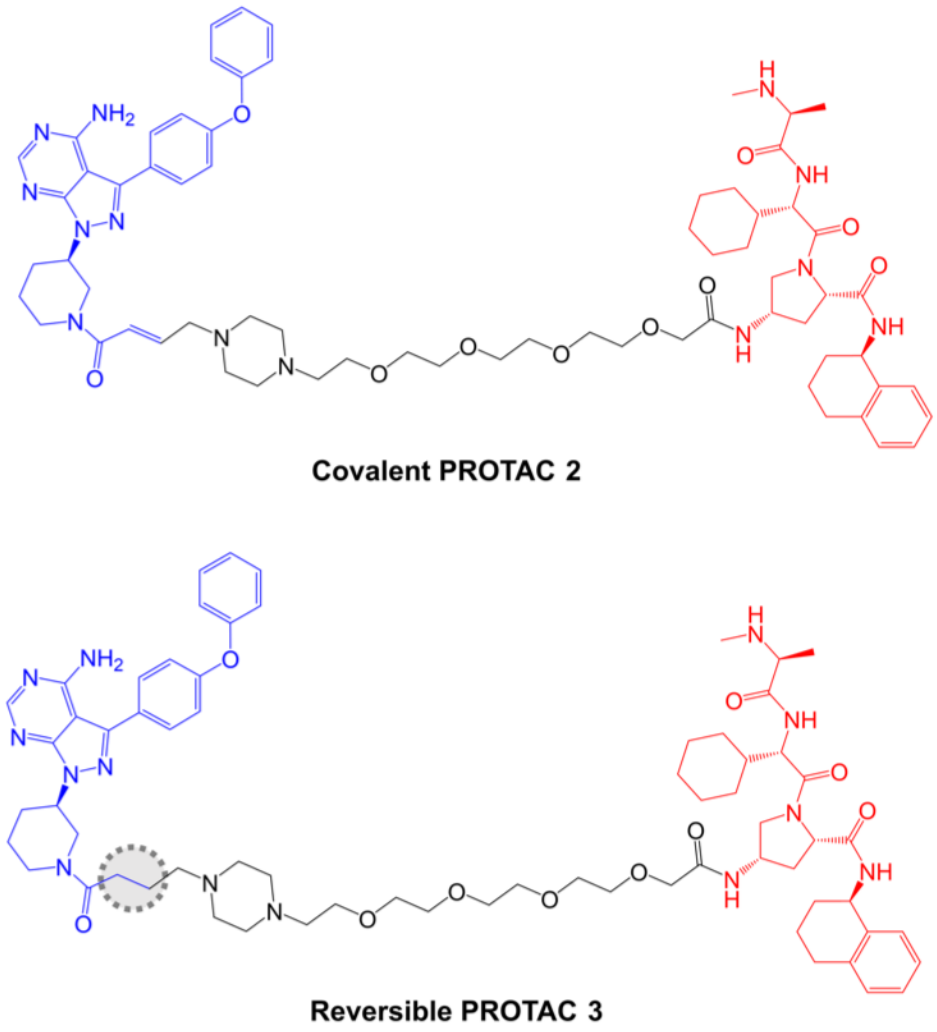

FIGURE 1-17: STRUCTURES OF COVALENT PROTAC 2 AND REVERSIBLE PROTAC 3.

BTK-inhibiting warheads derived from ibrutinib are coloured blue and IAP-targeting moieties are coloured red. The structural difference between covalent PROTAC 2 and reversible PROTAC 3 is highlighted by the grey region. Figure based on (Tinworth *et al.*, 2019).

In contrast, a more recent study has shown effective BTK degradation by a covalent PROTAC (Xue et al., 2020). The PROTAC comprised an ibrutinib-related BTK inhibitor (which retained the acrylamide group) linked to a VHL-recruiting element (**Figure 1-18**) and it was found to induce BTK degradation in K562 cells (derived from chronic myelogenous leukaemia) with a DC_{50} of ~150 nM in an 18 hour assay.

Sun *et al*. (Sun et al., 2019) have recently reported a compound (L18I; **Figure 1-19**) capable of inducing degradation of C481S mutant BTK in HBL1 cells (DC_{50} ~30 nM at 36 hours) as well as other BTK variants. This compound was also suitable for *in vivo* administration and they showed significant reduction in the accumulation of C481S mutant BTK-expressing HBL1 cells in a mouse xenograft model with no evidence of substantial toxicities. It is noteworthy that L18I was well tolerated in a short term, acute toxicity study in B6 mice.

Jaime-Figueroa *et al*. (Jaime-Figueroa et al., 2020) investigated improvement of pharmacokinetic properties of MT-802 . As other groups have shown, replacement of the CRBN-recruiting element with a VHL-recruiting element resulted in substantially reduced activity but replacement of the amide group that connected the linker to the CRBN-recruiting element with an ether and removal of one of the carbonyls within the CRBN-recruiting element resulted in improved pharmacokinetic properties. The resulting compound was termed SJF620 (**Figure 1-20**). Following intravenous administration in mice, SJF620 had a half-life of 1.64 hours and a C_{max} of 2.1 µg/ml, compared to values of 0.119 hours and 0.073 µg/ml for MT-802.

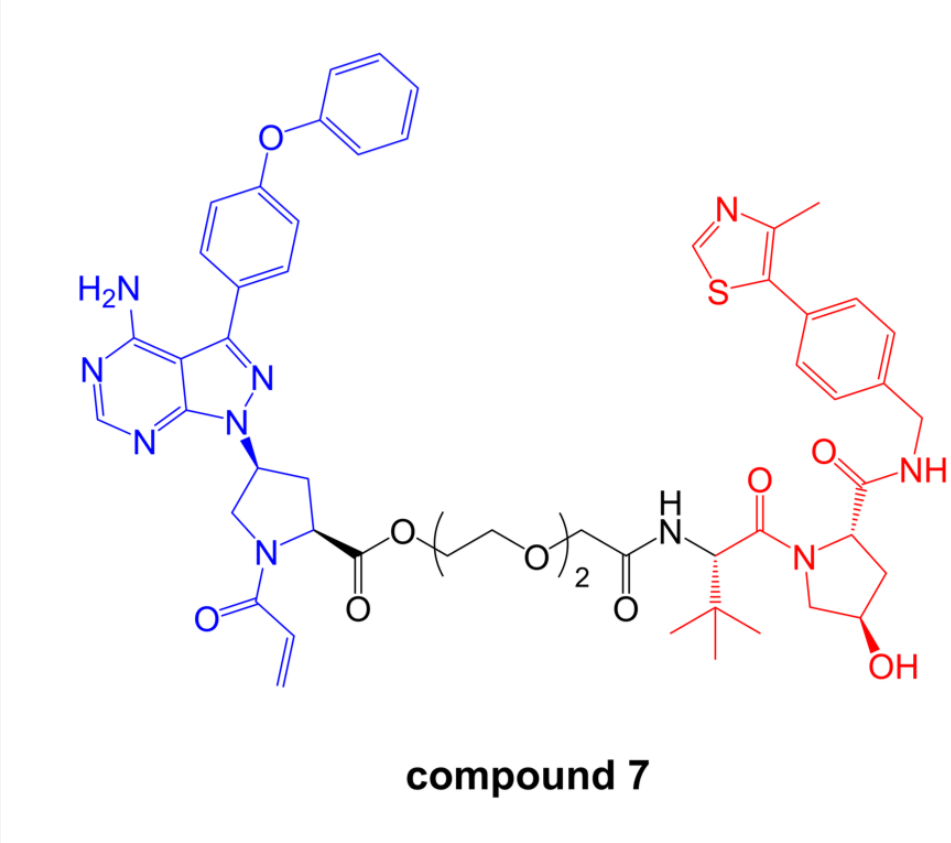

FIGURE 1-18: STRUCTURE OF COMPOUND 7, A COVALENT PROTAC.

BTK-inhibiting warhead related to ibrutinib is coloured blue and VHL-targeting moiety is coloured red.
Figure based on (Xue et al., 2020)

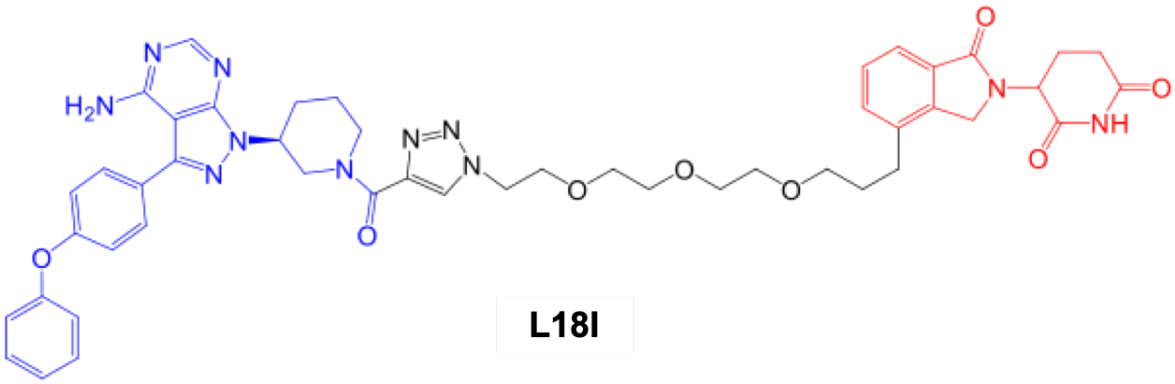

FIGURE 1-19: STRUCTURE OF L18I.

BTK-inhibiting warheads derived from ibrutinib are coloured blue and pomalidomide-derived CRBN-targeting moieties are coloured red. Figure based on (Sun et al., 2019).

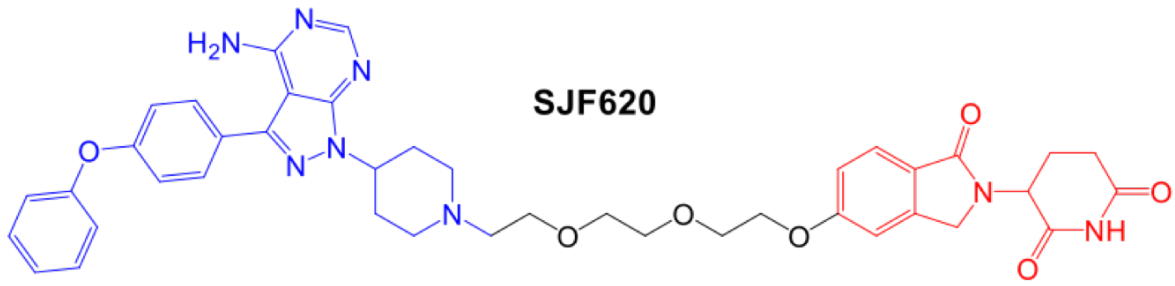

FIGURE 1-20: STRUCTURE OF SJF620.

The reversible BTK-inhibiting warhead related to ibrutinib is coloured blue and the CRBN-targeting moieties are coloured red. Figure based on (Jaime-Figueroa et al., 2020).

1.7 BTK "by-pass" signalling in CLL

Although BTK is classically considered as a key upstream regulator of PLCγ2 and iCa^{2+} release, there is evidence that not all CLL samples respond equally to ibrutinib (unpublished data from host group, G. Packham, personal communication). Thus, the degree of inhibition of anti-IgM-induced iCa^{2+} mobilisation by ibrutinib is variable with some samples showing full inhibition and others partial inhibition (**Figure 1-21**). These findings suggest that a BTK-independent pathway leading to iCa^{2+} release operates in a subset of samples.

Analysis of downstream responses suggests that this residual iCa^{2+} response seen in the presence of ibrutinib remains biologically relevant since it is associated with retained induction of Ca^{2+}-dependent NFAT or NF--κB target genes (including MYC, CCND1, CCND2, and BCL2A1) following anti-IgM stimulation in ibrutinib-pretreated cells (**Figure 1-22A**). Moreover, the ability of anti-IgM to induce expression of the pro-survival BCL2-related protein MCL1 and to suppress spontaneous CLL cell apoptosis is also at least partially retained in the presence of ibrutinib (**Figure 1-22B**). By contrast, all of these responses were fully blocked by upstream inhibition of SYK using tamatinib (also known as R406). Thus, a subset of CLL samples show evidence for residual anti-IgM-induced iCa^{2+} mobilisation despite inhibition of BTK using ibrutinib, and this is associated with retained pro-survival and NFAT/NF-κB signalling. Although these are *in vitro* observations, it is possible that such a pathway could limit the effectiveness of treatment or contribute to relapse in ibrutinib-treated patients. Investigating the nature of this BTK "by-pass" signal is the first aim addressed in this thesis.

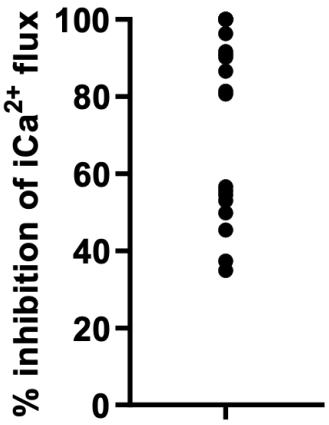

FIGURE 1-21: LEVEL OF INHIBITION OF iCA^{2+} MOBILISATION ACHIEVED WITH IBRUTINIB.

CLL samples were pretreated with ibrutinb or left untreated for 1 hour, and then loaded with calcium indicator dye. The calcium flux assay was carried out (**Section 2.3.2**) to determine the peak percentage of responding cells under the control and treated conditions. The percentage of inhibition by ibrutinib was then calculated for each sample. Data collected by Alex Wathan.

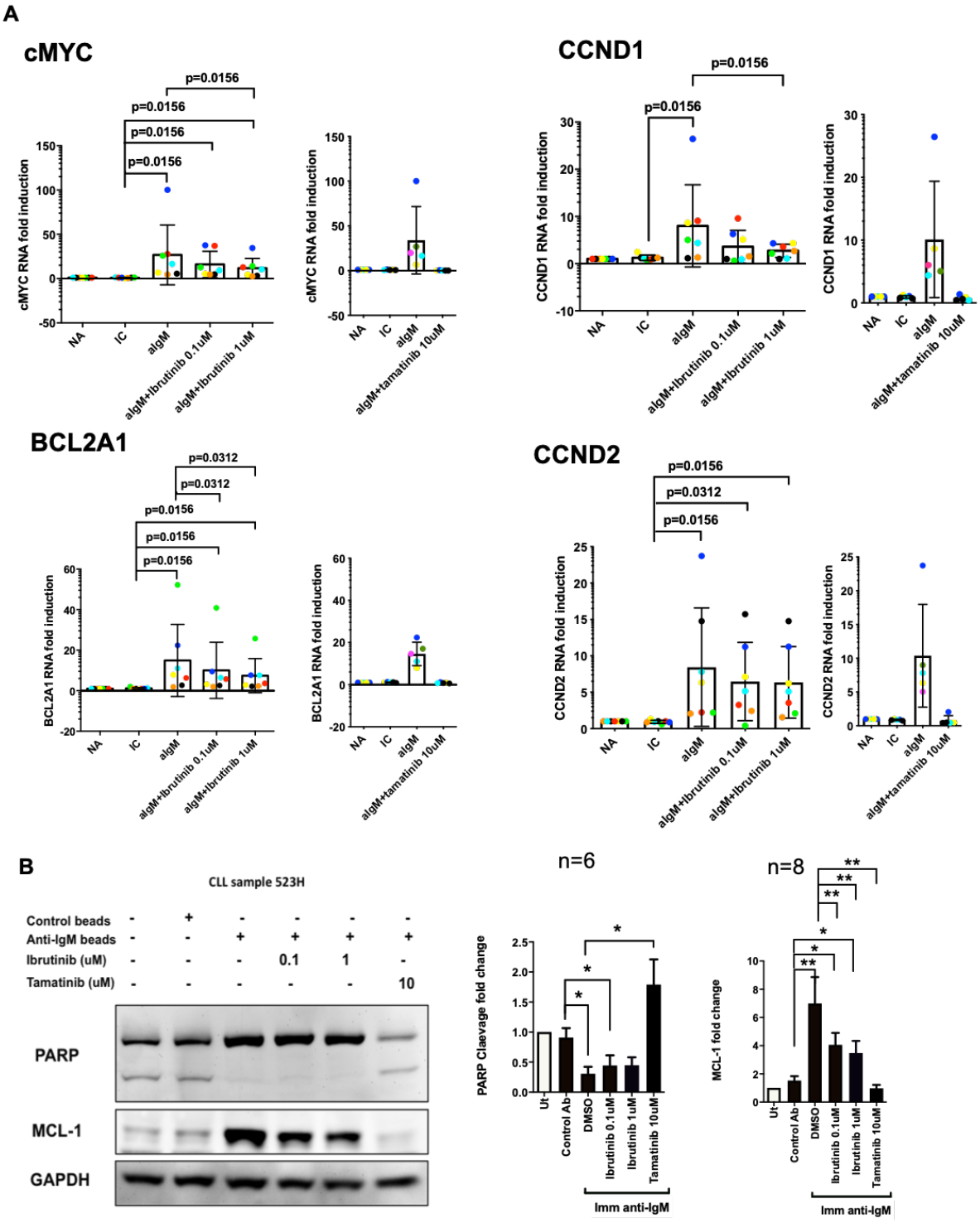

FIGURE 1-22: REGULATION OF CA^{2+}-SENSITIVE TRANSCRITPION FACTOR (NF-κB AND NFAT) TARGET GENES AND ASSESSMENT OF CLL CELL SURVIVAL FOLLOWING IBRUTINIB TREATMENT.

A. CLL samples were pretreated wuth ibrutinib or tamatinib (R406) for 1 hour prior to stimulation with anti-IgM for 6 hours. Q-PCR analysis of NF-κB and NFAT target genes (MYC, CCND1, BCL2A1, and CCND2) was performed and ibrutinib treatment shows partial inhibition. **B.** CLL samples were pretreated with ibrutinib or tamatinib for 1 hour prior to a 24 hour stimulation with anti-IgM. Anti-IgM-induced prosurvival effects were retained despite BTK inhibition. Statistical significance was determined by t tests and indicated on the graph. Data collected and analysed by Dr Beatriz Valle-Argos (University of Southampton, UK).

1.8 Importance of single-cell analysis

There are a number of techniques suitable for analysing single cells with the most widely used being microscopy and flow cytometry. Indeed, for CLL, flow cytometric analysis of iCa^{2+} can predict patient outcome (D'Avola et al., 2016). However, although this method can offer a high-throughput analysis, it has limitations. In particular, it has limited capacity for studying single cells over time. One consequence of this is that potential rare subpopulations may remain unidentified, limiting the predictive power of this tool. Therefore, the second aim of this thesis is to identify whether microwell arrays are a suitable platform for time-resolved, single-cell analysis of iCa^{2+} mobilisation in CLL cells. Microwell arrays comprise thousands of microwells designed to 'trap' single cells, and can be coupled with fluorescence microscopy to track iCa^{2+} fluxes in single cells. In this section, I describe the most commonly used methods for studying iCa^{2+} mobilisation, i.e. flow cytometry, microscopy and microwell array technology, and discuss their benefits and limitations.

1.8.1 Flow cytometric analysis of iCa^{2+} mobilisation

The current method of analysing iCa^{2+} mobilisation is with flow cytometry; outlined in **Section 2.3.2.** Flow cytometry offers a high-throughput, multi-parametric analysis of physical and molecular characteristics (Schiffenbauer et al., 2009). Cells are hydrodynamically focussed into a single-cell stream as they enter the flow cytometer and pass through a laser beam. When a cell interrupts the laser beam the light will be scattered, this light is filtered into different wavelengths to be analysed. Phenotypic properties, such as cell size and intracellular complexity are detected through forward and side scatter, respectively. The presence/absence of other intracellular and extracellular characteristics, labelled with fluorescent markers, can be detected through the appropriate use of filters. Flow cytometers can also be used to sort cell populations based on phenotypic features. However, there are significant restrictions associated with this method, particularly with heterogeneous clinical samples.

The primary restriction of using flow cytometry to analyse iCa^{2+} mobilisation is that it is not possible to track iCa^{2+} fluxes over time in an individual cell. Flow cytometry essentially provides a snapshot of a given cell at any given timepoint. The consequence of this is that the data obtained might mask intraclonal heterogeneity which may be critical for clinical predictions. Flow cytometry also requires relatively large cell numbers and the manual addition of reagents during

analysis introduces technical variability, which can be problematic for rapid responses, including iCa^{2+} mobilisation.

1.8.2 Microscopic analysis of iCa^{2+} mobilisation

An alternative approach to analysing single-cell iCa^{2+} mobilisation is using microscope-based approaches, which provides more visual information about morphology and spatial distribution of Ca^{2+} ions within individual cells than flow cytometry is capable of, and can be used to observe responses and properties over time (Schiffenbauer et al., 2009). In one such study, time-lapsed confocal microscopy was used to show that the Ca^{2+} ions were not equally distributed inside of the cells but became compartmentalised with pronounced subcellular dynamics (Junek et al., 2012). Through single-cell imaging, Junek et al. revealed small and locally restricted areas of high $i[Ca^{2+}]$ in resting B cells, and following BCR engagement discrete punctate structures were observed in the peripheral region of the cell. The authors also demonstrated that translocation of BLNK from the cytosol to the PM precedes the release of Ca^{2+} from the ER and that only tiny amounts of BLNK are required to pass the Ca^{2+} release threshold. This study highlights the usefulness of single-cell microscopic analysis providing very interesting, meaningful and valuable data, however it also demonstrates that this is a time consuming approach and not readily applicable for higher-throughput analyses.

1.8.3 Microwell arrays for analysing iCa^{2+} mobilisation

Microwell arrays consist of thousands of microwells that can "trap" single cells by sedimentation. The dimensions of the microwells can be modified to ensure that only one cell can fit into a microwell. Microwell arrays can be made with a variety of materials, including agarose, a biocompatible material, through soft lithography techniques whereby a 'template' can be used to essentially stamp the design into softer materials. The 'template' can be created by producing a wafer consisting of micropillars, fabricated using photolithography, onto which melted agarose can be poured. Therefore, multiple arrays can be produced from a single template. When coupled with real-time fluorescence imaging, they can be used to investigate intracellular signalling, including the time-resolved analysis of Ca^{2+} responses in individual cells. Such devices are capable of high-throughput single-cell measurement and have a variety of applications (Rettig and Folch, 2005; Schiffenbauer et al., 2009). These types of devices make it easier for studying rare cells and allow heterogeneous populations to be more fully described. The concept is shown in **Figure 1-23**.

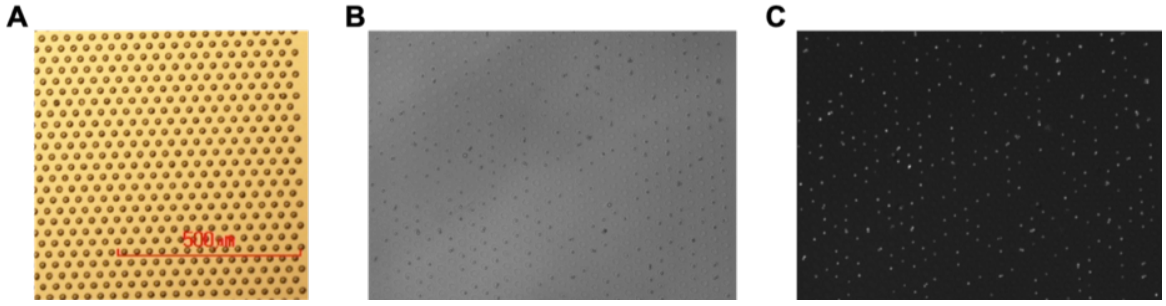

FIGURE 1-23: THE CONCEPT OF MICROWELL ARRAYS TRAPPING SINGLE CELLS.

A. Brightfield image of micropillar array (scale bar is 500 µm) made using SU8-3025 photoresist on a silicon substrate. **B.** Brightfield image of agarose microwell array showing 'trapped' cells. **C.** Fluorescent image of the agarose microwell array showing stained cells 'trapped' in the array.

There are many examples of the use of microwell arrays for trapping and analysing single cells including for cell:cell interactions, intracellular signalling and DNA damage (Schiffenbauer et al., 2009; Huang et al., 2016; Chung et al., 2011; Lee et al., 2010; Wood et al., 2010). Microwell arrays offer several advantages over standard flow cytometry and provide promise for probing intra-sample variation: (i) they have the potential to be coupled to microfluidic devices for the delivery of substrates/ligands minimising the time and variation associated with the manual addition of reagents, (ii) they have the ability to track the response of individual cells over time providing much more information about the behaviour of 'atypical' cellular responses, (iii) it is possible to retrieve individual cells (Yamamura et al., 2005; Ozawa et al., 2009), particularly those with unusual patterns of signalling behaviour, for further characterisation (e.g. genomic analysis), and (iv) the volumes of samples and reagents are much smaller leading to reduced cost, reduced waste and the ability to use smaller sample sizes. This is particularly beneficial for diseases where only small amounts of patient material can be acquired and where tumour cells are less readily available, e.g. DLBCL and follicular lymphoma.

As well as the ability to retrieve cells of interest from the microwell array, it is also possible to perform other analyses on cells remaining in the microwells. For example, single-cell western blotting has been described (Kang et al., 2014) and could be used to further investigate the BCR-associated signalling pathways. It is also possible to sequence RNA, providing a deeper understanding of the transcriptional state of the cells, using a method based on padlock probing, rolling-circle amplification and sequencing-by-ligation chemistry (Ke et al., 2013). Padlock probes have two target-complementary segments connected by a linker region, which can include

barcodes (Nilsson et al., 1994). The ends of the padlock probe can be joined by enzymatic ligation creating circular molecules attached to the target sequence (Banér et al., 1998). The DNA circle is then amplified and can be subjected to sequencing-by-ligation, whereby an anchor primer is hybridised next to the target sequence before the ligation of interrogation probes (consisting of a random sequence with one fixed position of A, C, G or T), which are labelled with fluorescent dyes (Ke et al., 2013). Following ligation, the sample can be imaged (the colour will correspond to the base) and the interrogation probe can be washed away before the next interrogation probe is added for the following base; this can be repeated until the desired number of bases has been read (Ke et al., 2013).

Developing this technology for the time-resolved singe-cell analysis of iCa^{2+} mobilisation might allow the identification of intraclonal heterogeneity or sub-clones with unusual characteristics which might be able to be used for better prediction of treatment plans, likelihood of treatment resistance or disease relapse and therefore might be used as a better predictor of prognosis than current technologies. This is particularly important within B cell malignancies as there is evidence that rare populations can alter clinical disease course. For example, p53 mutations can be rare in the CLL population but are still associated with poor prognosis (Dicker et al., 2009; Gonzalez et al., 2011; Rossi et al., 2009). Although it is not clear whether this applies to iCa^{2+} signalling capacity, improved technology might help overcome the limitations associated with flow cytometry and allow a greater depth of investigation into single-cell analysis.

1.9 Hypothesis and aims

1.9.1 Hypotheses

1. The inhibitory effects of BTKi on anti-IgM-induced iCa^{2+} fluxes are variable between CLL samples, reflecting the action of a BTK "by-pass" mechanism whereby activation of PLCγ2 and subsequent iCa^{2+} release occurs independently of BTK.

2. Microwell arrays are a suitable platform for analysis of single-cell, time-resolved analysis of iCa^{2+} signalling in malignant B cells.

1.9.2 Aims and objectives

1. To characterise B-cell receptor-induced iCa^{2+} signalling and response to BTK inhibitors using B-cell lines and primary CLL samples.
    a. Extend analysis of ibrutinib's inhibitory effect on anti-IgM-induced iCa^{2+} fluxes to additional CLL samples to confirm initial findings (**Figure 1-21**).
    b. Determine whether similar effects are observed with acalabrutinib, a more selective BTKi.
    c. Investigate potential correlations between clinical and biological features of CLL samples and variable responses to BTKi.
    d. Compare the effects of ibrutinib and a BTK-degrading PROTAC to investigate the potential contribution of BTK-mediated, kinase-independent pathways.
    e. Determine whether partial responses to BTKi are observed in other malignant B cells by analysing the efficacy of BTKi for inhibition of iCa^{2+} fluxes in DLBCL cell lines.

2. To investigate and characterise potential BTK "by-pass" mechanisms leading to iCa^{2+} mobilisation.
    a. Identify BTK-dependent and -independent PLCγ2/PLCγ1 phosphorylation events that may lead to iCa^{2+} mobilisation in primary CLL and DLBCL cell lines.
    b. Investigate the effect of enhanced signalling in CLL using IL-4, and the effect on BTK inhibition.

   c. Investigate the concentration dependency of inhibition of BTK by assessing drug occupancy of the active site of BTK and western blotting to assess phosphorylation events within the BCR-associated signalling pathway.

3. To develop and optimise microwell arrays for use with B-cell lines and primary CLL samples.
   a. Perform exploratory experiments using existing arrays to determine approximate suitable microwell sizes and proof of concept for data collection, including the comparison of Ca^{2+} indicator dyes.
   b. Design and fabricate wafers with a range of microwell diameters and heights.
   c. Identify optimal microwell size and cell seeding conditions for primary CLL samples.
   d. Quantify single-cell anti-IgM-induced iCa^{2+} signalling responses (including pre-treatment with kinase inhibitors) in CLL samples.

Chapter Two

Materials and Methods

2 Materials and Methods

2.1 Cell culture techniques and sample preparation

2.1.1 Materials

Material	Components
Complete RPMI-1640 (cRPMI)	RPMI 1640 (Sigma Aldrich, Missouri, United States) supplemented with 10% foetal bovine serum (FBS), 1% glutamine (Sigma) and 1% penicillin/streptomycin (Sigma)
Complete IMDM (cIMDM)	Iscove's Modified Dulbecco's Medium (Gibco™, US) supplemented with 20% FBS, 1% glutamine and 1% penicillin/streptomycin

2.1.2 Ethics

All primary CLL samples used in this project were collected at diagnosis or prior to treatment from patients recruited to the Lymphoproliferative disorder (LPD) study at the Department of Haematology, University Hospital Southampton NHS Foundation Trust. The study was approved by the Ethics Committee (REC reference 228/02/t) and conducted in accordance with the Declaration of Helsinki. Patients provided written informed consent prior to sample donation.

2.1.3 CLL sample preparation

The diagnosis of CLL was confirmed by flow cytometry and the characterisation of the samples, including mutational status of the *IGHV* gene, tumour cell population percentage ($CD19^+$ $CD5^+$ cells), percentage of CD38 positive, CD49d positive and ZAP-70 positive cells, and the calcium flux response as a percentage of cells responding to anti-IgM stimulation, was collected and recorded by research technicians. CLL samples were collected by isolating peripheral blood mononuclear cells (PBMCs) by gradient density centrifugation. PBMCs were resuspended in FBS with 10% (v/v) dimethyl sulfoxide (DMSO) (Sigma) and frozen in a cryo freezing container before transfer to liquid nitrogen (LN_2) for storage.

Each sample was prepared immediately prior to use by thawing rapidly in a 37 °C waterbath and adding to 10 ml warm cRPMI. The cells were collected by centrifugation at 350 g for 5 minutes at room temperature. The cell pellet was resuspended in 10 ml warm complete RPMI at which point the live cells were counted using a haemocytometer via the trypan blue exclusion assay. Trypan blue solution (Sigma) was mixed in equal volumes with PBMC cell suspension and 10 µl was pipetted on to the haemocytometer. Light microscopy was used to visualise cells and viable cells, which prevent trypan blue from entering, were counted (dead cells with a disrupted membrane allow trypan blue to enter the cell and therefore appear blue). The cells were collected by centrifugation at 350 g for 5 minutes at room temperature and the pellet was resuspended in cRPMI to a density of $1x10^7$ cells/ml. The cells were allowed to recover for 1 hour at 37°C, 5% CO_2. A table of CLL samples used during this project, with their characteristics, are listed in **Table 2-1**. A list of samples used for each experiment type can be found in **Appendix 1**.

2.1.4 Culture of DLBCL cell lines

DLBCL cell lines were cultured at 37 °C, 5% CO_2 and maintained at a density of $5x10^5$ cells/ml. All cell lines used (HBL1, HT, OCI-Ly18, SUDHL6 and TMD8) were cultured in cRPMI except OCI-Ly7 cells, which were cultured in cIMDM media. Cell lines were provided by other members of the B-cell malignancy research group. Identity of all human cell lines was confirmed using short tandem repeat analysis (Promega 16-plex kit) and absence of mycoplasma was confirmed by PCR analysis (ABM).

2.1.5 Cell membrane staining

Where applicable, cells were stained with 2 µM CellVue™ Maroon (a lipophilic cell membrane dye) (Invitrogen™, UK). Cells were collected by centrifugation at 350 g for 5 minutes and the pellet was resuspended in serum free RPMI-1640 (supplemented with glutamine and penicillin/streptomycin). The cell pellet was collected by centrifugation at 350 g for 5 minutes and resuspended in Diluent C (Invitrogen™, UK) to a density of $2x10^7$ cells/ml. An equal volume of a 4 µM dye solution in Diluent C was added to the cells to give a final dye concentration of 2 µM and a cell density of $1x10^7$ cells/ml. The cells were incubated at room temperature in the dark for 2 minutes. An equal volume of FBS was added to terminate staining, this was rested for 1 minute.

The cells were washed three times in cRPMI by centrifugation at 350 g for 5 minutes before resuspending the pellet in cRPMI to a density of $1x10^7$ cells/ml.

Alternatively, and where applicable, cells were stained with CellTracker™ Deep Red Dye (Invitrogen™). Cells were collected by centrifugation at 350 g for 5 minutes and the pellet was resuspended in CellTracker™ Deep Red working solution. The working solution was prepared by dissolving one vial of dye in 20 μl DMSO to create a 1 mM solution, and diluting in serum free medium to a final concentration of 5 μM. The cells were incubated for 30 minutes at 37 °C, 5% CO_2 before collection by centrifugation at 350 g for 5 minutes. Cells were resuspended in complete culture medium for use.

2.1.6 Cell treatments

Following the 1 hour recovery of primary cells, or with cell lines collected from culture flasks, the cells were treated with R406 (S2194, Selleckchem, UK), ibrutinib (S2680-SEL, Stratech, UK), or acalabrutinib (S8116, Selleckchem, UK) for 1 hour at 37 °C, 5% CO_2, or MT-802 (kindly provided by Dr Craig Crews, Yale University, United States), for either 4 or 24 hours at 37°C, 5% CO_2. These compounds were dissolved in DMSO, stored at -20 °C and then thawed on ice prior to use.

2.1.7 Determining cell diameter

2.1.7.1 Impedance cytometry

Cells were resuspended in filtered PBS to a density of $1x10^6$ cells/ml and mixed with calibration beads of known size. When measuring primary CLL cells, the calibration beads had a diameter of 3 μm, and when measuring DLBCL cell lines, the calibration beads had a diameter of 7 μm. The solution was injected into an impedance cytometer at a flow rate of 10 μl/min and a voltage was applied to the top electrodes and the current drawn at the bottom was measured and recorded (Sun et al., 2007) (Error! Reference source not found.). The voltage used for primary CLL cells was 1 MHz, and for DLBCL cell lines was 800 kHz. The data was acquired and analysed using MATLAB by Fabrizio Siracusa (Centre for Hybrid Biodevices, University of Southampton, UK).

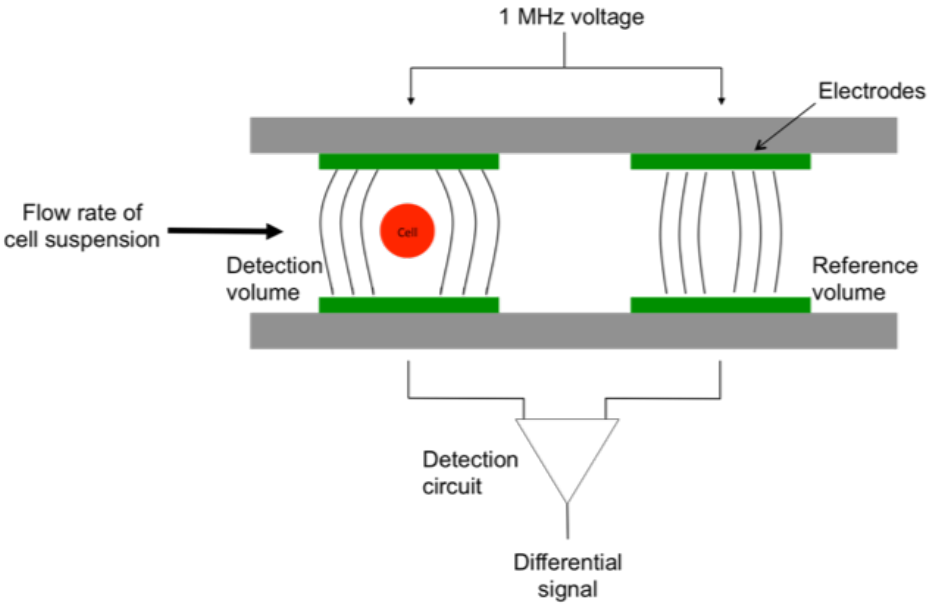

FIGURE 2-1: IMPEDANCE CYTOMETRY TO MEASURE DIAMETER OF CELLS.

Cells were injected at a flow rate of 10 µl/min. A voltage was applied to the top electrodes and the current drawn at the bottom electrodes was detected and recorded. Adapted from (Sun et al., 2007).

2.1.7.2 Microscopy

10 µl of primary CLL cells at a density of $2x10^6$ cells/ml in cRPMI were pipetted into a disposable counting slide (Immune Systems). Images were captured at 20x magnification using an Olympus CKX41 microscope integrated with Q-imaging camera and micromanager software. The 'Analyse Particles' function in ImageJ was used to determine the area of the cells and an area of 20 – 80 μm^2 was set as the threshold. Microsoft Excel was used to calculate the diameter of the cells from the area measurements.

TABLE 2-1: SUMMARY INFORMATION OF PRIMARY CLL SAMPLES USED.

CLL Sample Number	CD19 CD5 coexpressing cells (%)	sIgM MFI	Cells responding to anti-IgM[1] (%)	IGHV gene mutation status[2]
368D	97	52	35	M
409C	73	112	60	U
471B	96	77	81	M
480	86	50	32	M
482E	97	15	4	M
500C	92	60	12	U
523B	94	26	14	M
523D	95	48	65	M
523F	97	31	25	M
523H	92	45	39	M
564B	92	1700	83	M
575B	97	87	64	M
595D	95	36	20	U
604C	86	61	60	M
604F	87	54	79	M
609C	94	53	79	M
621B	93	49	49	M
635C	90	78	89	U
635D	95	50	78	U
643	92	25	26	M
674A	88	331	89	U
674B	84	295	89	U
674D	85	314	88	U
681	97	212	60	M
681A	98	185	31	M
681B	98	116	27	M
684A	92	31	14	M
684C	92	25	13	M
686	84	67	80	M
687B	72	252	81	U
689	97	41	15	U
705	96	70	16	M
709A	77	50	63	M
739	98	99	76	U
739A	97	83	75	U
740	74	23	11	M
747B	83	184	40	U
755	91	72	81	U
758	80	90	84	M
774	97	80	27	U

775	83	65	57	U
780	99	65	81	U
780A	99	81	81	U
780B	98	47	81	U
781	95	57	51	M
782A	87	155	69	M
791	87	43	27	M
791A	88	47	28	M
794	90	15	2	M
802	91	40	3	U
803	96	33	30	U
803A	94	33	31	U
803B	93	38	20	U
803C	95	30	31	U
803D	NK	NK	NK	ND
815	84	55	32	M
816B	89	43	70	U
816D	NK	NK	NK	ND
842A	94	91	49	U
895A	NK	NK	NK	ND
900A	NK	NK	NK	ND
908	92	144	NK	ND
960	96	76	NK	U
960A	98	61	58	U

[1] Measurement of intracellular Ca^{2+} flux as described by Mockridge et al., 2007. Analysis performed by research technicians.

[2] Sequencing carried out by Isla Henderson. U: unmutated, M: mutated, ND: not determined.

NK: not known.

N.B. The sample numbers (without letter) represent the first sample collected from a patient; a letter after the number denotes a subsequent sample from the same patient.

2.2 Protein analysis techniques

2.2.1 Materials

Material	Components
5X RIPA buffer	0.75M NaCl, 5% NP40, 2.5% Deoxycholate, 0.5% SDS, and 0.25 M Tris (pH 8.0)
10% acrylamide gel	5 ml H_2O, 3.3 ml 30% acrylamide (Sigma), 2.5 ml 1.5 M Tris (pH 8.8), 100 µl 10% SDS, 100 µl 10% ammonium persulfate (APS), and 4 µl TEMED (Sigma)
Stacking gel	2.7 ml H_2O, 670 µl 30% acrylamide, 500 µl 1.0 M Tris (pH 6.8), 40 µl 10 % SDS, 40 µl 10% APS, 3 µl TEMED
10X Running buffer	250 mM Tris base, 1.9 M glycine, 35 mM SDS
Transfer buffer	500 ml absolute ethanol, 200 ml 10X Running buffer, diluted in 2 L dH_2O
1% TBS-tween	10 mM Tris (pH 8.0), 150 mM NaCl diluted in 1 L dH_2O with 1 ml Tween-20 (Sigma)
Stripping buffer	25 mM Glycine (pH 2.0), 1% SDS (w/v) diluted in 1 L dH_2O
MIB lysis buffer	50 mM HEPES (pH 7.5) (Sigma), 150 mM NaCl, 0.5% Triton X-100, 1 mM EDTA, 1 mM EGTA, 10 mM NaF, 2.5 mM $NaVO_4$
High salt buffer	50 mM HEPES (pH 7.5), 1 M NaCl, 0.5% Triton X-100, 1 mM EDTA, 1 mM EGTA
Low salt buffer	50 mM HEPES (pH 7.5), 150 mM NaCl, 0.5% Triton X-100, 1 mM EDTA, 1 mM EGTA
Elution buffer	0.5% (w/v) SDS, 1% (v/v) β-mercaptoethanol (Sigma), 0.1 M Tris-HCl (pH 6.8), dH_20

2.2.2 Multi-inhibitor bead assay

NHS-activated Sepharose 4 Fast Flow beads (GE Healthcare Life Sciences) were coated with Ki-NET (CTx-0294885) (SYNkinase, USA), a multi-kinase inhibitor compound, and subsequently called multi-inhibitor beads (MIBs). The MIBs were stored at 4 °C and were made by Dr Adam Linley (University of Liverpool, UK).

$3x10^7$ cells per condition (at a density of $1x10^7$ cells/ml) were treated with inhibitors for 1 hour at 37 °C, 5% CO_2 before stimulating with 20 µg/ml of goat $F(ab')_2$ anti-human IgM-UNLB (Southern Biotechnology, Cambridge, UK) for 30 seconds at 37 °C. An equal volume of ice-cold PBS was

added to each sample before transferring it to ice to terminate reactions. The cell pellet was collected by centrifugation at 350 g for 5 minutes at 4 °C. The pellet was lysed in 500 µl MIBs lysis buffer, supplemented with protease inhibitor cocktail (Sigma), phosphatase inhibitor cocktail 2 (Sigma) and phosphatase inhibitor cocktail 3 (Sigma) at 1:100 dilutions. The cells were lysed on ice for 10 minutes before sonication three times for 10 seconds, allowing each sample to cool on ice between pulses. Lysates were clarified by centrifugation at 13000 rpm in a microfuge for 10 minutes at 4 °C and the supernatant was quantified for total protein content using the Bradford Assay, as described in **Section 2.2.3.2**.

Lysate containing 950 µg protein was made up to 3 ml with cold lysis buffer and brought to 1 M NaCl. 350 µl MIBs slurry was pipetted onto a filter column and washed with 2 ml high salt buffer. The lysate was pipetted onto the column containing the MIBs and allowed to flow through. The columns were washed with 5 ml high salt buffer, then 5 ml low salt buffer, followed by 500 µl 0.1 % SDS in low salt buffer. 500 µl elution buffer was added to each column and the cap was firmly secured before boiling for 15 minutes. The eluate was collected and the elution step repeated with a further 500 µl elution buffer. 10 µl 500 mM DL-DTT (Sigma) was added to each eluate and incubated at 60 °C for 25 minutes. The samples were brought to room temperature before the addition of 100 µl 200 mM iodoacetamide (Sigma) and incubated in the dark at room temperature for 30 minutes. A further 10 µl of 500 mM DL-DTT was added to each sample to bring the final concentration of DL-DTT to 10 mM and they were then incubated for a further 5 minutes at room temperature in the dark. The samples were concentrated in Millipore Amicon Ultra-4 (10K cutoff) spin columns (Merck) by centrifugation at 2000 g for 30 minutes at 4 °C. The concentrated samples were mixed with loading dye and analysed with 8% SDS-PAGE gels as described in **Section 2.2.3.3**. Following transfer to nitrocellulose membranes, they were incubated with antibody and imaged as described in **Section 2.2.3.4** and **Section 2.2.3.5**, respectively,

2.2.3 Western blotting

2.2.3.1 Protein extraction

$5x10^6$ cells per condition were treated with inhibitors for 1 hour at 37 °C, 5% CO_2 before stimulating with 20 µg/ml of goat $F(ab')_2$ anti-human IgM-UNLB or goat $F(ab')_2$ IgG-UNLB (both Southern Biotechnology, Cambridge, UK) for either 30 seconds (for proximal BCR-associated signalling molecules) or 15 minutes (for distal BCR-associated signalling molecules) at 37 °C. An

equal volume of ice-cold PBS was added to each sample before transferring it to ice to terminate reactions. The cell pellet was collected by centrifugation at 350 g for 5 minutes at 4 °C, followed by lysis in 50 µl RIPA buffer supplemented with protease inhibitor cocktail (Sigma), phosphatase inhibitor cocktail 2 (Sigma) and phosphatase inhibitor cocktail 3 (Sigma) at 1:100 dilutions. Lysates were clarified by centrifugation at 13000 rpm in a microfuge for 5 minutes at 4 °C and the supernatant was quantified for total protein content using the Bradford Assay.

2.2.3.2 Protein quantification

Bio-Rad Protein Assay Dye Reagent Concentrate (Bio-Rad, UK) is prepared by diluting in dH_20 at a ratio of 1:4. 250 µl of the prepared dye reagent is used per condition and each condition is analysed in duplicate. The dye reagent is added to the appropriate number of wells in a 96-well plate. A standard curve is measured using BSA, whereby known concentrations (0, 0.2, 0.4, 0.6, 0.8, and 1 µg/µl) are measured for their absorbance. 1 µl lysate is analysed for each sample condition, in duplicate. The absorbance is measured using Varioskan plate reader set to read absorbance at 595 nm. The protein concentration of the samples is calculated based on the BSA standard curve.

2.2.3.3 Gel electrophoresis and protein transfer to membrane

An equal concentration of protein, mixed with loading dye (Cell Signaling Technology, UK) containing dithiothreitol (DTT) was heated to 95 °C for 5 minutes to denature proteins and reduce protein-protein interactions. The proteins were separated on a polyacrylamide gel. The protein/dye solutions were loaded into wells of a 10% SDS-PAGE gel, made according to Molecular Cloning: A Laboratory Manual (Sambrook *et al*., 1989). Electrophoresis was carried out in running buffer at 120 V for approximately 1 hour, or until the dye front reached the bottom of the gel. Proteins are resolved by migrating through the gel according to their Stokes radius such that smaller proteins migrate more easily than larger proteins resulting in smaller proteins being towards the bottom of the gel and larger proteins being nearer the top. An approximation of the size of a protein was determined by running a protein ladder (PageRuler™ Plus Prestained Protein Ladder 10-250 kDa, ThermoScientific™) alongside the samples containing multiple proteins of known sizes.

Separated proteins were then transferred onto nitrocellulose membranes (Whatman Protran, GE Healthcare) in transfer buffer for 1 hour at 100 V. The membrane was blocked with 1 ml 5% BSA (w/v) in TBS-T for 1 hour at room temperature.

2.2.3.4 Antibody incubation

Primary antibodies (**Table 2-2**) were added to the membranes, diluted 1 in 1000, in 5 ml 5% (w/v) BSA in TBS-T, and incubated overnight at 4 °C, whilst being rocked. Membranes were washed 3 times for 5 minutes each with TBS-T before being incubated with 5 ml horseradish peroxidase (HRP)-conjugated secondary antibodies (**Table 2-3**) at a dilution of 1:2000 in 5% (w/v) BSA in TBS-T at room temperature for 1 hour, whilst being rocked. Membranes were again washed 3 times for 5 minutes each with TBS-T.

2.2.3.5 Imaging and band quantification

Imaging was performed using the SuperSignal™ West Pico PLUS chemiluminescent substrate (ThermoScientific™) or SuperSignal™ West Femto chemiluminescent substrate (ThermoScientific™). These reagents contain enhanced chemiluminescent HRP substrate that maintained the light emitted from the reaction of luminol in hydrogen peroxide with HRP. The proteins in the membrane were visualised with ChemiDoc-It™ imaging system with the BioChemi HR Camera (UVP, Cambridge, UK) controlled by VisionWorks software. Density of protein bands was quantified using ImageJ/Fiji.

2.2.3.6 Stripping and re-probing nitrocellulose membranes

After probing a membrane for a phospho-protein the membrane was stripped using stripping buffer to remove the primary and secondary antibodies. The membrane could then be re-probed for the total protein using the same method described above (**Section 2.2.3.4).** The membrane was incubated with 5 ml stripping buffer at room temperature for 5 minutes whilst being rocked. The membrane was then washed three times for 5 minutes with TBS-T before adding the primary antibody.

TABLE 2-2: PRIMARY ANTIBODY PRODUCT DETAILS USED IN WESTERN BLOT ANALYSES.

Primary Antibody	Product Number	Company
anti-phospho BTK Tyr223	5082	Cell Signaling Technology
anti-phospho BTK Tyr551	ab40770	Abcam
anti-BTK	8547	Cell Signaling Technology
anti-phospho SYK Tyr525/526	2710	Cell Signaling Technology
anti-SYK	2712	Cell Signaling Technology
anti-phopsho LYN Tyr396	ab226778	Abcam
anti-phospho LYN Tyr507	2731	Cell Signaling Technology
anti-LYN	2732	Cell Signaling Technology
anti-phospho BLNK Tyr84	ab174837	Abcam
anti-phospho BLNK Tyr96	3601	Cell Signaling Technology
anti-BLNK	12168	Cell Signaling Technology
anti-phospho PLCγ2 Tyr753	ab75659	Abcam
anti-phospho PLCγ2 Tyr759	ab227001	Abcam
anti-phospho PLCγ2 Tyr1197	ab75970	Abcam
anti-phospho PLCγ2 Tyr1217	ab52610	Abcam
anti-PLCγ2	3872	Cell Signaling Technology
anti-phospho PLCγ1 Tyr783	2821	Cell Signaling Technology
anti-PLCγ1	2822	Cell Signaling Technology
anti-phospho AKT Ser473	4060	Cell Signaling Technology
anti-AKT	9272	Cell Signaling Technology
anti-phospho ERK1/2 Thr202/Tyr204	9101	Cell Signaling Technology
anti-ERK1/2	9102	Cell Signaling Technology
anti-GAPDH	AM4300	Invitrogen

TABLE 2-3: SECONDARY ANTIBODY PRODUCT DETAILS USED IN WESTERN BLOT ANALYSIS.

Secondary ANtibody	Product Number	Company
Polyclonal Goat Anti-Rabbit Immunoglobulins/HRP	P044801-2	Dako, Agilent
Polyclonal Goat Anti-Mouse Immunoglobulins/HRP	P044701-2	Dako, Agilent

2.3 Flow cytometry assays

2.3.1 Materials

Material	Components
FACS buffer	1% BSA, 4 mM EDTA, 0.15 mM sodium azide in 1X phosphate buffered saline (PBS)

2.3.2 Ca^{2+} flux assay

sIgM signalling capacity was determined by measuring the percentage of CLL cells with increased iCa^{2+} following stimulation with soluble goat $F(ab')_2$ anti-IgM. Samples with a ≥5% cells responding to anti-IgM were classified as "signallers" (Mockridge et al., 2007).

$5x10^6$ cells per condition (pretreated with inhibitors as required, described in **Section 2.1.6**) were stained with 8 µg/ml Fluo-3, AM (Invitrogen™, UK) including 2 µl 10% (w/v) Pluronic F-127 (Sigma, UK) to increase permeabilization of the cell membrane and incubated for 30 minutes in the dark at 37 °C, 5% CO_2. Cells were washed in complete cell medium by centrifugation at 350 g for 5 minutes at room temperature and the pellets were resuspended to a density of $5x10^6$ cells/ml in cell media supplemented with inhibitors where applicable. $2.5x10^6$ cells were transferred to a FACS tube and kept at room temperature in the dark.

Directly prior to acquisition each sample was heated to 37 °C in a water bath for 5 minutes. All tubes were acquired on a low flow rate with the maximum number of events to be recorded and an automatic stopping time of 420 seconds. Following warming, each sample was briefly pulsed using a vortex and placed on the cytometer. Unstimulated cells were acquired and recorded for 30 seconds. After 30 seconds, the tube was carefully removed during recording and 20 µg/ml of goat $F(ab')_2$ anti-human IgM-UNLB or goat $F(ab')_2$ IgG-UNLB (both Southern Biotechnology, Cambridge, UK) was added and the tube replaced on the cytometer; data was acquired and recorded for 270 seconds. After this, tubes were again removed from the cytometer, whilst still recording data to add 1µM ionomycin (Sigma, UK) as a positive control. The tube was replaced on the cytometer and data acquired and recorded for a further 120 seconds.

Flow cytometry was carried out using a BD FACS Canto with FACS Diva software to acquire and record data, which was acquired through the FITC channel as Fluo-3, AM emits at 488 nm. Data was analysed using FlowJo (v 9.8.1) software using the kinetics function. A cell was counted as responsive if it increased above 85% of the unstimulated data (**Figure 2-2**).

The peak percentage of responding cells was calculated using the following formula (tumour population (%) was calculated during routine phenotyping for the standard processing of CLL samples available for research and available in the database):

$$\%\ responding\ cells = \left(\frac{Peak\ (Stimulation) - MeanY\ (Unstimulated)}{Tumour\ population\ (\%)}\right) \times 100$$

The area under the curve (AUC) was calculated automatically in FlowJo for the gate between 30 – 300 seconds (excluding pre-stimulation/ionomycin effects).

The relative anti-IgM-induced iCa^{2+} response was calculated using the following formula:

$$relative\ anti\ IgM\ induced\ iCa\ response = \frac{Peak\ (Stimulation)}{MeanY\ (Unstimulated)}$$

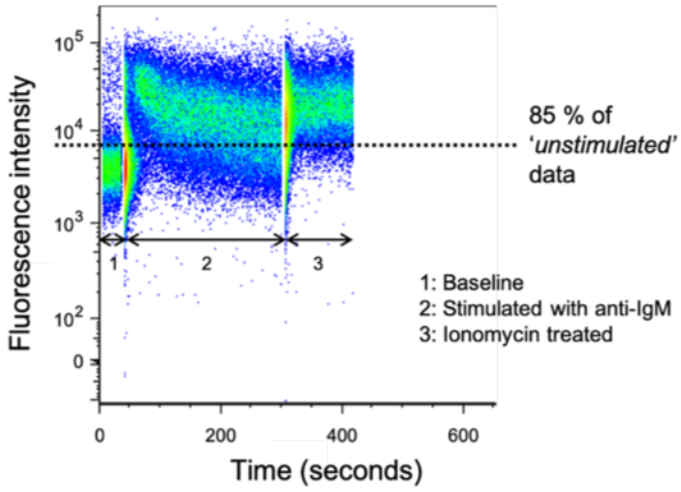

FIGURE 2-2: THRESHOLD OF ACTIVATION FOR CA^{2+} FLUX ASSAY.

Dot plot showing fluorescence intensity over time (seconds) using OCI-Ly7 cells stained with Fluo-3 AM for 30 minutes before data acquisition with flow cytometry. The cells were stimulated with anti-IgM at 30 seconds and Ionomycin at 300 seconds. The first 30 seconds of data represent baseline fluorescence. The threshold is set at 85% of this portion of data. The following 2 sections of data (the anti-IgM stimulated cells, and the ionomycin treated cells) are compared to the baseline data and an event is recorded as a 'responder' if it crosses the threshold.

2.3.3 sIgM expression on CLL cells

Primary CLL cells, prepared as described in **Section 2.1.3**, were treated with 10 ng/ml IL-4 for 24 hours (as described by Aguilar-Hernandez *et al*., 2016), or left untreated as a control (the control cells were analysed at 0 hours and at 24 hours post recovery). Cells were incubated at 37 °C, 5% CO_2 for 24 hours. $1x10^6$ cells per condition were aliquoted into FACS tubes. Cells were collected by centrifugation at 350 g for 5 minutes and resuspended in 100 µl FACS buffer supplemented with 5 µl Pacific Blue™ anti-human CD19 (BioLegend®), 5 µl PerCP/Cy5.5 anti-human CD5 antibody (BioLegend®), with either 5.6 µl rabbit F(ab')2/RPE control antibody (DAKO, Agilent, UK) or 10 µl polyclonal rabbit anti-human IgM/RPE, affinity-isolated F(ab')2 antibody (DAKO, Agilent, UK). A fully unstained sample was also analysed as an additional control.

The cells were incubated on ice for 30 minutes in the dark, before washing twice by centrifugation at 350 g for 5 minutes, in 500 µl FACS buffer. The cell pellet was then resuspended in 100 µl and kept on ice in the dark. Samples were analysed using a BD FACS Canto with FACS Diva software to acquire and record data. All tubes were acquired on a low flow rate with an automatic stopping setting of 10,000 events. Data was analysed using FlowJo (v 10.6.2) software. The gating strategy used is shown in **Figure 2-3**.

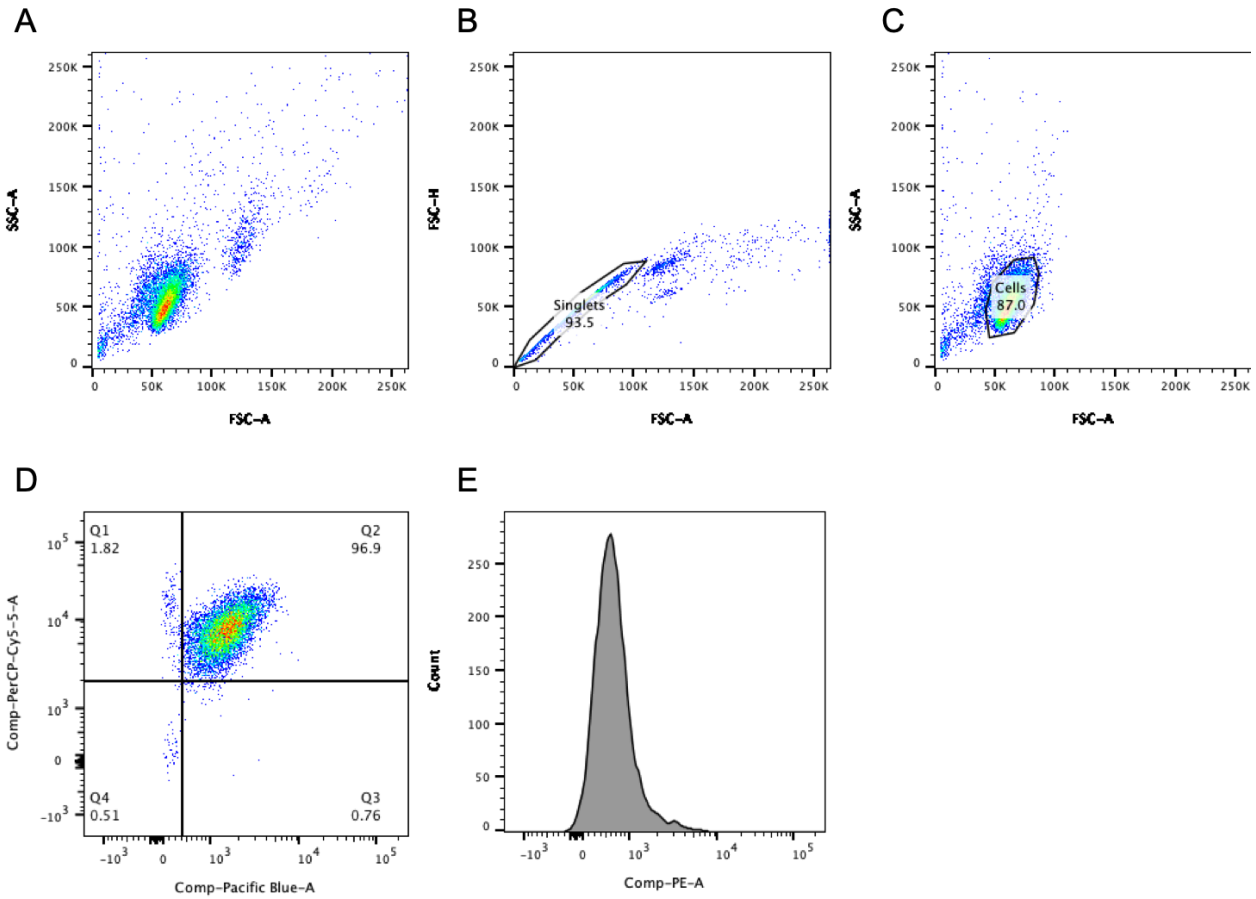

FIGURE 2-3: GATING STRATEGY FOR DETERMINATION OF SIGM EXPRESSION ON PRIMARY CLL CELLS.

CLL cells were treated with IL-4 for 24 hours or left untreated and were subsequently stained for CD19 and CD5 with either an IgM antibody or an isotype control antibody for 30 minutes. Following data acquisition (**A**), the single cells were selected (**B**) to exclude doublets, and were then subsequently gated on the cell population (**C**). The CD19+ and CD5+ cells were selected (**D**) and the PE fluorescence was measured (**E**) to calculate the sIgM expression in each sample.

2.4 Design and fabrication of microwell arrays

2.4.1 Mask design

The mask was designed using DraftSight software and manufactured by JD PhotoData, UK.

2.4.2 Wafer fabrication

Wafers were produced by standard photolithography procedures (summarised in **Figure 2-4**). 4 inch diameter silicon wafers (Inseto, UK) were rinsed with acetone and isopropyl alcohol (IPA) and dehydrated overnight at 210 °C. Ti Prime was poured onto the wafer to cover approximately one third of the surface and spin coated using Brewer Science CEE-200 Spin Coater with the following recipe parameters: 5 seconds at 500 rpm, 30 seconds at 3000 rpm and 5 seconds at 500 rpm. The wafer was baked for 2 minutes at 120 °C and placed immediately back in the spin coater for the SU-8 3025 deposition. SU-8 3025 was poured onto the centre of the wafer until it covered approximately one third of the surface. It was spun for 5 seconds at 500 rpm to spread the photoresist on the wafer, 30 seconds at a variable rpm to achieve the desired thickness of the photoresist (**Table 2-4**) and 5 seconds at 500 rpm to enhance uniformity of the substrate. The wafer was soft baked at 65 °C and 95 °C (length of bake depends on thickness of photoresist (**Table 2-4**) before being transferred to the mask aligner. The wafers were exposed to a wavelength of 365 nm and the total dose depends on the thickness of photoresist (**Table 2-4**) and the exposure time varies depending on the intensity of the lamp. This causes the exposed areas of the substrate to become cross-linked. After exposure, the wafer was post-baked at 65 °C and 95 °C (**Table 2-4**) before being allowed to cool for at least 30 minutes in order to reach room temperature. The wafer was developed in ethylene carbonate and rinsed with IPA before being dried with nitrogen gas. The thickness and sharpness of the obtained features were checked using a profilometer.

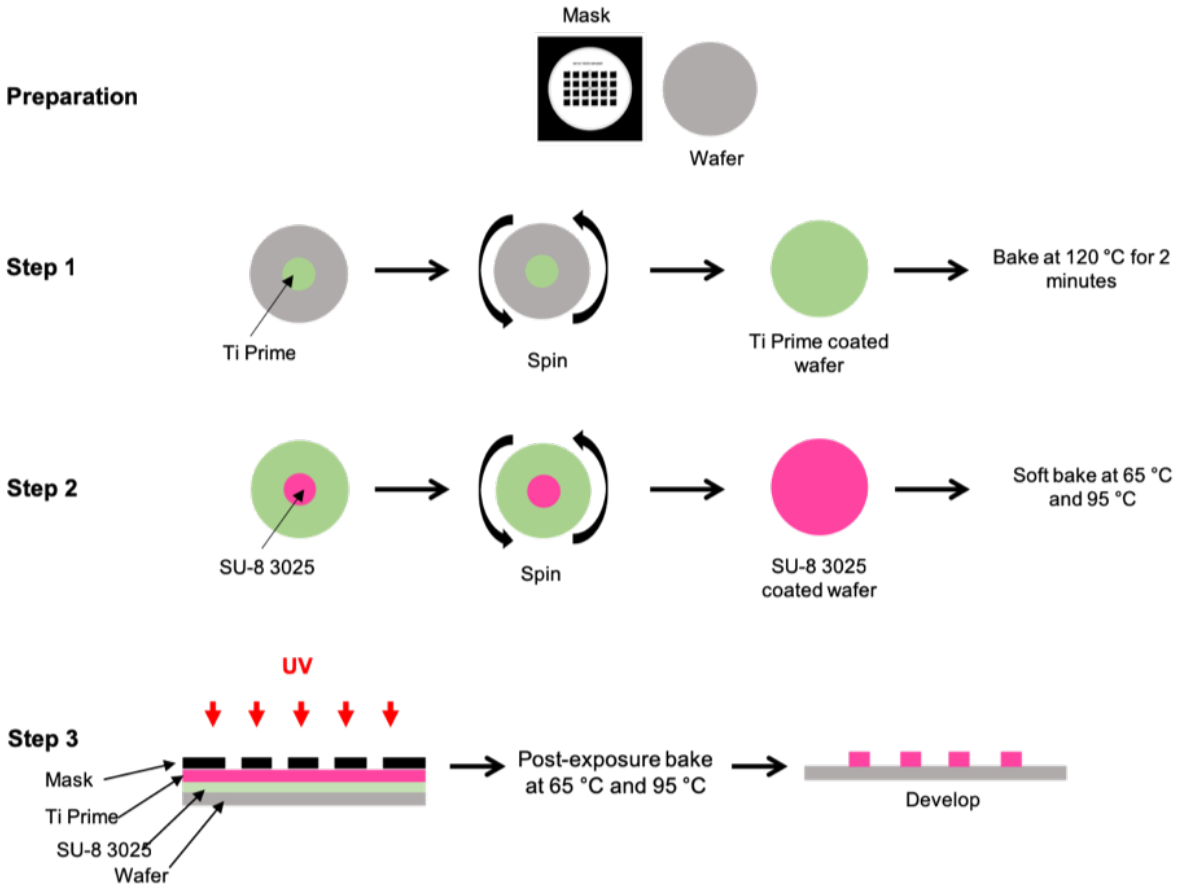

FIGURE 2-4: WAFER FABRICATION BY PHOTOLITHOGRAPHY.

In the preparation step the silicon wafer is cleaned with acetone and isopropyl alcohol and dehydrated overnight. Step 1 shows the spin coating process using Ti Prime followed by baking and step 2 shows the spin coating process using the negative photoresist (SU-8 3025) followed by baking. The speed used to spin coat the wafer can be altered to allow the production of wafers with features of different heights. The wafer is an inverse copy of the agarose array so the heights of the features create the depth of the wells. Step 3 represents the wafer and mask being loaded into the mask aligner, which exposes the wafer to a wavelength of 365 nm to allow the crosslinking of the substrate. This is then developed in solvent.

TABLE 2-4: RECIPE PARAMETERS FOR PHOTOLITHOGRAPHY PROTOCOL TO ACHIEVE SPECIFIC DESIRED FEATURE HEIGHT.

Desired thickness of photoresist (μm)	Program for spin-coating resist	Soft-bake time	Exposure energy (mJ/cm^2)	Post-exposure bake time
20	5 s at 500 rpm 30 s at 4000 rpm 5 s at 500 rpm	2 min at 65 °C 10 min at 95 °C	150	2 min at 65 °C 5 min at 95 °C
25	5 s at 500 rpm 30 s at 3000 rpm 5 s at 500 rpm	5 min at 65 °C 15 min at 95 °C	180	5 min at 65 °C 10 min at 95 °C

Parameters based on information from product datasheet from MicroChem [http://microchem.com/pdf/SU-8%203000%20Data%20Sheet.pdf, accessed September 2018].

2.4.3 Agarose array production

The agarose microwell arrays are produced by standard soft lithography (**Figure 2-5**). 2% agarose in PBS was melted and cooled to approximately 55°C. The agarose was poured onto the wafer, within a poly(methyl methacrylate) (PMMA) ring, and left to cure. The PMMA ring was removed and the agarose array transferred to a plastic support and cut to size. The arrays were placed inside a petri dish and kept in an incubator at 37 °C, 5% CO_2.

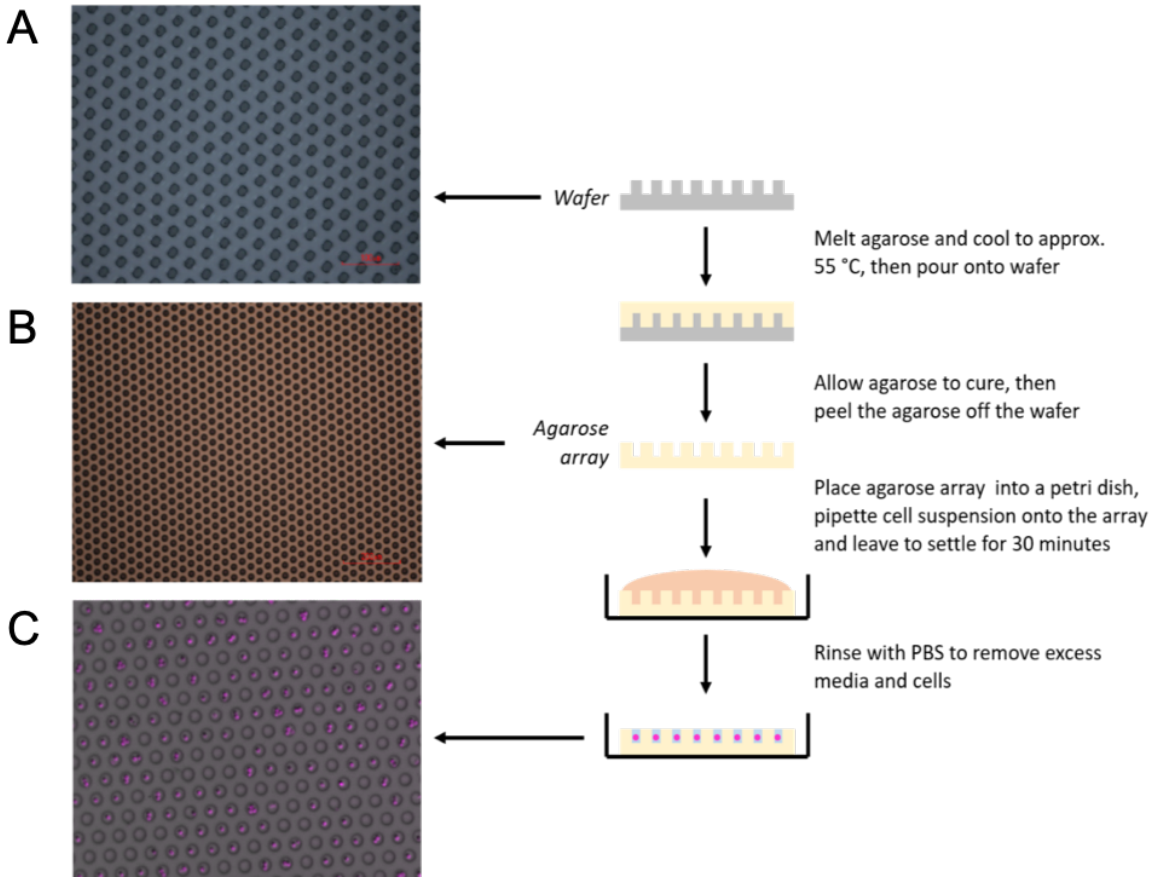

FIGURE 2-5: AGAROSE MICROWELL ARRAY PRODUCTION.

The silicon wafer, shown in (A) where the image was captured at 20x magnification (scale bar = 100 µm), is produced by standard photolithography procedures. To produce the agarose array, 2% agarose in PBS is melted and cooled to approximately 55 °C. This is poured onto the wafer and allowed to cure. The agarose can then be peeled off the wafer, cut to size if necessary and placed in a petri dish. Image (B) shows an agarose array captured at 10x magnification (scale bar is 200 µm). The agarose array is placed in the incubator at 37 °C, 5% CO_2 and the cells are pipetted onto the surface of the array. The cells are allowed to settle for 30 minutes, following which, the arrays are rinsed with PBS to remove excess media and cells from the surface of the array. Image (C) is a composite fluorescent image captured at 20x magnification with an exposure time of 150 ms and shows primary CLL cells stained with CellVue™ Maroon occupying the microwells.

2.4.4 Cell seeding of microwell arrays

Cells were stained with Fluo-3, AM, as described above, or with 5 μM Fluo-8, AM (Statech, UK) as follows: cells at a density of $1x10^7$ cells/ml were stained with 5 μM Fluo-8 for 30 minutes at 37 °C, 5% CO_2 in the dark. The pellet was collected by centrifugation at 350 g for 5 minutes and resuspended in complete cell medium to the required density for the experiment.

200 μl cells, at variable densities, were pipetted onto the agarose array, and incubated at 37 °C, 5% CO_2 for 30 minutes to allow the cells to settle into the microwells. The agarose array was rinsed with PBS and occupancy visually assessed using a light microscope and the rinsing was repeated if necessary (**Figure 2-5**).

2.5 Microscopy and image analysis

Following entrapment of cells in the agarose arrays, fluorescent and brightfield images were captured using a fluorescence microscope (AX10 Image MIm, Zeiss) integrated with a computer-operated motorised stage, filter sets and a digital camera (AxioCam MRm, Zeiss). Fluo-3 AM and Fluo-8 AM were excited using a mercury lamp and a FITC filter. The cells were stimulated with soluble anti-IgM, control antibody or ionomycin (experiment dependent, see results) and data acquired using AxioVision Rel 4.8 or Zen software. 120 or 180 frames for the time series' were captured at 500 ms intervals with an experiment-dependent exposure time. Images were analysed using ImageJ and MATLAB scripts (developed in-house by Dr Anna Desalvo, University of Southampton, UK).

2.6 Statistical analyses

All data analysis and graph preparation were performed using GraphPad Prism. In general, parametric tests were carried out but where Gaussian distribution could not be assumed, non-parametric tests were calculated instead. Spearman's rank correlation coefficient was calculated to determine strength of association between parameters.

Chapter Three

Results: Characterisation of BTK by-pass signalling downstream of the B-cell receptor in primary CLL samples and DLBCL cell lines

3 Characterisation of BTK by-pass signalling downstream of the B-cell receptor in primary CLL samples and DLBCL cell lines

3.1 Introduction

BTK, one of the key kinases in the BCR-associated signalling pathway (**Figure 1-4**), has been demonstrated to be a significant molecule for inducing iCa^{2+} responses acting via phosphorylation of PLCγ2 (Scharenberg et al., 1998). The role of BTK within this pathway implies that it has a canonical role upstream of NFAT and NF-κB, Ca^{2+}-dependent transcription factors, involved in the upregulation of many genes including *MYC, CCND1, CCND2* and *BCL2A1* (Duyao et al., 1990; Iwanaga et al., 2008; Pahl, 1999; Vogler, 2012), highlighting the clinical significance of BTK as a potential therapeutic target. Ibrutinib is a clinically approved BTK inhibitor used for the treatment of CLL and other B-cell malignancies. However, there are limitations with ibrutinib, including toxicities and resistance, therefore alternative therapies are required. A second-generation BTK inhibitor, acalabrutinib, is more specific for BTK than ibrutinib (Byrd et al., 2016) helping to reduce toxicities associated with the off-target effects of ibrutinib (Patel et al., 2017), and BTK-specific PROTACs that target BTK for proteasomal degradation are under investigation and show promising results in initial *in vivo* experiments (Sun et al., 2019; Jaime-Figueroa et al., 2020; Arthur et al., 2020).

Previous work has shown that iCa^{2+} mobilisation can be used as a biomarker to assess the signalling capacity of the BCR (Mockridge et al., 2007) and this assay was utilised to investigate the effect of ibrutinib in primary CLL cells. Preliminary data suggested that not all CLL samples are equally affected by ibrutinib (G. Packham, personal communication) (**Figure 1-21**) raising the question of whether therapies are effective on all malignant B-cells within a sample or whether there are a subset of cells less affected by drug, which might be contributing to treatment resistance and disease relapse. The implication of CLL samples, or at least a proportion of cells within the sample, not responding to BTK-inhibitor treatment suggests that there is a BTK "by-pass" mechanism operating. Since iCa^{2+} release is driven by IP_3 production, which in turn is produced by the activity of PLCγ2, it suggests that there is an alternative route from the BCR to

PLCγ2 that is independent of at least the kinase activity of BTK. It is important to understand this potential "by-pass" mechanism as it may provide opportunities for more effective blockade of this critical signalling pathway.

3.2 Hypothesis and aims

The experiments in this chapter were designed to investigate the hypothesis that the inhibitory effects of BTKi on anti-IgM-induced iCa^{2+} fluxes are variable between CLL samples, and to determine whether BTK has any kinase-independent functions leading to iCa^{2+} release.

This was addressed by 5 main aims:

1. Extend analysis of ibrutinib's inhibitory effect on anti-IgM-induced iCa^{2+} fluxes to additional CLL samples to confirm initial findings (**Figure 1-21**).
2. Determine whether similar effects are observed with acalabrutinib, a more selective BTKi.
3. Investigate potential correlations between clinical and biological features of CLL samples and variable responses to BTKi.
4. Compare the effects of ibrutinib and a BTK-degrading PROTAC to investigate the potential contribution of BTK-mediated, kinase-independent pathways.
5. Determine whether partial responses to BTKi are observed in other malignant B cells by analysing the efficacy of BTKi for inhibition of iCa^{2+} fluxes in DLBCL cell lines.

3.3 Effect of ibrutinib on anti-IgM-induced iCa^{2+} fluxes in CLL cells

My first experiments used flow cytometry to analyse the effect of ibrutinib on anti-IgM-induced iCa^{2+} fluxes in 20 CLL samples, to extend the initial analysis performed previously in the host laboratory (**Figure 1-21**). The protocol used was the same as this previous study, to allow direct comparison of results. Following recovery from cryopreservation, each CLL sample was pretreated with ibrutinib, DMSO (solvent control), or left untreated. The concentration of ibrutinib used in these studies (1 μM) was relatively high but was selected to ensure full BTK inhibition. After 1 hour, cells were stained with a calcium indicator dye for 30 minutes, washed and resuspended in media supplemented with ibrutinib or DMSO, or without supplementation (as required). Although ibrutinib is a covalent inhibitor, it does have a slow off-rate, measurable in biochemical assays (Reiff et al., 2018), and ibrutinib was therefore re-added after washing to ensure BTK inhibition

was maintained. Samples were transferred to the flow cytometer and baseline data was recorded for 30 seconds before addition of anti-IgM or control antibody (20 μg/ml). $F(ab')_2$ antibodies were used to prevent binding to Fc receptors. Data was collected for an additional 4.5 minutes before addition of ionomycin (a calcium ionophore) as a positive control.

The CLL samples selected for the analyses represented a range of BCR signalling activity and included examples of U- and M-CLL; see (**Table 2-1**) for sample characteristics. Since the goal was to investigate effects of ibrutinib on signalling, all selected samples were classed as "signallers" with an anti-IgM-induced iCa^{2+} flux response of ≥5% (based on analysis performed routinely for all samples with the tumour bank).

Figure 3-1A shows primary data obtained using two representative samples to highlight the variability in BCR signalling capacity. To quantitatively summarise the results for all samples, I first analysed the peak percentage of cells which fluxed iCa^{2+} in response to anti-IgM stimulation, as originally used for analysis of these type of results (Mockridge et al., 2007). This was calculated by subtracting the mean baseline value from the peak percentage of cells responding to anti-IgM (details of the calculation provided in **Section 2.3.2**). **Figure 3-1B** shows the variability in peak anti-IgM response for control (DMSO treated) cells for all samples, ranging from ~5 to 80%. **Figure 3-1B** also shows that ibrutinib significantly reduced this anti-IgM-induced response. However, the extent of this reduction varied substantially between samples with some showing partial inhibition (as low as ~20% reduction) and others full inhibition.

Although peak anti-IgM response is a meaningful indicator of the BCR signalling response and has been used widely in the literature (Mockridge et al., 2007; Krysov et al., 2012; D'Avola et al., 2016; Le Roy et al., 2012), it does not provide information on the kinetics of iCa^{2+} flux, which may be particularly important in determining the extent of engagement of downstream pathways (Dolmetsch et al., 1997). Therefore, additional approaches were used to quantify the variable effects of ibrutinib on anti-IgM-induced iCa^{2+} responses, including the area under the curve (AUC) and the relative anti-IgM-induced response (details of these calculations are provided in **Section 2.3.2**). Briefly, the AUC calculation integrates the response over a defined time window (between 30 and 300 seconds, i.e. excluding pre-stimulation/ionomycin effects), whereas the relative anti-IgM-induced response determines the degree of inhibition by ibrutinib independent of the strength of the anti-IgM-induced signal in control cells. Both of these additional analyses

confirmed that the extent of inhibition of anti-IgM-induced iCa^{2+} fluxes by ibrutinib was variable between samples (**Figure 3-1C - D**).

In summary, the results from this extended analysis confirm the initial findings in the host laboratory (**Figure 1-21**) that the effectiveness of ibrutinib in inhibiting anti-IgM-induced iCa^{2+} signalling varies substantially between samples.

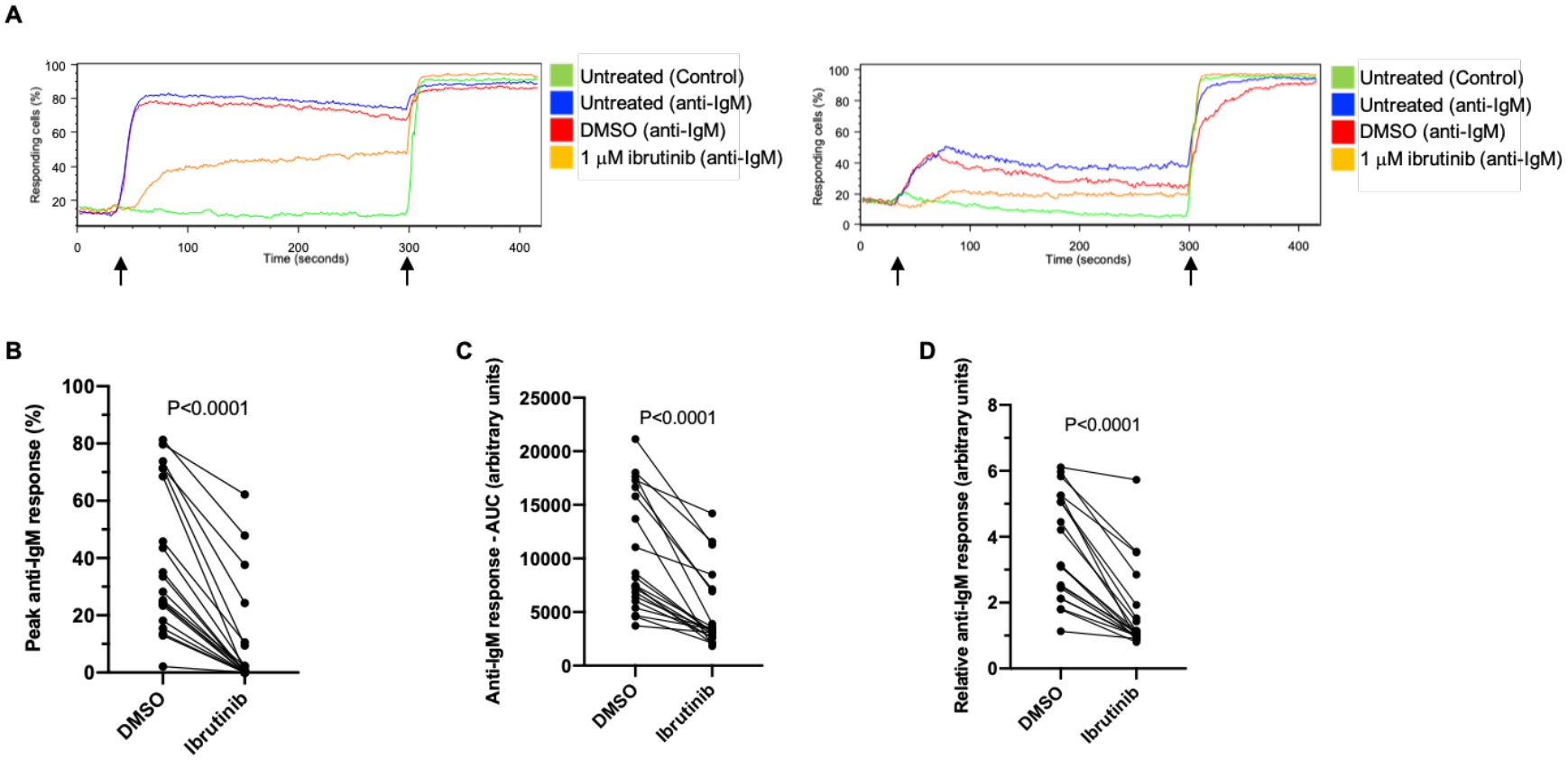

FIGURE 3-1: EFFECT OF IBRUTINIB ON ANTI-IGM-INDUCED ICA^{2+} FLUX.

A. Representative CLL samples (CLL780A (left) and CLL681A (right)) were pre-treated with ibrutinib (orange), or DMSO as a vehicle control (red), or left untreated (green and blue) for 1 hour and then loaded with calcium indicator dye. Baseline data was recorded for 30 seconds prior to addition of anti-IgM (or control antibody (green)), indicated by the first arrow along the x axis of each graph. Ionomycin was added at 5 minutes as a positive control, indicated by the second arrow along the x axis of each graph. **B-D.** Summary data for 20 CLL samples showing peak percentage of cells responding to anti-IgM (**B**), area under the curve post-anti-IgM stimulation (**C**), and the relative response to anti-IgM (**D**). Statistical significance of the differences between DMSO and ibrutinib treated cells, determined by paired t tests, are indicated on the graphs.

3.4 Effect of acalabrutinib, a more selective BTKi, on anti-IgM-induced iCa^{2+} fluxes in CLL cells

Variability in anti-IgM-induced iCa^{2+} fluxes following pretreatment with ibrutinib could, at least in part, be caused by off-target effects of ibrutinib. Therefore, a second generation and more specific BTKi, acalabrutinib (Byrd et al., 2016), was used in a similar set of experiments to investigate whether the observed effects were specific for ibrutinib or a class effect.

Eighteen CLL samples were included in this study, 15 of which had been investigated in parallel for inhibition by ibrutinib in the experiment shown above (**Figure 3-1**). As above, all samples were defined as "signallers" and they represented a range of anti-IgM-induced signalling capacity, and included examples of both U- and M-CLL (**Table 2-1**). The overall experimental design was identical to the previous analysis using ibrutinib to allow comparison of results. Thus, acalabrutinib was also tested at 1 μM.

Figure 3-2A shows primary data from two representative CLL samples and quantitative summaries of results for all samples are shown in **Figure 3-2B – 3-2D** including (as above), the peak anti-IgM response (**Figure 3-2B**), AUC (**Figure 3-2C**), and relative anti-IgM response (**Figure 3-2D**). Similar to ibrutinib, acalabrutinib significantly inhibited anti-IgM-induced iCa^{2+} fluxes for all analytical approaches and the extent of inhibition was highly variable between samples.

I directly compared the inhibitory responses to ibrutinib and acalabrutinib for the 15 samples that were shared between the two studies, using peak anti-IgM response to quantify the results (**Figure 3-3**). In general, ibrutinib inhibited the response to a greater extent than acalabrutinib, but this difference was not statistically significant (**Figure 3-3A**). Overall, there was a strong correlation between effects of ibrutinib and acalabrutinib for individual samples (**Figure 3-3B**).

These results suggest that variable inhibition of anti-IgM-induced iCa^{2+} fluxes in CLL cells following BTKi treatment is not ibrutinib-specific but a general effect associated with BTK inhibition.

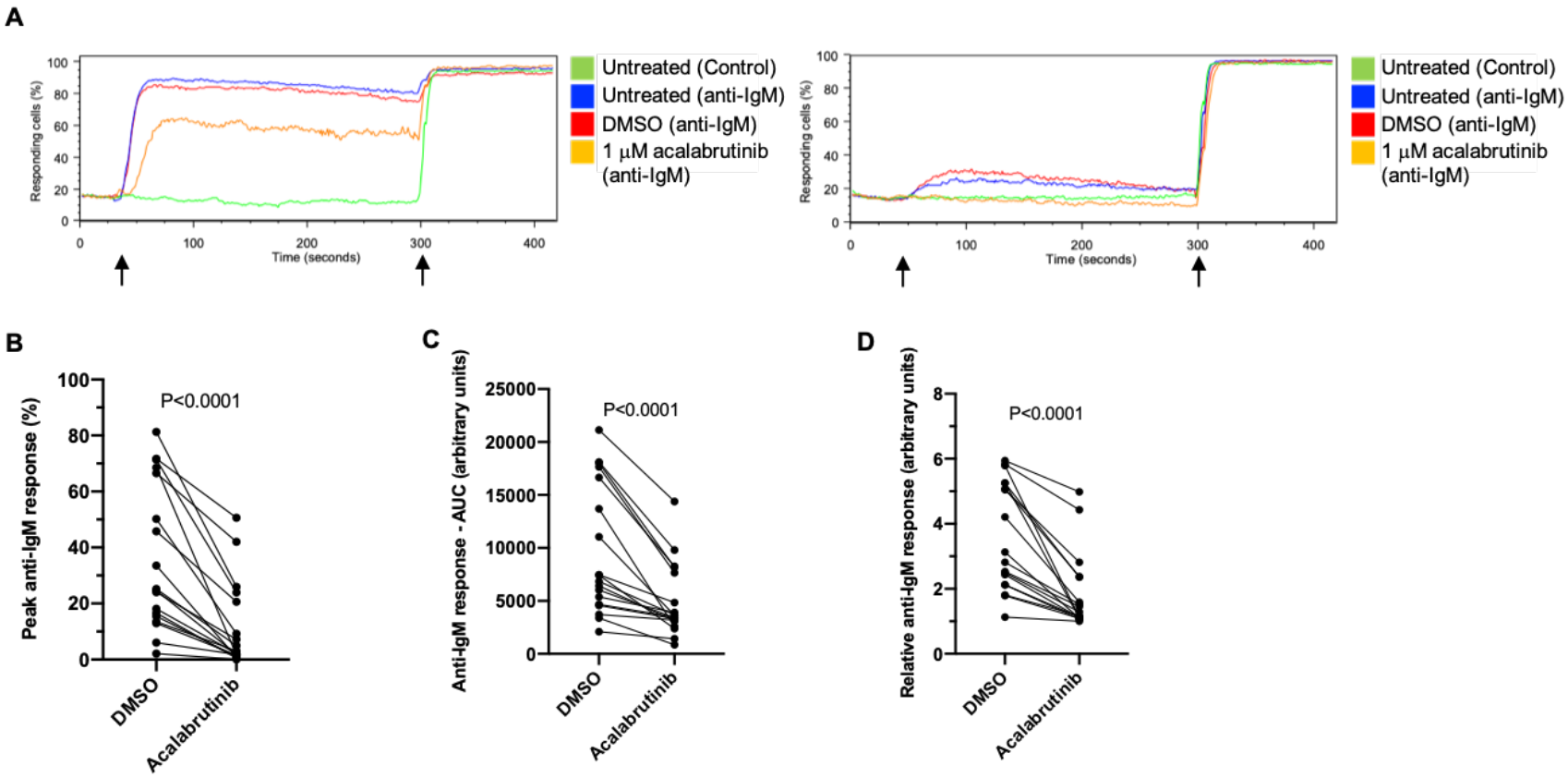

FIGURE 3-2: EFFECT OF ACALABRUTINIB ON ANTI-IGM-INDUCED ICA^{2+} FLUX.

A. Representative CLL samples (CLL780A (left) and CLL523H (right)) were pretreated with acalabrutinib (orange), or DMSO as a vehicle control (red), or left untreated (green and blue) for 1 hour and then loaded with calcium indicator dye. Baseline data was recorded for 30 seconds prior to addition of anti-IgM (or control antibody (green)), indicated by the first arrow along the x axis of each graph. Ionomycin was added at 5 minutes as a positive control, indicated by the second arrow along the x axis of each graph. **B-D.** Summary data of 18 CLL samples showing peak percentage of cells responding to anti-IgM (**B**), area under the curve post-anti-IgM stimulation (**C**), and the relative response to anti-IgM (**D**). Statistical significance of the differences between DMSO and acalabrutinib treated cells, determined by paired t tests, are indicated on the graphs.

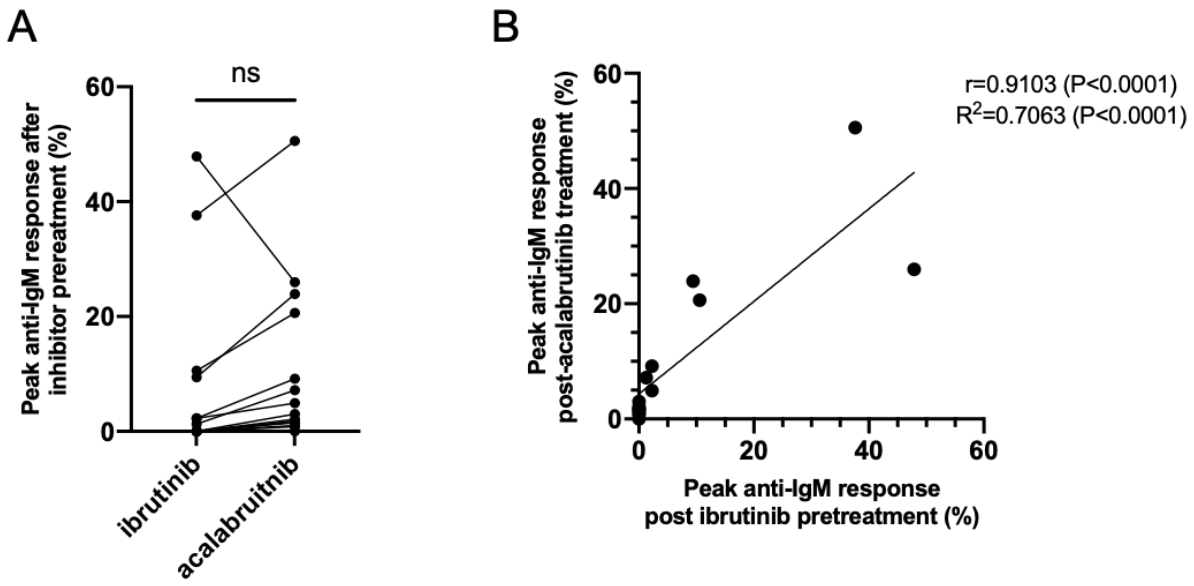

FIGURE 3-3: COMPARISON OF iCA^{2+} FLUX INHIBITION IN CLL CELLS FOLLOWING PRETREATMENT WITH IBRUTINIB OR ACALABRUTINIB.

Peak anti-IgM response of 15 CLL samples pretreated with either ibrutinib (from **Figure 3-1**) or acalabrutinib (from **Figure 3-2**) (both at 1 μM) for 1 hour prior to Ca^{2+} flux analysis. **A.** Statistical significance of the difference in peak response between ibrutinib and acalabrutinib treated cells, determined by paired t test, is indicated on the graph. **B.** Results of linear regression and Spearman's correlation are shown on the graph.

3.5 Correlations between clinical and biological features of CLL samples and responses to BTKi

I next investigated whether the variable inhibitory effect of BTKi on anti-IgM-induced iCa^{2+} responses was associated with any of the available clinical or biological features of the samples. For these analyses, I combined my data (**Figure 3-1 - Figure 3-3**) with the initial data generated in the host laboratory to increase study power. This resulted in cohorts of 32 and 28 samples for analysis with ibrutinib or acalabrutinib, respectively. However, it should be noted that not all clinical/biological data was available for all samples.

I first investigated whether the extent of inhibition by BTKi was related to clinically relevant biomarkers, including *IGHV* gene mutation status and expression of CD38, ZAP70 or CD49d (**Figure 3-4 and Figure 3-5**). The extent of inhibition induced by either ibrutinib or acalabrutinib was not significantly different between U- and M-CLL (**Figure 3-4A and Figure 3-5A**, respectively). There was also no statistically significant correlation between extent of inhibition and proportion of cells that expressed CD38, ZAP70 or CD49d (**Figure 3-4B - Figure 3-4D** and **Figure 3-5B and 3-5C**) with the exception of the extent of inhibition by acalabrutinib and proportion of cells expressing CD49d, where a weak, positive correlation was observed (**Figure 3-5D**).

I next investigated the relationship between the extent of inhibition by BTKi and features of sIgM (**Figure 3-6**) i.e. signalling capacity, and sIgM expression, which is itself positively correlated with sIgM signal capacity (Mockridge et al., 2007). There was a relatively strong correlation between the strength of the anti-IgM response (i.e. peak response without inhibitor) and the extent of inhibition by BTKi, calculated as residual anti-IgM-induced response. This was observed for both ibrutinib and acalabrutinib (**Figure 3-6A and 3-6C**, respectively). Thus, the partial inhibitory effects of BTKi are associated with stronger anti-IgM responses. Consistent with this, the extent of inhibition induced by ibrutinib correlated with sIgM expression (higher sIgM associated with less inhibition) (**Figure 3-6B and 3-6D**). However, this correlation was not as strong as the correlation between extent of ibrutinib-mediated inhibition and sIgM signalling capacity, and was not clearly apparent for acalabrutinib (**Figure 3-6D**).

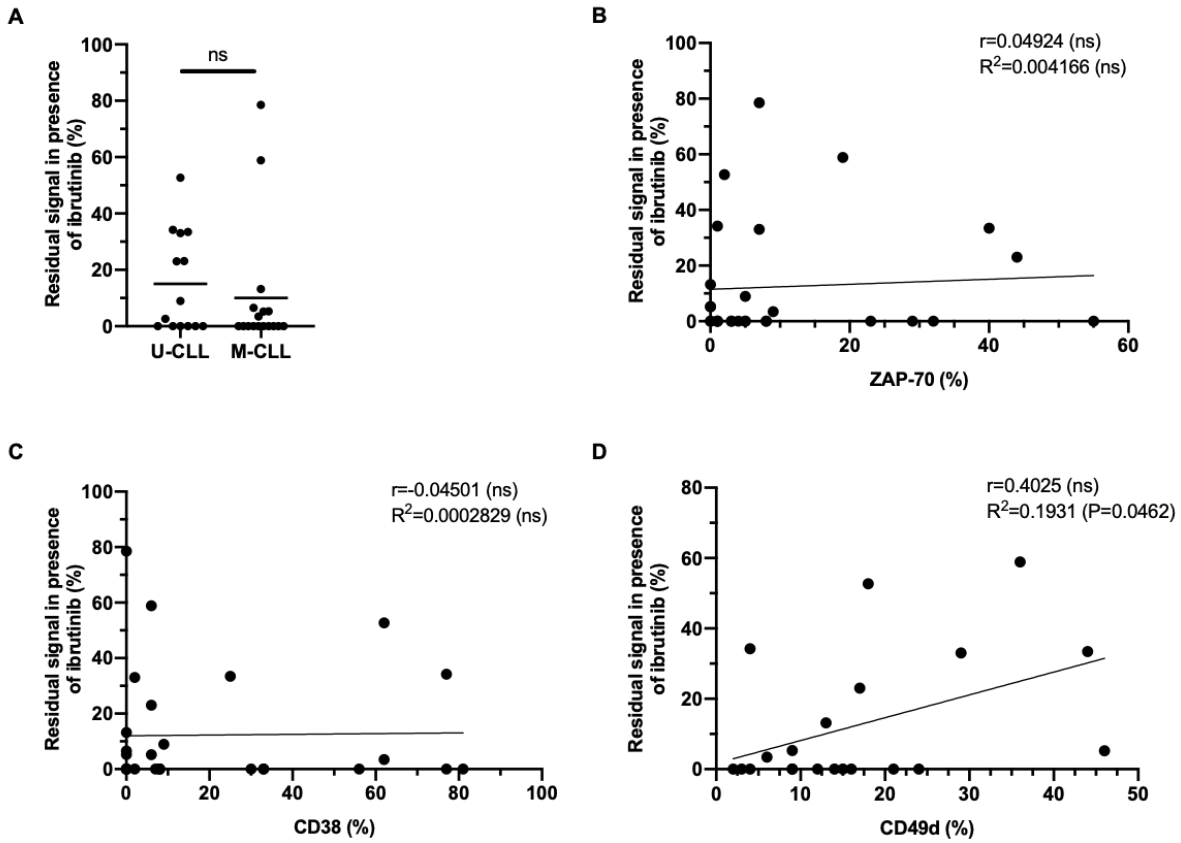

FIGURE 3-4: CORRELATIONS OF EXTENT OF IBRUTINIB-MEDIATED INHIBITION OF ANTI-IGM-INDUCED iCa^{2+} FLUX AND CLINICAL FEATURES.

The residual ibrutinib-induced inhibition of anti-IgM-induced iCa^{2+} flux (peak anti-IgM response of ibrutinib treated sample as a percentage of the peak anti-IgM response of sample treated with DMSO) was compared to various biological and clinical features including **(A)** *IGHV* mutation status (n=31 [U-CLL n=14; M-CLL n=17]), **(B)** percentage of ZAP-70 positive cells (n=28), **(C)** percentage of CD38 positive cells (n=29), and **(D)** percentage of CD49d positive cells (n=21). Graphs show results of paired t test **(A)**, or linear regression and Spearman's correlation **(B, C and D).**

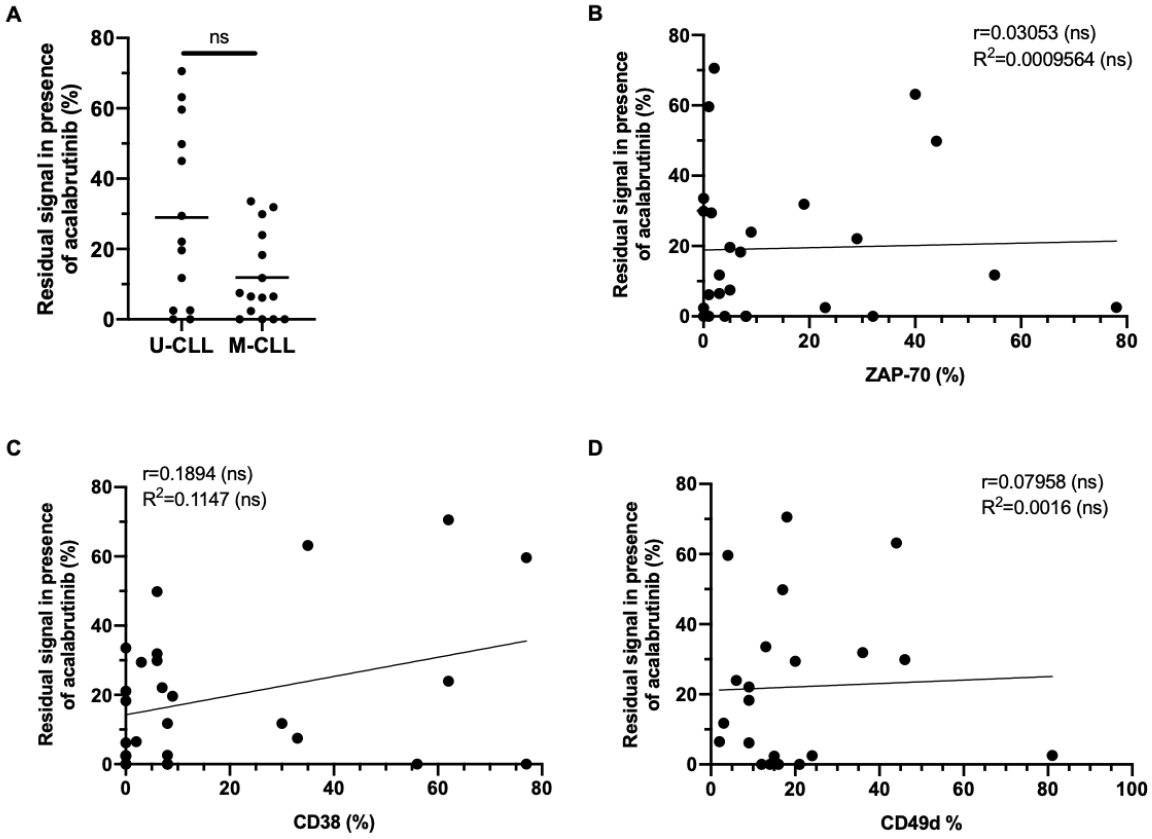

FIGURE 3-5: CORRELATIONS OF EXTENT OF ACALABRUTINIB-MEDIATED INHIBITION OF ANTI-IGM-INDUCED iCa^{2+} FLUX AND CLINICAL FEATURES.

The residual acalabrutinib-induced inhibition of anti-IgM-induced iCa^{2+} flux (peak anti-IgM response of acalabrutinib treated sample as a percentage of the peak anti-IgM response of sample treated with DMSO) was compared to various biological and clinical features including **(A)** *IGHV* mutation status (n=28 [U-CLL n=13; M-CLL n=15]), **(B)** percentage of ZAP-70 positive cells (n=26), **(C)** percentage of CD38 positive cells (n=27), and **(D)** percentage of CD49d positive cells (n=21). Graphs show results of paired t test **(A)**, or linear regression and Spearman's correlation **(B, C and D).**

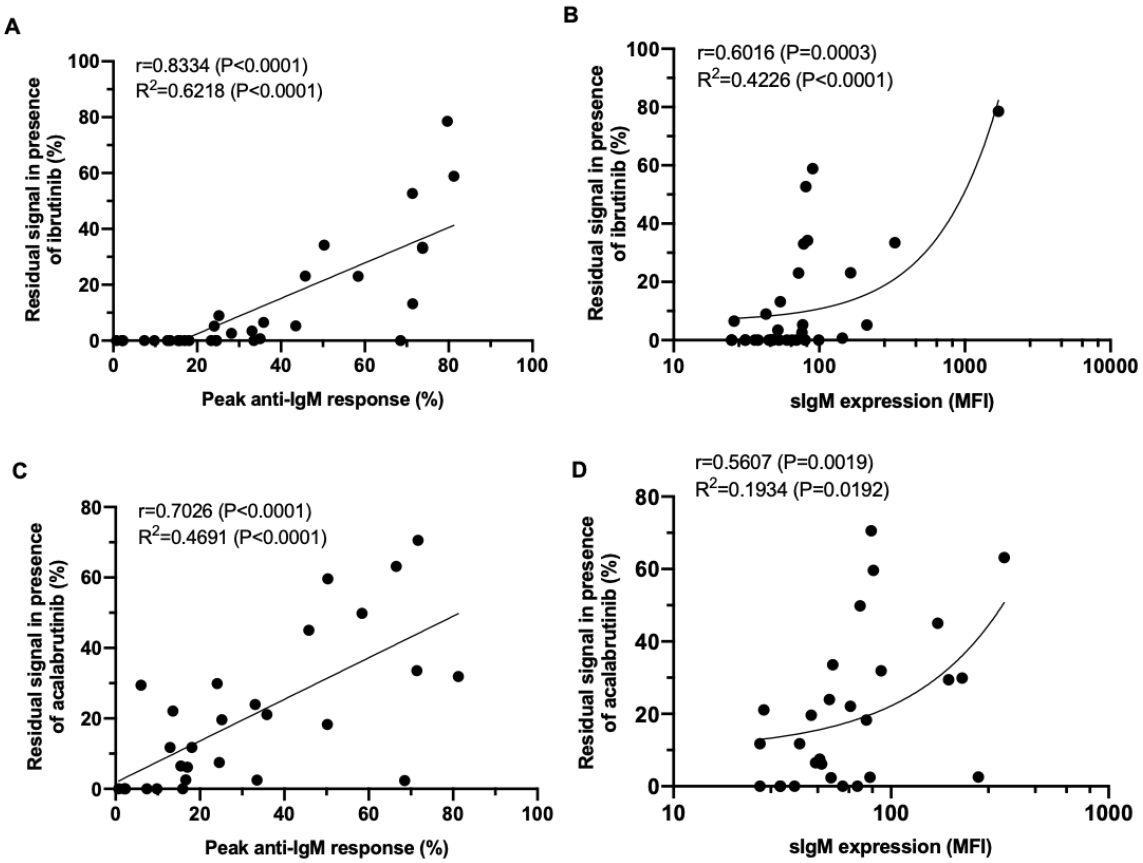

FIGURE 3-6: CORRELATIONS OF EXTENT OF BTKI-MEDIATED INHIBITION OF ANTI-IGM-INDUCED iCa^{2+} AND BIOLOGICAL FEATURES.

The correlation between the the residual ibrutinib-induced inhibition of anti-IgM-induced iCa^{2+} flux (peak anti-IgM response of ibrutinib treated sample as a percentage of the peak anti-IgM response of sample treated with DMSO) and **(A)** the peak anti-IgM response (%) of control (DMSO-treated) cells (n=32), or **(B)** sIgM expression (n=32). The correlation between the the residual acalabrutinib-induced inhibition of anti-IgM-induced iCa^{2+} flux (peak anti-IgM response of acalabrutinib treated sample as a percentage of the peak anti-IgM response of sample treated with DMSO) and **(C)** the peak anti-IgM response (%) of control (DMSO-treated) cells (n=28), or **(D)** sIgM expression (n=28). Graphs show results of linear regression and Spearman's correlation.

3.6 Comparison of the effects of ibrutinib and a BTK-degrading PROTAC to investigate the potential contribution of BTK-mediated, kinase-independent pathways

Experiments described to this point show that a subset of CLL samples (especially those with strong sIgM signalling capacity) at least partly engage an alternate pathway leading to iCa^{2+} mobilisation downstream of sIgM which is not inhibited by BTKi. One possibility is that this "by-pass" is entirely independent of BTK. However, kinase-independent roles of BTK in signalling to iCa^{2+} have been described (Saito et al., 2003; Tomlinson et al., 2001; Middendorp et al., 2003) and an alternate possibility is that this "by-pass" may be mediated by BTK, but independently of its kinase activity. To distinguish between these possibilities, I compared the effects of BTK targeting using a BTKi (ibrutinib) and a BTK-specific PROTAC. PROTACs work catalytically to bind the protein of interest and, through ubiquitylation, target the protein to the proteasome for degradation (Buhimschi et al., 2018; Arthur et al., 2020) (described in **Section 1.6.1**). Whereas ibrutinib would be expected to only inhibit kinase-dependent functions of BTK, PROTAC-mediated degradation will ablate all functions of BTK. I selected the BTK-specific PROTAC, MT-802, which has been shown to effectively degrade BTK in CLL cells (Buhimschi et al., 2018). MT-802 was a kind gift of Professor Craig Crews (Yale University, United States).

3.6.1 Characterisation of PROTAC-mediated BTK degradation

Initial MT-802 dose response and time course experiments were performed to identify appropriate conditions for effective BTK depletion. CLL samples were treated with various concentrations of MT-802 (5 μM to 1 nM), 5 μM SJF-6625 (an inactive control compound (Buhimschi et al., 2018)), DMSO as a vehicle control, or left untreated for 24 hours. Protein lysates were analysed by immunoblotting and a representative blot, using CLL 803A, is shown in **Figure 3-7A** with a summary of the quantification of multiple samples shown in **Figure 3-7B**. Concentrations of MT-802 ≥ 50 nM significantly reduced BTK expression in CLL samples, but a concentration of 500 nM MT-802 was selected for further work to ensure that maximal BTK degradation would occur. The control compound, SJF-6625, showed no effect on the level of BTK detected.

To identify a suitable time point for effective BTK depletion, CLL cells were treated with 500 nM MT-802 or DMSO as a vehicle control for 1, 2, 4, 6, 8 or 24 hours, or were left untreated for 24 hours as an additional control. Protein lysates were analysed by immunoblotting and a representative blot, using CLL 635D, is shown in **Figure 3-8A** with a summary of the quantification of three samples shown in **Figure 3-8B**. BTK expression was significantly reduced as early as 1 hour. However, BTK was still readily detectable at this time point and a 4 hour incubation time with 500 nM MT-802 was selected to achieve a more complete reduction in BTK expression in follow-on experiments. Although more extensive BTK depletion was observed at later time points, 4 hours was chosen to minimise spontaneous apoptosis that occurs when CLL cells are placed in culture for extended periods.

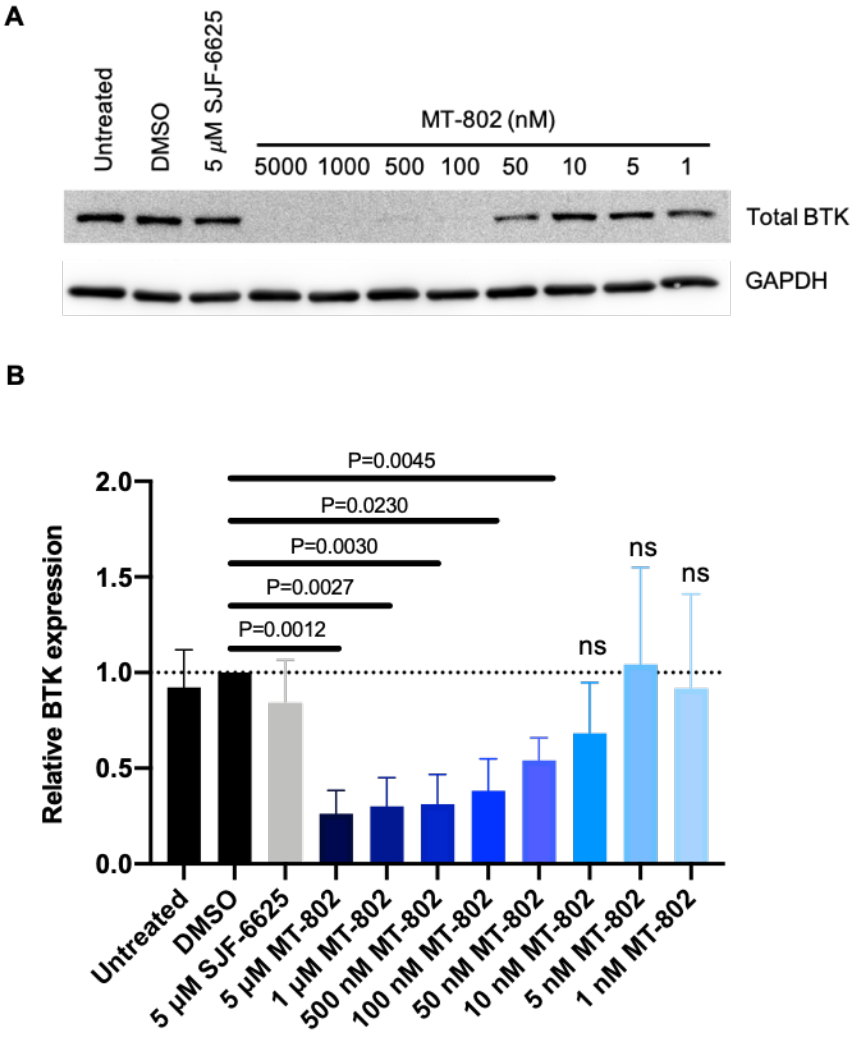

FIGURE 3-7: EFFECT OF DIFFERENT CONCENTRATIONS OF BTK-TARGETED PROTAC, MT-802, ON BTK EXPRESSION IN CLL CELLS.

CLL samples were treated with MT-802 (indicated concentrations), SJF-6625 (5 μM), DMSO or left untreated as a control for 24 hours. Expression of BTK and GAPDH, used as a loading control, were analysed by immunoblotting. Figure shows **(A)** representative results (sample 803A) and **(B)** quantification for all samples analysed (n=4 (except for 100 nM MT-802 where n=3)). Graph shows mean (with standard deviation) relative BTK expression with values for DMSO control cells set to 1.0. The statistical significance between MT-802 and DMSO treated cells is indicated (paired t test).

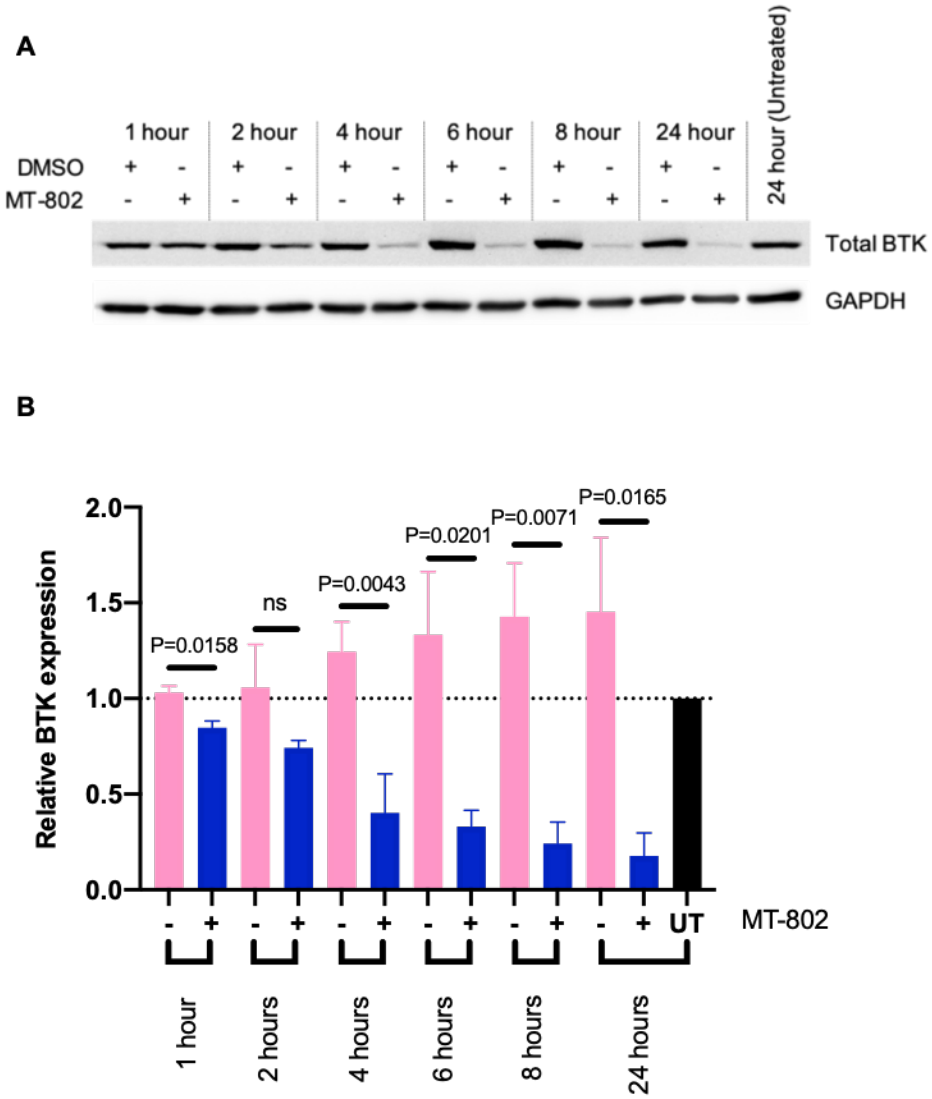

FIGURE 3-8: EFFECT OF BTK-TARGETED PROTAC, MT-802, ON BTK EXPRESSION IN CLL CELLS OVER TIME.

CLL samples were treated with MT-802 (500 nM) or DMSO for the indicated times, or left untreated for 24 hours. Expression of BTK and GAPDH, used as a loading control, were analysed by immunoblotting. Figure shows **(A)** representative results (sample 635D) and **(B)** quantification for all samples analysed (n=3). Graph shows mean (with standard deviation) relative BTK expression with values for 24 hour untreated control cells set to 1.0. The statistical significance between MT-802 and DMSO treated cells at each time point is indicated (paired t test).

3.6.2 Comparison of effects of ibrutinib and PROTAC-induced BTK degradation on anti-IgM-induced iCa^{2+} mobilisation

To compare the effects of inhibition and MT-802 on anti-IgM-induced iCa^{2+} mobilisation, CLL samples were treated with 500 nM MT-802 for 4 hours or 1 μM ibrutinib for 1 hour, DMSO as a vehicle control, or left untreated prior to analysis of iCa^{2+} responses. Representative data, using CLL 635C, is shown in **Figure 3-9A**, and summary data of the peak anti-IgM response and AUC for multiple samples is shown in **Figure 3-9B and 3-9C**, respectively. Samples defined as "signallers" were selected to ensure that any effect of MT-802 and ibrutinib could be clearly observed.

There was a clear, but partial inhibition of iCa^{2+} mobilisation by both ibrutinib and MT-802. Similarly to previous analysis (**Figure 3-1**), ibrutinib statistically significantly reduced the iCa^{2+} response compared with control cells. Overall, the magnitude of the response to MT-802 was very similar. The effects of MT-802 did not reach statistical significance but this likely reflects the relatively small numbers of samples analysed. Importantly, there was no statistically significant difference in the extent of inhibition induced by ibrutinib and MT-802. This was particularly clear for sample CLL 564B (represented by the triangle in **Figure 3-9**), which had a very strong signal response and was relatively unaffected by either compound. Overall, the results suggest that BTK "by-pass" signalling first revealed using BTKi is largely independent of BTK (and not just its kinase activity) as MT-802 does not provide clearly stronger inhibition than ibrutinib.

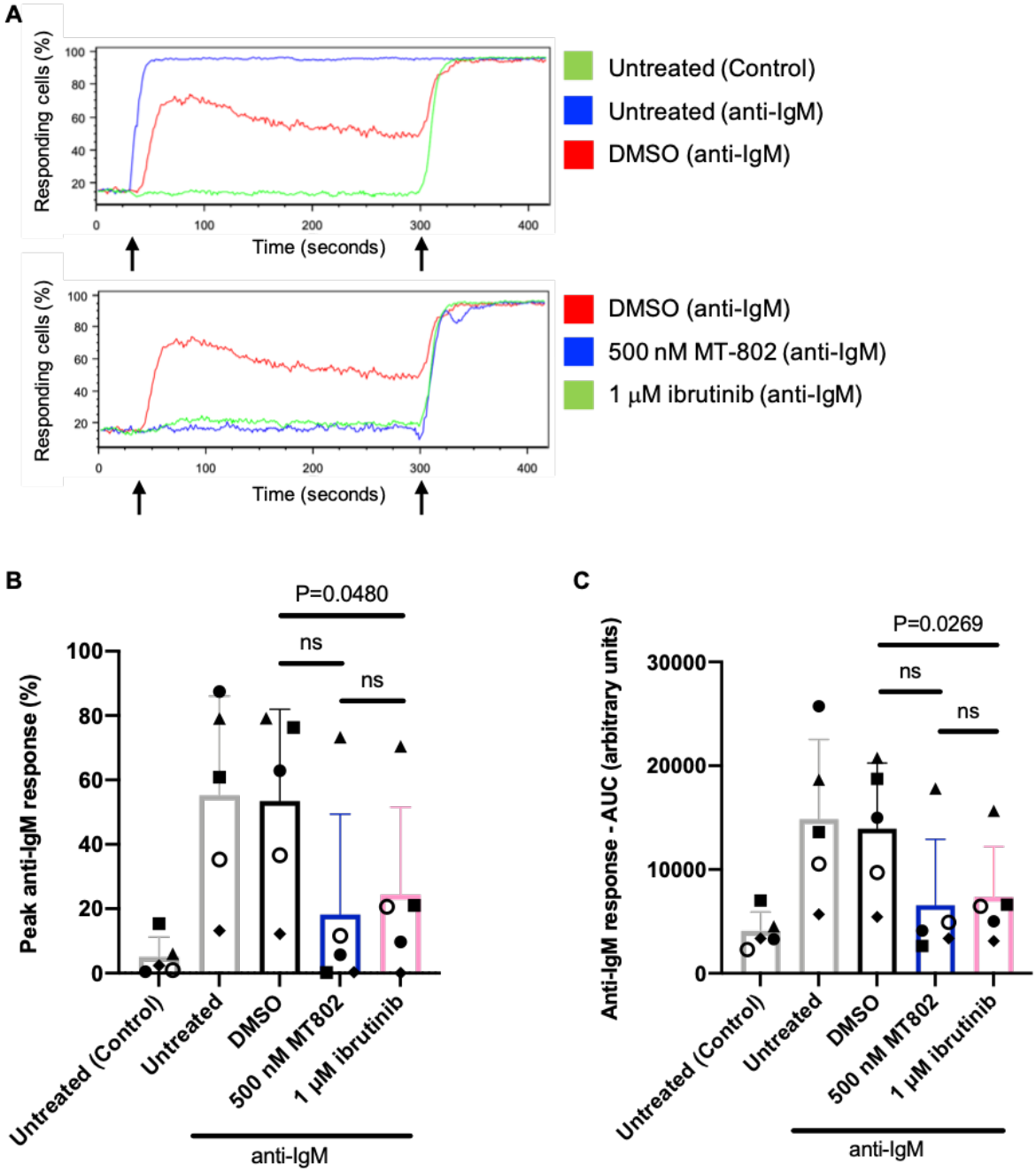

FIGURE 3-9: EFFECT OF MT-802 AND IBRUTINIB ON ANTI-IGM-INDUCED CA^{2+} FLUX.

CLL samples were pretreated with MT-802 (500 nM) for 4 hours, or ibrutinib (1 μM), DMSO, or left untreated as a control for 1 hour before loading with calcium indicator dye. iCa^{2+} fluxes were analysed following addition of anti-IgM (or control antibody). Figure shows **(A)** representative results for sample 635C, **(B)** the peak percentage of responding cells, and **(C)** the area under the curve for each sample analysed (n=5). In **A**, the first arrow shows time of addition of antibody following baseline data recording for 30 seconds and the second arrow shows time of addition of ionomycin as a positive control. In **B** and **C**, the bars show mean and standard deviation, with individual samples represented by different symbols. Statistical significance, determined by paired t tests, of the difference between control (DMSO-treated) cells and either MT-802- or ibrutinib-treated cells, and between MT-802- and ibrutinib-treated cells is indicated.

3.6.3 Comparison of effects of ibrutinb and PROTAC-induced BTK degradation on anti-IgM-induced phosphorylation of BCR-associated signalling molecules

In parallel to analysis of iCa^{2+} mobilisation, I compared the effects of ibrutinib and MT-802 on expression and phosphorylation of additional BCR-associated signalling molecules, AKT and ERK, to determine whether MT-802-mediated degradation of BTK had a broader inhibitory effect than ibrutinib on signalling responses. Representative western blots, using CLL 635D, is shown in **Figure 3-10** and a summary of data for all samples analysed is shown in **Figure 3-11**.

Anti-IgM strongly increased phosphorylation of AKT Ser^{473} and ERK1/2 Thr^{202}/Tyr^{204} (**Figure 3-10**). Overall, both MT-802 and ibrutinib partially reduced anti-IgM-induced AKT Ser^{473} and ERK1/2 Thr^{202}/Tyr^{204} phosphorylation with similar degrees of effectiveness (**Figure 3-11**). Importantly, there was no statistically significant difference between the effect of ibrutinib and MT-802 supporting the conclusion that BTK does not have any additional kinase-independent functions within the BCR-associated signalling pathway. The leve of total AKT or ERK detected was unchanged following pretreatment with ibrutinib or MT-802.

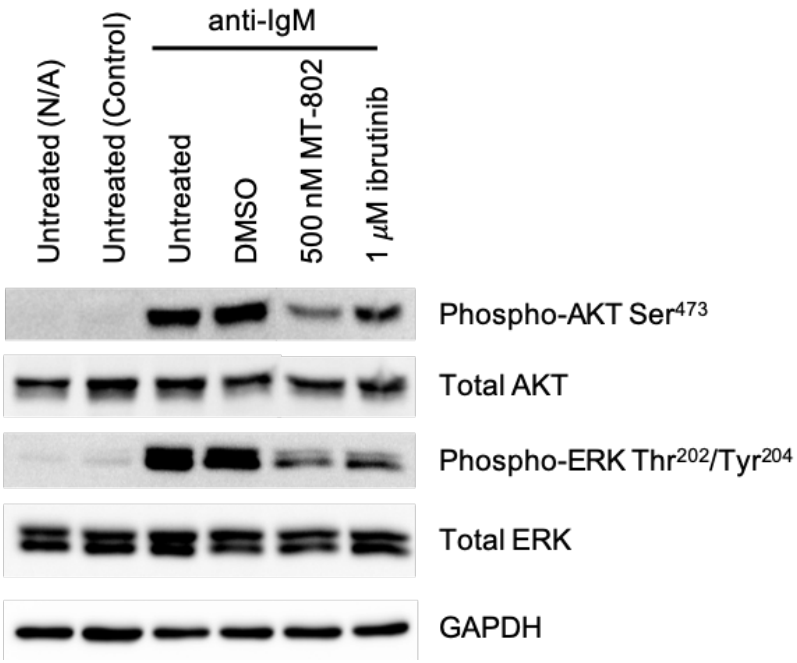

FIGURE 3-10: EFFECT OF MT-802 AND IBRUTINIB ON EXPRESSION AND ANTI-IGM-INDUCED PHOSPHORYLATION OF BCR-ASSOCIATED SIGNALLING PROTEINS.

CLL samples were pretreated with MT-802 (500 nM) for 4 hours, or ibrutinib (1 μM), DMSO, or left untreated as a control for 1 hour before treatment with anti-IgM or control antibody (Untreated (Control)). As an additional control, some cells were left untreated for the duration of the experiment (Untreated (N/A)). Cells were collected after 15 minutes and expression of phosphorylated and total proteins as indicated on the figure, along with GAPDH as a loading control, were analysed by immunoblotting. Figure shows representative results for sample 635D.

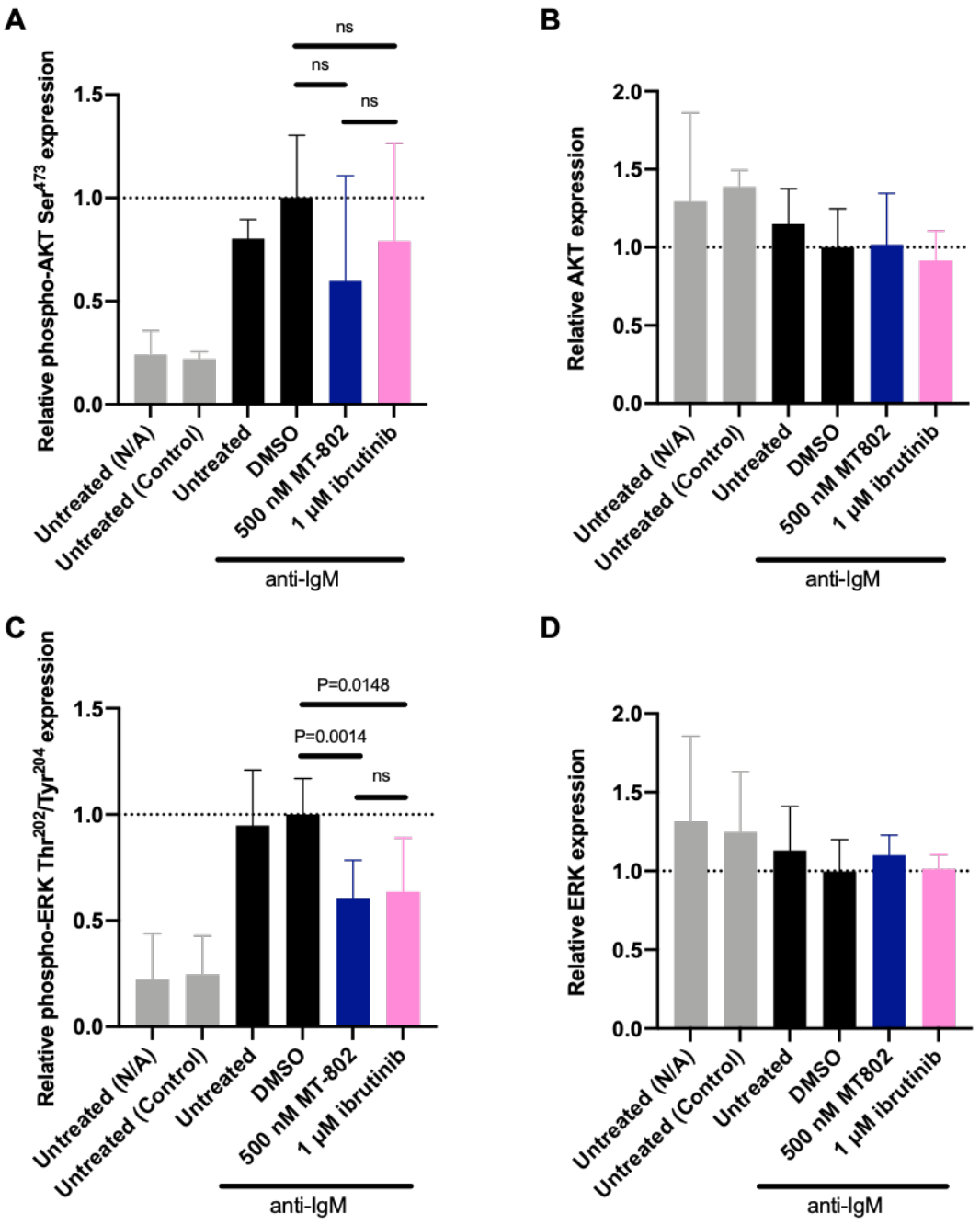

FIGURE 3-11: SUMMARY OF THE EFFECT OF MT-802 AND IBRUTINIB ON EXPRESSION AND ANTI-IGM-INDUCED PHOSPHORYLATION OF BCR-ASSOCIATED SIGNALLING PROTEINS.

CLL samples were pretreated with MT-802 (500 nM) for 4 hours, or ibrutinib (1 μM), DMSO, or left untreated as a control for 1 hour before treatment with anti-IgM or control antibody (Untreated (Control)). As an additional control, some cells were left untreated for the duration of the experiment (Untreated (N/A)). Cells were collected after 15 minutes and expression of phosphorylated and total proteins as indicated, along with GAPDH as a loading control, were analysed by immunoblotting. Figure shows quantification for all samples analysed (n=4). Graphs show mean (with standard deviation) relative protein expression/phosphorylation. The statistical significance of the difference between control (DMSO treated) and test conditions and the difference between MT-802-treated or ibrutinib-treated cells was assessed (paired t test), and the results are indicated on the graphs.

3.7 Effect of ibrutinib and acalabrutinib on anti-IgM-induced iCa^{2+} fluxes in DLBCL cell lines

Finally, I investigated the effects of BTKi on iCa^{2+} responses in lymphoma-derived cell lines to determine whether the BTK "by-pass" phenomena was specific for CLL or more broadly for malignant B cells. I selected DLBCL cell lines for this analysis as DLBCL is the most common high-grade lymphoma and ibrutinib can induce clinical responses in a subset of ABC-DLBCL cases (Phelan et al., 2018).

3.7.1 Analysis of anti-IgM-induced iCa^{2+} fluxes in DLBCL cell lines

The first aim was to identify cell lines suitable for analysis of anti-IgM-induced iCa^{2+} fluxes. A small panel of six DLBCL cell lines were chosen (detailed in **Table 3-1**), including examples of both ABC- and GCB-DLBCL. Of specific interest were the TMD8 and HBL1 cell lines as these are examples of the ABC type that are reported to be highly sensitive to ibrutinib associated with the presence of My-T-BCR complex (Phelan et al., 2018). Initial profiling experiments to characterise anti-IgM responses were performed once for each cell line to allow selection of two cell lines for detailed analysis of the response to BTKi and are shown in **Supplementary Figure 1**.

Based on these results, I selected OCI-Ly7 and TMD8 cell lines for further analysis because they showed both strong and sustained responses to anti-IgM, with relatively little effect of the control antibody. Moreover, these represented the GCB- and ABC-DLBCL subtypes, respectively. OCI-Ly18 and SU-DHL-6 cell lines were not selected because there was not a substantial increase in iCa^{2+} mobilisation following anti-IgM stimulation compared with that of addition of control antibody. HT was subsequently found not to express sIgM (Havranek et al., 2017) so was excluded from further analysis. HBL1 was not selected due to the relatively short-lived response to anti-IgM stimulation compared with the chosen cell lines.

TABLE 3-1: SUMMARY OF DIFFUSE LARGE B-CELL LYMPHOMA (DLBCL) CELL LINES.

Cell Line	DLBCL Type[1]	IgM light chain	B-cell markers	Genomics	References
OCI-Ly7	GCB	kappa	CD10+, CD19+, CD20+, CD37+, CD38+, sIgM+	t(8:14)	(Tweeddale et al., 1987, 1989; Chang et al., 1995)
TMD8	ABC	kappa	CD5+, CD19+, CD20+, sIgM+		(Tohda et al., 2006; Zhang et al., 2013a)
HBL1	ABC	kappa	CD20+, CD24+, sIgM+		(Abe et al., 1988; Nozawa et al., 1988)
OCI-Ly18	GCB	lambda	CD10+, CD19+, CD20+, CD38+, sIgM+	t(8;14) t(8;18;14)	(Chang et al., 1992, 1995)
SU-DHL-6	GCB	lambda	CD20+, CD24+, sIgM+	t(14;18)	(Epstein et al., 1978; Winter et al., 1984)
HT	GCB	kappa	CD19+, CD20+, CD21+, $CD22^{+}$		(Beckwith et al., 1990)

[1]*GCB: germinal centre B-cell like, or ABC: activated B-cell like*

3.7.2 Effect of BTKi on anti-IgM-induced iCa^{2+} fluxes in OCI-Ly7 and TMD8 cells

I next investigated the effect of kinase inhibitors on anti-IgM-induced iCa^{2+} release using the selected lines. The inhibitors tested included ibrutinib and acalabrutinib (at both 1 and 10 μM) and the SYK inhibitor, R406, at 10 μM (as a positive control for proximal BCR pathway inhibition). The concentrations of BTKi used here were relatively high, but these initial experiments were designed to identify cell lines with residual anti-IgM-induced iCa^{2+} mobilisation despite full BTK blockade. In each experiment, a sample of cells were treated with DMSO or left untreated before stimulation as controls.

Representative data along with a summary of the peak percentage of cells responding to anti-IgM and the AUC for multiple experiments with OCI-Ly7 and TMD8 cells is shown in **Figure 3-12** and **Figure 3-13**, respectively.

OCI-Ly7 cells showed strong induction of iCa^{2+} mobilisation upon anti-IgM stimulation (**Figure 3-12A, *top panel***). The peak anti-IgM response was reached within 30 seconds of stimulation and was then followed by an initial rapid decline followed by a slower decline back to control cell levels at 5 minutes. This response was unaffected by DMSO (**Figure 3-12A, *second panel***) but, as expected, R406, completely blocked anti-IgM-induced iCa^{2+} mobilisation (**Figure 3-12A, *third panel***). Interestingly, at 10 μM, ibrutinib delayed the timing of the peak of the anti-IgM iCa^{2+} by approximately 30-40 seconds and reduced the size of this peak by ~50% (**Figure 3-12A, *fourth panel***). At 1 μM, ibrutinib had no effect on the initial phase of the anti-IgM response but resulted in an acceleration of its decline. In contrast, acalabrutinib (at either concentration) partially inhibited the peak anti-IgM reponse (but did not alter its timing) and substantially accelerated its subsequent decay (**Figure 3-12A, *fifth panel***).

The effects of ibrutinib on iCa^{2+} fluxes were quantified using both peak anti-IgM response (%) and AUC (**Figure 3-12B and 3-12C,** respectively) and were statistically significant for the AUC, but not peak anti-IgM response. The effects of either concentration of acalabrutinib were statistically significant for peak anti-IgM response (**Figure 3-12B**), but only 10 μM acalabrutinib statistically significantly reduced the AUC (**Figure 3-12C**).

TMD8 cells also showed strong induction of iCa^{2+} mobilisation upon anti-IgM stimulation (**Figure 3-13A, *top panel***). The peak anti-IgM response was reached very quickly and a gradual decline was observed but the response did not return to baseline within the time analysed. The anti-IgM-induced iCa^{2+} response was unaffected by DMSO (**Figure 3-13A, *second panel***), but was completely inhibited by ibrutinib at 10 μM (and R406 at 10 μM) (**Figure 3-13A, *third and fourth panels***). By contrast, 1 μM ibrutinib (which would still be expected to fully block BTK activity), only partially inhibited the peak iCa^{2+} response and did seem to accelerate its decline. Acalabrutinib (at 1 or 10 μM) partially reduced the peak anti-IgM response but did not affect its timing (**Figure 3-13A, *fifth panel***). However, the iCa^{2+} response appeared to decline more rapidly in acalabrutinib-treated cells compared with control cells.

The effects of ibrutinib on iCa^{2+} fluxes were quantified using both peak anti-IgM response (%) and AUC (**Figure 3-13B and 13C,** respectively) and were statistically significant for the AUC (**Figure 3-13C**), but only statistically significant for peak anti-IgM response following 10 μM ibrutinib pretreatment (**Figure 3-13B**). The effects of both concentrations of acalabrutinib were statistically significant for the AUC (**Figure 3-13C**), but only 10 μM acalabrutinib statistically significantly reduced the peak anti-IgM response (**Figure 3-13B**).

Overall, these results demonstrate that, similar to CLL cells, BTKi only partially inhibited anti-IgM-induced iCa^{2+} responses in OCI-Ly7 and TMD8 cells. There were interesting differences in the effects of the two compounds, but it is important to bear in mind that the concentrations tested here are high so there is strong potential for off-target effects, especially for ibrutinib.

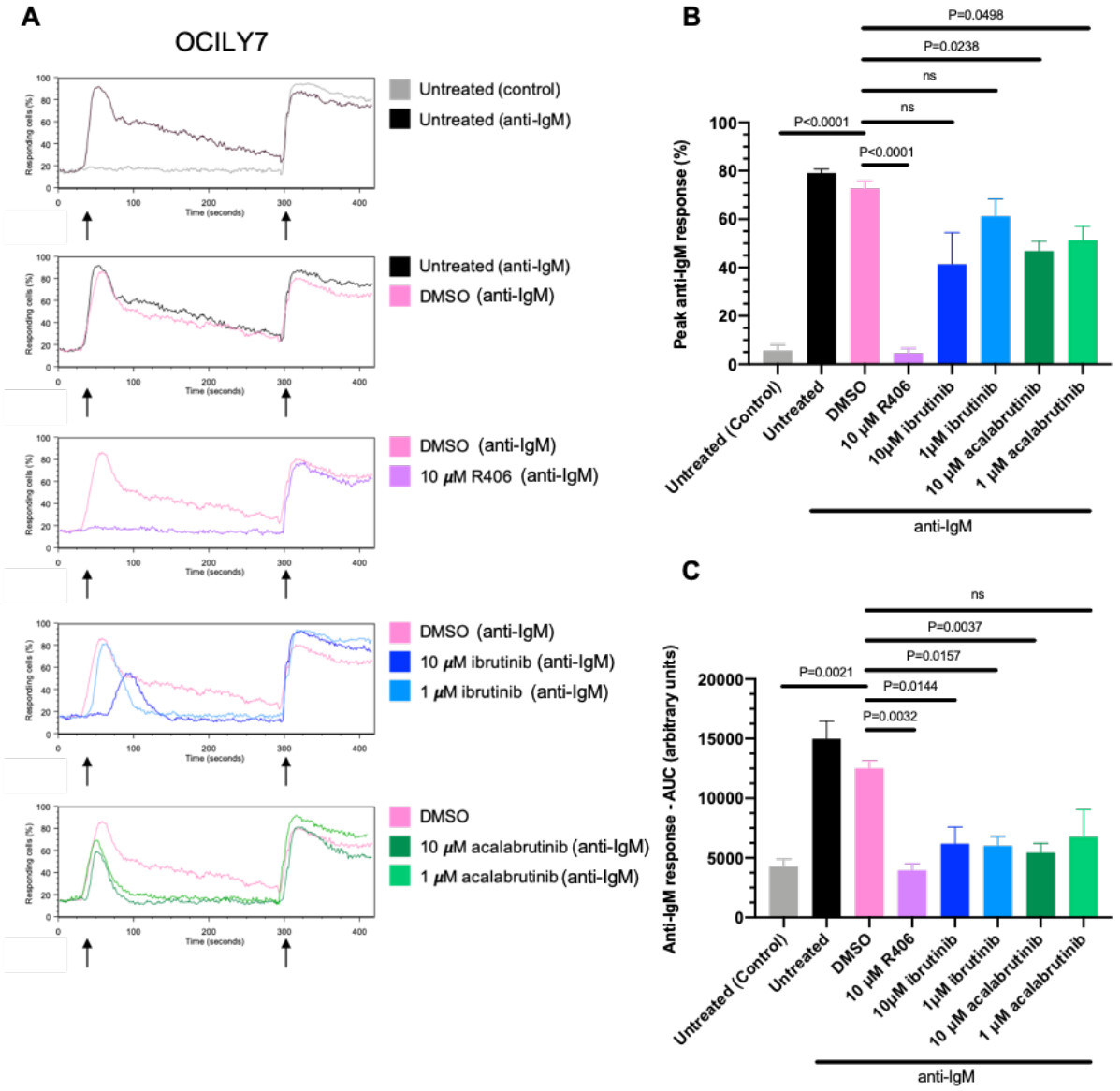

FIGURE 3-12: ANALYSIS OF BTKI-INDUCED INHIBITION OF ANTI-IGM-INDUCED iCa^{2+} FLUX IN OCI-LY7 CELLS.

A. iCa^{2+} fluxes were analysed in OCI-Ly7 cells following addition of anti-IgM (or control antibody). The first arrow shows time of addition of antibody following baseline data recording for 30 seconds. The second arrow shows time of addition of ionomycin as a positive control. Untreated cells were stimulated with anti-IgM (black) or control antibody (grey). Each of the conditions is compared to the DMSO treated (vehicle control) cells stimulated with anti-IgM (pink). Cells were pretreated with either 10 μM R406 (purple), 10 μM ibrutinib (dark blue), 1 μM ibrutinib (light blue), 10 μM acalabrutinib (dark green), or 1 μM acalabrutinib (light green) before stimulation with anti-IgM. Summary data of the peak percentage of responding cells **(B)** and the area under the curve **(C)** is shown; bars represent the mean and standard deviation (n=3). Statistical significance of the difference between DMSO and each condition determined by paired t tests is indicated on the graphs.

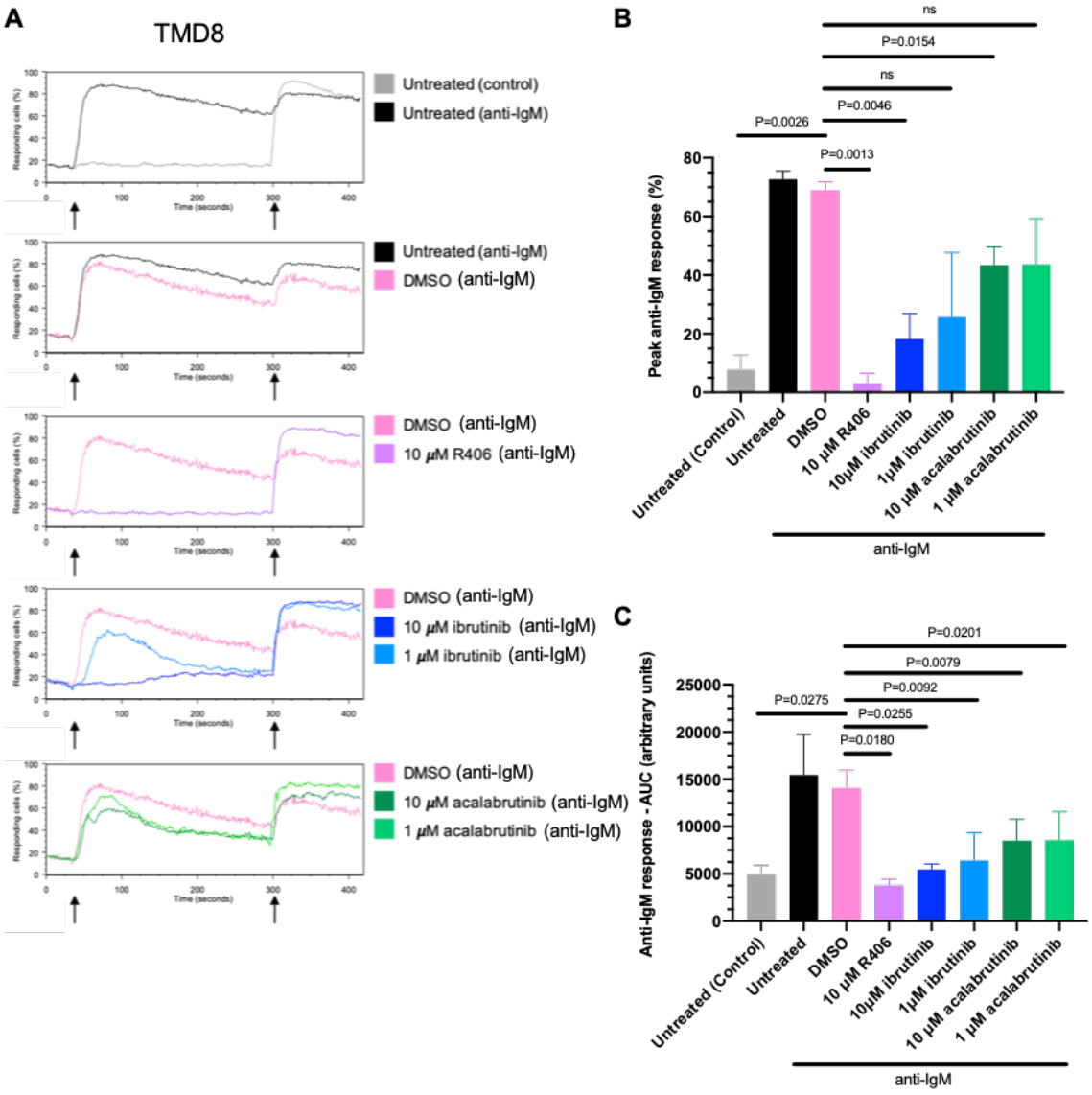

FIGURE 3-13: ANALYSIS OF BTKI-INDUCED INHIBITION OF ANTI-IGM-INDUCED iCa^{2+} FLUX IN TMD8 CELLS.

A. iCa^{2+} fluxes were analysed in TMD8 cells following addition of anti-IgM (or control antibody). The first arrow shows time of addition of antibody following baseline data recording for 30 seconds. The second arrow shows time of addition of ionomycin as a positive control. Untreated cells were stimulated with anti-IgM (black) or control antibody (grey). Each of the conditions is compared to the DMSO treated (vehicle control) cells stimulated with anti-IgM (pink). Cells were pretreated with either 10 μM R406 (purple), 10 μM ibrutinib (dark blue), 1 μM ibrutinib (light blue), 10 μM acalabrutinib (dark green), or 1 μM acalabrutinib (light green) before stimulation with anti-IgM. Summary data of the peak percentage of responding cells **(B)** and the area under the curve **(C)** is shown; bars represent the mean and standard deviation (n=3). Statistical significance of the difference between DMSO and each condition determined by paired t tests is indicated on the graphs.

3.8 Discussion

Preliminary data from the host group showing variability in the signalling capacity of the BCR and inhibitor responses between primary CLL samples was suggestive of a BTK "by-pass" mechanism operating in at least some CLL samples. The overall goal of this chapter was to investigate the inhibitory effects of BTKi on anti-IgM-induced iCa^{2+} fluxes and begin to characterise the potential BTK "by-pass" mechanism. To achieve this, I addressed five specific aims:

1. Extend analysis of ibrutinib's inhibitory effect on anti-IgM-induced iCa^{2+} fluxes to additional CLL samples to confirm initial findings (**Figure 1-21**).
2. Determine whether similar effects are observed with acalabrutinib, a more selective BTKi.
3. Investigate potential correlations between clinical and biological features of CLL samples and variable responses to BTKi.
4. Compare the effects of ibrutinib and a BTK-degrading PROTAC to investigate the potential contribution of BTK-mediated, kinase-independent pathways.
5. Determine whether partial responses to BTKi are observed in other malignant B cells by analysing the efficacy of BTKi for inhibition of iCa^{2+} fluxes in DLBCL cell lines.

Summary of main findings:

- Ibrutinib variably, but generally only partially, inhibited iCa^{2+} fluxes in CLL samples.
- Acalabrutinib, a more selective BTKi, variably (but generally only partially) inhibits iCa^{2+} fluxes in CLL samples.
- There are strong positive correlations (determined by Spearman's correlation) between peak anti-IgM responses following DMSO treatment alone (i.e. strength of signal) with the residual signal in the presence of BTKi.
- There are strong positive correlations (determined by Spearman's correlation) between sIgM expression and the residual signal in the presence of BTKi.
- There is no significant difference between the effect of ibrutinib and the BTK-degrading PROTAC, MT-802, on iCa^{2+} flux or phosphorylation of AKT or ERK.
- The partial inhibition observed following BTKi pretreatment is observed in the DLBCL cell lines OCI-Ly7 and TMD8, determined by Ca^{2+} flux assay.

The results presented in this chapter provide new evidence of a BTK "by-pass" pathway in B-cell malignancies. This is likely to be a general feature of BTK inhibition, as opposed to ibrutinib-specific, as a very similar pattern of signalling behaviour and inhibitor response is observed with acalabrutinib. It is also suggestive that it is not specific to CLL as it was seen in cell models of DLBCL. The BTK "by-pass" mechanism appears to be largely BTK independent, not just independent of its kinase activity, as the effect of BTK kinase inhibition with ibrutinib was not significantly altered following BTK degradation with MT-802. The mechanism seems to associate more closely with strong signalling via the BCR, suggesting that it is acquisition of "by-pass" which actually mediates strong signal.

3.8.1 Effect of BTK kinase inhibition in CLL cells

Preliminary work in the host laboratory investigating the effect of ibrutinib on iCa^{2+} release suggested that not all samples are affected to the same extent by ibrutinib-mediated BTK kinase inhibition. However, since ibrutinib has many off-target effects, it was not known whether this variability in response was an ibrutinib-specific phenomenon or whether it was a general feature of BTK inhibition. I therefore decided to extend the analysis with ibrutinib to assess more samples as well as include the pretreatment of acalabrutinib, which is known to be more selective for BTK than ibrutinib (Byrd et al., 2016).

The data presented here confirmed the initial findings that not all samples respond to the same extent following ibrutinib pretreatment *in vitro* (**Figure 3-1**). In general, only partial inhibition was achieved but the samples with a stronger signalling capacity were only weakly inhibited whereas samples with a weaker signalling capacity could be inhibited to a much greater extent. This was also the case for acalabrutinib pretreated cells, whereby the variability in inhibitor responses suggested that stronger signallers were weakly, or partially, inhibited but weaker signallers experienced a more pronounced inhibition (**Figure 3-2**). Whilst ibrutinib generally inhibited samples to a greater extent than acalabrutinib, the difference was not statistically significant (**Figure 3-3A**), and could be due to the known off-target effects of ibrutinib, e.g. binding SYK (Honigberg et al., 2010), and its increased potency compared with acalabrutinib (Hopper et al., 2020). There was a strong correlation between effects of ibrutinib and acalabrutinib for individual samples whereby samples that exhibited weak inhibition by ibrutinib also displayed weak inhibition by acalabrutinib and samples showing greater inhibition by ibrutinib also showed greater inhibition by acalabrutinib (**Figure 3-3B**). Overall, the effects of ibrutinib and acalabrutinib

were very similar but there were some modest differences seen in primary CLL. This confirms that the observation of variability in inhibitor responses is not based on the off-target effects of ibrutinib but is more likely a class effect of BTK inhibition. However, it is important to recognise that the concentrations used here were relatively high. A more detailed investigation into the dose response effects of lower concentrations is included in **Chapter 4.**

There were no clear correlations between the extent of BTK inhibition and clinical features (**Figure 3-4** and **Figure 3-5**), which may be due to lack of power (relatively small sample size). However, there is an inherent bias in the cohort since only samples classified as "signallers" were selected. Since low ZAP-70 and CD38 expression, and M-CLL status is associated with weaker sIgM signalling capacity (Mockridge et al., 2007; Damle et al., 1999), there was a tendancy for samples with these features to be excluded from the cohort. In the future, analysis could be extended to include genomic features, since some have been shown to correlate with signalling capacity e.g. CLL samples with del(17p) had significantly higher signalling capacity than those with del13q (D'Avola et al., 2016).

There were strong correlations found between extent of BTK inhibition with both the signalling capacity (peak anti-IgM response (%)) and sIgM expression (**Figure 3-6**), whereby samples with low sIgM expression/signalling capacity could be inhibited to a much greater extent than those with high sIgM expression/signalling capacity. Since high concentrations of inhibitors were used in this analysis, it is unlikely that partial inhibition was solely a consequence of higher levels of BTK activation itself (which might then need higher drug concentrations for effective inhibition). I speculate that the BTK "by-pass" mechanism mediates the strong signal and that BCR engagement can activate two pathways (canonical and "by-pass") depending on the initial input whereby a higher threshold of activation is required to engage the "by-pass" mechanism (Wist et al., 2020).

3.8.2 Effect of BTK kinase inhibition in lymphoma-derived cell lines

The analysis was extended to OCI-Ly7 and TMD8 DLBCL cell lines. This is useful for three main reasons: (i) it is clinically relevant, particularly TMD8, the ABC-DLBCL cell line, (ii) it shows distinct modes of signalling, particularly with My-T-BCR complex in TMD8 cell line, and (iii) the cell lines

could provide a transfectable system for future functional studies (discussed further in **Section 6.5**).

Overall, the conclusions were similar to those made with CLL, whereby the strong signalling cell lines could only be partially inhibited by BTKi treatment, used at concentrations to ensure full BTK inhibition (**Figure 3-12** and **Figure 3-13**). This supports the conclusion that the partial inhibition achieved is not ibrutinib-specific and not specific to CLL. There may be a role in a wider range of B-cell malignancies, specifically DLBCL. This is particularly interesting because the BCR might be functioning in different ways, since the signalling between GCB- and ABC-DLBCL differs. GCB-DLBCL relies on tonic BCR signalling, transmitted via SYK primarily to activate the PI3K/AKT pathway (Havranek et al., 2017) and ABC-DLBCL are dependent on chronic signalling, a subset of which express the My-T-BCR, which promotes sensitivity to ibrutinib (Phelan et al., 2018). Despite the variation in cellular activity and sensitivity to stimulation and inhibition, it appears that BTK "by-pass" is a more generalised mechanism.

However, there are some interesting features comparing ibrutinib and acalabrutinib and the kinetics which are not seen so clearly in CLL. Differences between ibrutinib and acalabrutinib may be due to ibrutinib having more off-target effects than acalabrutinib (Honigberg et al., 2010; Dubovsky et al., 2013; Atkinson et al., 2003). Following pretreatment with 10 μM ibrutinib in OCI-Ly7 cells, a delayed response to anti-IgM-induced iCa^{2+} flux was seen (**Figure 3-12A**). In a set of experiments performed by Wist et al., (Wist et al., 2020), which explored anti-IgM-induced iCa^{2+} mobilisation in $BTK^{-/-}$ DT40 cells reconstituted with either wild type BTK (BTK^{WT}) or a kinase-inactive mutant BTK (BTK^{K430R}), the authors showed that the lag time observed in BTK^{WT} cells following anti-IgM stimulation was reduced as the concentration of anti-IgM stimulation was increased. They also showed that as the concentration of anti-IgM increases, the ability of kinase-inactive BTK^{K430R} to induce iCa^{2+} mobilisation increases suggesting that the strength of the signal determines whether a kinase-inactive BTK can contribute to cellular activation. Acalabrutinib treatment of the DT40 cells inhibited iCa^{2+} mobilisation, but the inhibitory effect of acalabrutinib was reduced as the concentration of anti-IgM was increased (Wist et al., 2020). Taken together, the authors conclude that with a stronger BCR-mediated signal, the kinase-independent function of BTK takes over and contributes to PLCγ2 activation (Wist et al., 2020). It is therefore important to consider the level of stimulation in *in vitro* assays and how it is comparable to the level of stimulation experienced *in vivo* because there is a clear effect on the level of pathway inhibition that can be achieved by inhibiting BTK kinase activity.

3.8.3 Kinetic analysis of iCa^{2+} mobilisation

Previous work has used the peak percentage of cells responding to anti-IgM stimulation measured by Ca^{2+} flux assay to quantify the signalling capacity of the BCR (Mockridge et al., 2007). Whilst this is a useful parameter, particularly in determining whether to classify a sample as a strong or weak signaller, or non-responder, there are limitations with looking at just this one parameter as it does not consider the kinetics of iCa^{2+} mobilisation over time.

As mentioned above, particularly with high concentrations of ibrutinib in DLBCL cell lines, a delayed response to anti-IgM-induced iCa^{2+} release is observed. The duration of the response after BTKi pretreatment is also variable with some samples having short-term duration of iCa^{2+} release whereby the level of iCa^{2+} measured returns to baseline within the time frame, whereas others exhibit a reduced but consistent level of iCa^{2+} mobilisation over the time course. These differences are all masked by only using the peak anti-IgM response as a measure of signalling capacity. These features could be important in determining whether the responses are kinase-dependent or -independent (Wist et al., 2020), which may be useful for the development of alternative therapies that target more than kinase inhibition, e.g. PROTAC-mediated degradation of BTK. Furthermore, peak iCa^{2+} response and the sustained iCa^{2+} response are caused by different methods of increasing $i[Ca^{2+}]$, through release from internal stores and influx of extracellular Ca^{2+}, respectively (Scharenberg et al., 2007; Fluckiger et al., 1998). These two phases of the iCa^{2+} response have different downstream effector functions (Dolmetsch et al., 1997, 1998; Healy et al., 1997), which might indicate different biological responses depending on the type of inhibition achieved. In the future, this could be useful for identifying alternative therapies, or combinations of therapies, on a per sample basis to improve inhibition of the BCR-associated signalling pathway therefore reducing likelihood of disease relapse and progression.

Based on these observations, the iCa^{2+} flux data presented in this thesis includes the peak anti-IgM response as well as the AUC to create a fuller, more robust picture of the responses seen, since neither parameter describes the data completely.

3.8.4 Nature of BTK "by-pass"

Previous studies have suggested the possible role of kinase-independent activity of BTK within the BCR signalling pathway (Takata and Kurosaki, 1996; Tomlinson et al., 2001) so one of the primary aims of this chapter was to investigate whether a kinase-independent activity of BTK (e.g. scaffolding function) was contributing to a "by-pass" mechanism whereby BTK acted as a docking site allowing functional interactions between other kinases/signalling molecules for the continued activation of downstream pathways. This was investigated by exploiting BTK-specific PROTAC-mediated degradation.

A comparison between BTK kinase inhibition by ibrutinib and BTK degradation by PROTAC allowed the conclusion to be made that the "by-pass" mechanism was largely BTK-independent. There was no further inhibition of iCa^{2+} release following BTK degradation by MT-802 compared with BTK inhibition by ibrutinib (**Figure 3-9**). Further investigation into more distal BCR-associated signalling molecules (AKT and ERK) showed no significant differences between the effects of ibrutinib or MT-802 (**Figure 3-11**).

Saito *et al*. (Saito et al., 2003) suggested that BTK promotes recruitment of PIP5K to the PM independently of its kinase activity. PIP5K catalyses production of $PI(4,5)P_2$ thereby implicating BTK in the increased and sustained levels of $PI(4,5)P_2$ which is required for production of IP_3 by PLCγ2 to cause an increase in iCa^{2+} release. PI3K converts $PI(4,5)P_2$ to PIP_3 which activates AKT (Stokoe et al., 1997). Based on this model, inhibition of BTK by ibrutinib will allow the continued recruitment of PIP5K and production of $PI(4,5,)P_2$, whereas BTK degradation by MT-802 will prevent the accumulation of $PI(4,5)P_2$ at the PM so there will not be sufficient substrate for PI3K activity to promote the activation of AKT. Therefore, the results presented here support the idea that BTK kinase-independent activity is, at least in part, required for AKT activation.

Overall, these results provide new evidence of a BTK "by-pass" pathway in B-cell malignancies, which appears to be largely BTK independent and not just independent of its kinase activity. This mechanism appears to associate more closely with strong signalling via the BCR, suggesting that it is acquisition of "by-pass" which actually mediates strong signal.The next chapter will probe potential mechanisms for this "by-pass" signalling in further detail.

Chapter Four

Results: BTK “by-pass” pathway analysis

4 BTK "by-pass" pathway analysis

4.1 Introduction

Results presented in the previous chapter confirmed the preliminary findings that CLL samples respond variably to BTK kinase inhibition with some samples (particularly those with a strong signalling capacity in the absence of BTK inhibition) only experiencing a partial inhibition. Thus, an alternative BTK-independent pathway can lead to iCa^{2+} mobilisation in these cells. This phenomenon was not mediated by kinase-independent functions of BTK and was also observed in DLBCL cell lines. The overall goal of the experiments presented in this chapter was to probe potential mechanisms for this "by-pass" signalling.

The current paradigm for BCR-induced iCa^{2+} release is initiation via the BCR, activating a signalling cascade via SYK, activating BTK, which subsequently phosphorylates and activates PLCγ2. Activated PLCγ2 catalyses the breakdown of $PI(4,5)P_2$ to produce DAG and IP_3, the latter of which initiates release of Ca^{2+} from ER stores. This paradigm is summarised in **Figure 1-4.** However, these schematics and proposed pathways are, in general, simplified versions of the full biological mechanism and possible alternative pathways may account for BTK "by-pass". The nature of these potential pathways was investigated by characterising the effect of BTKi on phosphorylation of key BCR-associated signalling molecules in both DLBCL cell lines and primary CLL (a summary of phosphorylation sites analysed in the work is shown in **Table 4-1**).

For CLL, some experiments were performed in the presence of IL-4, as previous studies have shown that IL-4 boosts sIgM signalling capacity and confers reduced inhibition of iCa^{2+} responses by ibrutinib (i.e. seems to enhance "by-pass" signalling) (Aguilar-Hernandez et al., 2016). IL-4 has a variety of roles within a normal immune system, especially within T-cell biology but also including the promotion of B-cell differentiation (Rush and Hodgkin, 2001) and is also involved with upregulation of the major histocompatibility complex class II (MHCII) and promotion of Ig class-switching (Hou et al., 1994). IL-4 has also been implicated in the pathogenesis of leukaemia (Pangault et al., 2010) and lymphoma (Amé-Thomas et al., 2015). As well as being a useful tool with which to compare signalling responses within CLL samples, a larger proportion of IL-4-

positive T-cells are found in CLL patients with progressive disease (Rossmann et al., 2002) and CLL patients have raised levels of IL-4 compared with normal donors (Kay et al., 2001). Therefore, the presence of IL-4 is biologically relevant in the setting of BCR-mediated signalling in CLL and might be implicated in effects of BTK "by-pass" signalling.

TABLE 4-1: PHOSPHORYLATION SITES OF BCR-ASSOCIATED SIGNALLING MOLECULES.

Signalling molecule	Phosphorylation site(s)
LYN	Tyr^{396} Tyr^{507}
SYK	$Tyr^{525/526}$ (autophosphorylation)
BLNK	Tyr^{84} Tyr^{96}
BTK	Tyr^{223} (autophosphorylation) Tyr^{551}
PLCγ2	Tyr^{753} Tyr^{759} Tyr^{1197} Tyr^{1217}
PLCγ1	Tyr^{783}

4.2 Hypothesis and aims

The experiments in this chapter were designed to investigate the hypothesis that BCR-associated kinases (independent of BTK) phosphorylate and activate PLCγ2, leading to iCa^{2+} mobilisation, "by-passing" the requirement for BTK. Experiments used various concentrations of inhibitors to probe the concentration dependency of responses and identify potential "on-target" and "off-target" effects.

This was addressed with 3 main aims:

1. Identify BTK-dependent and -independent PLCγ2/PLCγ1 phosphorylation events that may lead to iCa^{2+} mobilisation in primary CLL and DLBCL cell lines.
2. Investigate the effect of enhanced signalling in CLL using IL-4, and the effect on BTK inhibition.
3. Investigate the concentration dependency of inhibition of BTK by assessing drug occupancy of the active site of BTK and western blotting to assess phosphorylation events within the BCR-associated signalling pathway.

4.3 Investigating the concentration dependency of BTKi-mediated inhibition of iCa^{2+} fluxes

In the previous chapter, analysis of BTKi used relatively high drug concentrations to ensure full BTK blockade. Before proceeding to detailed molecular analysis, it was important, therefore, to probe the concentration-dependency of BTKi effects. This was particularly important for ibrutinib which is known to have many off-target effects, especially at higher concentrations (see **Section 1.6**). I therefore investigated the effects of different concentrations of ibrutinib or acalabrutinib on anti-IgM-induced iCa^{2+} fluxes in both primary CLL cells (without IL-4) and OCI-Ly7 and TMD8 cell lines.

4.3.1 iCa^{2+} fluxes in primary CLL cells

Three primary CLL samples were selected for iCa^{2+} flux analysis (**Table 2-1**). The samples were pretreated with a range of concentrations of ibrutinib or acalabrutinib (10 μM, 1 μM, 100 nM, 10 nM or 1 nM), 10 μM R406 (to inhibit all signalling downstream of SYK), DMSO, or left untreated for 1 hour prior to iCa^{2+} flux analysis. An example iCa^{2+} flux analysis using CLL 674D is shown (**Figure 4-1**) and summary data of the peak anti-IgM response (%) and AUC in response to anti-IgM is shown in **Figure 4-2A and 4-2B**, respectively.

For representative sample 674D, R406 completely blocked the response (**Figure 4-1, *top panel***). The inhibitory effects of ibrutinib were clearly concentration dependent. The response was partially inhibited with 1 nM ibrutinib and the extent of inhibition then increased with increasing drug concentration, such that iCa^{2+} release was fully inhibited by 10 μM ibrutinib (**Figure 4-1, *middle panel***). Acalabrutinib at 1 nM also partially inhibited the response. However, in contrast to ibrutinib, the maximal extent of inhibition (still partial) was observed with 10 nM drug and increasing the concentration of acalabrutinib above 10 nM did not lead to a greater effect (**Figure 4-1, *bottom panel***).

Similar effects were observed when the summarised data for the three samples were analysed, for both peak anti-IgM response (%) (**Figure 4-2A**) and AUC (**Figure 4-2B**). Thus, partial inhibitory

effects were observed for both drugs at 1 nM, and stronger inhibition at 10 nM, for peak response and AUC. However, the effects of acalabrutinib were maximal at 10 nM, and only for ibrutinib at 10 μM was complete inhibition observed. Statistical significance between control (DMSO-treated) cells and inhibitor-treated cells, calculated using Wilcoxon tests, was not reached in this experiment. This is likely to be due to the small sample size and the more stringent statistical test used because a normal distribution could not be assumed.

Although it is not possible to determine robust IC_{50} measurements from these data, the results demonstrate that, at 1 nM, acalabrutinib has partial inhibitory effects on iCa^{2+} release, whereas the maximal effects of this drug are reached at 10 nM, indicating that BTK is partially inhibited in these cells at ~1 nM and maximally inhibited at ~10 nM. However, even at 10 nM there is a substantial proportion of the response remaining (i.e. “by-pass” operates), and this component of the response is not further reduced by increasing the drug concentration beyond 10 nM. A similar degree of inhibition is observed with ibrutinib at 1 nM and 10 nM. However, in contrast to acalabrutinib, higher concentrations of ibrutinib lead to a greater extent of inhibition (full at 10 μM). It seems likely that these stronger ibrutinib-specific inhibitory effects are mediated by off-target inhibition at higher drug concentrations.

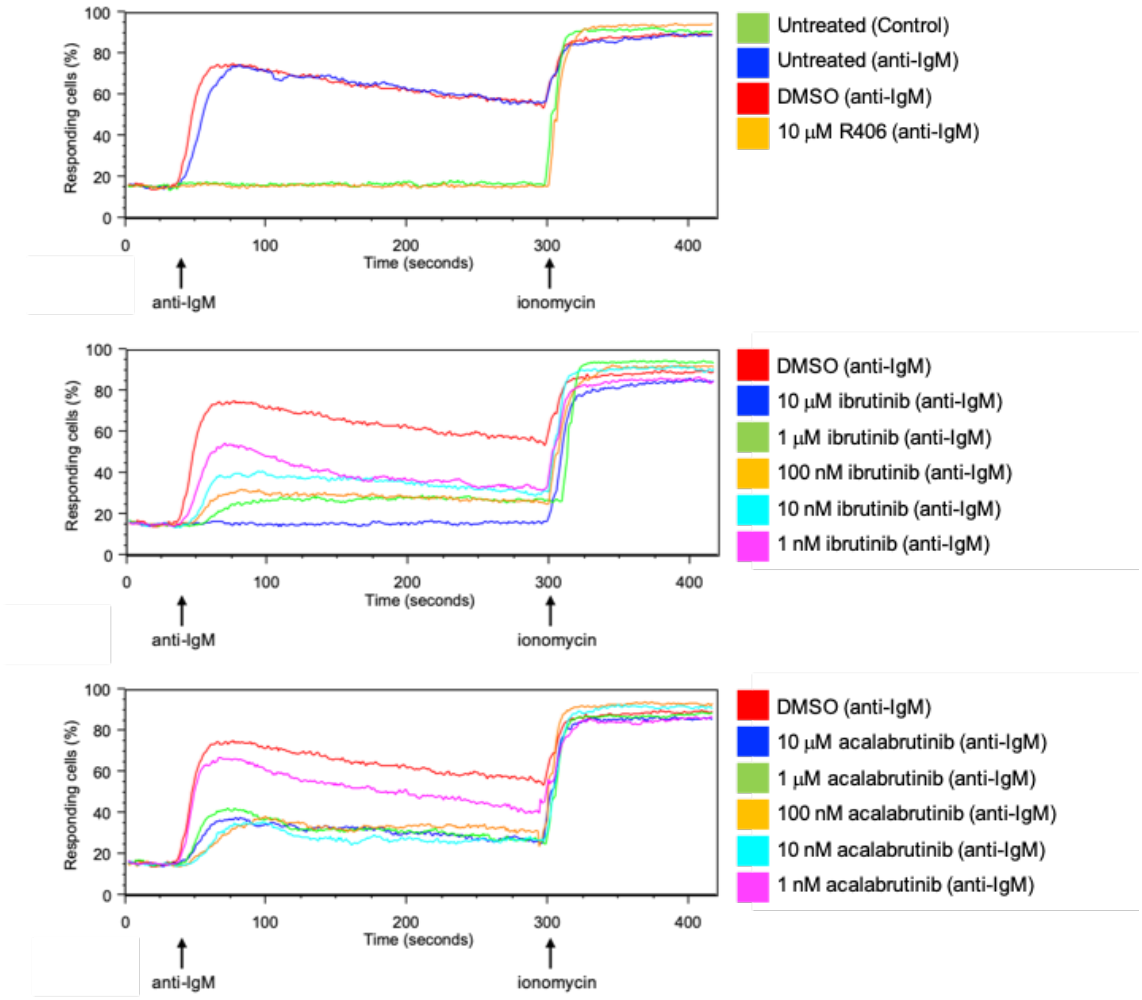

FIGURE 4-1: EXAMPLE DOSE-RESPONSE EFFECT OF BTK INHIBITION ON ANTI-IGM-INDUCED iCa^{2+} MOBILIZATION IN CLL 674D.

Representative iCa^{2+} fluxes analysed in a primary CLL sample (CLL 674D) following addition of anti-IgM (or control antibody). The first arrow indicates time of addition of antibody following baseline data acquisition for 30 seconds. The second arrow indicates time of addition of ionomycin as a positive control. *Top panel:* Untreated cells were stimulated with anti-IgM (blue) or control antibody (green), DMSO treated cells (red), used as a vehicle control, and 10 μM R406 treated cells (orange) were stimulated with anti-IgM. *Middle panel:* Cells were pretreated for 1 hour with either 10 μM (blue), 1 μM (green), 100 nM (orange), 10 nM (turquoise), or 1 nM (pink) ibrutinib before anti-IgM stimulation and compared with the DMSO control (red). *Bottom panel:* Cells were pretreated for 1 hour with either 10 μM (blue), 1 μM (green), 100 nM (orange), 10 nM (turquoise), or 1 nM (pink) acalabrutinib before anti-IgM stimulation and compared with the DMSO control (red).

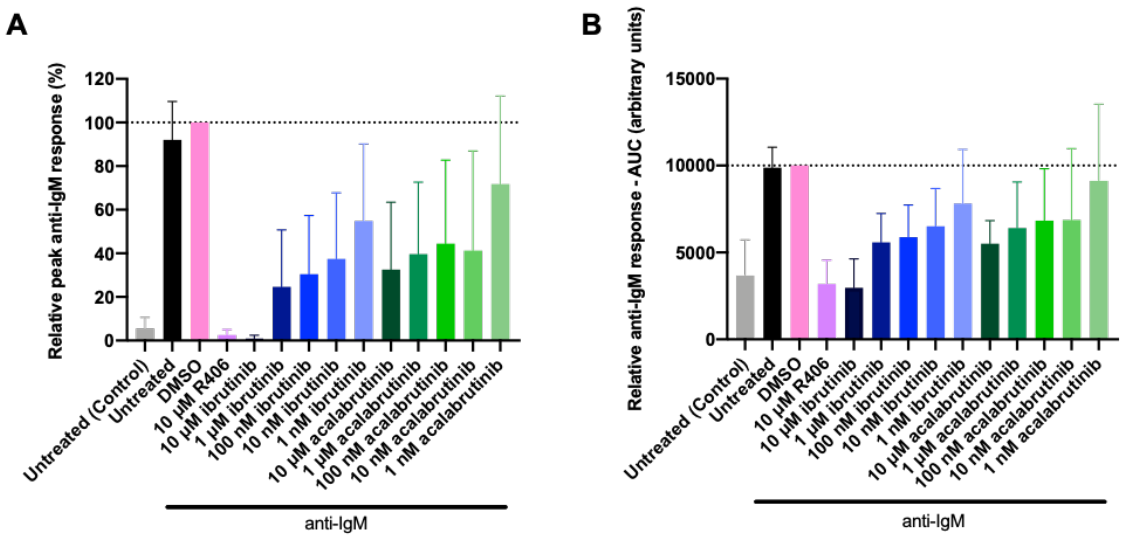

FIGURE 4-2: THE DOSE-RESPONSE EFFECT OF BTK INHIBITION ON ANTI-IGM-INDUCED iCa^{2+} MOBILIZATION IN PRIMARY CLL SAMPLES.

Summary data of the relative peak percentage of cells responding to anti-IgM (response of cells pre-treated with DMSO is set to 100%) **(A)** and the area under the curve (response of cells pre-treated with DMSO is set to 10000 arbitrary units) **(B)** measured using iCa^{2+} flux assay by flow cytometry is shown; bars represent the mean and standard deviation (n=3). No statistical significance was determined by Wilcoxon tests between the DMSO control and each test condition.

4.3.2 iCa^{2+} fluxes in lymphoma-derived cell lines

Ca^{2+} flux analysis was carried out using the lymphoma-derived cell lines, OCI-Ly7 and TMD8, selected in **Chapter 3**, following the same protocol and inhibitor concentrations as above (**Section 4.3.1**). Representative iCa^{2+} flux data for OCI-Ly7 cells and TMD8 cells are shown in **Figure 4-3** and **Figure 4-5,** respectively, and summary data for the three replicates performed of the peak anti-IgM response (%) and AUC in response to anti-IgM are shown for OCI-Ly7 cells (**Figure 4-4**) and TMD8 cells (**Figure 4-6**). The data is summarised in **Table 4-2.**

OCI-Ly7 cells exhibited a strong anti-IgM-induced iCa^{2+} response and R406 very effectively blocked the response (**Figure 4-4**). By contrast, ibrutinib at 1 nM to 1 μM had relatively little effect on the timing or magnitude of the peak response, but did result in a more rapid decline of $i[Ca^{2+}]$ after the peak (as seen previously for 1 μM ibrutinib in **Figure 3-12)**. This accelerated decline in the response in ibrutinib-treated cells was concentration dependent. The effect was reflected in the quantitative data as, over this concentration range, the peak anti-IgM response was relatively unaffected by ibrutinib, but there was a clear trend for reduced AUC with increasing ibrutinib concentration. However, none of these differences reached statisitical significance in these experiments. Interestingly, treatment with 10 μM ibrutinib led to a clear delay in the timing (by approximately 30-40 seconds) and magnitude (by ~50%) of the peak anti-IgM-induced response. Again, this is similar to results obtained in previous experiments (**Figure 3-12**). Overall, 10 μM ibrutinib did significantly reduce the iCa^{2+} response when analysed using AUC (**Figure 4-4B**). Acalabrutinib had a similar effect as ibrutinib on iCa^{2+} responses when tested at 1 nM to 1 μM (i.e. a concentration dependent acceleration of the curtailment of the response with little effect on the timing or magnitude of the peak). However, in contrast to ibrutinib at 10 μM, acalabrutinib at 10 μM did not effect the timing of the peak response.

TMD8 cells also exhibited a strong anti-IgM-induced iCa^{2+} response and R406 completely blocked the response (**Figure 4-6**). The magnitude of the peak response was relatively unaffected by 1 nM ibrutinib and inhibited only weakly by 10 nM ibrutinib. However, similar to OCI-Ly7 cells, ibrutinib did cause a concentration-dependent acceleration in the decline of iCa^{2+}. Interestingly, increasing the drug concentration further (to 100 nM or 1 μM) only very modestly increased the extent of inhibition. These effects were reflected in the quantitative data as, over this concentration range, the peak anti-IgM response was generally not significantly affected by ibrutinib, but ibrutinib did significantly reduce the AUC at all concentrations. Similar to CLL cells (and as shown previously for

TMD8 cells in **Figure 3-13**), 10 μM ibrutinib completely ablated the anti-IgM-induced response. Acalabrutinib at 1 nM did not seem to substantially affect the magnitude of the peak response, but did accelerate the decline. At 10 nM, acalabrutinib modestly decreased the peak response, as well as accelerating the post-peak decline in i[Ca^{2+}]. Interestingly, both of these effects were maximal with 10 nM acalabrutinib (i.e. additional drug did not lead to more pronounced effects).

A summary for the results obtained with CLL cells, and OCI-Ly7 and TMD8 cell lines is presented in **Table 4-2**. In summary, the predominant effect of BTKi in CLL cells is to partially reduce the magnitude of the response, with little effect on kinetics (either peak time or rate of subsequent decline). For acalabrutinib, partial effects are seen with 1 nM drug and the maximum effect of drug is seen with 10 nM, suggesting that 10 nM acalabrutinib is sufficient for effective BTK inhibition in cells. The effects of increasing drug concentration are more complex for ibrutinib. Effects of ibrutinib and acalabrutinib were similar at 1 nM and 10 nM, however, at higher concentrations of ibrutinib, there was increasingly effective inhibition of the iCa^{2+} response, which was maximal at 10 μM. These additional effects associated with higher ibrutinib concentrations are presumably due to off-target effects.

In both OCI-Ly7 and TMD8 cells, the magnitude of the peak anti-IgM response was relatively unaffected by BTKi at most concentrations (consistent with operation of BTK-independent "by-pass" signalling). Interestingly, the predominant effect of BTKi on the iCa^{2+} response was to accelerate the rate of decline in iCa^{2+} following the peak. Again, 10 nM acalabrutinib was sufficient for maximal drug effect (consistent with this concentration being sufficient for full BTK inhibition). In TMD8 cells, only at a high concentration of 10 μM was ibrutinib able to ablate anti-IgM-induced responses, and this inhibition is likely driven by off-target effects. By contrast, in OCI-Ly7 cells, 10 μM ibrutinib caused a substantial delay in the timing (and magnitude) of, but did not prevent, the anti-IgM-induced response.

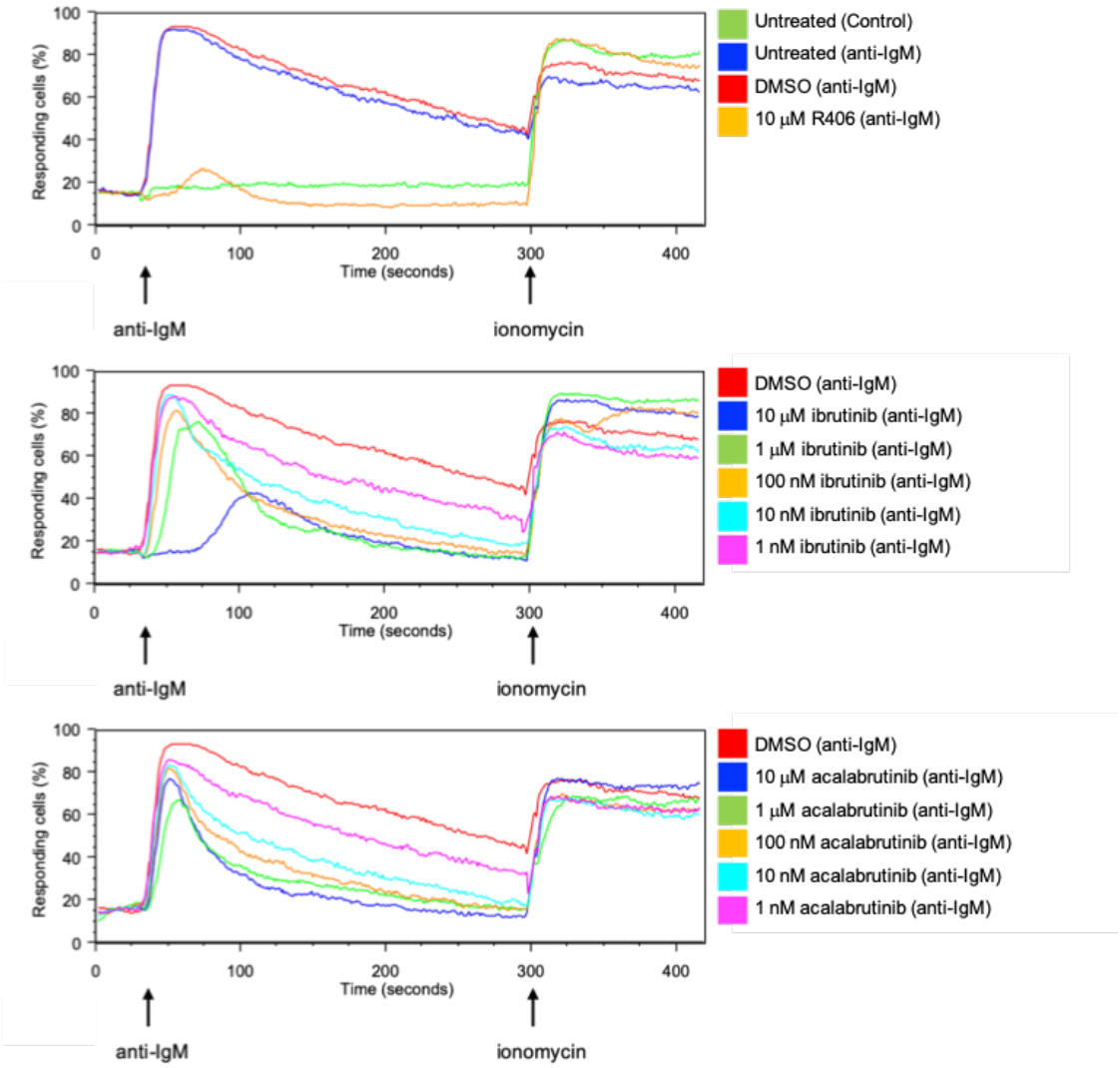

FIGURE 4-3: REPRESENTATIVE DOSE-RESPONSE EFFECT OF BTK INHIBITION ON ANTI-IGM-INDUCED iCa^{2+} MOBILIZATION IN OCI-LY7 CELLS.

Representative iCa^{2+} fluxes analysed in OCI-Ly7 cells following addition of anti-IgM (or control antibody). The first arrow shows time of addition of antibody following baseline data acquisition for 30 seconds. The second arrow shows time of addition of ionomycin as a positive control. *Top panel:* Untreated cells were stimulated with anti-IgM (blue) or control antibody (green), DMSO treated cells (red), and 10 μM R406 treated cells (orange) were stimulated with anti-IgM. *Middle panel:* Cells were pretreated for 1 hour with either 10 μM (blue), 1 μM (green), 100 nM (orange), 10 nM (turquoise), or 1 nM (pink) ibrutinib before anti-IgM stimulation and compared with the DMSO control (red). *Bottom panel:* Cells were pretreated for 1 hour with either 10 μM (blue), 1 μM (green), 100 nM (orange), 10 nM (turquoise), or 1 nM (pink) acalabrutinib before anti-IgM stimulation and compared with the DMSO control (red).

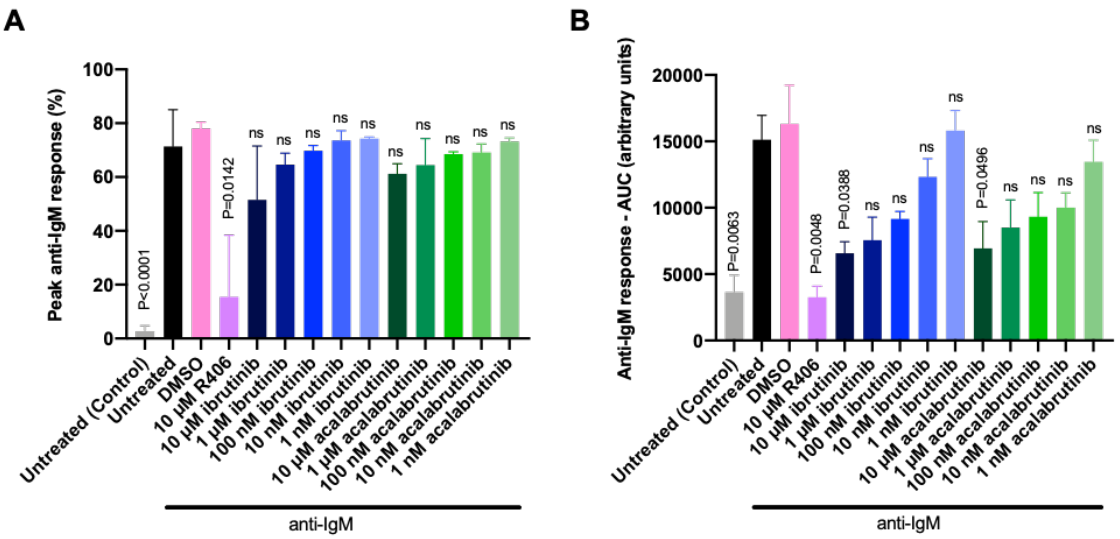

FIGURE 4-4: THE DOSE-RESPONSE EFFECT OF BTK INHIBITION ON ANTI-IGM-INDUCED iCa^{2+} MOBILIZATION IN OCI-LY7 CELLS.

Summary data of the peak percentage of cells responding to anti-IgM **(A)** and the area under the curve **(B)** measured using iCa^{2+} flux assay by flow cytometry is shown; bars represent the mean and standard deviation (n=3). Statistical significance of the difference between DMSO and each condition determined by paired t tests are indicated on the graphs.

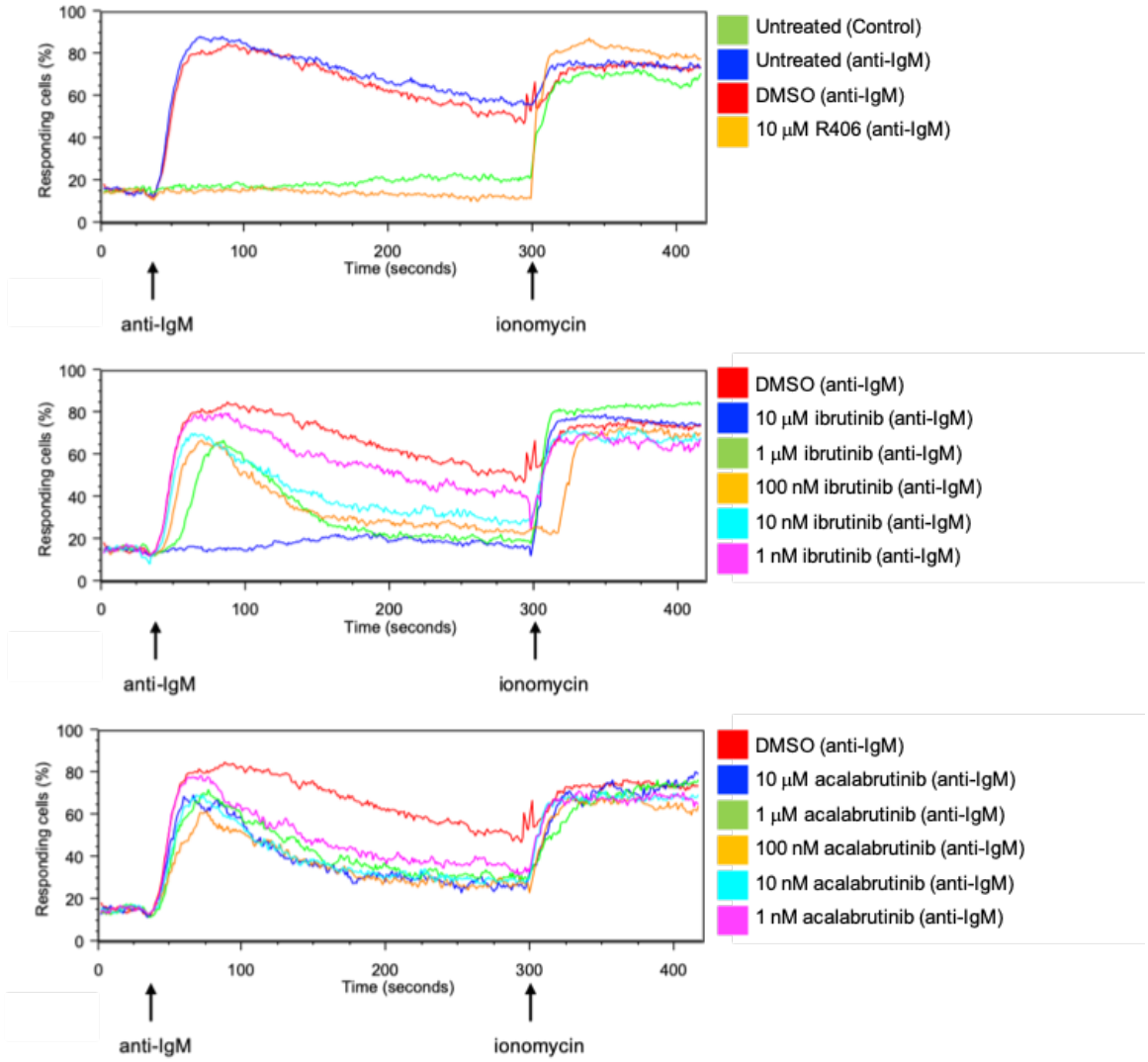

FIGURE 4-5: REPRESENTATIVE DOSE-RESPONSE EFFECT OF BTK INHIBITION ON ANTI-IGM-INDUCED iCa^{2+} MOBILIZATION IN TMD8 CELLS.

Representative iCa^{2+} fluxes analysed in TMD8 cells following addition of anti-IgM (or control antibody). The first arrow shows time of addition of antibody following baseline data acquisition for 30 seconds. The second arrow shows time of addition of ionomycin as a positive control. *Top panel:* Untreated cells were stimulated with anti-IgM (blue) or control antibody (green), DMSO only treated cells (red), and 10 μM R406 treated cells (orange) were stimulated with anti-IgM. *Middle panel:* Cells were pretreated with for 1 hour with either 10 μM (blue), 1 μM (green), 100 nM (orange), 10 nM (turquoise), or 1 nM (pink) ibrutinib before anti-IgM stimulation and compared with the DMSO control (red). *Bottom panel:* Cells were pretreated with for 1 hour with either 10 μM (blue), 1 μM (green), 100 nM (orange), 10 nM (turquoise), or 1 nM (pink) acalabrutinib before anti-IgM stimulation and compared with the DMSO control (red).

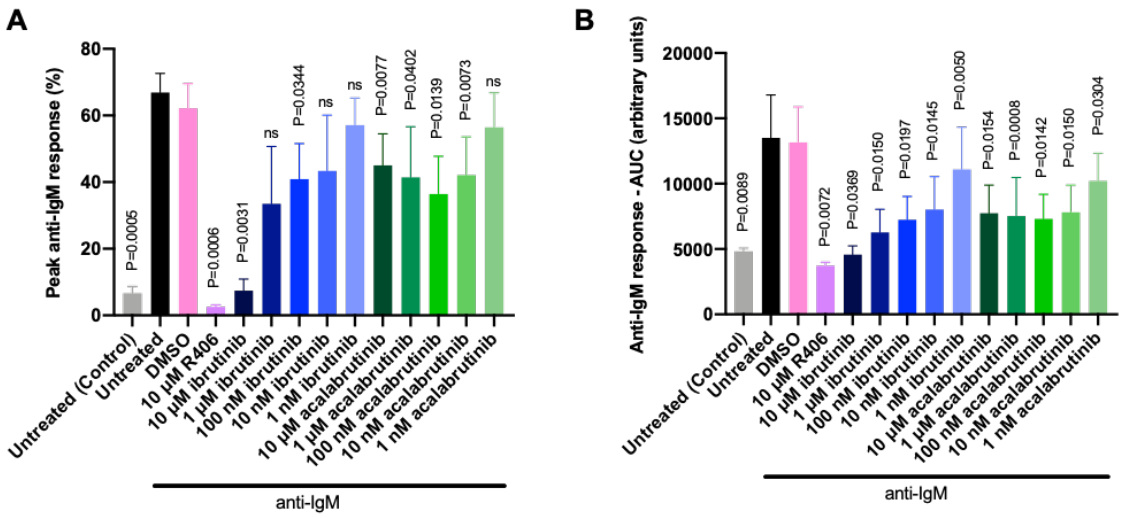

FIGURE 4-6: THE DOSE-RESPONSE EFFECT OF BTK INHIBITION ON ANTI-IGM-INDUCED iCa^{2+} MOBILIZATION IN TMD8 CELLS.

Summary data of the peak percentage of cells responding to anti-IgM **(A)** and the area under the curve **(B)** measured using iCa^{2+} flux assay by flow cytometry is shown; bars represent the mean and standard deviation (n=3). Statistical significance of the difference between DMSO and each condition determined by paired t tests are indicated on the graphs.

TABLE 4-2: SUMMARY OF THE EFFECT OF BTKI ON PEAK ANTI-IGM RESPONSE AND AUC IN PRIMARY CLL AND DLBCL CELL LINES.

Cell type	Ibrutinib		Acalabrutinib	
	Peak magnitude	Kinetics	Peak magnitude	Kinetics
Primary CLL	Full inhibition at 10 μM, but partial inhibition ≤1 μM; concentration-dependent.	No clear effect on kinetics of response.	Partial inhibition at all concentrations (10 nM > 1 nM). Maximal effect at 10 nM.	No clear effect on kinetics of response.
OCI-Ly7	Very little effect at 1 nM to 1 μM. Trend for stronger reduction in magnitude at 10 μM.	Concentration-dependent acceleration of the curtailment of response at 1 nM to 1 μM. Strong delay in timing of peak response at 10 μM.	Very little effect at any concentration.	Concentration dependent acceleration of the curtailment of response.
TMD8	Full inhibition with 10 μM, but partial inhibition with ≤1 μM; concentration-dependent.	Concentration-dependent acceleration of the curtailment of response at 1 nM to 1 μM.	Partial inhibition at all concentrations (10 nM > 1 nM). Maximal effect at 10 nM.	Concentration-dependent acceleration of the curtailment of response (10 nM > 1 nM). Maximal effect at 10 nM.

4.4 Identification of BTK-dependent and -independent phosphorylation events that may lead to iCa^{2+} mobilisation in DLBCL cell lines

The results from the **Chapter 3** comparing BTK inhibition by ibrutinib with BTK degradation by MT-802 (a BTK-specific PROTAC) suggests that "by-pass" is largely independent of BTK function *per se*, not just its kinase activity. PLCγ2 is a direct substrate for BTK-mediated phosphorylation and I therefore mapped the BTK-dependency of anti-IgM-induced PLCγ2 phosphorylation. The sites analysed were Tyr^{753}, Tyr^{759}, Tyr^{1197} and Tyr^{1217} within PLCγ2. In addition, I analysed phosphorylation of LYN (Tyr^{396} and Tyr^{507}), SYK ($Tyr^{525/526}$), BLNK (Tyr^{84} and Tyr^{96}), and BTK itself (Tyr^{223} and Tyr^{551}). I also investigated the phosphorylation of PLCγ1 (on Tyr^{783}), which is predominantly expressed in T cells, but is also expressed in B cells and has a similar catalytic activity to PLCγ2. Tyr^{783} in PLCγ1 is critical for its activation (Law et al., 1996). A large series of pilot experiments were performed (see **Supplementary Figure 2**) to select antibodies that were suitable for analysis of these BCR signalling responses. As above, BTKi were tested at a wide range of concentrations to allow analysis of concentration-dependent effects and directly compare effects on iCa^{2+} mobilisation as a downstream readout (**Figure 4-3** to **Figure 4-6**) and molecular effects on phosphorylation.

Cells were treated with 10 μM, 1 μM, 100 nM, 10 nM or 1 nM ibrutinib/acalabrutinib, 10 μM R406, DMSO, or left untreated for 1 hour prior to anti-IgM stimulation. The untreated sample was stimulated with either anti-IgM or control antibody, or left unstimulated as an additional control. The cells were stimulated with anti-IgM (or treated with control antibody) for 30 seconds. Neither drug affected total expression of any BCR-associated signalling molecule studied at any concentration (**Figure 4-7 - Figure 4-10**). I have presented cell line data first as strong BCR responses can be detected in these cells by immunoblotting, followed by results obtained with CLL samples which typically exhibit weaker signalling responses.

4.4.1 OCI-Ly7 cells

Figure 4-7 shows example immunoblots of OCI-Ly7 cells treated with decreasing concentrations of ibrutinib (*left panel*) and acalabrutinib (*right panel*) with the corresponding control conditions. Since the data is complex, results from multiple experiments were summarised using heatmaps (**Figure 4-8**), where each square represents the mean of 3 separate determinations. Values obtained for each phospho-protein were normalised to the total protein, and total protein was

normalised to GAPDH loading control. The value for DMSO is set to 1.0. In the heatmaps, the values assigned 1.0 were coloured purple, whereas a lower phosphorylation value (either in control antibody treated cells, or anti-IgM-treated cells pretreated with inhibitors) had values ≤1.0 and were coloured lighter shades of purple to white. Full densitometry data can be found in **Supplementary Figure 3 and 4**.

4.4.1.1 BTK phosphorylation

In evaluating the data, I first considered BTK Tyr^{223} autophosphorylation (located in the active site of BTK), since this would provide a direct measure of the concentration of BTKi required for BTK inhibition. There was a strong induction of anti-IgM-induced phosphorylation of Tyr^{223} (although in some experiments detection of basal phosphorylation was slightly increased), which was completely inhibited by R406 pretreatment (**Figure 4-8, Supplementary Figure 3 and 4**). Pretreatment with ≥10 nM of ibrutinib strongly inhibited phosphorylation of Tyr^{223}, whereas 1 nM ibrutinib had a less dramatic effect. Similar results were obtained for acalabrutinib, although overall, this drug was somewhat less effective compared to equimolar concentrations of ibrutinib in reducing BTK Tyr^{223} phosphorylation (**Figure 4-8, Supplementary Figure 4**). These concentration effects appear broadly in line with those observed in iCa^{2+} flux experiments (**Figure 4-4**) where 10 nM acalabrutinib effectively inhibited the response, and effects of 1 nM of either drug was partial.

There was also a strong induction of anti-IgM-induced phosphorylation of BTK Tyr^{551} (also with some experiments displaying increased detection of basal phosphorylation), which was completely inhibited by R406 pretreatment (**Figure 4-8, Supplementary Figure 3 and 4**). Phosphorylation of Tyr^{551} was unaffected by any concentration of ibrutinib or acalabrutinib ≤1 μM. Phosphorylation of Tyr^{551} was reduced by ibrutinib, but not acalabrutinib, at 10 μM (**Figure 4-8, Supplementary Figure 3 and 4**). Overall, BTK Tyr^{551} phosphorylation is relatively unaffected by BTKi, except at the very high concentrations of ibrutinib where off-target effects are likely to contribute.

4.4.1.2 Proximal phosphorylation events

The first kinase in the BCR-associated signalling pathway is LYN, which has two key phosphorylation sites: Tyr^{396} and Tyr^{507}. There was a strong induction of phosphorylation at both Tyr^{396} and Tyr^{507} following anti-IgM stimulation compared with the controls, and this induction

was completely inhibited following treatment with R406 (**Figure 4-8)**. Similar to BTK Tyr^{551}, phosphorylation of LYN at Tyr^{396} and Tyr^{507} was largely unaffected by any BTKi concentration. Importantly phosphorylation of LYN at Tyr^{396} and Tyr^{507} was unaffected by ibrutinib at 10 nM, a concencentration which is sufficient for effective BTK inhibition as determined by analysis of BTK autophosphorylation (**Figure 4-8, Supplementary Figure 3 and 4**).

The next kinase in the pathway is SYK, with an autophosphorylation site at Tyr$^{525/526}$. There is a very strong induction of anti-IgM induced phosphorylation at Tyr$^{525/526}$ compared with the controls and R406 completely inhibits all phosphorylation as expected (**Figure 4-8, Supplementary Figure 3 and 4)**. This proximal phosphorylation was unaffected by ibrutinib or acalabrutinib at concentrations up to 1 μM. At 10 μM, SYK phosphorylation was strongly inhibited by ibrutinib, and to a lesser extent, by acalabrutinib.

The adapter molecule BLNK is the next protein to become phosphorylated and activated in the signalling pathway and this has two key phosphorylation sites: Tyr^{84} and Tyr^{96}. A strong induction of anti-IgM-induced phosphorylation was observed at both of these sites and treatment with R406 completely inhibited all phosphorylation (**Figure 4-8, Supplementary Figure 3 and 4**). The effect of BTKi on BLNK phosphorylation at these sites was similar to results obtained with analysis of BTK Tyr^{551}, i.e. reduction only with ibrutinib (and not acalabrutinib) at 10 μM (**Figure 4-8, Supplementary Figure 3 and 4**).

Overall, this analysis shows that at concentrations of BTKi sufficient for effective BTK inhibition (10 nM), proximal phosphorylation of LYN, SYK and BLNK is relatively unaffected. However, at high concentrations (10 μM), ibrutinib (and to a lesser extent acalabrutinib), exerted broader inhibitory effects, likely due to off-target effects.

4.4.1.3 Distal phosphorylation events

The key effector molecule downstream of BTK is PLCγ2 with four major phosphorylation sites. There was clear induction of anti-IgM-induced phosphorylation at Tyr^{753}, Tyr^{759} and Tyr^{1217}, whereas induced phosphorylation at Tyr^{1197} was harder to reliably detect (**Supplementary Figure 3 and 4**). Induction of phosphorylation at all sites was effectively inhibited following pretreatment

with R406 (**Supplementary Figure 3 and 4**). Following 10 nM ibrutinib or acalabrutinib pretreatment, phosphorylation of Tyr^{1217} was strongly inhibited, whereas pretreatment with 1 nM had less effect (**Figure 4-8, Supplementary Figure 3 and 4**). By contrast, phosphorylation of PLCγ2 at Tyr^{753} and Tyr^{759} was completely unaffected by ibrutinib at 10 nM. Effects on Tyr^{1197} were harder to evaluate (due to low level of induction) but results for acalabrutinib indicated that phosphorylation at this site was susceptible to inhibition by BTKi at 10 nM. Like R406, high concentrations of ibrutinib, but not acalabrutinib (10 μM), inhibited induced phosphorylation at all four PLCγ2 sites, likely due to off-target effects. Overall, these results indicate that phosphorylation of PLCγ2 at Tyr^{753} and Tyr^{759}, but not $Tyr^{1197}$and Tyr^{1217}, is dependent on BTK in OCI-Ly7 cells.

Finally, strong anti-IgM-induced phosphorylation of PLCγ1 at Tyr^{783} was detected, which was completely inhibited by R406 pretreatment (**Figure 4-8**). PLCγ1 Tyr^{783} phosphorylation was partially reduced by ibrutinib and acalabrutinib at 10 nM (**Figure 4-8**), indicating that, like PLCγ2 Tyr^{753} and Tyr^{759} phosphorylation, may be at least partly dependent on BTK in OCI-Ly7 cells.

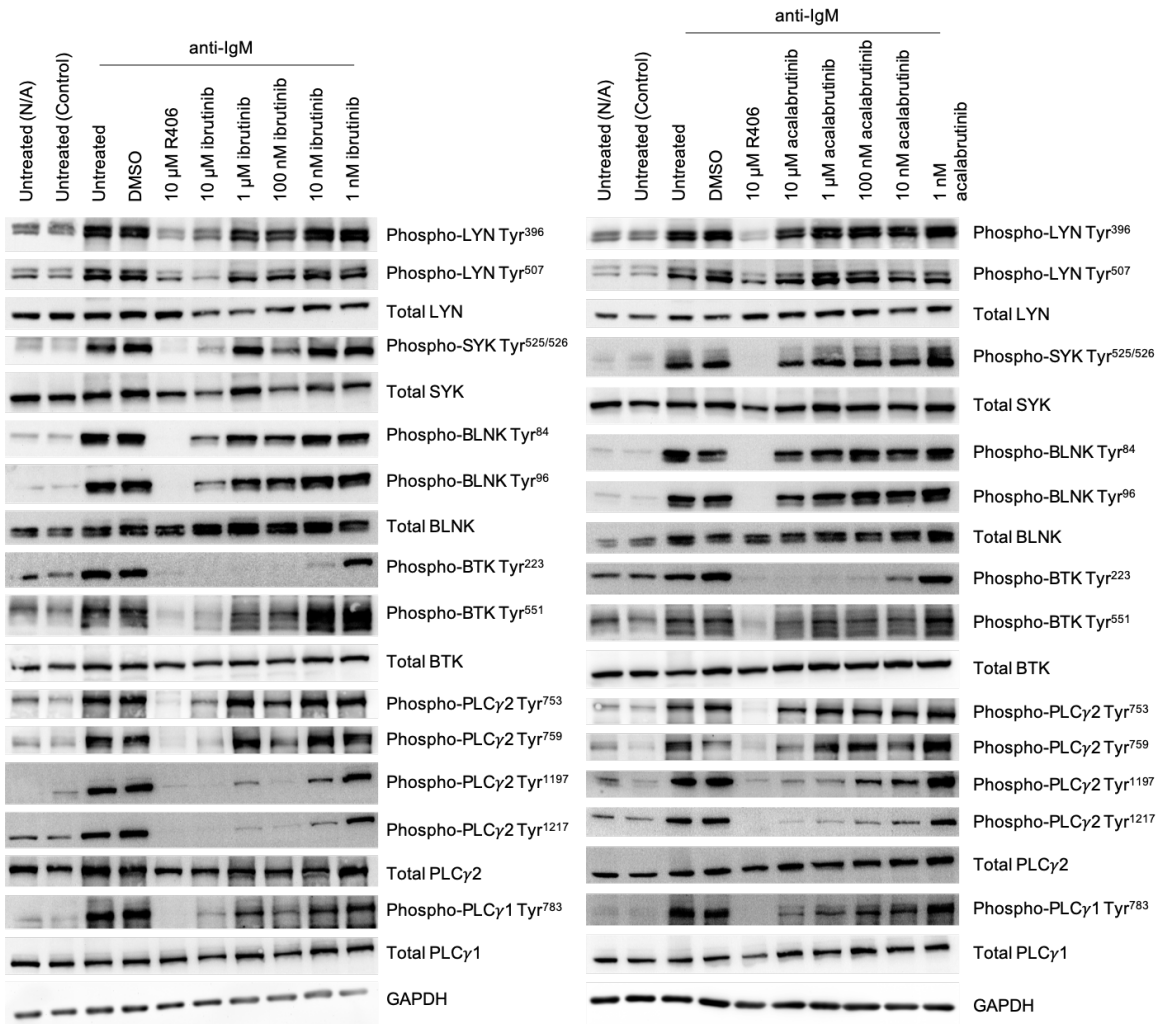

FIGURE 4-7: EFFECT OF BTK INHIBITION ON ANTI-IGM-INDUCED PHOSPHORYLATION OF BCR-ASSOCIATED SIGNALLING PROTEINS IN OCI-LY7 CELLS.

OCI-Ly7 cells were pretreated with 10 μM, 1 μM, 100 nM, 10 nM or 1 nM ibrutinib *(left panel)* or 10 μM, 1 μM, 100 nM, 10 nM or 1 nM acalabrutinib *(right panel),* 10 μM R406, DMSO (as a vehicle control), or left untreated as a control for 1 hour before treatment with anti-IgM or control antibody [Untreated (Control)]. As an additional control, some cells were left untreated for the duration of the experiment [Untreated (N/A)]. Cells were collected after 30 seconds of anti-IgM treatment and expression of phosphorylated and total proteins as indicated on the figure, along with GAPDH as a loading control, were analysed by immunoblotting. Figure shows an example immunoblot.

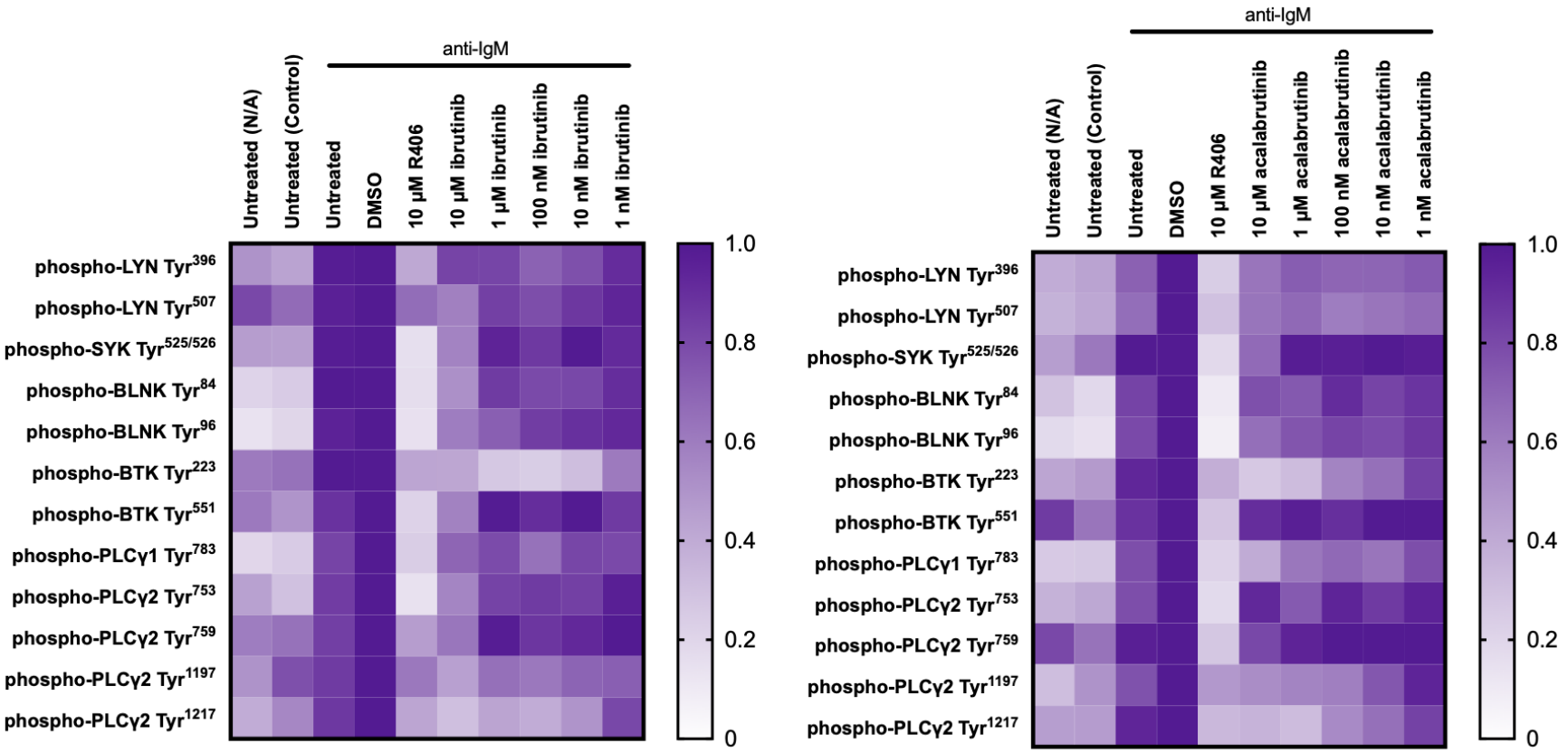

FIGURE 4-8: SUMMARY OF THE EFFECT OF BTK INHIBITION ON ANTI-IGM-INDUCED PHOSPHORYLATION OF BCR-ASSOCIATED SIGNALLING PROTEINS IN OCI-LY7 CELLS.

OCI-Ly7 cells were pretreated with 10 μM, 1 μM, 100 nM, 10 nM or 1 nM ibrutinib *(left panel)* or 10 μM, 1 μM, 100 nM, 10 nM or 1 nM acalabrutinib *(right panel),* 10 μM R406, DMSO (as a vehicle control), or left untreated as a control for 1 hour before treatment with anti-IgM or control antibody [Untreated (Control)]. As an additional control, some cells were left untreated for the duration of the experiment [Untreated (N/A)]. Cells were collected after 30 seconds of anti-IgM treatment and expression of phosphorylated and total proteins as indicated on the figure, along with GAPDH as a loading control, were analysed by immunoblotting. Figure shows quantification for all samples analysed, calculated as relative protein expression, with each square representing the mean of n=3. The values for the DMSO-treated cells are set to 1.0.

4.4.2 TMD8 cell line

A similar experiment was carried out using the TMD8 cell line. **Figure 4-9** shows example immunoblots of TMD8 cells treated with decreasing concentrations of ibrutinib (*left panel*) and acalabrutinib (*right panel*) with the corresponding control conditions. The results from multiple experiments were summarised using heatmaps (**Figure 4-10**), where each square represents the mean of 3 separate determinations. Values obtained for each phospho-protein were normalised to the total protein, and values for total protein were normalised to GAPDH loading control. The values for DMSO are set to 1.0. In the heatmaps, values of 1.0 were coloured purple, whereas lower phosphorylation values (either in control antibody treated cells, or anti-IgM-treated cells pretreated with inhibitors) were assigned values <1.0 and coloured ligher shades of purple to white. Full densitometry data can be found in **Supplementary Figure 5 and 6**.

4.4.2.1 BTK phosphorylation

Results obtained for analysis of BTK autophosphorylation in TMD8 cells were generally similar to those obtained for OCI-Ly7 cells. Thus, BTK phosphorylation at Tyr^{223} was effectively inhibited by 10 nM of either BTKi (**Figure 4-10, Supplementary Figure 5 and 6**). Results for Tyr^{551} phosphorylation were less clear as even the lowest concentrations of drug reduced phosphorylation to some extent (**Figure 4-10**). However, inhibitory effects of BTKi were not dose-dependent, and Tyr^{551} phosphorylation was relatively unaffected with 1 μM of drugs. Therefore, as for OCI-Ly7, Tyr^{551} phosphorylation appears to be relatively unaffected by BTKi, expect in cells treated with 10 μM ibrutinib (but not acalabrutinib), which reduced phosphorylation to a similar extent to R406 (**Figure 4-10**).

4.4.2.2 Proximal phosphorylation events

There was a modest induction of phosphorylation at Tyr^{396} of LYN following anti-IgM stimulation, however an induction in phosphorylation of Tyr^{507} was not observed since basal phosphorylation at this site remained high throughout. R406 did effectively reduce the modest increase in Tyr^{396} phosphorylation (**Figure 4-10**). Effects of BTKi were similar to OCI-Ly7 cells; LYN phosphorylation was relatively unaffected by either BTKi at 10 nM, and strong inhibition was only seen with high concentrations of ibrutinib, but not acalabrutinib (10 μM ibrutinib) (**Figure 4-10, Supplementary Figure 5 snd 6**).

Again, similarly to OCI-Ly7 cells, there was a very strong anti-IgM-induced phosphorylation of SYK $Tyr^{525/526}$ and BLNK Tyr^{84} and Tyr^{96}. These responses were inhibited by pretreatment with either R406 or 10 μM ibrutinib, but were generally unaffected by either BTKi (**Figure 4-10, Supplementary Figure 5 and 6**).

4.4.2.3 Distal phosphorylation events

A clear anti-IgM-induced phosphorylation of each of the four tyrosine residues within PLCγ2 (Tyr^{753}, Tyr^{759}, Tyr^{1197} and Tyr^{1217}) was observed (**Figure 4-10**). Similar to OCI-Ly7 cells, phosphorylation at Tyr^{753} and Tyr^{759} was relatively unaffected by acalabrutinib, whereas there was clear inhibition of PLCγ2 phosphorylation at Tyr^{1217} with this drug (**Figure 4-10, Supplementary Figure 6**). Results for PLCγ2 Tyr^{1197} were harder to evaluate, as inhibition by R406 was not observed consistently, suggesting that there were some technical limitations in evaluating phosphorylation at this site. However, for the representative experiment shown in **Figure 4-9**, where R406 was effective, in did appear that, like Tyr^{1217}, Tyr^{1197} phosphorylation was reduced by acalabrutinib, compared to DMSO-treated cells. Results for ibrutinib were also less clear than for OCI-Ly7 cells; partial inhibition was observed at all sites, although effective inhibition was only obtained with 10 μM drug (**Figure 4-10, Supplementary Figure 5**).

PLCγ1 was challenging to detect in TMD8 cells but anti-IgM-induced phosphorylation of Tyr^{783} was observed. This phosphorylation seemed relatively independent of BTK as it was only effectively inhibited by ibrutinib at 10 μM, or R406 (**Figure 4-10**).

Overall, results obtained for analysis of BCR-associated signalling molecules in TMD8 cells were similar to those obtained with OCI-Ly7 cells. Thus, at concentrations of BTKi sufficient for effective BTK inhibition (10 nM), proximal phosphorylation of LYN, SYK and BLNK is relatively unaffected. However, at higher concentrations, ibrutinib (and to a lesser extent acalabrutinib), can exert broader inhibitory effects, likely due to off-target effects. Results for phosphorylation of PLCγ2 were less clear for ibrutinib, but did confirm for acalabrutinib that phosphorylation at Tyr^{753} and Tyr^{759} were independent of BTK, whereas phosphorylation at Tyr^{1217} was BTK dependent.

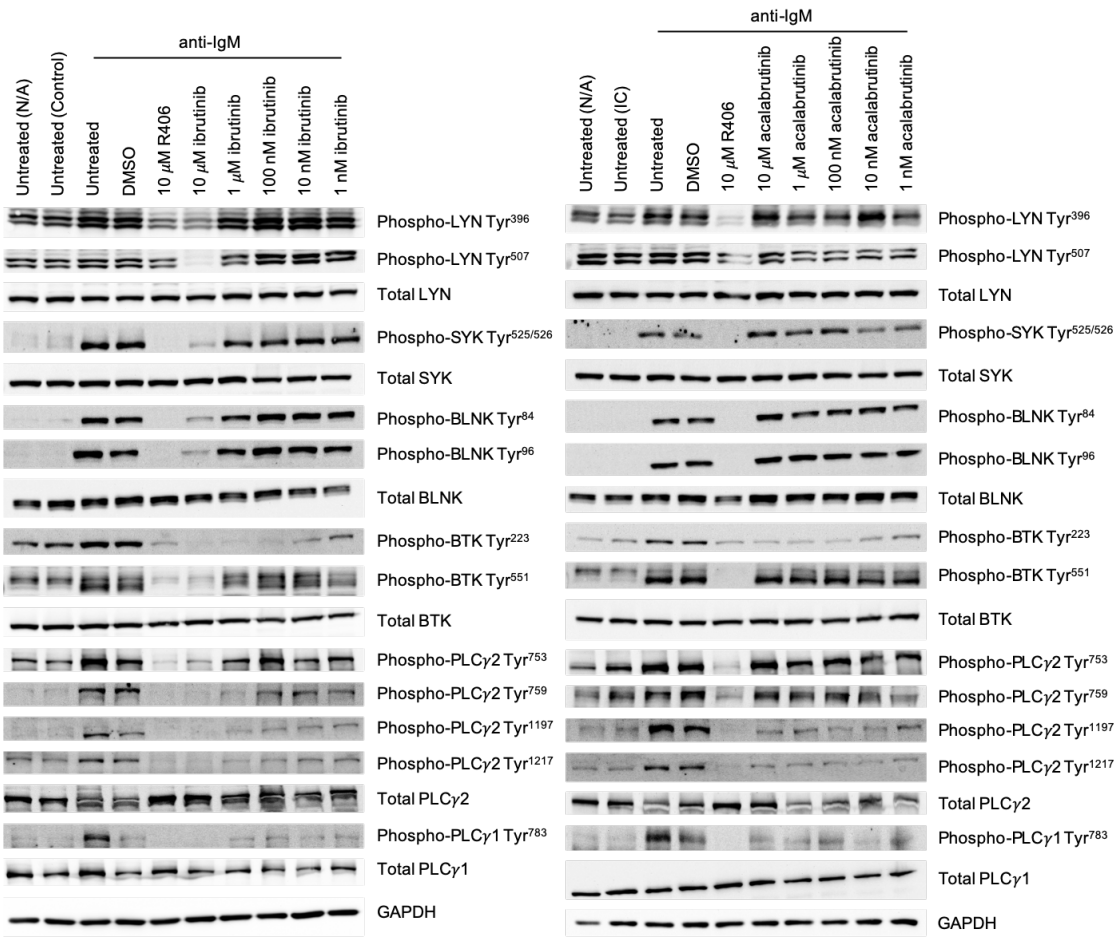

FIGURE 4-9: EFFECT OF BTK INHIBITION ON ANTI-IGM-INDUCED PHOSPHORYLATION OF BCR-ASSOCIATED SIGNALLING PROTEINS IN TMD8 CELLS.

TMD8 cells were pretreated with 10 μM, 1 μM, 100 nM, 10 nM or 1 nM ibrutinib *(left panel)* or 10 μM, 1 μM, 100 nM, 10 nM or 1 nM acalabrutinib *(right panel),* 10 μM R406, DMSO (as a vehicle control), or left untreated as a control for 1 hour before treatment with anti-IgM or control antibody [Untreated (Control)]. As an additional control, some cells were left untreated for the duration of the experiment [Untreated (N/A)]. Cells were collected after 30 seconds of anti-IgM treatment and expression of phosphorylated and total proteins as indicated on the figure, along with GAPDH as a loading control, were analysed by immunoblotting. Figure shows an example immunoblot.

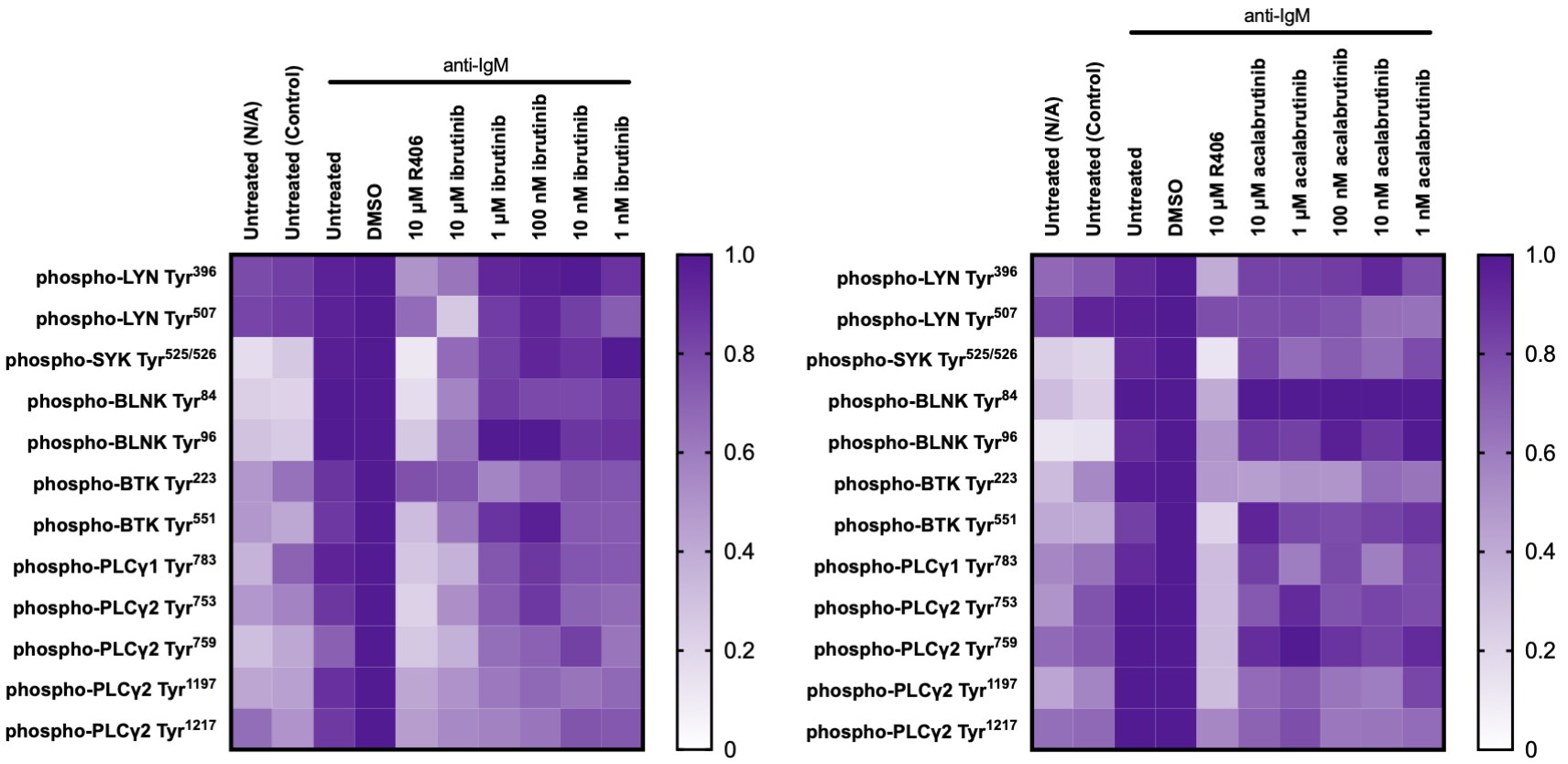

FIGURE 4-10: SUMMARY OF THE EFFECT OF BTK INHIBITION ON ANTI-IGM-INDUCED PHOSPHORYLATION OF BCR-ASSOCIATED SIGNALLING PROTEINS IN TMD8 CELLS.

TMD8 cells were pretreated with 10 μM, 1 μM, 100 nM, 10 nM or 1 nM ibrutinib *(left panel)* or 10 μM, 1 μM, 100 nM, 10 nM or 1 nM acalabrutinib *(right panel),* 10 μM R406, DMSO (as a vehicle control), or left untreated as a control for 1 hour before treatment with anti-IgM or control antibody [Untreated (Control)]. As an additional control, some cells were left untreated for the duration of the experiment [Untreated (N/A)]. Cells were collected after 30 seconds of anti-IgM treatment and expression of phosphorylated and total proteins as indicated on the figure, along with GAPDH as a loading control, were analysed by immunoblotting. Figure shows quantification for all samples analysed, calculated as relative protein expression, with each square representing the mean of n=3. The values for the DMSO-treated cells are set to 1.0.

4.5 Identification of BTK-dependent and -independent phosphorylation events that may lead to iCa^{2+} mobilisation in primary CLL

A similar analysis was carried out in primary CLL samples to identify BTK-dependent and -independent phosphorylation events. Three CLL samples were analysed in the first set of experiments. However, it was challenging to quantify changes in protein phosphorylation due to the overall low signalling response of CLL cells (Petlickovski et al., 2005). This was particularly true for low signallers, but it was important to be able to analyse a range of signalling capacities to investigate whether there was a difference in behaviour between low- and high-signallers. To address this, follow-on experiments were performed using samples exposed to IL-4 before BTKi treatment as IL-4 increases sIgM expression and strength of signalling responses, and reduces the effectiveness of ibrutinib treatment (Aguilar-Hernandez et al., 2016).

4.5.1 Primary CLL cells in the absence of IL-4

Figure 4-11 shows an example immunoblot of CLL 780A pretreated with different concentrations of ibrutinib or acalabrutinib before anti-IgM stimulation. A summary of the data, is shown in **Figure 4-12**, where each bar represents the mean and standard deviation of results obtained using three different samples. Each phospho-protein is normalised to the total protein and total protein is normalised to the GAPDH loading control. The values for DMSO are set to 1.0. Although I performed western blotting for the full panel of targets described above for cell lines, the data shown is for BTK and PLCγ2 phosphorylation events that were reliably detected in all three samples. Notably, it was very difficult to reliably detect PLCγ2 at Tyr^{1197} and Tyr^{1217} in these experiments.

Anti-IgM-induced autophosphorylation of BTK at Tyr^{223} was observed (although basal phosphorylation was readily detectable), and this was fully inhibited by R406 pretreatment. In general, both ibrutinib- and acalabrutinib-mediated inhibition reduced detection of Tyr^{223} phosphorylation at all concentrations tested (**Figure 4-12A**), but large variation was seen between experiments. Anti-IgM-induced phosphorylation of Tyr^{551} was also observed, which was also completely inhibited by R406 pretreatment. Surprisingly, both ibrutinib- and acalabrutinib-mediated inhibition statistically significantly reduced detection of Tyr^{551} phosphorylation irrespective of concentration (**Figure 4-12B**), with the exception of 1 nM ibrutinib which was not

sufficient to significantly reduce phosphorylation of Tyr^{551}. Notably, 100 nM and 1 μM acalabrutinib did not reach statistical significance but this is likely due to the variation between multiple experiments. The level of total BTK across all conditions remained consistent (**Figure 4-11**), although it appears that BTK was reduced following acalabrutinib treatment (**Supplementary Figure 7**), but this is likely to be a technical fault in the immunoblotting process caused by improper transfer of the proteins to nitrocellulose membrane.

Only two phosphorylation sites of PLCγ2 could be effectively analysed: Tyr^{753} and Tyr^{759}. The other two key sites (Tyr^{1197} and Tyr^{1217}) could not be detected robustly in these experiments. There was a strong induction of anti-IgM-induced phosphorylation of Tyr^{753}, which was completely inhibited by pretreatment with R406. Neither ibrutinib nor acalabrutinib inhibited phosphorylation of this site (**Figure 4-12C**), which is in agreement with the data collected from the DLBCL cell lines (i.e. BTK independence). There was also a strong induction of anti-IgM-induced phosphorylation of Tyr^{759} (although basal phosphorylation of this site was also readily detected), which was completely inhibited by R406 pretreatment. Ibrutinib pretreatment appears to fully block phosphorylation of this site (except at 1 nM) which is in contrast to the data collected from the cell lines, but acalabrutinib appears to have little effect on this site or cause only partial inhibition (**Figure 4-12D**). The level of total PLCγ2 across all conditions remained consistent (**Supplementary Figure 7**).

Overall, analysis of phosphorylation events by immunoblotting was challenging, due to low levels of response and/or high levels of basal phosphorylation in the absence of stimulation. However, it did seem clear that, similar to results from cell lines, anti-IgM-induced PLCγ2 Tyr^{753} phosphorylation was independent of BTK. As introduced above, follow-on experiments were performed by exposing CLL cells to IL-4 before stimulation, in an attempt to boost signal strength.

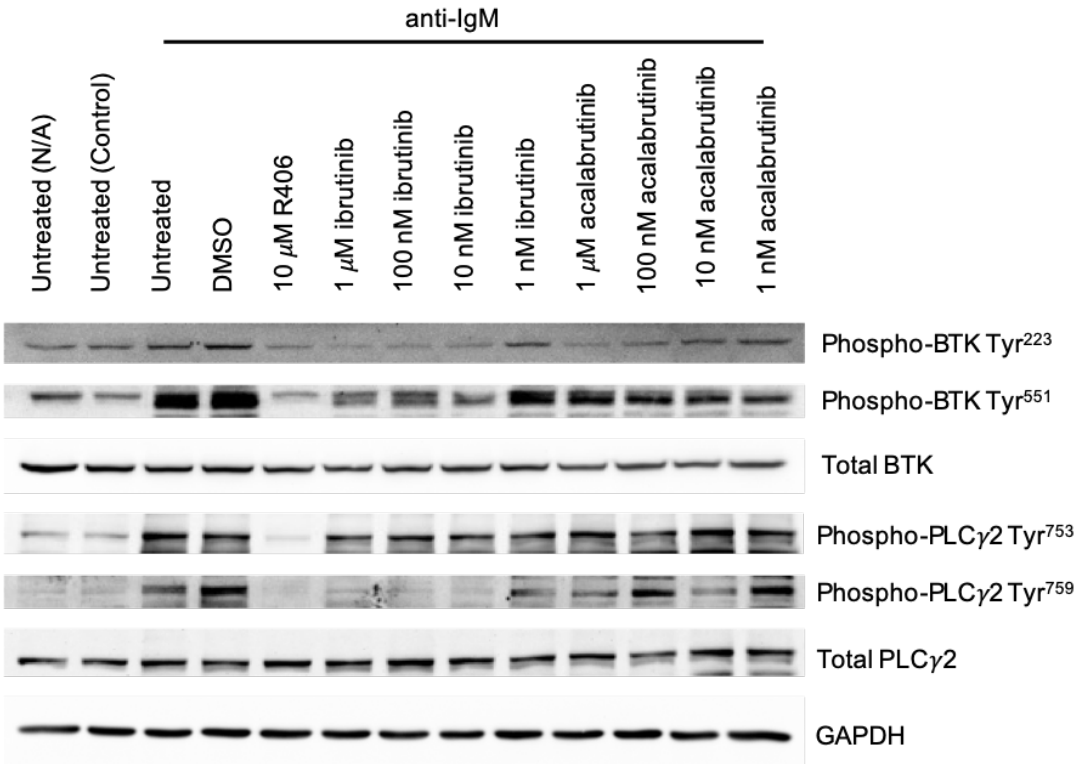

FIGURE 4-11: EFFECT OF BTK INHIBITION ON ANTI-IGM-INDUCED PHOSPHORYLATION OF BCR-ASSOCIATED SIGNALLING PROTEINS IN CLL 780A.

CLL samples were pretreated with 1 μM, 100 nM, 10 nM or 1 nM ibrutinib or 1 μM, 100 nM, 10 nM or 1 nM acalabrutinib, 10 μM R406, DMSO (as a vehicle control), or left untreated as a control for 1 hour before treatment with anti-IgM or control antibody [Untreated (Control)]. As an additional control, some cells were left untreated for the duration of the experiment [Untreated (N/A)]. Cells were collected after 30 seconds of anti-IgM treatment and expression of phosphorylated and total proteins as indicated on the figure, along with GAPDH as a loading control, were analysed by immunoblotting. Figure shows an example immunoblot for CLL780A.

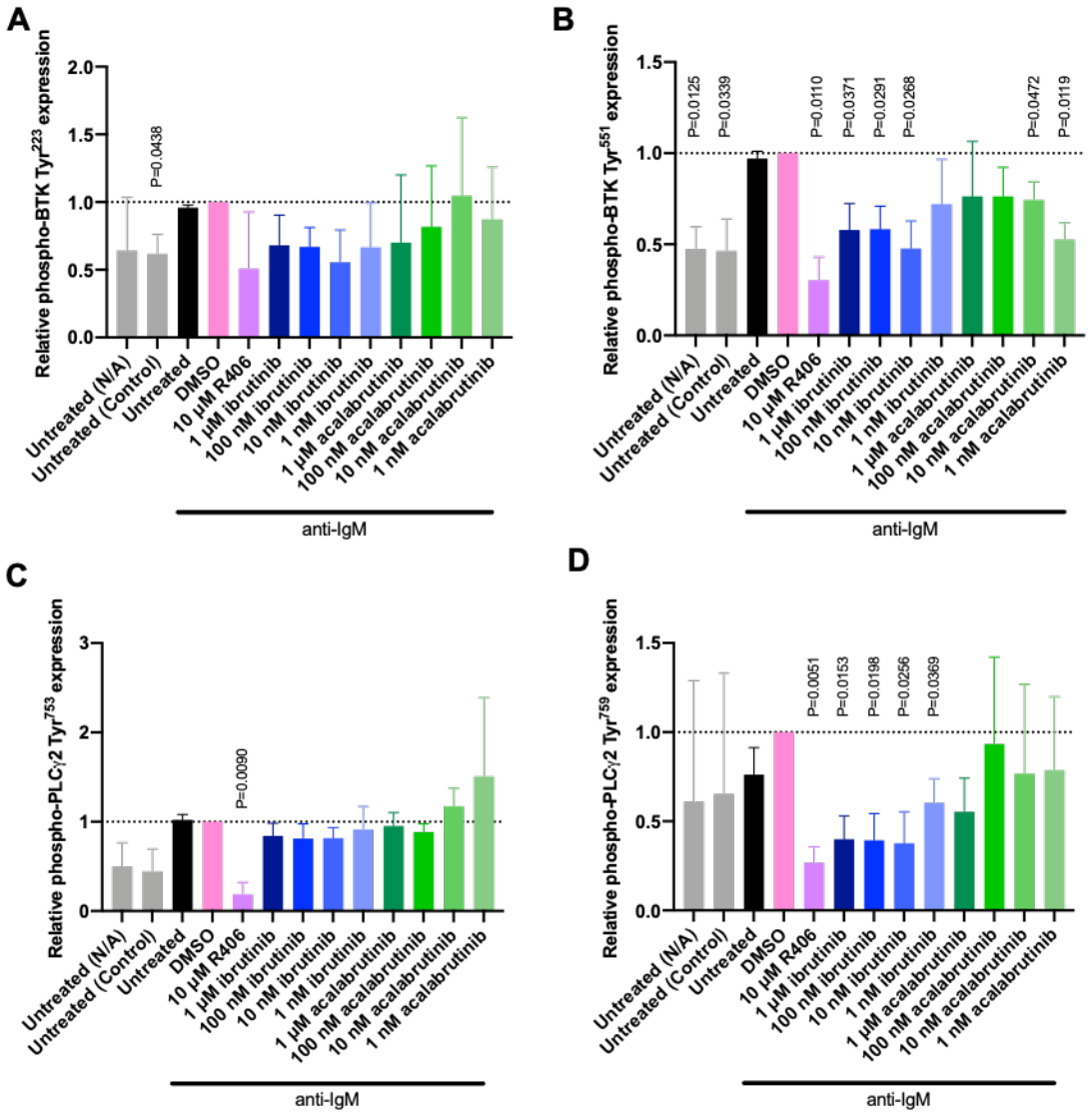

FIGURE 4-12: SUMMARY OF THE EFFECT OF BTK INHIBITION ON ANTI-IGM-INDUCED PHOSPHORYLATION OF BCR-ASSOCIATED SIGNALLING PROTEINS IN PRIMARY CLL SAMPLES.

CLL samples were pretreated with 1 μM, 100 nM, 10 nM or 1 nM ibrutinib or 1 μM, 100 nM, 10 nM or 1 nM acalabrutinib, 10 μM R406, DMSO (as a vehicle control), or left untreated as a control for 1 hour before treatment with anti-IgM or control antibody [Untreated (Control)]. As an additional control, some cells were left untreated for the duration of the experiment [Untreated (N/A)]. Cells were collected after 30 seconds of anti-IgM treatment and expression of phosphorylated and total proteins as indicated on the figure, along with GAPDH as a loading control, were analysed by immunoblotting. Figure shows quantification for all samples analysed, calculated as relative protein expression, with each bar representing the mean and standard deviation of n=3 . The mean for the DMSO-treated cells is set to 1.0. Statistical significance, determined by paired t test, of the difference between DMSO and each condition is indicated on the graph. Where no P value is provided the results were not significant.

4.5.2 Primary CLL in the presence of IL-4

4.5.2.1 Validation of IL-4 effect

For analysis of IL-4-exposed CLL samples, samples were cultured in the presence or absence of IL-4 for 24 hours (Aguilar-Hernandez et al., 2016). Before analysis of the downstream effect of BTK inhibition on activation/phosphorylation of other signalling molecules by immunoblotting, I characterised sIgM expression and analysed the effect on signalling and inhibitor responses using iCa^{2+} release, to confirm expected enhancing effects of IL-4 (Aguilar-Hernandez et al., 2016).

For analysis of sIgM, CLL samples were either left untreated or were treated with IL-4 for 24 hours before cell surface staining for CD19 and CD5, along with sIgM (or isotype control antibody). Cells were analysed by flow cytometry and the MFI of the sIgM stain of the $CD19^+$ $CD5^+$ cells was calculated (gating strategy in **Figure 2-3**). **Figure 4-13A** shows results for fourteen samples. IL-4 statistically significantly increased sIgM expression on CLL cells.

CLL samples that had either been left untreated or treated with IL-4 for 24 hours were also treated with 1 μM ibrutinib (concentration selected to directly replicate the experiment performed by Aguilar-Hernandez *et al*., 2016), DMSO alone (as a vehicle control), or left untreated for 1 hour at the end of the 24 hour incubation period prior to iCa^{2+} flux analysis. An example iCa^{2+} flux analysis using CLL 960A is shown **Figure 4-13B**. The top panel shows untreated cells being stimulated with either anti-IgM (blue) or control antibody (green) and DMSO treated cells stimulated with anti-IgM (red). The bottom panel shows DMSO treated cells stimulated with anti-IgM (red), ibrutinib-treated cells stimulated with anti-IgM (green), IL-4 stimulated cells treated with DMSO alone and stimulated with anti-IgM (blue) and IL-4 stimulated cells treated with ibrutinib and stimulated with anti-IgM (orange). This was carried out using nine CLL samples and the summary data showing peak percentage of responding cells is shown in **Figure 4-13C**. The data shows that IL-4 stimulation significantly increases anti-IgM-induced iCa^{2+} mobilisation in cells treated with DMSO alone and shows that ibrutinib is statistically significantly less effective in cells stimulated with IL-4.

These experiments used 1 μM ibrutinib, to directly replicate the work by Aguilar-Hernandez *et al*. (2016) however, I also tested the effect of 100 nM ibrutinib on IL-4 pretreated cells, as this is

sufficient for full BTK inhibition (shown above in **Figure 4-12**), along with the effect of MT-802 (BTK-specific PROTAC) (**Figure 4-14**).

Again CLL samples were either left untreated or were treated with IL-4 for 24 hours and either treated with 500 nM MT-802 or DMSO alone as a vehicle control for 4 hours, or 100 nM ibrutinib for 1 hour, or left untreated as an additional control prior to iCa^{2+} flux analysis. An example iCa^{2+} flux analysis using CLL 480 is shown in **Figure 4-14A** and the summary data for multiple experiments showing peak percentage of responding cells is shown in **Figure 4-14B**. The data again shows that IL-4 stimulation significantly increases anti-IgM-induced iCa^{2+} mobilisation in cells treated with DMSO alone and that treatment with 100 nM ibrutinib is significantly less effective in cells stimulated with IL-4. It also appears that MT-802 was less effective at inhibiting anti-IgM-induced iCa^{2+} flux following IL-4 pretreatment, however the difference did not reach statistical significance.

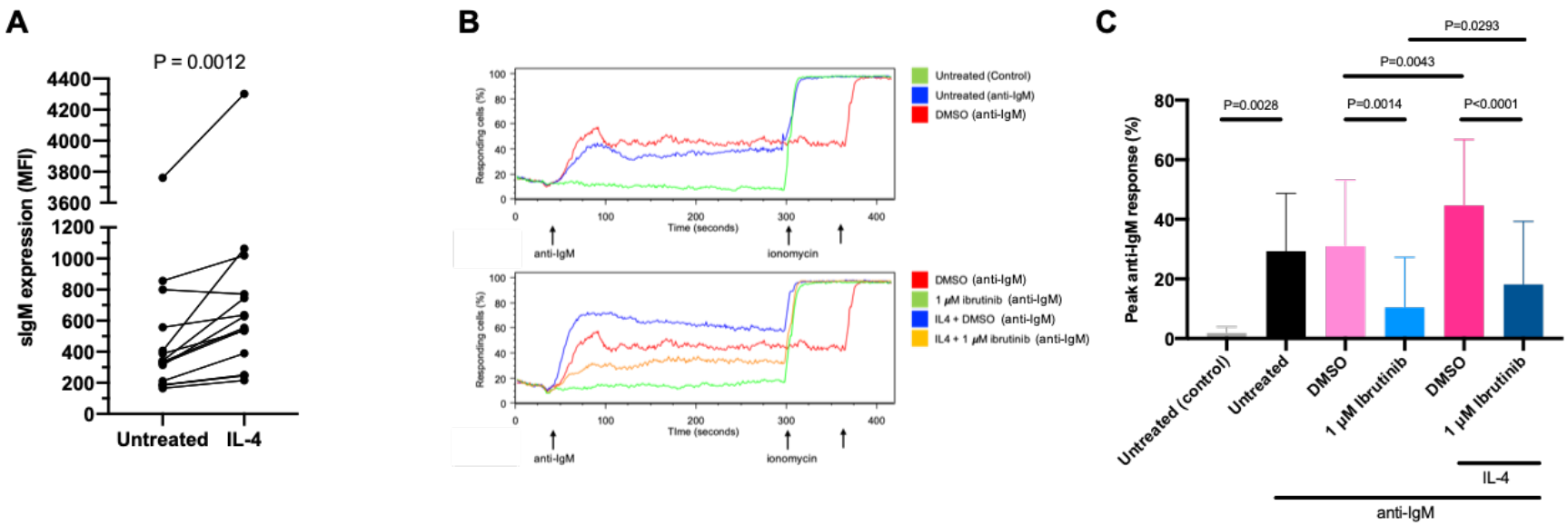

FIGURE 4-13: VALIDATION OF THE EFFECT OF IL-4 ON SURFACE IGM EXPRESSION AND iCA^{2+} FLUX IN PRIMARY CLL SAMPLES.

A. CLL samples (n=14) were treated with IL-4, or left untreated as a control, for 24 hours before sIgM expression (MFI) was analysed by flow cytometry. Statistical significance, calculated using a paired t test, is indicated on the graph. **B and C.** CLL samples were treated with IL-4, or left untreated, for 23 hours, and then treated with 1 μM ibrutinib or DMSO (as a vehicle control) for 1 hour before calcium indicator staining. Representative data for CLL 960A **(B)** shows *(top panel)* DMSO treated cells (red) stimulated with anti-IgM following 30 seconds of baseline data acquisition, with the addition of ionomycin at 360 seconds as a positive control, untreated cells stimulated with anti-IgM (blue), or control antibody (green), following 30 seconds of baseline data acquisition, with the addition of ionomycin at 300 seconds. The bottom panel shows cells pretreated with IL-4 (blue), 1 μM ibrutinib (green) or IL-4 and 1 μM ibrutinib (orange) prior to stimulation with anti-IgM following baseline data acquisition for 30 seconds compared with the DMSO control (red). Summary data **(C)** of the peak percentage of cells responding to anti-IgM is shown; bars represent mean and standard deviation (n=9) and statistical significance, determined by paired t tests, is indicated on the graphs.

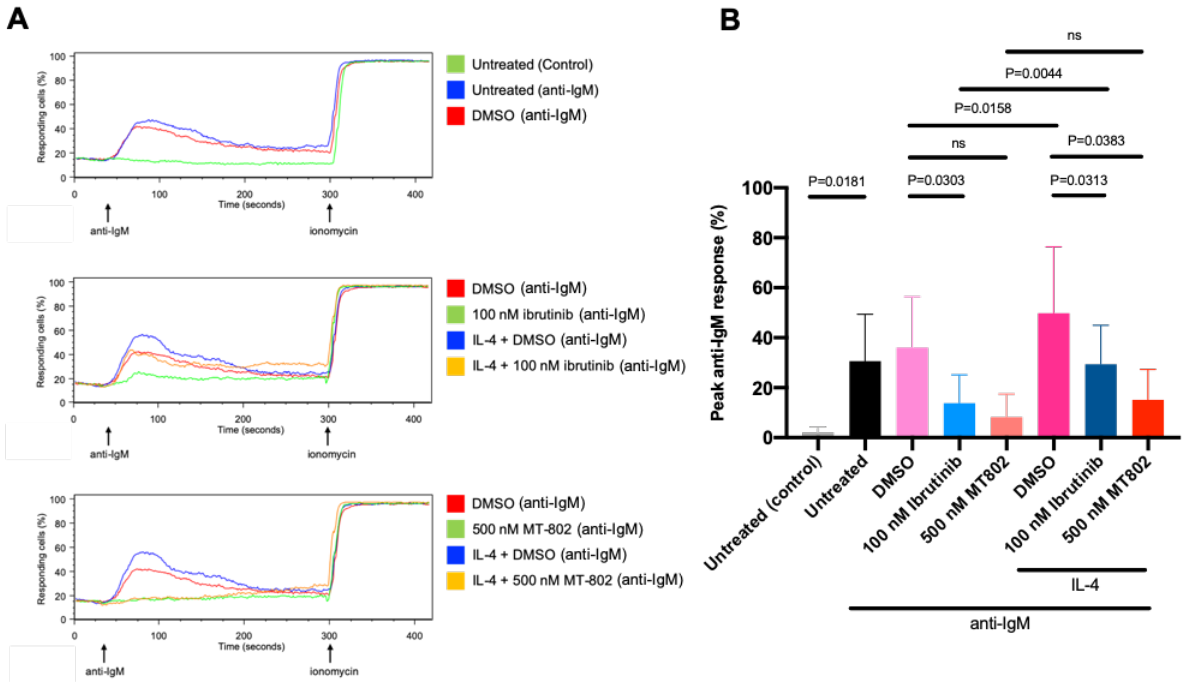

FIGURE 4-14: EFFECT OF IL-4 ON iCa^{2+} FLUX IN PRIMARY CLL SAMPLES PRETREATED WITH IBRUTINIB OR MT-802.

CLL samples were treated with IL-4 for 23 hours, or left untreated, and then treated with 100 nM ibrutinib, or DMSO (as a vehicle control) for 1 hour, or they were treated with IL-4 for 20 hours, or left untreated, and then treated with 500 nM MT-802, or DMSO (as a vehicle control) for 4 hours, before calcium indicator staining. Representative data for CLL 480 **(A)** shows *(top panel)* DMSO treated cells (red) stimulated with anti-IgM and untreated cells stimulated with anti-IgM (blue), or control antibody (green), following 30 seconds of baseline data acquisition, with the addition of ionomycin at 300 seconds as a positive control. The middle panel shows cells pretreated with IL-4 (blue), 100 nM ibrutinib (green) or IL-4 and 100 nM ibrutinib (orange) prior to stimulation with anti-IgM following baseline data acquisition for 30 seconds are compared with the DMSO control (red). The bottom panel shows cells pretreated with IL-4 (blue), 500 nM MT-802 (green) or IL-4 and 500 nM MT-802 (orange) prior to stimulation with anti-IgM following baseline data acquisition for 30 seconds compared with the DMSO control (red). Summary data **(B)** of the peak percentage of cells responding to anti-IgM is shown; bars represent mean and standard deviation (n=6; except for MT-802 where n=5) and statistical significance, determined by paired t tests, is indicated on the graph.

4.5.2.2 Effect of BTKi +/- IL-4

Having validated the effect of IL-4 stimulation in CLL, I next investigated the BCR-associated downstream signalling pathway in CLL samples stimulated with IL-4 to enhance signalling. CLL samples were either left untreated or were treated with IL-4 for 24 hours and were also treated with 500 nM MT-802 or DMSO (as a vehicle control) for 4 hours, or 100 nM, 10 nM, or 1 nM ibrutinib, 10 μM R406 or left untreated for 1 hour at the end of the 24 hour incubation prior to anti-IgM stimulation. The untreated sample was stimulated either with anti-IgM or control antibody for 30 seconds. Although it would have been preferable to include acalabrutinib in these experiments, I decided to focus on ibrutinib. This was due to the limited amount of primary material available for these experiments and including both drugs in the presence or absence of IL-4 would not be possible. I also did not test ibrutinib at 10 μM, since it was clearly inducing off-target effects at this concentration.

Figure 4-15 shows a representative immunoblot using CLL 960A, and the quantitation of multiple experiments is shown in **Figure 4-16.** The detection of total proteins remained constant between experiments and was unaffected by pretreatment of the cells, with the exception of BTK following MT-802 pretreatment, which was degraded as expected (**Supplementary Figure 8**).

A strong anti-IgM-induced phosphorylation of SYK at $Tyr^{525/526}$ was observed, and this was increased further (by ~40% on average) after IL-4 pretreatment, consistent with the increased iCa^{2+} flux detected in these cells (**Figure 4-16A**). R406 strongly inhibited SYK phosphorylation regardless of IL-4 treatment. Pretreatment with ibrutinib appeared to have no effect on the level of SYK phosphorylation, irrespective of IL-4 stimulation. MT-802 also had no effect on the level of SYK phosphorylation, as expected.

High basal (auto)phosphorylation of BTK at Tyr^{223} was detected in these samples and anti-IgM did not increase these levels (**Figure 4-16B**). Phospho-BTK Tyr^{223} was unaffected by any of the inhibitors. By contrast, there was a clear increase in detection of phospho-BTK Tyr^{551} following anti-IgM stimulation (**Figure 4-16C**). Phosphorylation at this site was largely unaffected by MT-802 and ibrutinib, but was effectively inhibited by R406.

Detection of phosphorylation of PLCγ2 at Tyr^{753} and Tyr^{759} did increase modestly following anti-IgM, and there seemed to be a further enhancement of Tyr^{759} phosphorylation in cells exposed to IL-4 (**Figure 4-16E and 4-16F**). However, in the presence or absence of IL-4, PLCγ2 phosphorylation at these sites was not inhibited by ibrutinib or MT-802, but was effectively inhibited by R406. There was no clear increase in phosphorylation of PLCγ2 at Tyr^{1217} (**Figure 4-16G**) (and Tyr^{1197} phosphorylation was not reliably detected despite addition of IL-4 to boost responses).

Phosphorylation of PLCγ1 at Tyr^{783} was also very challenging to detect in primary CLL despite the IL-4 stimulation (**Figure 4-16D**). The data suggest that there is no effect of ibrutinib or MT-802 on phosphorylation of this site irrespective of IL-4 stimulation.

In summary, despite the addition of IL-4 to boost signalling strength and engage a higher degree of "by-pass", analysis of phosphorylation events in CLL cells remained challenging, due to the overall low level of response and/or raised basal levels of phosphorylation. However, even this restricted analysis did support the conclusion from cell lines that anti-IgM-induced phosphorylation of PLCγ2 at Tyr^{753} and Tyr^{759} is independent of BTK as phosphorylation at these sites was not substantially reduced by either BTKi.

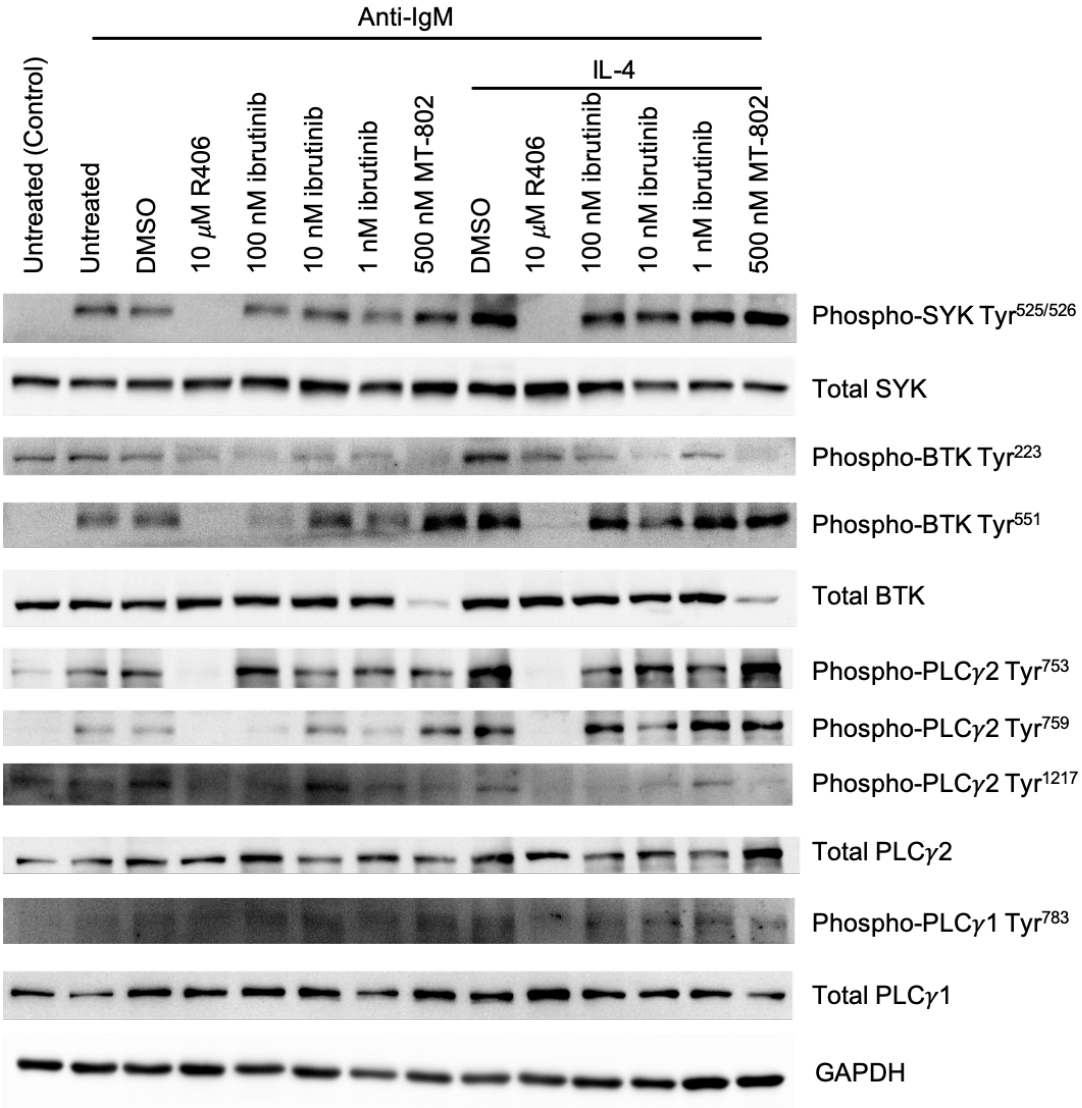

FIGURE 4-15: EFFECT OF BTK INHIBITION ON ANTI-IGM-INDUCED PHOSPHORYLATION OF BCR-ASSOCIATED SIGNALLING PROTEINS IN CLL 960A FOLLOWING IL-4 STIMULATION.

CLL samples were left untreated or treated with IL-4 for a total of 24 hours with the addition of 500 nM MT-802, or DMSO (as a vehicle control) for 4 hours, or with 100 nM, 10 nM or 1 nM ibrutinib, 10 μM R406, or left untreated as a control for 1 hour before treatment with anti-IgM or control antibody. Cells were collected after 30 seconds of anti-IgM (or control antibody) treatment and expression of phosphorylated and total proteins, as indicated on the figure, along with GAPDH as a loading control, were analysed by immunoblotting. Figure shows an example immunoblot for CLL 960A.

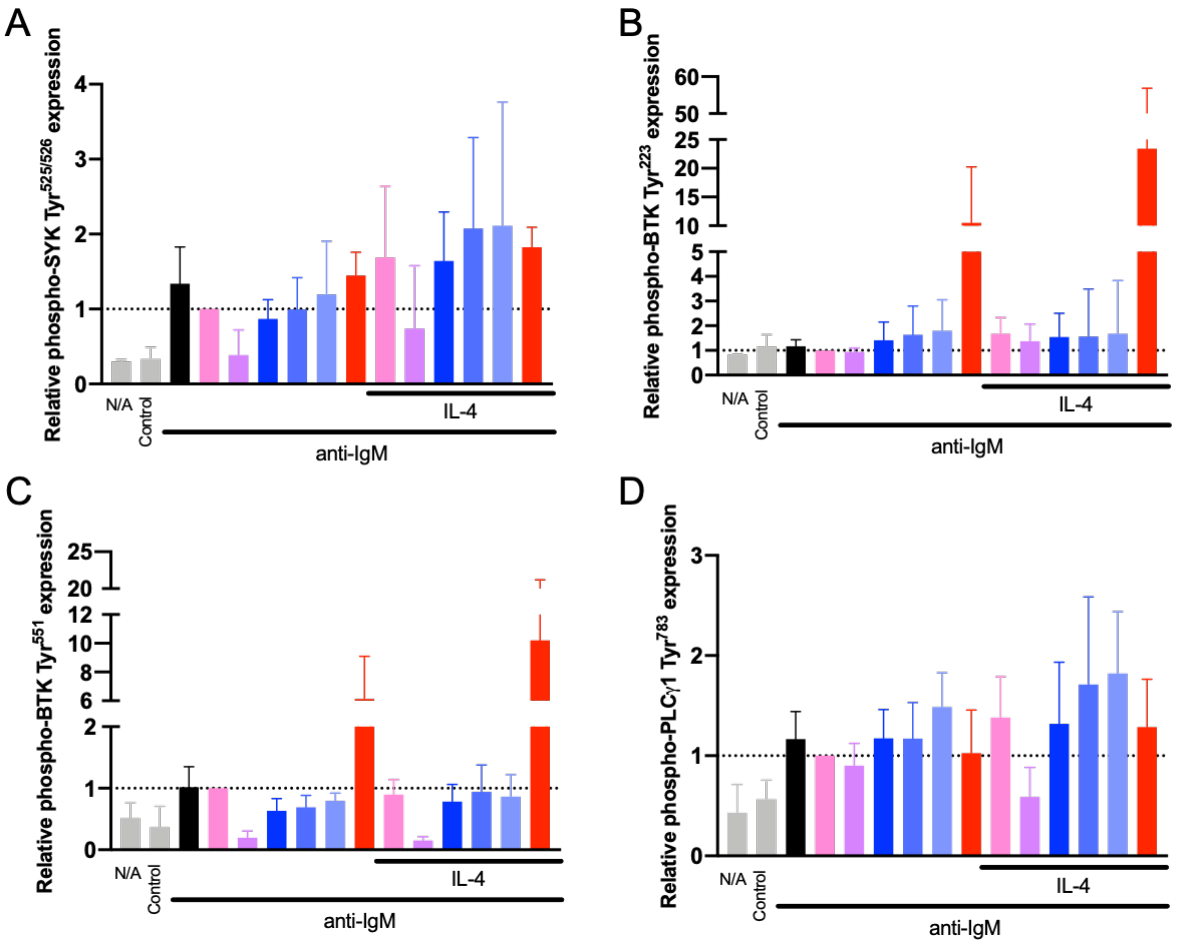
A
Relative phospho-SYK Tyr525/526 expression
0
1
2
3
4
N/A
Control
IL-4
anti-IgM
B
Relative phospho-BTK Tyr223 expression
0
1
2
3
4
5
10
15
20
25
50
60
N/A
Control
IL-4
anti-IgM
C
Relative phospho-BTK Tyr551 expression
0
1
2
6
8
10
12
20
25
N/A
Control
IL-4
anti-IgM
D
Relative phospho-PLCγ1 Tyr783 expression
0
1
2
3
N/A
Control
IL-4
anti-IgM

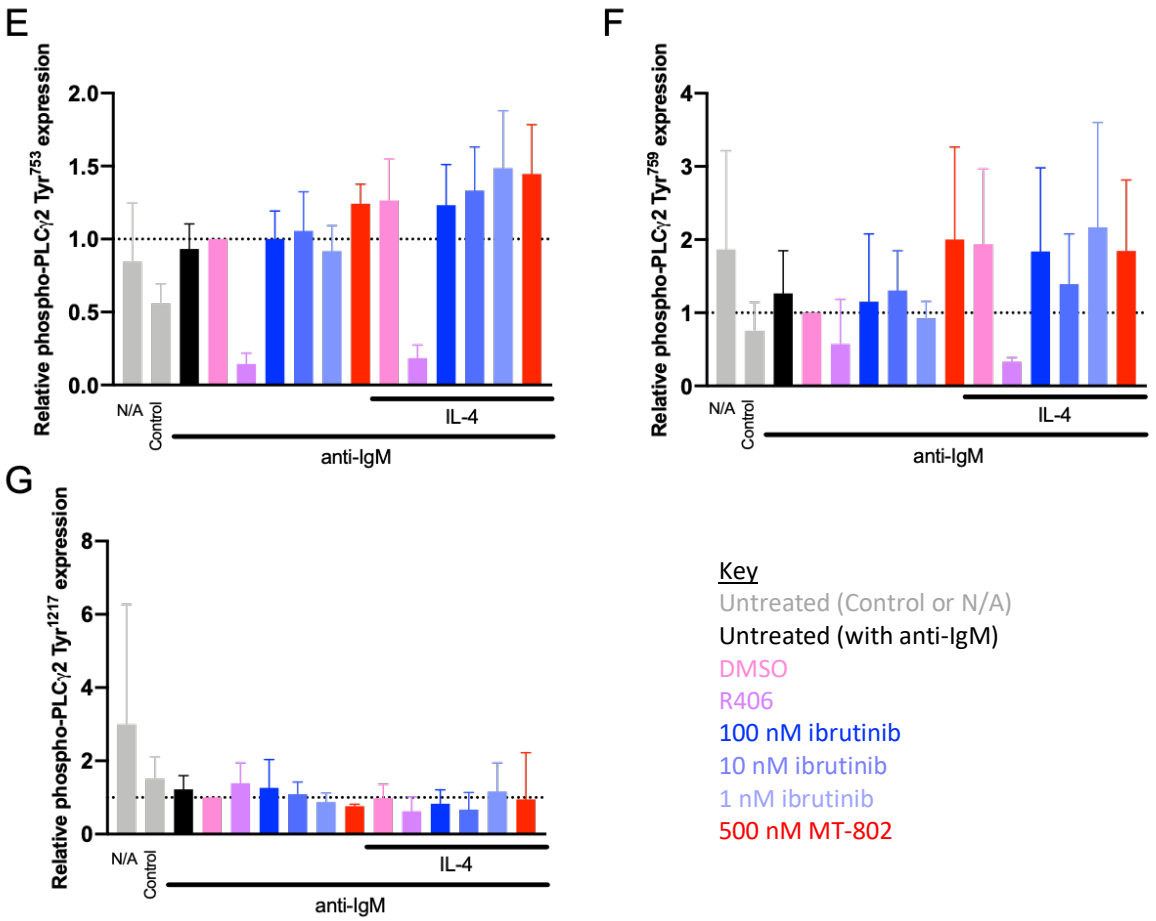

FIGURE 4-16: SUMMARY OF THE EFFECT OF BTK INHIBITION ON ANTI-IGM-INDUCED PHOSPHORYLATION OF BCR-ASSOCIATED SIGNALLING PROTEINS IN PRIMARY CLL SAMPLES FOLLOWING IL-4 STIMULATION.

CLL samples (n=5) were left untreated or treated with IL-4 for a total of 24 hours with the addition of 500 nM MT-802 (n=3), or DMSO for 4 hours, or with 100 nM, 10 nM or 1 nM ibrutinib, 10 μM R406, or left untreated as an additional control for 1 hour before treatment with anti-IgM or control antibody. Cells were collected after 30 seconds of anti-IgM (or control antibody) treatment and expression of phosphorylated and total proteins, along with GAPDH as a loading control, were analysed by immunoblotting. Figure shows quantification for all samples analysed, calculated as relative protein expression, with each bar representing the mean and standard deviation of n=5 (except MT-802 treated cells where n=3). The values for the DMSO-treated cells (without IL-4 pretreatment) are set to 1.0.

4.6 Analysis of the occupancy of the BTK active site by ibrutinib

As discussed previously (**Section 1.6**), ibrutinib has many off-target effects which are likely to contribute to some of the effects observed with this inhibitor in my experiments, especially at higher concentrations. This seemed particularly evident in my results where inhibition of kinases upstream of BTK (e.g. LYN and SYK) were inhibited following 10 μM ibrutinib pretreatment (**Figure 4-7 - Figure 4-10**). For any chemical compound it is clearly essential to relate variable biological effects to the degree of target engagement. In this chapter, this has been addressed indirectly by analysing effects of BTKi on the BTK autophosphorylation site (Tyr^{223}) as a readout of BTK inhibition. However, it was important to probe this further and I therefore also used a biochemical approach to directly investigate the degree of occupancy of the BTK active site by various concentrations of ibrutinib.

This analysis was performed using multi-inhibitor beads (MIB). Protein lysates were bound to the MIBs which, in this case, are beads coated with a low specificity kinase inhibitor (**Section 2.2.2**) capable of binding many kinases, including BTK (Zhang et al., 2013b). Immobilised small-molecule kinase inhibitors are one of the most efficient kinase-capture techniques because all protein kinases possess a highly conserved ATP binding pocket so ATP competitive kinase inhibitors can be designed to recognise a broad range of kinases (Zhang et al., 2013b). Therefore, this will be competitive with other kinases that bind the ATP binding pocket, for example ibrutinib (a class VI inhibitor that covalently binds the target protein in the ATP binding pocket (Roskoski (Jr.), 2016)). Unbound kinases are washed away and kinases which were retained by interaction on the MIBs are eluted and can be characterised by immunoblotting. However, if the kinase active site is blocked (e.g. in the case of BTK, by binding of ibrutinib) then the kinase will not be retained on the MIBs. Although used here primarily to study BTK, it is important to note that binding of many distinct kinases can be measured in this assay and some additional experiments were also performed to investigate the effect of ibrutinib on capture of additional BCR signalling kinases. The assay required a relatively large number of cells and beads so was performed using OCI-Ly7 cells and a restricted range of concentrations of ibrutinib. These experiments were performed at University of Liverpool with the assistance of Dr Adam Linley (University of Liverpool, UK).

4.6.1 BTK occupancy

OCI-Ly7 cells were treated with 50 nM or 5 nM ibrutinib or left untreated for 1 hour before stimulation with anti-IgM, or control antibody, for 30 seconds. Protein lysates were collected and bound to MIBs. Bound kinases where then eluted and analysed by immunoblotting.

Figure 4-17 shows a representative immunoblot for analysis of BTK protein and a quantitative summary for multiple experiments. BTK was readily captured in control cells and this was not substantially increased by anti-IgM stimulation, suggesting that, in OCI-Ly7 cells, BTK is constitutively present in an "open" conformation. Pretreatment with 50 nM ibrutinib very effectively reduced capture of BTK, demonstrating that 50 nM ibrutinib is sufficient to bind almost all BTK molecules. At 5 nM, the effects of ibrutinib were not significantly different from control, indicating that at this concentration, the majority of BTK active sites are not bound by drug. Although not directly comparable to the concentration of ibrutinib used in iCa^{2+} flux and western blot analysis (**Figure 4-3** and **Figure 4-7**), the results are consistent with the conclusion that 10 nM ibrutinib is sufficient for robust inhibition of BTK in cells.

I also investigated the phosphorylated status of the captured BTK in these experiments (**Supplementary Figure 9**). Phosphorylated BTK was challenging to reliably detect in these experiments; phospho-BTK Tyr^{223} was only detected in one experiment whereas phospho-BTK Tyr^{551} was detected in two experiments, but could not be quantified due to very low signal. It was possible to detect an increase in phosphorylation at Tyr^{223} (the autophosphorylation site) following anti-IgM stimulation. Interestingly, capture of Tyr^{223} phosphorylated BTK was decreased by both concentrations of ibrutinib. At 50 nM, this is presumably because capture of BTK *per se* was dramatically reduced by ibrutinib. However, it was surprising to observe a similar reduction in capture of Tyr^{223} phosphorylated BTK in cells treated with 5 nM ibrutinib, because this concentration of ibrutinib did not clearly reduce BTK binding (and therefore would not be expected to inhibit autophosphorylation).

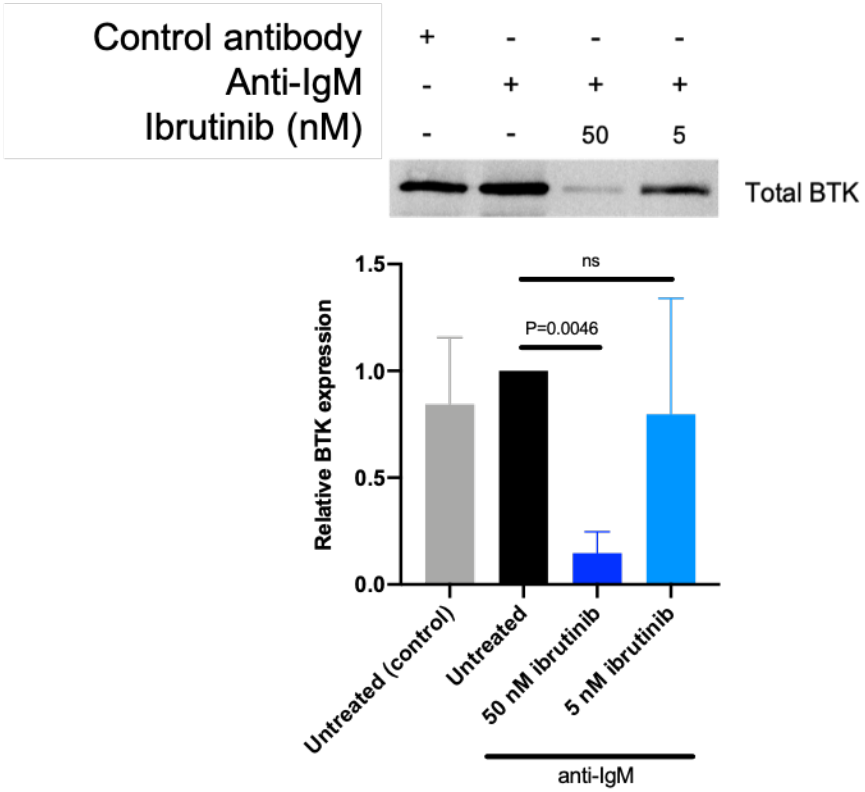

FIGURE 4-17: EFFECT OF IBRUTINIB TREATMENT ON THE OCCUPANCY OF THE BTK ACTIVE SITE.

OCI-Ly7 cells were pretreated with 50 nM or 5 nM ibrutinib or left untreated for 1 hour prior to treatment with anti-IgM or control antibody. Cells were collected after 30 seconds of anti-IgM treatment and protein lysates were passed through multi-inhibitor beads (MIBs) to capture kinases with available active sites. Bead-bound proteins were eluted and analysed by immunoblotting (representative immunoblot shown in *top panel*) and figure shows a summary of the quantification of relative BTK expression (*bottom panel*) with each bar representing the mean and standard deviation of n=3. The untreated cells stimulated with anti-IgM is set to 1.0. Statistical significance, determined by paired t tests, is indicated on the graph.

4.6.2 Analysis of additional kinases

An advantage of the MIBs assay is that any kinase present and retained by the beads can be analysed. Indeed, the assay is primarily used with proteomics for broad analysis of the kinome in cells and to investigate the effects of inhibitors (Médard et al., 2015; Golkowski et al., 2017). To extend my analysis, I probed the same eluates as **Figure 4-17** with antibodies against SYK and ERK to investigate their regulation by anti-IgM and ibrutinib (**Figure 4-18**). These proteins were much easier to detect in their phosphorylated forms than BTK.

Figure 4-18 shows a representative immunoblot (**Figure 4-18A**) with a quantitative summary for multiple experiments (**Figure 4-18B – 4-18E**). SYK and ERK were readily captured in control cells and binding was not substantially increased by anti-IgM stimulation (**Figure 4-18C and 4-18E**, respectively), suggesting that, in OCI-Ly7 cells, these kinases are constitutively present in an "open" conformation. This capture was also not significantly affected by either concentration of ibrutinib (**Figure 4-18C and 4-18E**). The apparent reduction in SYK following 5 nM ibrutinib pretreatment seen in the illustrative sample in **Figure 4-18A** was not consistently observed and is likely to be due to technical variation in this specific experiment.

I also investigated the phosphorylated status of the captured SYK and ERK in these experiments (**Figure 4-18B and 4-18D**, respectively). In contrast to BTK, these proteins were relatively easy to detect. There was a clear increase in capture of phosphorylated forms of SYK and ERK with anti-IgM stimulation, consistent with previous data which showed an increase in phosphorylation of these proteins upon anti-IgM stimulation when investigating the effect of ibrutinib pretreatment in OCI-Ly7 cells and primary CLL cells (**Figure 4-7** and **Figure 3-11**). This capture was not significantly affected by either concentration of ibrutinib (**Figure 4-18B and 4-18D**) and again, the apparent reduction in $Tyr^{525/526}$ phosphorylated SYK seen in the illustrative sample (**Figure 4-18A)** following 5 nM ibrutinib pretreatment was not consistently observed and likely to be due to technical variation. These results suggest that phosphorylation of SYK and ERK is independent of their kinase active site conformation.

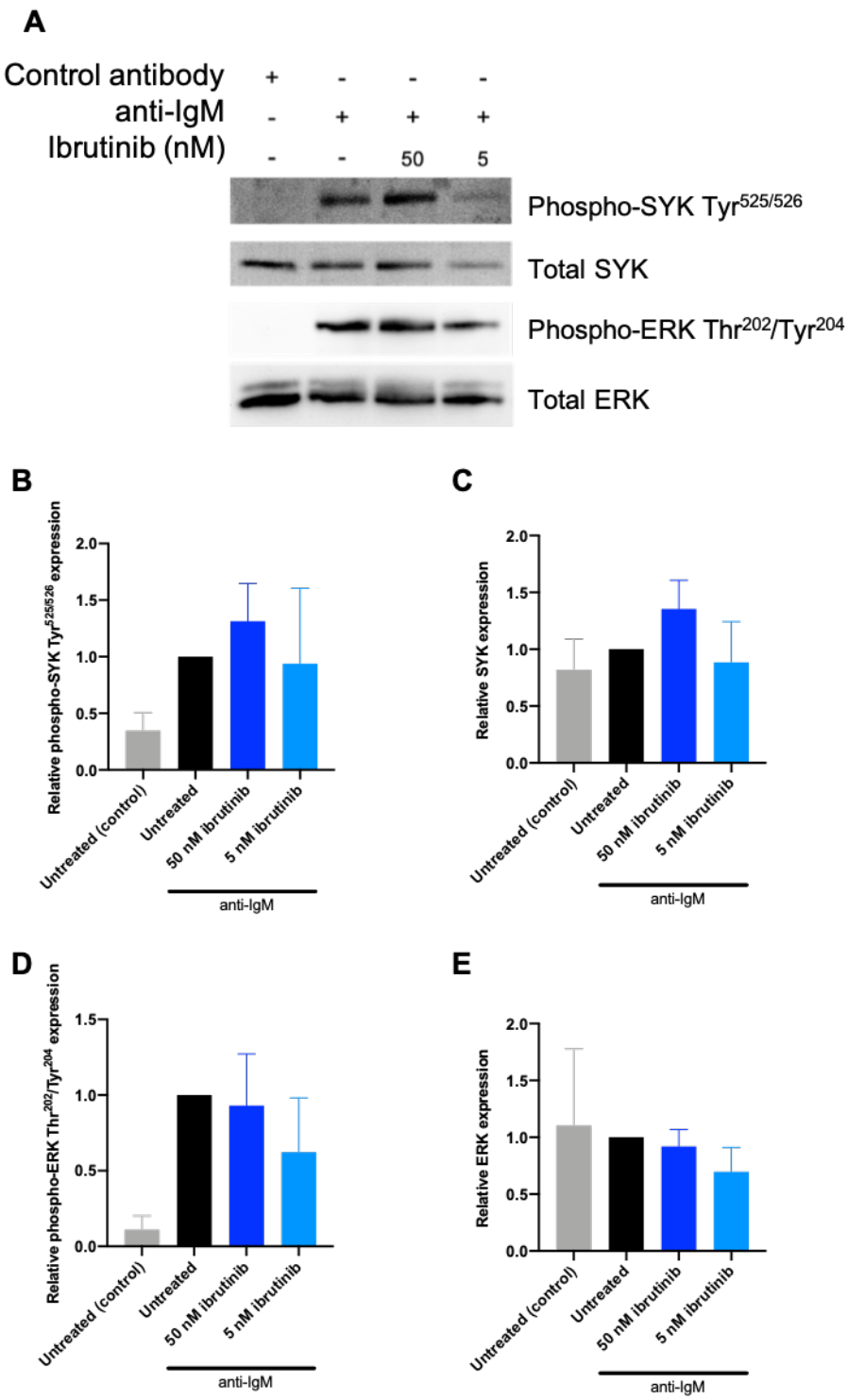

FIGURE 4-18: EFFECT OF IBRUTINIB TREATMENT ON THE OCCUPANCY OF OTHER BCR-ASSOCIATED KINASE ACTIVE SITES.

OCI-Ly7 cells were pretreated with 50 nM or 5 nM ibrutinib or left untreated for 1 hour prior to treatment with anti-IgM or control antibody. Cells were collected after 30 seconds of anti-IgM treatment and protein lysates were passed through multi-inhibitor beads (MIBs) to capture kinases with available active sites and the bead-bound fraction was eluted and collected. Protein expression was analysed by immunoblotting (representative immunoblot shown in **A**) and figure shows a summary of the quantification of relative protein expression **(B-E)** as indicated with each bar representing the mean and standard deviation of n=3. The untreated cells stimulated with anti-IgM is set to 1.0.

4.7 Discussion

The results shown in this chapter follow on from the studies described in **Chapter 3** that confirmed that ibrutinib/acalabrutinib-mediated BTK independence in some CLL samples, especially in samples termed "high signallers", along with DLBCL cell lines. This BTK-independence was not mediated by kinase independent functions of BTK, and therefore suggests it is linked to signalling. The overall goal of the results in this chapter was therefore to determine potential mechanisms of "by-pass" by investigating the hypothesis that BCR-associated kinases (independent of BTK) phosphorylate and activate PLCγ2, leading to iCa^{2+} mobilisation, "by-passing" the requirement for BTK. This was addressed by the following aims:

1. Identify BTK-dependent and -independent PLCγ2/PLCγ1 phosphorylation events that may lead to iCa^{2+} mobilisation in primary CLL and DLBCL cell lines.
2. Investigate the effect of enhanced signalling in CLL using IL-4, and the effect on BTK inhibition.
3. Investigate the concentration dependency of inhibition of BTK by assessing drug occupancy of the active site of BTK and western blotting to assess phosphorylation events within the BCR-associated signalling pathway.

Summary of main findings:

- Experiments using various concentrations of BTKi indicated that the maximal, on-target effect of ibrutinib/acalabrutinib on iCa^{2+} release was achieved with 10 nM drug, whereas 1 nM exerted less dramatic effects.
- Inhibitory effects of acalabrutinib were "saturated" at 10 nM, consistent with full BTK inhibition, as addition of higher concentrations of drug did not result in further inhibitory effects.
- Increasing the concentration of ibrutinib above 10 nM did result in additional inhibition (especially at 10 μM), although these effects are likely to be due to off-target effects.
- At 10 nM, ibrutinib/acalabrutinib, effectively inhibited anti-IgM-induced BTK autophosphorylation in CLL cells and DLBCL cell lines, but had little effect on BTK Tyr^{223} phosphorylation, or upstream phosphorylation of LYN, SYK and BLNK.

- Anti-IgM-induced PLCγ2 phosphorylation at Tyr^{753} and Tyr^{759} appeared to be largely independent of BTK, providing a potential molecular explanation for PLCγ2 activation despite BTK inhibition. This was evident in DLBCL cell lines and, for Tyr^{753}, in CLL cells in the presence or absence of IL4.
- Phosphorylation of the key site within PLCγ1 (Tyr^{783}) also appears to be at least partly BTK-independent.
- MIBs assay confirms that 50 nM ibrutinib is sufficient to fully block the active site of BTK in OCI-Ly7 cell line.

The results presented in this chapter suggest that a continued activation of PLCγ2 (associated with Tyr^{753} and Tyr^{759} phosphorylation), despite full BTK blockade, leading to continued Ca^{2+} release is a potential BTK "by-pass" mechanism. I speculate that PLCγ2 can be directly phosphorylated by SYK since pretreatment with R406 inhibits all downstream signalling responses.

4.7.1 Critical BTKi concentrations

A more detailed and thorough investigation of the response to a range of concentrations of ibrutinib and acalabrutinib to inhibit BTK was carried out to establish the concentration of drug required to fully block BTK. Although these drugs have an IC_{50} for BTK inhibition of ~1 nM in an *in vitro* kinase assay, it is likely that higher concentrations are required for BTK inhibition in cells. This was important to allow comparison of these *in vitro* results with drug concentration in patients receiving ibrutinib therapy, to understand the relevance and application of *in vitro* studies for patients. It is also important in differentiating possible alternate pathways leading to downstream effector function to validate BTK "by-pass" mechanisms. Although it was not possible to determine robust IC_{50} measurements from my data, it is possible to draw estimations of the concentrations required to inhibit the responses observed.

In primary CLL, the data suggests that concentrations of ~10 nM BTKi are sufficient to strongly inhibit the response for both the peak anti-IgM response (%) and AUC (**Figure 4-2**). In the cell lines, the predominant effect of BTKi was to accelerate the decline in iCa^{2+} after the peak, and again this effect was induced effectively by 10 nM BTKi. Intepretation of concentration effects was clearest for acaclabrutinib as its inhibitory effects (on the magnitude of the peak in CLL cells and on the rate of decline in cell lines) was maximal at 10 nM and not further increased by adding

additional drug. Increasing the concentration of ibrutinib did result in more profound inhibitory effects on iCa^{2+} release, but this seemed likely to be driven by off-target effects.

It is also important to understand how effects on iCa^{2+} compare links to the phosphorylation of BTK at Tyr^{223} (the autophosphorylation site) as a measure of BTK inhibition. Consistent with the Ca^{2+} flux data, immunoblotting suggested that 10 nM ibrutinib/acalabrutinib is sufficient to inhibit phosphorylation of BTK Tyr^{223} in both primary CLL and the DLBCL cell lines (**Figure 4-8** to **Figure 4-13**). In the cell lines, this inhibition was achieved by both ibrutinib and acalabrutinib without inhibiting upstream kinases or adaptor molecules suggesting that this concentration does not cause off-target effects.

Consistent with these inhibitor dose-response assays, data from the MIBs assay showed that 50 nM ibrutinib is sufficient to bind almost all BTK molecules with an available active site (**Figure 4-17**) without an impact on other BCR-associated kinases (**Figure 4-18**). Further analysis revealed that 50 nM ibrutinib blocked phosphorylation of Tyr^{223} of BTK but did not prevent phosphorylation of Tyr^{551} (**Supplementary Figure 9**). Phosphorylated BTK was very difficult to detect in these samples (with Tyr^{223} detectable in 1 experiment (of 3 repeats) and Tyr^{551} detectable in 2 experiments (of 3 repeats)) so robust conclusions cannot be drawn at this stage. Matched whole lysates were also analysed for two of these experiments, which show reduced detection of phospho-BTK at Tyr^{223} following 50 nM ibrutinib with no effect on phospho-BTK at Tyr^{551} (**Supplementary Figure 9**). Honigberg *et al*. (Honigberg et al., 2010) previously reported that 10 nM ibrutinib (using a fluorescently tagged derivative of ibrutinib) was sufficient to fully occupy the active site of healthy primary B cells *in vitro*. I therefore speculate that the method would allow conclusions to be drawn from whole lysates regarding the minimum concentration required for full BTK blockade based on phosphorylation of Tyr^{223} data, but further data is needed to support this. This evidence supports the conclusion of Honigberg et al. that suggests the concentration of ibrutinib required to bind BTK is well correlated with the inhibition of B-cell activation (Honigberg et al., 2010).

The results presented here are in line with concentrations of ibrutinib detected in treated patients, whereby a standard dose (420 mg/d) is equivalent to a mean intracellular concentration of ~20 nM ibrutinib (Chen et al., 2018). This is discussed further in **Section 6.4**.

4.7.2 BTK-independent PLCγ2 phosphorylation

The detailed investigation of the response to a range of concentrations of ibrutinib and acalabrutinib also provided information on the key downstream effector molecule of BTK within the iCa^{2+} release pathway; PLCγ2. In DLBCL cell lines, concentrations of ibrutinib/acalabrutinib sufficient to inhibit phosphorylation of BTK at Tyr^{223} (10 nM) was not sufficient to inhibit phosphorylation of PLCγ2 at Tyr^{753} and Tyr^{759}, whereas phosphorylation of Tyr^{1197} and Tyr^{1217} was substantially reduced or not detectable following pretreatment with >1 nM ibrutinib/acalabrutinib (**Figure 4-8** to **Figure 4-11**). Similarly, in primary CLL, phosphorylation of PLCγ2 at Tyr^{753} was detectable despite BTK inhibition, although it appears that phosphorylation of Tyr^{759} was inhibited in CLL samples, but this could be due to proteins being difficult to detect (**Figure 4-12** and **Figure 4-13**).

Interestingly, pretreatment with IL-4 did seem to increase phosphorylation of the BCR-associated signalling molecules including SYK, BTK and PLCγ2 Tyr^{759} (**Figure 4-15** and **Figure 4-16**). Enhanced sIgM expression and the subsequent increase in iCa^{2+} signalling through IL-4 pretreatment had been established previously (Aguilar-Hernandez et al., 2016) and was confirmed in my results (**Figure 4-13** and **Figure 4-14**). Aguilar-Hernandez *et al.* also showed that ibrutinib pretreatment was less effective in inhibiting the IL-4-enhanced iCa^{2+} signalling and this effect was also confirmed in my results (**Figure 4-13** and **Figure 4-14**). The investigation by Aguilar-Hernandez *et al*. did not extend to analysis of other BCR-associated signalling molecules but the results presented here show that phosphorylation of PLCγ2 Tyr^{759} was substantially increased following IL-4 pretreatment and that ibrutinib was not effective at reducing phosphorylation (**Figure 4-15** and **Figure 4-16**). This was less clear at Tyr^{1217}, since this site was more difficult to detect in CLL. However, the level of phosphorylation of downstream signalling molecules following pretreatment with R406 was unaffected by IL-4 pretreatment (**Figure 4-15** and **Figure 4-16**).

Taken together the data suggest that Tyr^{753} and Tyr^{759} are BTK-independent and Tyr^{1197} and Tyr^{1217} are largely BTK-dependent phosphorylation sites. This is an interesting finding as it remains unclear what the function of each phosphorylation site is, but specifically within the setting of BCR-associated signalling, this finding adds further evidence to the potential BTK "by-pass" mechanism operating through BTK-independent activation of PLCγ2. The similarity in results

between CLL and DLBCL cell lines suggest that these lines could be used as models for further detailed analyses in the future.

The dose-response experiments carried out show that BTK autophosphorylation (Tyr^{223}) is effectively blocked with ~10 nM ibrutinib/acalabrutinib but phosphorylation of Tyr^{753} and Tyr^{759} of PLCγ2 is still operational in the presence of 1000 nM ibrutinib/acalabrutinib. Therefore, it is possible to conclude that any kinases which is even >100-fold less potently inhibited by ibrutinib or acalabrutinib than BTK itself cannot participate in "by-pass" signalling (since we would expect these kinases to be inhibited with 1000 nM inhibitor where phosphorylation of Tyr^{753} and Tyr^{759} still occurs). There are a number of kinases (both receptors and soluble) along with growth factor receptors that can directly phosphorylate PLCγ1 and PLCγ2. These include epidermal growth factor receptor (EGFR) (Nishibe et al., 1990; Wahl et al., 1989) along with Src-family kinases (e.g. LYN, FYN, LCK and SRC), SYK and Tec-family kinases (e.g. BTK and ITK) (Law et al., 1996; Humphries et al., 2004; Rodriguez et al., 2001; Fluckiger et al., 1998).

In an extensive screening experiment Honigberg et al. (Honigberg et al., 2010) calculated the potency and selectivity of ibrutinib for BTK against a panel of other kinases; see **Table 4-3** for relevant kinases. Since my results have established that the kinase(s) responsible for the BTK-independent phosphorylation of PLCγ2 need to be >100-fold less sensitive to ibrutinib this rules out the majority of the candidates. Kinome screening also reduces the possible candidates by ruling out those not detected in CLL cells (e.g. ITK and EGFR) (Linley *et al*., 2020). Thus, SYK appears to be the most likely candidate for direct PLCγ2 phosphorylation and subsequent activation. This is supported by the data presented in this thesis which consistently shows that pretreatment with R406 (used as a positive control in this work) fully inhibits iCa^{2+} release and phosphorylation of all BCR-associated signalling molecules downstream of SYK (including SYK itself). However, it is not possible to conclude, based on these data obtained with R406 alone, whether SYK is directly acting on PLCγ2, or acts upstream of an unknown intermediate. Based on the relative potencies presented in **Table 4-3**, SRC could be considered as a candidate, but there is no known significant effect of SRC in the BCR-associated signalling pathway (Linlet *et al*., 2020).

Alternatively, phosphorylation-independent activation of PLCγ2 might, at least, contribute to the continued activation of iCa^{2+} mobilisation and the associated downstream effector functions through the SYK-dependent activation of Vav, a Rac2 activator that in turn activates PLCγ2

through direct protein-protein interactions (Piechulek et al., 2005). This is discussed further in **Section 6.3.**

TABLE 4-3: IC_{50} VALUES FOR INHIBITION OF ENZYMATIC ACTIVITY BY IBRUTINIB.

Kinase/Growth factor	IC_{50} (nM)	Relative potency compared to BTK
BTK	0.5	1
EGFR*	5.6	0.09
ITK*	10.7	0.05
LCK*	33	0.02
TEC*	78	0.006
FYN*	96	0.005
SRC	171	0.003
SYK	>10000	0.00005

Adapted from (Honigberg et al., 2010). Based on the observations that (i) ibrutinib inhibits BTK effectively in cells at a concentration of 10 nM (**Figure 4-7 - Figure 4-10**) and (ii) anti-IgM-induced PLCγ2 Tyr^{753} and Tyr^{759} phosphorylation is retained in cells treated with 1000 nM ibrutinib (**Figure 4-7 - Figure 4-10**), it seems likely that kinases with <100-fold reduced potency compared to BTK (marked *) can not contribute to BTK "by-pass" signalling.

Overall, these results suggest that a continued activation of PLCγ2, despite full BTK blockade, leading to continued Ca^{2+} release is a potential BTK "by-pass" mechanism. In the next chapter, I present experiments for the design and fabrication of a suitable device to analyse iCa^{2+} mobilisation in primary CLL samples.

Chapter Five

Results: Fabrication and development of microwell arrays for analysis of malignant B cells

5 Fabrication and development of microwell arrays for analysis of malignant B-cells

5.1 Introduction

A number of techniques suitable for analysing single cells have been described (Schiffenbauer et al., 2009; Junek et al., 2012; Rettig and Folch, 2005) with the most common and widely used method being flow cytometry. Flow cytometry offers many advantages including its high-throughput capability and bulk population analysis, however this also creates drawbacks since there is limited capacity for studying single cells over time. Microscopy can be used to overcome this limitation of flow cytometry, as described by Junek *et al*. (Junek et al., 2012), but this method is generally much more labour-intensive and time-consuming.

More recently, devices (e.g. microfluidic devices and microwell arrays) have gained popularity as valuable tools within biological and medical sciences and have a variety of applications, including the separation and subsequent study of single cells. These types of devices make it easier for studying rare cells and allow heterogeneous populations to be more fully described. Some of the key advantages of these devices over standard laboratory techniques are that the volumes of samples and reagents are much smaller leading to reduced cost, reduced waste and the ability to use smaller sample sizes. This is particularly beneficial for diseases where only small amounts of patient material can be acquired and where tumour cells are less readily available.

The devices used in this thesis are designed to “trap” single cells by sedimentation and are known as microwell arrays, which, when coupled to fluorescence microscopy, can be used to track iCa^{2+} responses over time in individual cells. The main advantages of using microwell arrays in this project is the potential to collect more information about the behaviour of “atypical” signalling and inhibitor responses which are likely formed by rare cells within the population. This is important because it is possible this could provide information on the likely clinical course, either disease progression or treatment resistance, that an individual experiences, whereby a small subset of malignant cells are able to evade treatment contributing to a disease-resistant subclone that promotes disease relapse or progression. Evidence that rare populations can alter clinical

disease course comes from p53 mutations, which can be present in infrequent subclones within the bulk CLL cell population but are still associated with poor prognosis (Dicker et al., 2009; Gonzalez et al., 2011; Rossi et al., 2009). It is not clear whether the same is true for signalling capacity but there is evidence of an association between signalling capacity and clinical outcome whereby "high-signallers" have a poorer median survival than "low-signallers" (D'Avola et al., 2016). This highlights the need for new technology which can overcome the limitations associated with flow cytometry to investigate single-cells to a greater depth and increase the sensitivity of the assay.

The microwell arrays used in this chapter are made from agarose, created in a soft lithography process (**Figure 2-5**), from a master silicon wafer which comprises features of various diameters to create microwell arrays with microwells with various diameters to allow the identification of the feature size most suitable for "trapping" CLL cells. Each slide analysed contains multiple arrays, but only one array is imaged and analysed per experiment. This allows one slide to be used for multiple repeats of an experiment, or to allow different conditions to be analysed i.e. one array can be analysed following anti-IgM addition and one can be analysed following ionomycin addition. Each array is "seeded" with cells, by pipetting a small volume of media containing cells on top of the array, which are allowed to settle into the microwells (**Figure 2-5**). The excess is carefully rinsed from the surface of the array before imaging can begin. Prior to cell seeding, the cells can be treated with inhibitors as required and be stained with dyes (e.g. general membrane stains or specific surface markers) and loaded with the Ca^{2+} indicator dye. Single images are captured to assess the occupancy of the microwell array and then a series of images are captured whereby a suitable exposure time is selected, along with an interval time, to acquire a set of images (which can be viewed as time course video) to observe the changes in fluorescence over time as cells are stimulated with ionomycin, anti-IgM or control antibody. The fluorescence intensity of each cell in each frame captured can be extracted to plot the fluorescence intensity over time of each cell trapped in the array.

As already mentioned, there are many advantages of using microwell arrays over standard flow cytometry for analysing iCa^{2+} mobilisation, but the technique still requires careful consideration and optimisation to ensure robust results can be obtained, these include: (i) potential issues with photobleaching of Ca^{2+} indicator dye over the time period that images are acquired (meaning that signal will be reduced due to continued light exposure, as opposed to being a biologically relevant signal), (ii) the method of ligand delivery to the cells in the array (preliminary experiments using

DLBCL cell lines showed that the best way to introduce ligand was by pipetting directly onto the array [**Supplementary Figure 11]),** and (iii) the time critical window in which the array can be used (since agarose will dry out when left exposed at room temperature). In addition, data analysis, carried out using Matlab, was conducted with scripts written by a previous PhD student (Anna Desalvo, PhD thesis) for similar work, and these required refining and editing for the purposes of this project.

5.2 Research goal and aims

The experiments in this chapter were designed to allow fabrication of a suitable device and optimisation of the device for use with primary CLL cells. The devices were then used to analyse iCa^{2+} mobilisation in primary CLL samples. As an additional aim, the experiments were also designed to investigate whether the method could be extended to other B-cell malignancies by using OCI-Ly7 cells.

This was addressed by 4 main aims:

1. Perform exploratory experiments using existing arrays to determine approximate suitable microwell sizes and proof of concept for data collection, including the comparison of Ca^{2+} indicator dyes.
2. Design and fabricate wafers with a range of microwell diameters and heights.
3. Identify optimal microwell size and cell seeding conditions for primary CLL samples.
4. Quantify single-cell anti-IgM-induced iCa^{2+} signalling responses (including pre-treatment with kinase inhibitors) in CLL samples.

5.3 Comparison of Ca^{2+} indicator dyes in primary CLL cells

Since cells will be imaged at multiple time points it was important to consider potential effects of photobleaching where fluorescence intensity of the dyes decreases due to multiple, or continuous, exposure to light, rather than reflecting a biological effect. This can be minimised by using more sensitive and brighter dyes allowing the exposure time to be reduced. To address this, I compared cells stained with Fluo-3 AM and Fluo-8 AM, a newer, brighter Ca^{2+}-responsive probe. The microwell arrays used for these experiments were produced from wafers already available in

the laboratory, designed and fabricated by Anna Desalvo (University of Southampton, UK). The microwells had a diameter of 12 μm and a depth of 18 μm.

Primary CLL cells were stained with either Fluo-3 AM or Fluo-8 AM, as described in **Section 2.3.2 or 2.4.4**, and seeded in the microwell arrays before addition of ionomycin (**Figure 5-1**). Baseline data was acquired for approximately 30 seconds before 10 μl of ionomycin solution was pipetted onto the surface of the array and data was acquired for a further 90 seconds. A concentration of 1 μM ionomycin was selected to replicate the conditions used for flow cytometry, and a volume of 10 μl was chosen as this is sufficient to cover the section of the array being imaged, without flooding the whole surface of the array. This therefore protects cells in neighbouring arrays from being stimulated so they can be used for other analysis. Images of Fluo-3 AM stained cells (**Figure 5-1A and 5-1B**) were captured with an exposure time of 2 seconds and images of Fluo-8 AM stained cells (**Figure 5-1D and 5-1E**) were captured with an exposure time of 1 second.

Figure 5-1A and 5-1D show baseline fluorescence of Fluo-3 AM stained cells and Fluo-8 AM stained cells, respectively, and **Figure 5-1B and 5-1E** show a representative frame (at 40 seconds) following ionomycin addition in Fluo-3 AM stained cells and Fluo-8 AM stained cells, respectively. **Figure 5-1C and 5-1F** show the MFI over time for each individual cell detected (top graph of each pair) along with the average fluorescence (and standard deviation) of the population of cells (bottom graph of each pair). The average fluorescence of cells stained with Fluo-3 AM is higher than in those stained with Fluo-8 AM following ionomycin addition, but the standard deviation of those stained with Fluo-8 AM is smaller. However, baseline fluorescence was more readily detected in cells stained with Fluo-8 AM, even though exposure time was halved compared to Fluo-3 AM stained cells. Analysis of OCI-Ly7 cells confirmed that Fluo-8 AM was also suitable for microwell array analysis of iCa^{2+} responses in cell lines (**Supplementary Figure 12**). Therefore, the Fluo-8 AM Ca^{2+} indicator dye was selected for all future experiments.

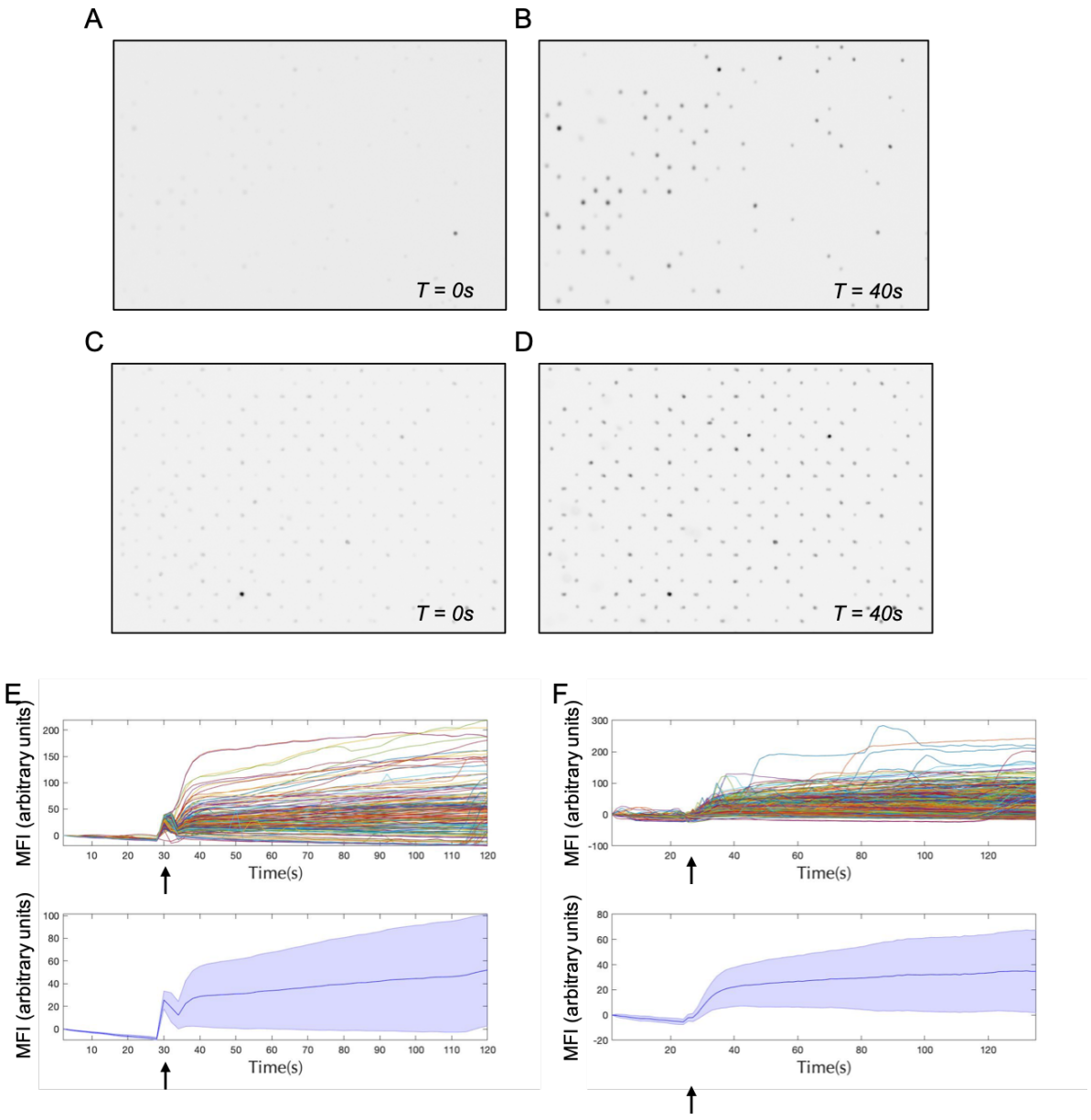

FIGURE 5-1: COMPARISON OF CALCIUM INDICATOR DYES IN CLL CELLS.

CLL cells were stained with Fluo-3 AM **(A and B)** or Fluo-8 AM **(C and D)** prior to cell seeding into the microwell array. Baseline data was captured for approximately 30 seconds before the addition of ionomycin. **A and C** show baseline images. **B and D** show images captured at 40 seconds, post ionomycin addition. The top panel of **E and F** show the fluorescence over time of single cells, stained with Fluo-3 AM (E) or Fluo-8 AM (F). The bottom panels shows the mean and standard deviation MFI of the cell population. The arrows on the graphs indicate the time of ionomycin addition. Fluo-3 AM stained cells were imaged at 2 s intervals for 120 seconds with an exposure time of 2 s. Fluo-8 AM stained cells were imaged at 1.5 s intervals for 135 seconds with an exposure time of 1 s.

5.4 Preliminary Ca^{2+} mobilisation data acquisition in primary CLL samples trapped in microwell arrays

I next used existing arrays (as described above) to perform some preliminary experiments to analyse iCa^{2+} mobilisation data in primary CLL samples.

CLL samples were selected to represent both U- and M-CLL, and high and low Ca^{2+} signallers according to flow cytometry data (**Table 2-1**). Images were captured at 500 ms intervals although the precise exposure time varied between experiments. Since the software used to control capture of images adds the set interval time to the exposure time to calculate the actual interval between each frame, the interval between frames is therefore different in each experiment. In each experiment baseline data was captured for approximately 10 frames before the addition of anti-IgM, control antibody or ionomycin. In these pilot experiments, the cells were either stimulated once, or were stimulated with anti-IgM or control antibody, followed by the addition of ionomycin as a positive control. The response following addition of anti-IgM or control antibody was recorded for a further 110 frames and, where applicable, the response following ionomycin addition was recorded for another 60 frames. In addition, one sample was pretreated with kinase inhibitors for 1 hour prior to staining with Ca^{2+} indicator dye. For this set of experiments, CLL samples were stained with CellVue™ Maroon, a lipophilic cell membrane dye, used as a generic cell stain to identify cells and CellVue™ Maroon fluorescence imaging was used to determine the number of occupied microwells.

In these experiments, cells were seeded at a density of 100 cells per microwell and 30 minutes was given for the cells to settle into the microwells before rinsing the surface of the array. However, occupancy of the microwells varied between 12 – 80%. This highlighted the importance of optimising the microwell size and the cell seeding method in future design of optimised arrays and assay protocol.

Figure 5-2 shows representative images and corresponding graphs for CLL 686 following addition of anti-IgM (**Figure 5-2A)**, control antibody followed by ionomycin (**Figure 5-2B**), or ionomycin alone (**Figure 5-2C**) (see **Videos 1-3** as examples of data collected). According to the flow cytometry data determined within the tumour bank, 80% of cells would be expected to mobilise

iCa^{2+} in response to anti-IgM stimulation. In **Figure 5-2**, frame 1 shows a baseline image and frame 120 shows an image following ligand addition (**Figure 5-2B** shows an image after addition of control antibody). Each graph shows the fluorescence intensity over time of single cells, where each line corresponds to a single cell. The overall cell response to anti-IgM for this sample was highly variable with some cells seemingly showing no response and others relatively strong and sustained responses (**Figure 5-2A**). By contrast, there was little evidence for induced iCa^{2+} fluxes in cells treated with control antibody (**Figure 5-2B**). The "sharp" peaks seen in these graphs are artefacts caused by cells that were dislodged from microwells during reagent addition and moved across the array so fluorescence was captured once at any specific location. This is also evident in the video recording of this experiment (see **Video 1 and 2**). Addition of ionomycin (**Figure 5-2C**) induced a clear response in a substantial proportion of the cells. However, there was still substantial inter-cell variability in terms of the magnitude and the kinetics of the response. Results obtained with addition of ionomycin after control antibody (**Figure 5-2B**) were less clear. Because of serial treatments, it was possible that cells were beginning to respond towards the end of the data capture period but that the overall period was too short to fully capture the response.

Figure 5-3 shows representative images and corresponding graphs for CLL 482E (4% anti-IgM responsive cells by flow cytometry). Baseline fluorescence is represented by frame 1 images and frame 120 shows fluorescence following addition of anti-IgM stimulation (**Figure 5-3A**) or ionomycin (**Figure 5-3B**). There is a large variability in responsiveness of the cells to both anti-IgM stimulation and ionomycin addition, although there are very few convincingly responsive cells to anti-IgM stimulation (**Figure 5-3A**). The response to ionomycin addition is very similar to the previous sample analysed whereby a large proportion of the cells showed a clear response, but there was still substantial inter-cell variability. Addition of control antibody was not carried out with this sample due to low cell numbers and technical issues with agarose array production and cell seeding. Again the "sharp" peaks seen in **Figure 5-3A** are cells that were moving across the surface of the array.

Figure 5-4 shows representative images and corresponding graphs for CLL 775. Baseline fluorescence is represented by frame 1, fluorescence following anti-IgM (**Figure 5-4A**) or control antibody (**Figure 5-4B**) addition is represented by frame 60, and fluorescence following ionomycin addition is represented by frame 180. The data captured here shows very few cells responding to anti-IgM (or control antibody) despite flow cytometry analysis reporting that 57% cells respond to

anti-IgM. Although the analysis only captured the earliest phase of the response, the response to ionomycin appears to be highly variable within the cell population.

To further probe the responses, I also investigated the effect of kinase inhibitors. **Figure 5-5** shows data for CLL 780B, pretreated with SYK and BTK inhibitors prior to Fluo-8 AM staining. Baseline data was captured for approximately 10 seconds before addition of control antibody (**Figure 5-5A**) or anti-IgM (**Figure 5-5B – 5-5G**). After data was captured for 2 minutes, 100 μM ionomycin was added to each array and data captured for a further minute. The increased ionomycin concentration was used to identify whether a lack of ligand was responsible for the low sensitivity of the responses observed in previous experiments. Flow cytometry data indicated that 81% of cells in this sample responded to anti-IgM stimulation.

Following addition of control antibody (**Figure 5-5A**), cells showed very little response although there were a few cells with a modest (~20 MFI arbitrary units) increase of Ca^{2+} mobilisation during this period. Cells pretreated with DMSO (**Figure 5-5B**) had a varied response to anti-IgM stimulation with a few cells responding very strongly, but the majority of the population displayed a relatively weak or no response. Reponses were much stronger following subsequent ionomycin addition, but were still highly variable between cells. Compared to DMSO-treated cells, pretreatment with R406 or ibrutinib (10 or 1 μM) (**Figure 5-5C – 5-5E**) appeared to very effectively inhibit the response to anti-IgM (but not subsequent ionomycin treatment). Inhibition by acalabrutinib (**Figure 5-5F and 5-5G**) was less apparent. As described above, some traces had substantial numbers of “sharp” peaks caused by displaced cells moving across the surface of the array (especially **Figure 5-5D and 5-5F**).

Overall, this data provided some evidence for detecting anti-IgM responses, which was verified by the use of kinase inhibitors that successfully inhibited the responses. There were significant challenges associated with variable occupancy of the microwell arrays and displacement of cells upon ligand addition. Moreover, the responses showed considerable variability even for ionomycin addition, which would be expected to act more consistently within and between samples. Therefore, there is evidence for the need of new arrays to improve the well size to improve cell trapping and prevention of cell displacement.

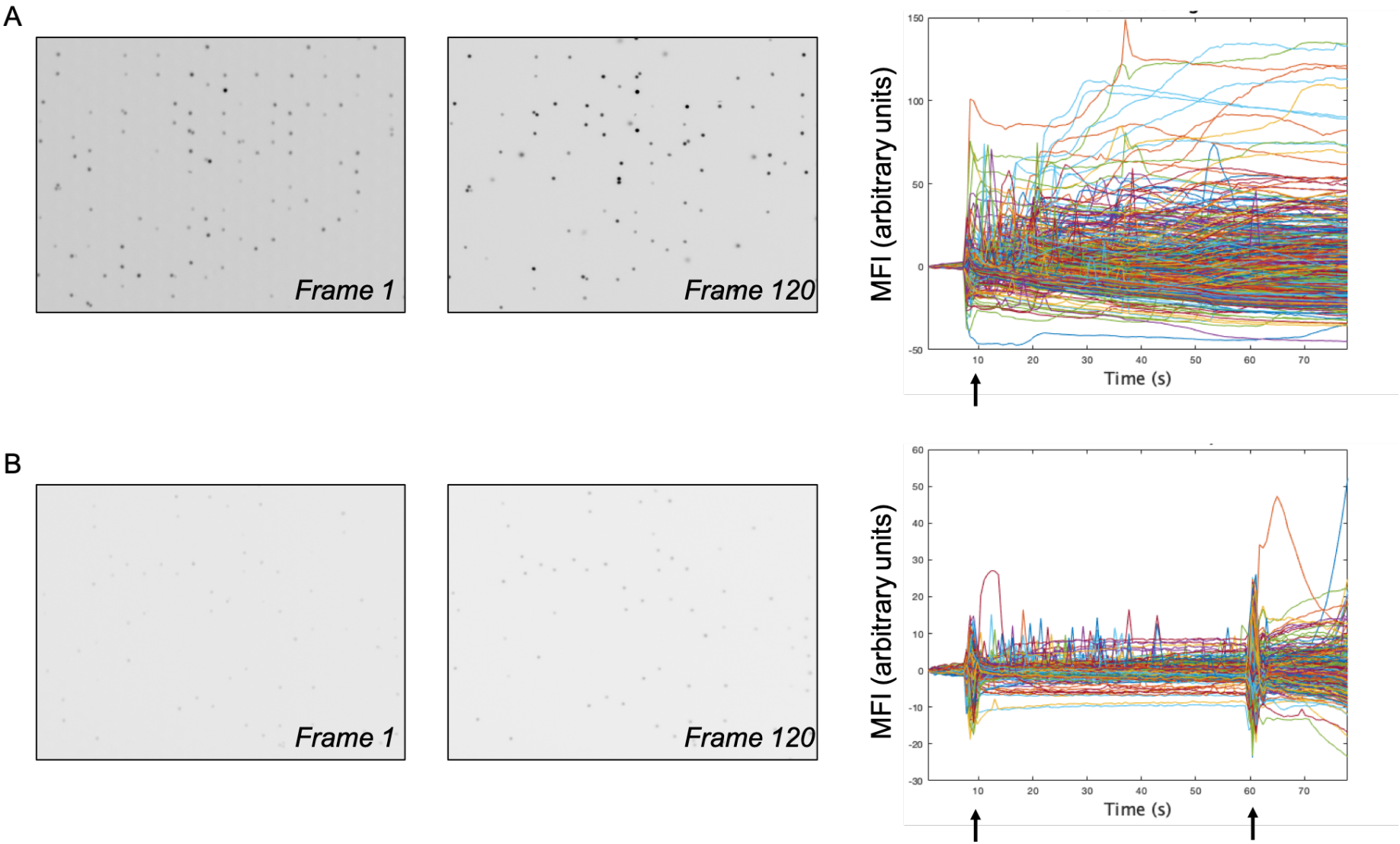
A
Frame 1
Frame 120
MFI (arbitrary units)
Time (s)
B
Frame 1
Frame 120
MFI (arbitrary units)
Time (s)

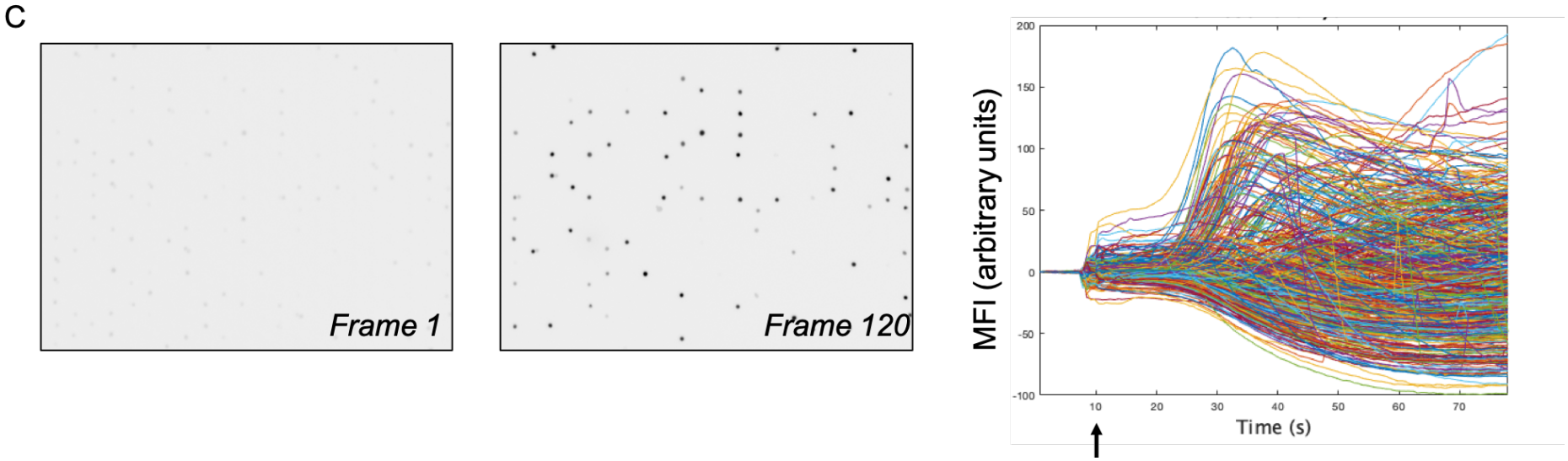

FIGURE 5-2: CA^{2+} MOBILISATION ANALYSIS USING CLL 686.

CLL cells were stained with CellVue Maroon™ and Fluo-8 AM prior to imaging. Images were captured at 500 ms intervals with an exposure time of 150 ms. Baseline data was collected for approximately 10 seconds (left hand images) before stimulation (right hand images) with anti-IgM **(A)**, control antibody **(B)**, or ionomycin **(C)**. The graphs show the fluorescence over time for each individual cell (one line corresponds to one cell), and the arrows on the x axis represent addition of ligand, in part B control antibody is added at the first arrow, and ionomycin at the second arrow.

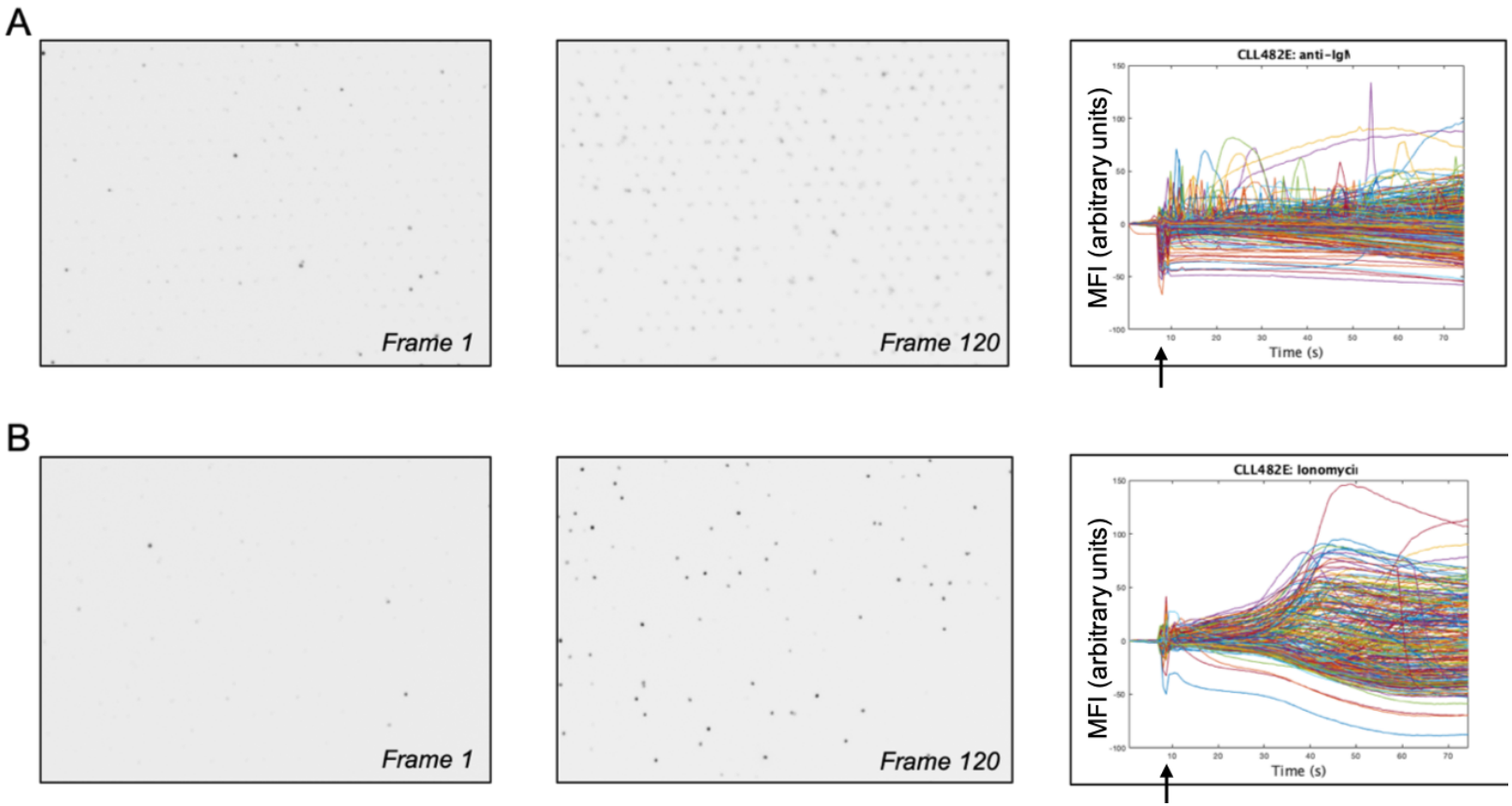

FIGURE 5-3: CA^{2+} MOBILISATION ANALYSIS USING CLL 482E.

CLL cells were stained with CellVue Maroon™ and Fluo-8 AM prior to imaging. Images were captured at 500 ms intervals with an exposure time of 120 ms. Baseline data was collected for approximately 10 seconds (left hand images) before stimulation (right hand images) with anti-IgM **(A)**, or ionomycin **(B)**, indicated by arrows on the x axis of each graph. The graphs show the fluorescence over time for each individual cell (one line corresponds to one cell).

A

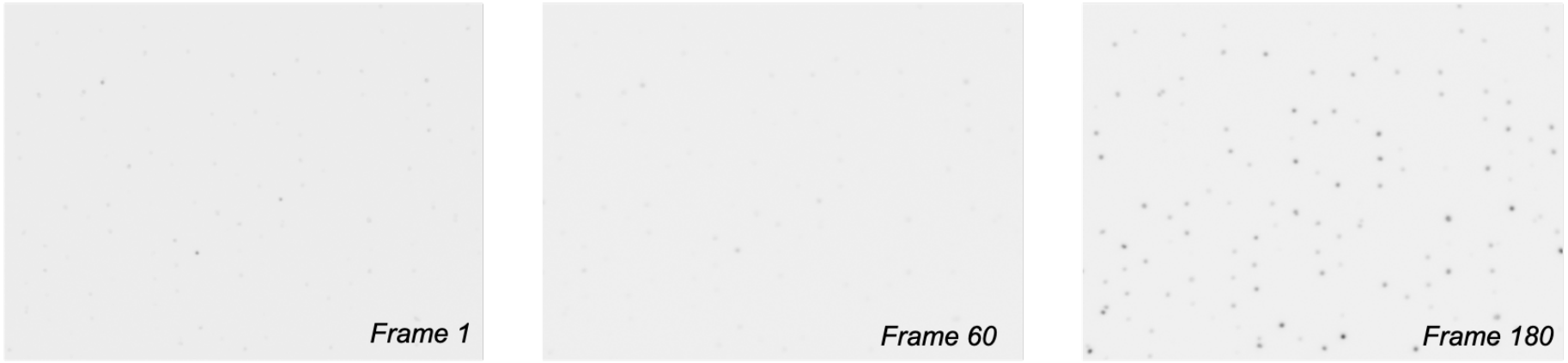

B

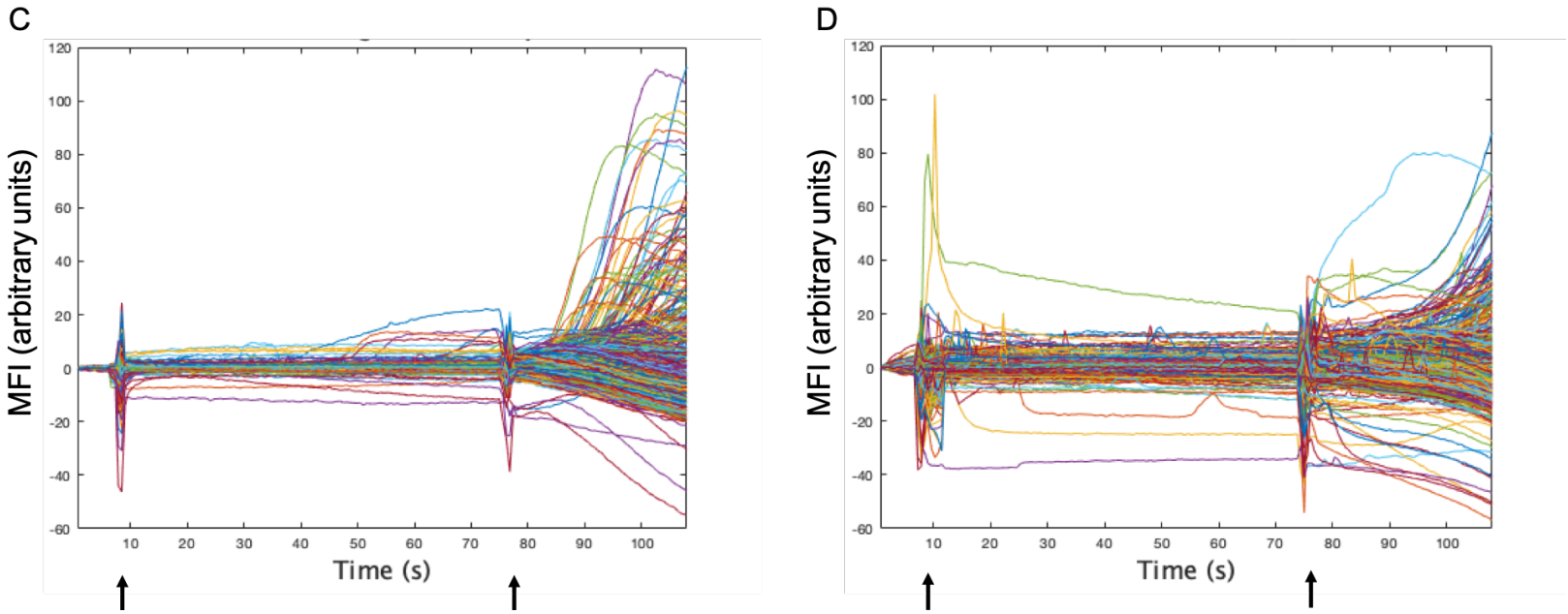

FIGURE 5-4: CA^{2+} MOBILISATION ANALYSIS USING CLL 775.

CLL cells were stained with Fluo-8 AM prior to imaging. Images were captured at 500 ms intervals with an exposure time of 100 ms. Baseline data was collected for approximately 10 seconds (*left hand images*) before stimulation with anti-IgM **(A)**, control antibody **(B)** (*middle images*), and ionomycin (*right hand images*). The graphs show the fluorescence over time for each individual cell (one line corresponds to one cell) stimulated with anti-IgM and ionomycin **(C)** or control antibody and ionomycin **(D)**, indicated by the arrows on the x axis of each graph.

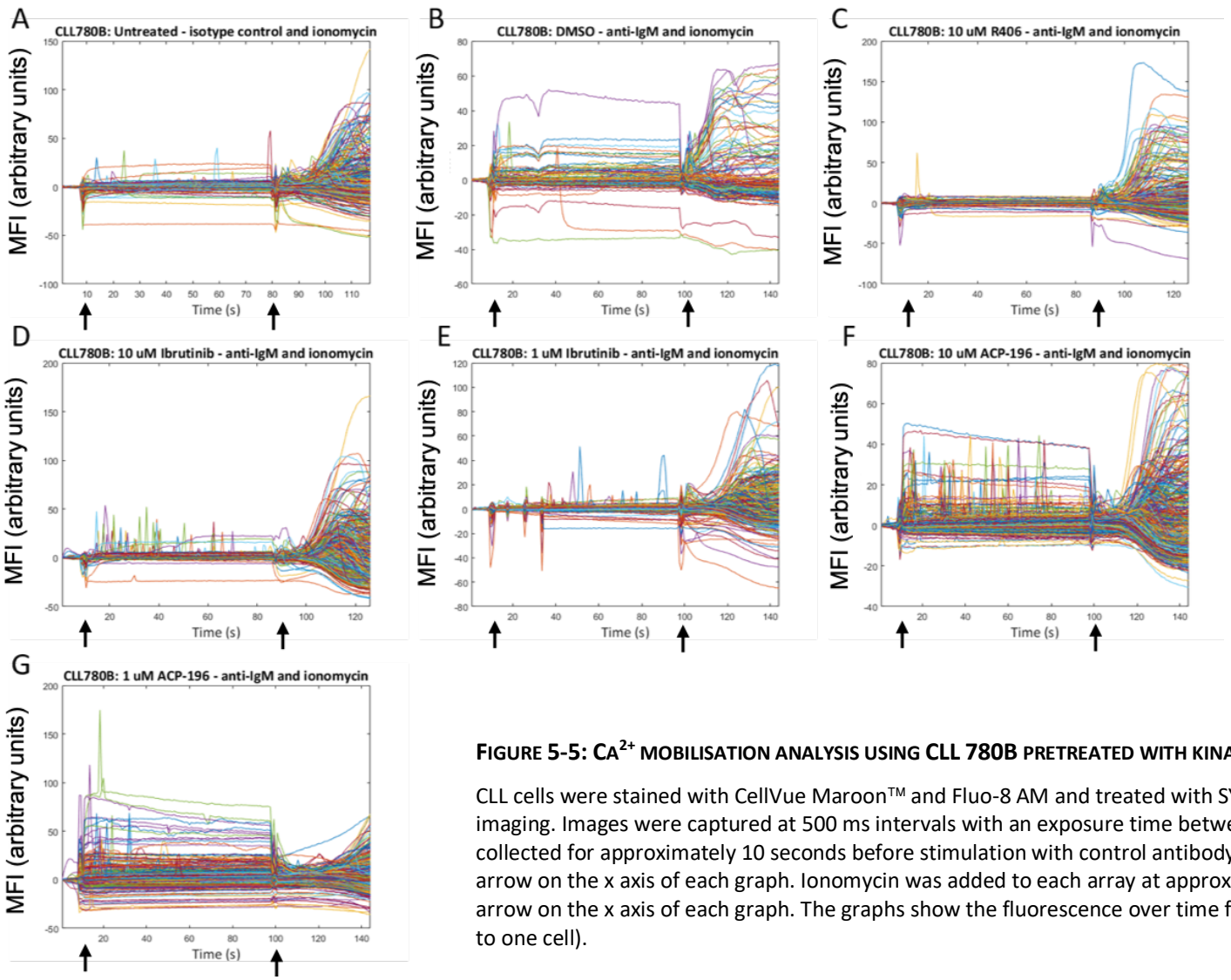

FIGURE 5-5: CA^{2+} MOBILISATION ANALYSIS USING CLL 780B PRETREATED WITH KINASE INHIBITORS.

CLL cells were stained with CellVue Maroon™ and Fluo-8 AM and treated with SYK and BTK inhibitors for 1 hour prior to imaging. Images were captured at 500 ms intervals with an exposure time between 150 to 300 ms. Baseline data was collected for approximately 10 seconds before stimulation with control antibody **(A)** or anti-IgM **(B-G)**, indicated by the first arrow on the x axis of each graph. Ionomycin was added to each array at approximately 100 seconds, indicated by the second arrow on the x axis of each graph. The graphs show the fluorescence over time for each individual cell (one line corresponds to one cell).

5.5 Design and fabrication of microwell arrays

5.5.1 Cell diameter of primary CLL cells and DLBCL cell lines

Before designing new arrays, it was important to know the diameter of the cells of interest that are required to be "trapped" in the microwell array. I therefore used impedance cytometry and microscopy to measure the diameter of CLL cells (including examples of both U- and M-CLL). Impedance cytometry was also used to measure the diameter of OCI-Ly7 and TMD8 cells.

5.5.1.1 Impedance cytometry to measure cell diameter of CLL cells

Impedance cytometry works by applying a potential between a pair of electrodes and measuring the resulting current flowing through the system. The impedance is the ratio of the voltage to the current, and dielectric properties of cells can be derived from this measurement through appropriate models (Holmes D., Webb B.L.J., 2012). The size of the cells were determined by comparing a reference measurement between two electrodes and a detection measurement between two electrodes that contains either a cell or a calibration bead (of known diameter).

Seven primary CLL samples (**Table 2-1**) were analysed using this method (carried out and analysed by Fabrizio Siracusa, Centre for Hybrid Biodevices, University of Southampton, UK) and the data is summarised in **Table 5-1**. The average diameter of all CLL samples measured is 6.65 μm (6.4 μm – 7.0 μm, n=7). **Figure 5-6A** shows an example of the raw data using CLL 780 where the cell population is circled in red and the calibration beads are circled in green.**Figure 5-6B** shows the number of particles measured with the corresponding size of the particles as a histogram showing that the size of cells has a normal distribution. There was little variation both within and between each sample.

TABLE 5-1: SUMMARY DATA FOR THE MEASUREMENTS OF PRIMARY CLL CELL DIAMETER ANALYSED BY IMPEDANCE CYTOMETRY.

CLL Sample Number	Mean diameter of cells (μm)	Standard deviation of diameter of cells (μm)	Cell count
689	6.9474	0.6271	1548
739	6.6726	0.5364	3818
780	6.3672	0.331	494
781	6.5833	0.5756	4134
791	6.4770	0.6023	2809
794	6.6597	0.6068	3193
802	6.8602	0.6675	3420

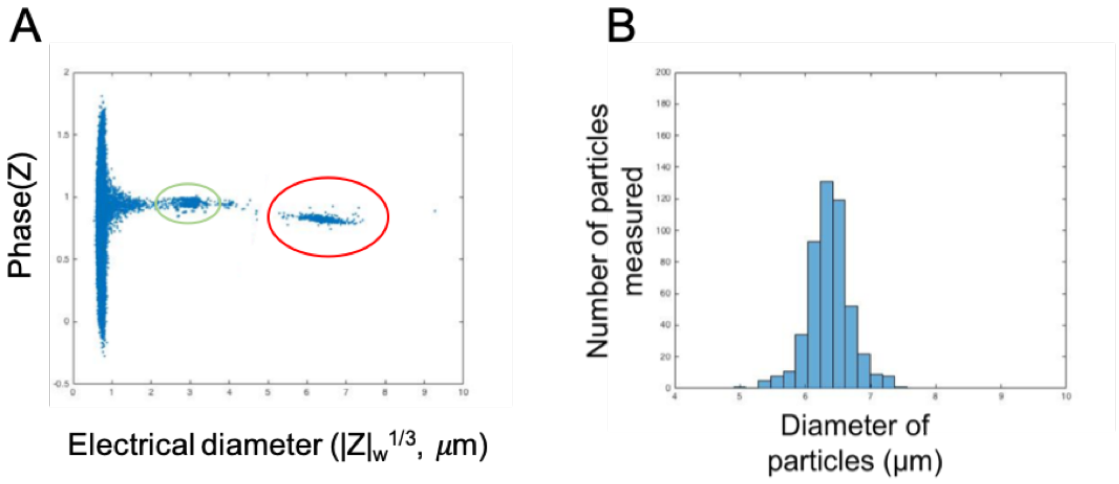

FIGURE 5-6: CELL DIAMETER OF CLL CELLS USING IMPEDANCE CYTOMETRY.

Cells (circled in red), at a density of $1x10^6$ cells/ml, were mixed with 3 μm diameter calibration beads (circled in green). A voltage of 1 MHz was applied to the top electrodes and the voltage detected at the bottom electrode was recorded. Example raw data from CLL 780 **(A)** and the summary data of CLL 780 **(B)** showing the number of cells measured and the diameter of the cells. Data collected and analysed by Fabrizio Siracusa (University of Southampton, UK).

5.5.1.2 Microscopy to measure cell diameter of CLL cells

The cell diameter of 6 primary CLL samples was calculated by measuring the area of the cells with ImageJ using images captured by microscopy (**Figure 5-7A and 5-7B**). **Table 5-2** shows summary data for each of the 6 samples and **Figure 5-7C** shows the size distribution of primary CLL cells.

The mean cell diameter was calculated as 7.57 µm with a standard deviation of 1.09 µm and there was little variation within and between samples. CLL cells are very bright under the microscope, which causes a 'halo' effect. This is where the cell appears to be surrounded by a ring of light, which can make it difficult to determine where the edge of the cell is. This could, in part, explain the difference between the mean cell diameter measured using microscopy and that measured using impedance cytometry.

TABLE 5-2: SUMMARY STATISTICS FOR THE CELL DIAMETER OF 6 PRIMARY CLL SAMPLES.

CLL Sample Number	Mean cell diameter (µm)	Standard deviation of cell diameter (µm)	Cell count
689	7.78	0.87	93
740	8.07	0.98	183
780B	7.41	1.17	841
791	7.25	0.78	430
794	8.56	0.81	206
802	7.17	0.91	130

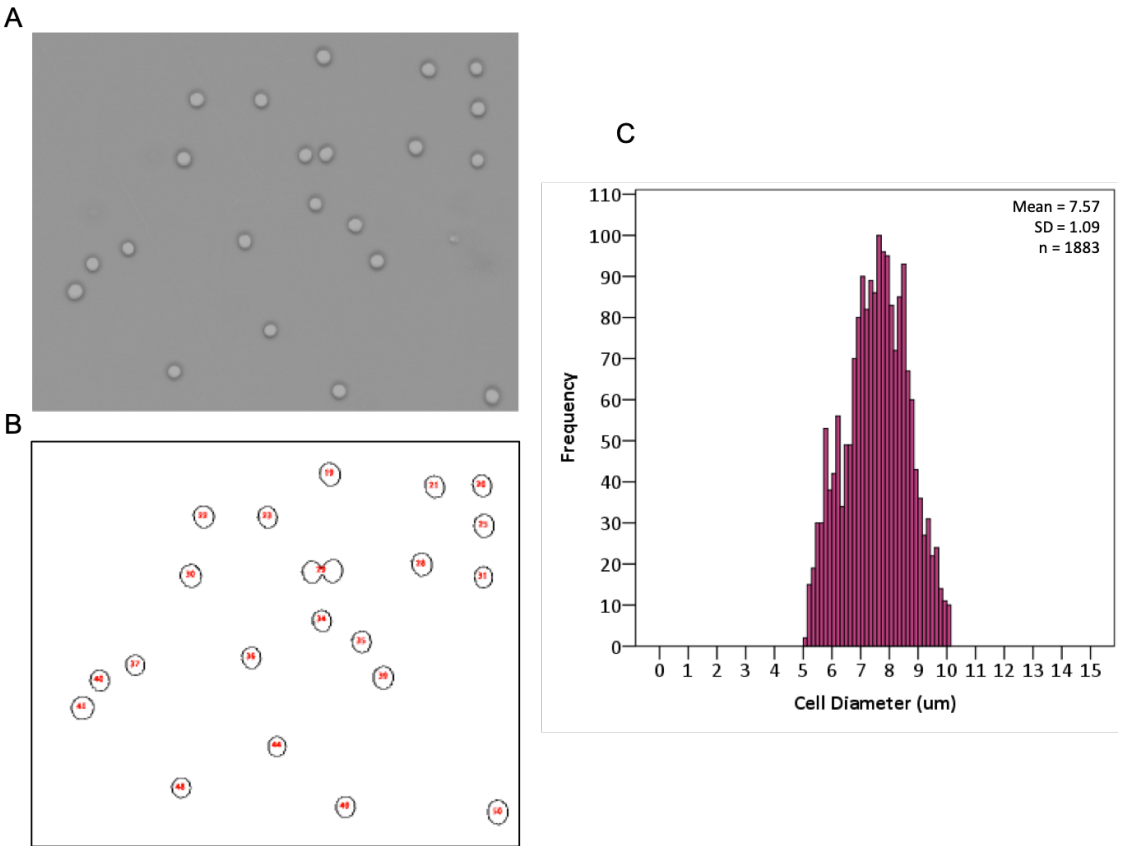

FIGURE 5-7: CELL DIAMETER OF CLL SAMPLES MEASURED BY MICROSCOPY.

CLL samples were imaged, example using CLL 791 **(A)** and cell diameter was measured in Fiji after making the image an 8-bit binary image **(B)**. Summary of 6 CLL samples measured **(C)** showing distribution of cell diameters.

5.5.1.3 Impedance cytometry to measure cell diameter of DLBCL cell lines

OCI-Ly7 and TMD8 cells were analysed by impedance cytometry to determine the cell diameter (data was acquired and analysed by Fabrizio Siracusa, Centre for Hybrid Biodevice, University of Southampton, UK). The data is summarised in **Table 5-3**. The average diameter of OCI-Ly7 cells is ~10 μm and there is little variation within the sample analysed. The average diameter of TMD8 cells is ~13 μm, but this was more variable. Both cell lines were split the day before impedance analysis, but the variation seen is most likely due to the rapid proliferation of the cell lines, i.e. the size increases as the cell progresses through the cell cycle. **Figure 5-8A** shows the raw data for OCI-Ly7 and **Figure 5-8B** shows the raw data for TMD8. In both cases the cell population is circled in red and the calibration beads are circled in green.

TABLE 5-3: SUMMARY DATA FOR THE MEASUREMENTS OF DLBCL CELL LINE DIAMETER ANALYSED WITH IMPEDANCE CYTOMETRY.

DLBCL Cell lines	Mean cell diameter (μm)	Standard deviation of cell diameter (μm)	Cell count
OCI-Ly7	9.92	1.06	2039
TMD8	13.22	2.32	4579

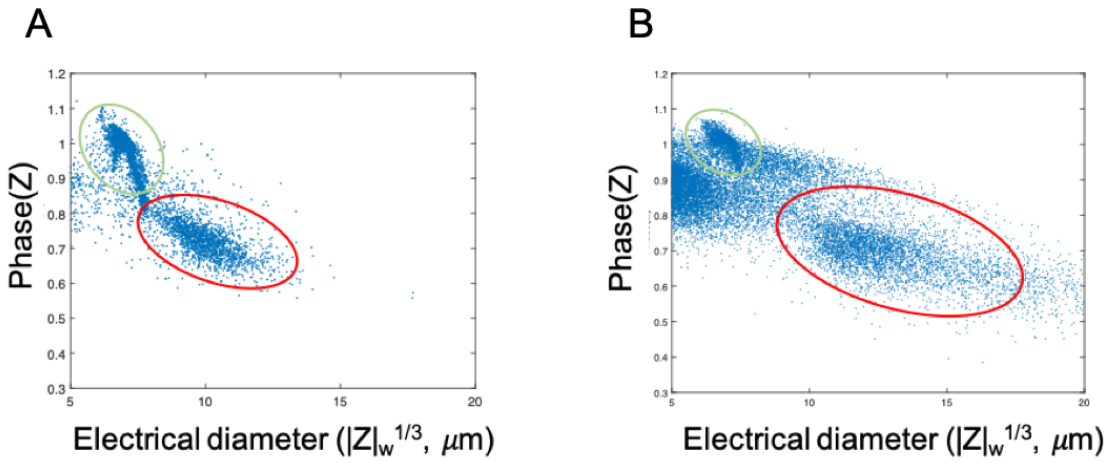

FIGURE 5-8: CELL DIAMETER OF DLBCL CELL LINES USING IMPEDANCE CYTOMETRY.

Cells (circled in red), at a density of $1x10^6$ cells/ml, were mixed with 7 μm diameter calibration beads (circled in green). A voltage of 800 kHz was applied to the top electrodes and the voltage detected at the bottom electrode was recorded. Raw data for OCI-Ly7 cell line **(A)** and TMD8 cell line **(B)**. Data collected and analysed by Fabrizio Siracusa (University of Southampton, UK).

5.5.1.4 Cell diameter summary

Overall, CLL cells have an approximate diameter of 7 µm, which is similar to the previously reported data by Kuse *et al*. (Kuse *et al*., 1985) who used Coulter analysis to report a diameter of ~6.8 µm. Although the two methods used here have slightly differing results, each method has very little variation within and between samples suggesting that one optimal microwell size could be achieved for use with primary CLL samples.

The cell lines were only measured once by impedance cytometry and showed larger variation between cells than the CLL samples. Further measurements should be analysed to draw more robust conclusions and alternative methods, for example microscopy, could be used for confirmation of results. However, since the measurements collected by impedance cytometry for CLL were in line with the expected diameter (based on Kuse *et al*., 1985 , along with the microscopy data), it is sufficient to use the data collected for the cell lines as a reasonable estimate of the cell size.

Therefore, the microwell diameters to be included for CLL cells should range between ~10 – 12 µm, for OCI-Ly7 cells should range between ~14 – 18 µm, and for TMD8 cells should range between ~18 – 25 µm. These microwell sizes are based on requiring a microwell large enough for the cell to displace any cell media and settle into the microwell, but not large enough for multiple cells to settle into a single microwell.

5.5.2 Mask design

The mask consists of arrays of circles, to allow light to pass through during exposure of the photoresist-coated wafer during the fabrication process (Figure 2-4) to produce a wafer consisting of micropillars which will form the template for creating agarose microwell arrays. The mask will contain features of varying sizes to create microwell arrays suitable for use with a range of cell sizes. The mask is made of glass with the design produced with chrome on one surface of the mask, it is a 6-inch square mask to contain the design for a 4-inch diameter wafer.

The mask design consists of arrays of circles arranged in the "square" pattern seen in **Figure 5-9A**. Each small square, as depicted by **Figure 5-9B**, consists of 1250 circles (which will eventually create the microwells) and this is what is referred to as a single "microwell array". Each large "square" in **Figure 5-9A** contains circles with a different diameter, so from top left, working across each row the diameters are as follows:

Top row: 10 , 11, 12 µm

Second row: 13, 14, 15, 16 µm

Third row: 18, 20, 22, 24 µm

Fourth row: 26, 28, 30 µm

The circles in the arrays in the top two rows are 50 µm apart, measuring from the centre of the circles (**Figure 5-9C**), but this distance is increased to 100 µm in the bottom two rows since the diameters of the circles are larger.

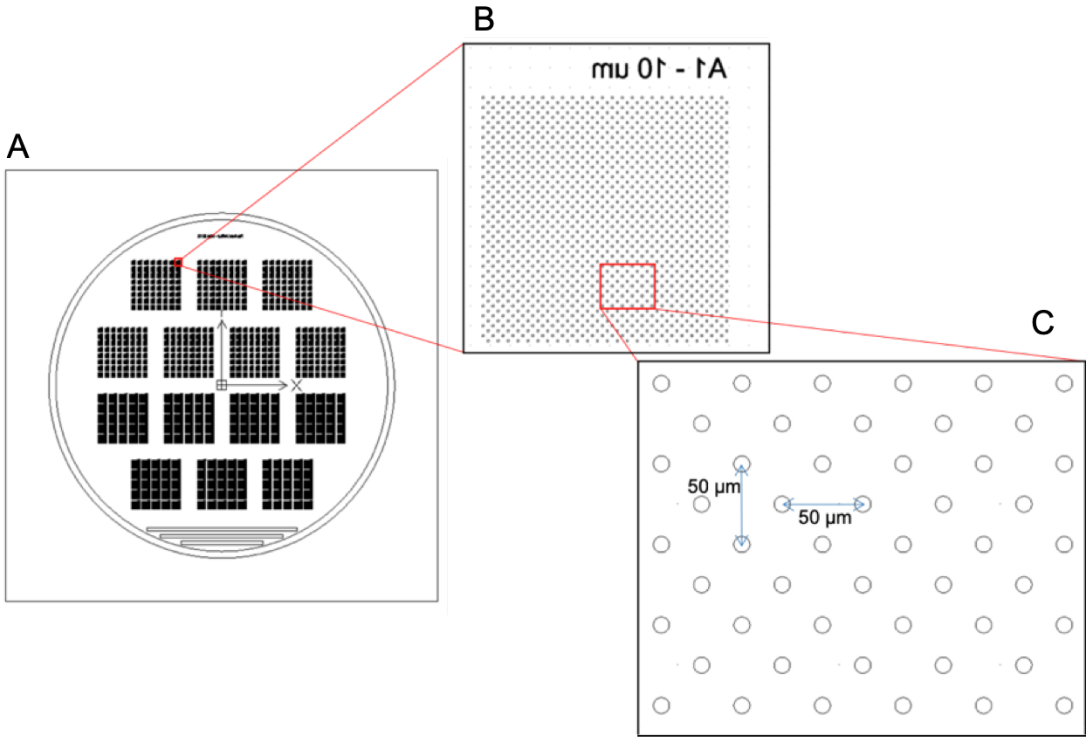

FIGURE 5-9: PHOTOMASK DESIGN FOR MICROWELL ARRAYS.

The design includes features ranging from 10 µm to 30 µm in diameter to allow capture of both CLL and DLBCL cells. Produced using DraftSight software.

5.5.3 Wafer fabrication

The silicon wafer was fabricated as per the protocol outlined in (**Section 2.4.2**). There are several parameters in the method that can be altered to allow successful fabrication of the wafer including the speed and duration of the spin to coat the wafer with the photoresist (this will determine the height of the features), the exposure energy, the bake times and the development time.

It was determined, as per the datasheet, that to achieve a thickness of the photoresist of 15 – 20 μm, it had to be spun at 4000 rpm for 30 seconds with an acceleration of 500 rpm/s. The bake times were also selected based on the thickness of the photoresist and chosen as per the datasheet. It was the exposure energy that required more fine tuning. With a photoresist thickness of 15 – 20 μm, the datasheet suggests that an exposure energy between 125 – 250 mJ/cm^2 would be appropriate. Underexposing the photoresist would not allow for sufficient crosslinking of the photoresist, which would then likely be washed away upon development. Overexposure of the photoresist can lead to diffraction of the UV radiation causing a larger area of the photoresist to crosslink and therefore the features will not be an accurate, or necessarily a uniform, size. An initial exposure energy of 150 mJ/cm^2 was chosen but further optimisation revealed that an exposure energy of 100 mJ/cm^2 was more appropriate and provided the most accurate feature diameters (**Figure 5-10**).

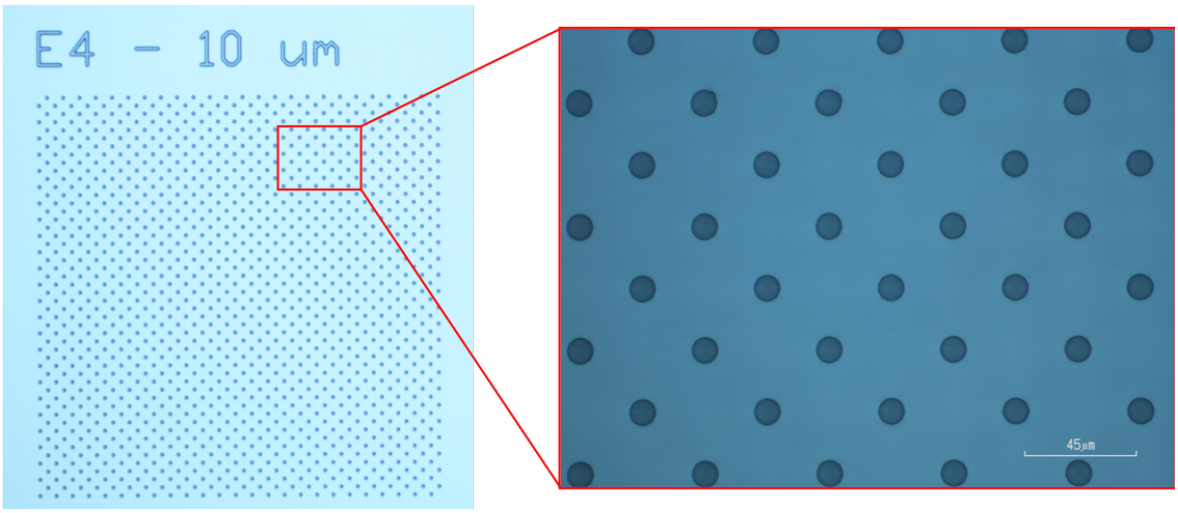

FIGURE 5-10: FABRICATION OF WAFER.

Following photolithography a wafer consisting of micropillars is produced. Images show one array containing 1250 micropillars of 10 μm diameter taken at 5x magnification (*left hand image*) and an image at 20x magnification (*right hand image*). Scale bar on the right hand image is 45 μm.

5.5.4 Agarose microwell array production

The standard method for agarose microwell array production, as outlined in (**Section 2.4.3**), states that melted agarose be cooled to 55 °C prior to pouring over the wafer and allowing to cure. Curing time varied between experiments depending on the temperature of the laboratory and therefore was not necessarily reproducible each time. The method of peeling the agarose array off the wafer also introduces some variability and causes some distortion of the microwells caused by the angle at which the agarose is removed from the wafer (**Figure 5-11**).

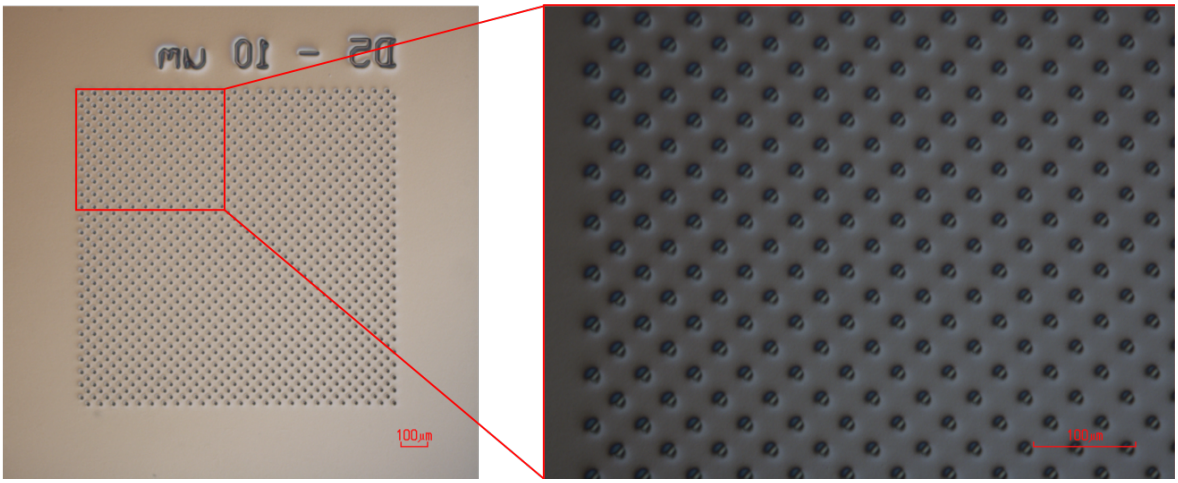

FIGURE 5-11: AGAROSE MICROWELL ARRAY.

Melted agarose is poured onto the wafer and allowed to cure, it is then peeled off the wafer for use. Images show one mircowell array consisting of 1250 microwells taken at 5x magnification (*left hand image*) and an image at 10x magnification (*right hand image*). Scale bars are 100 μm.

5.6 Identification of the optimal microwell diameter and cell seeding conditions

A series of experiments using four CLL samples was carried out to determine the optimal microwell size required for use with primary CLL cells along with the optimal cell seeding conditions to achieve the highest single-cell occupancy of the microwells. The aim was to achieve ≥80 % occupancy to ensure that a statistically relevant number of cells could be analysed.

Since CLL cells have an average diameter of ~7 μm, the arrays used to test for highest occupancy had diameters of 10, 11, or 12 μm; anything larger than this would allow for too many microwells to contain multiple cells or would be large enough for the cells to be easily washed out of the microwells. Each relevant section of the device contains 64 microwell arrays each consisting of 1250 microwells, therefore a total of 80,000 microwells were available for each diameter size. I tested 4 different cell seeding densities: 100, 50, 20 or 10 cells per microwell so either $8x10^6$, $4x10^6$, $1.6x10^6$, or $8x10^5$ cells were resuspended in a total volume of 200 μl cRPMI before being pipetted onto the array. This volume was chosen because it readily covers the surface of the array without pouring off the edges of the array. In all cases, cells were stained with CellTracker™ Deep Red dye prior to seeding in the arrays and were then left to settle for 30 minutes before the excess was rinsed from the surface of the array with PBS and then imaged. Brightfield and fluorescent images were captured but the fluorescent images were used to automatically count the cells using Fiji. This analysis did not necessarily exclude multiple cells per well. If the cells could be identified as multiple cells they were counted as separate cells, hence some of the data suggest >100% occupancy.

Figure 5-12 shows representative images of the occupancy of 11 μm diameter microwells at the four different cell seeding ratios (10:1 cells per microwell in **Figure 5-12A**, 20:1 in **Figure 5-12B**, 50:1 in **Figure 5-12C**, and 100:1 in **Figure 5-12D**). The left-hand image of each pair shows the brightfield image and the right-hand image of each pair shows the corresponding fluorescent image (the colours have been inverted using Fiji). **Figure 5-13** shows the summary data for multiple experiments of occupancy analysis. Technical issues with production of agarose arrays (where features are not always formed perfectly) along with variability in the cell seeding method that is difficult to control (i.e. washing with PBS is difficult to keep consistent) means that the average occupancy does not reach the desired level. However several conditions do span the 80%

occupancy mark. This gives a suggestion of the optimal microwell diameter and the cell seeding ratio but is also indicative that the method could be improved further.

The cell seeding ratio of 10 cells per microwell shows very few cells become trapped in the device regardless of the microwell dimensions. In each of the other cell seeding conditions, the microwells with a diameter of 11 μm had the highest occupancy regardless of the number of cells being loaded onto the array. There was very little difference between the cell seeding density of 50 cells per microwell and 20 cells per microwell for both 11 and 12 μm diameter microwells and these four conditions gave the highest occupancy overall. Whilst the mean never reached 80%, the standard deviation of these four conditions did encompass 80% occupancy (**Figure 5-13**).

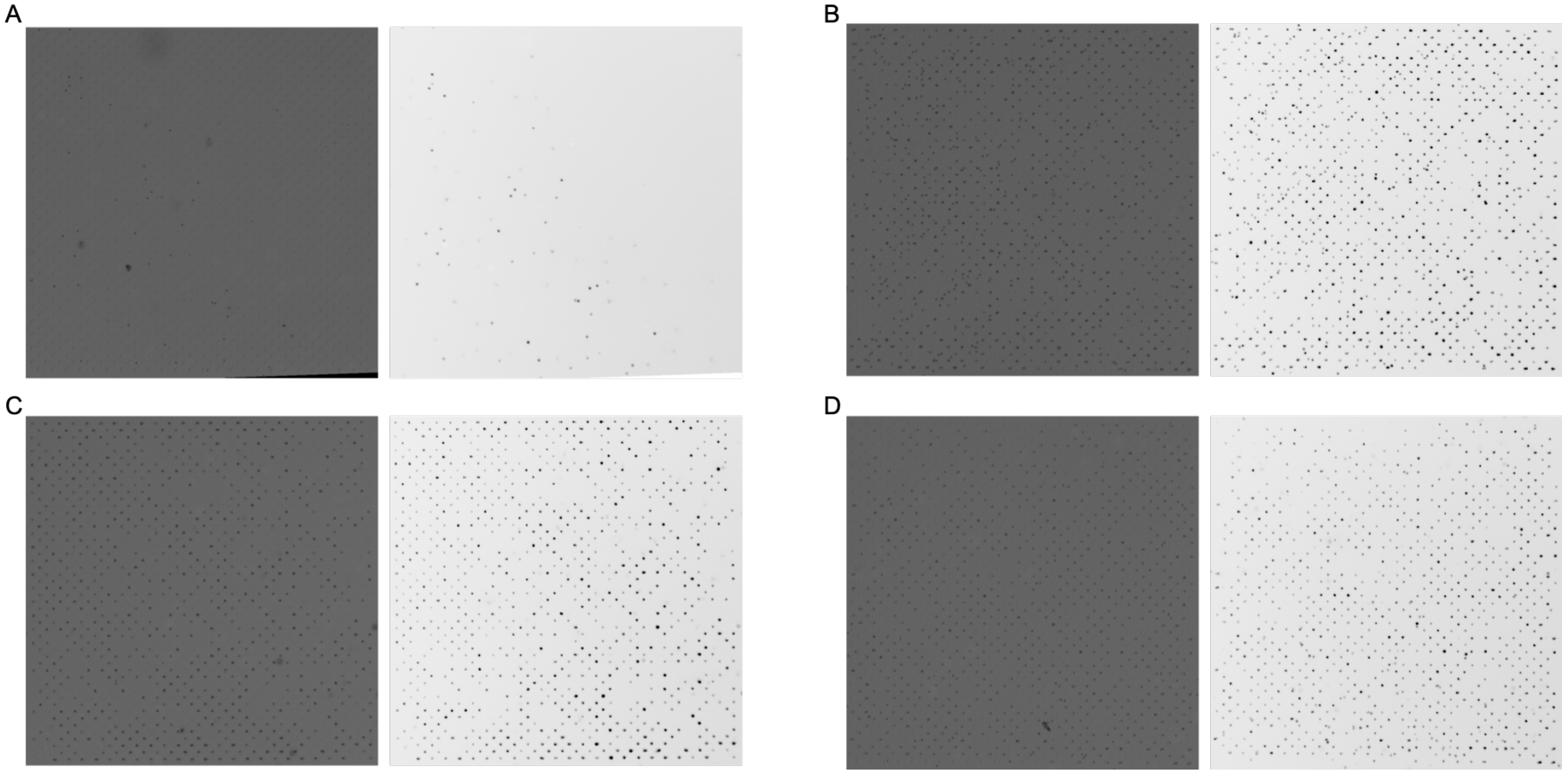

FIGURE 5-12: REPRESENTATIVE IMAGES OF CELL SEEDING DENSITIES TO DETERMINE HIGHEST MICROWELL OCCUPANCY USING ARRAYS WITH 11 μM DIAMETER MICROWELLS.

CLL cells stained with CellTracker Deep Red were seeded onto the arrays at a ratio of (A) 10, (B) 20, (C) 50, or (D) 100 cells per microwell. Brightfield images (left hand images) and fluorescent images (right hand images) using the Cy5 filter and taken at 0.3 s (A) or 0.25 s (B-D) exposure were captured.

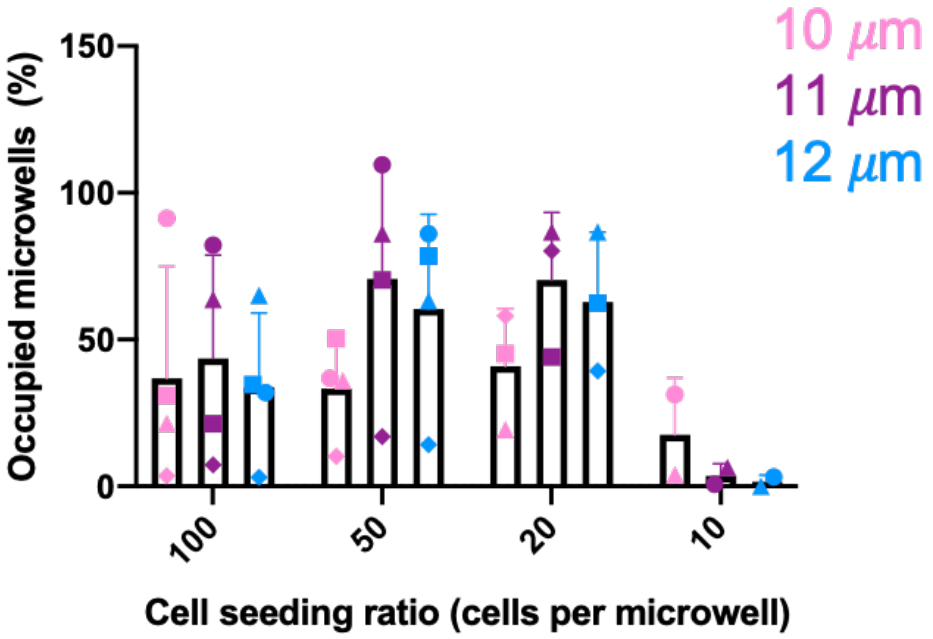

FIGURE 5-13: SUMMARY OF OCCUPIED MICROWELLS USING DIFFERENT CELL SEEDING RATIOS.

CLL samples were loaded into 10 (pink), 11 (purple), and 12 μm (blue) diameter microwell arrays at densities of 10, 20, 50, or 100 cells per microwell. Brightfield and fluorescent images were captured and occupied microwells were counted using Fiji. Bars represent mean and standard deviation of n=4 for 100 and 50 cells per microwell, n=3 for 20 cells per microwell and n=2 for 10 cells per microwell.

5.7 Ca^{2+} flux analysis in primary CLL samples using microwell arrays

Eight CLL samples were analysed using the new microwell arrays to measure iCa^{2+} flux by fluorescence microscopy following addition of ionomycin, or anti-IgM (with or without SYK or BTK inhibitor pretreatment), or control antibody. The CLL samples were selected to include both U- and M-CLL as well as low and high signallers (**Table 2-1**), as determined by flow cytometric analysis. Due to the relatively low number of samples analysed and the preliminary nature of the investigation I have presented results for each sample separately, focussing first on the responses to ionomycin (where all samples are expected to respond relatively consistently) and then anti-IgM-stimulation (where both inter- and intra-sample variation is expected). Finally, I have presented results for effects of inhibitors for the samples where an anti-IgM response was observed. The full results for each sample are included in **Supplementary Figure 13 - 20**.

The main steps in data analysis for this series of experiments are illustrated in **Figure 5-14**. Fluorescent images were captured at set intervals (which differed between experiments) and the fluorescence of each cell in each frame was extracted. First, the raw data was plotted as a heat scatter plot (**Figure 5-14A**). To account for variability in baseline fluorescence, the data was then normalised by taking the fluorescence at any given time point and subtracting the fluorescence measured in the first frame of the corresponding cell thereby setting all cell baselines to zero. The resulting normalised data was also presented as a heat scatter plot (**Figure 5-14B**). Finally, data were plotted as a line graph where each line corresponds to the normalised fluorescence of a single cell over time (**Figure 5-14C**). As discussed above, the sharp peaks observed in **Figure 5-14C** are likely to represent detection of displaced cells that were moving across the surface of the array and were therefore not imaged consistently in any specific position on the arrays. By contrast, the peaks at approximately 30 seconds are an artefact caused by the addition of ligand to the array at this time.

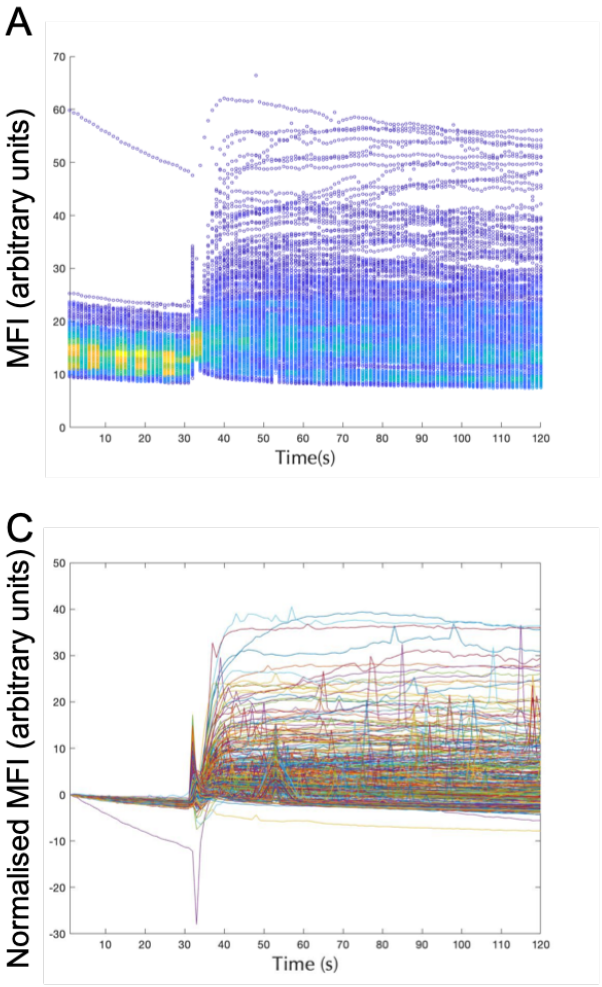

FIGURE 5-14: REPRESENTATIVE GRAPHS OF DATA ANALYSIS STEPS.

The raw data, fluorescence of each cell over time, is initially plotted as a heat scatter plot **(A)**. This data is normalized to the first frame and replotted as a heat scatter plot **(B)**, which is subsequently plotted as a line graph **(C)** where each line represents a single cell.

5.7.1 Response to ionomycin

Fluorescent images were captured to determine the exposure time necessary to visualise cells and then the interval time could be set to ensure that the series of images were captured for a total of 2 minutes. Images were captured at the set interval time for approximately 30 seconds, to represent baseline fluorescence, before the addition of ionomycin. Data was then acquired for a further 90 seconds. **Figure 5-15** shows the response of each sample to ionomycin addition. For most samples, ionomycin was added to previously untreated cells. However, for sample 681 (**Figure 5-15B**), the analysis shown is for cells that had been pretreated with DMSO as the array with previously untreated cells moved during the image capture (caused by the pipette tip touching the array during ligand addition).

In general, there was a large variation in the response to ionomycin between samples. Most cells in CLL 780 appeared to respond to addition of ionomycin (**Figure 5-15A**) although the majority of cells only exhibited a modest increase in fluorescence. However, there is a very small percentage of cells that increase more considerably than the bulk population. The majority of cells in sample CLL 681 showed very little response to ionomycin addition, with a few cells exhibiting a response with a greater magnitude compared with the rest of the population (**Figure 5-15B**). Addition of ionomycin to CLL 674B (**Figure 5-15C**) shows a varied response within the population. Whilst the majority of the cells appear to have a relatively minimal increase in iCa^{2+} flux, there are a number of cells which have a stronger response to ionomycin. The sharp peaks are caused by displaced cells moving across the array. CLL 635D exhibits an increase in fluorescence in almost the whole population in response to ionomycin (**Figure 5-15D**), with a small population of cells exhibiting a more substantial response than the rest of the population. The same pattern of the vast majority of cells exhibiting only a minimal response to ionomycin addition with a very small population of cells responding with a greater magnitude compared with the rest of the sample is seen in the other CLL samples tested (CLL 774 [**Figure 5-15E**], CLL 803B [**Figure 5-15F**], CLL 709A [**Figure 5-15G**], and CLL 781 [**Figure 5-15H**]). Note that cells which appear to lose fluorescence below baseline measurements following stimulation (seen in **Figure 5-15B – 5-15G**) have been displaced from the microwell array and therefore this is just a measurement of an empty microwell.

This response pattern is interesting in that ionomycin, as a Ca^{2+} ionophore, would be expected to cause complete iCa^{2+} release in every cell, but there is clearly still variation within this response both between and within samples.

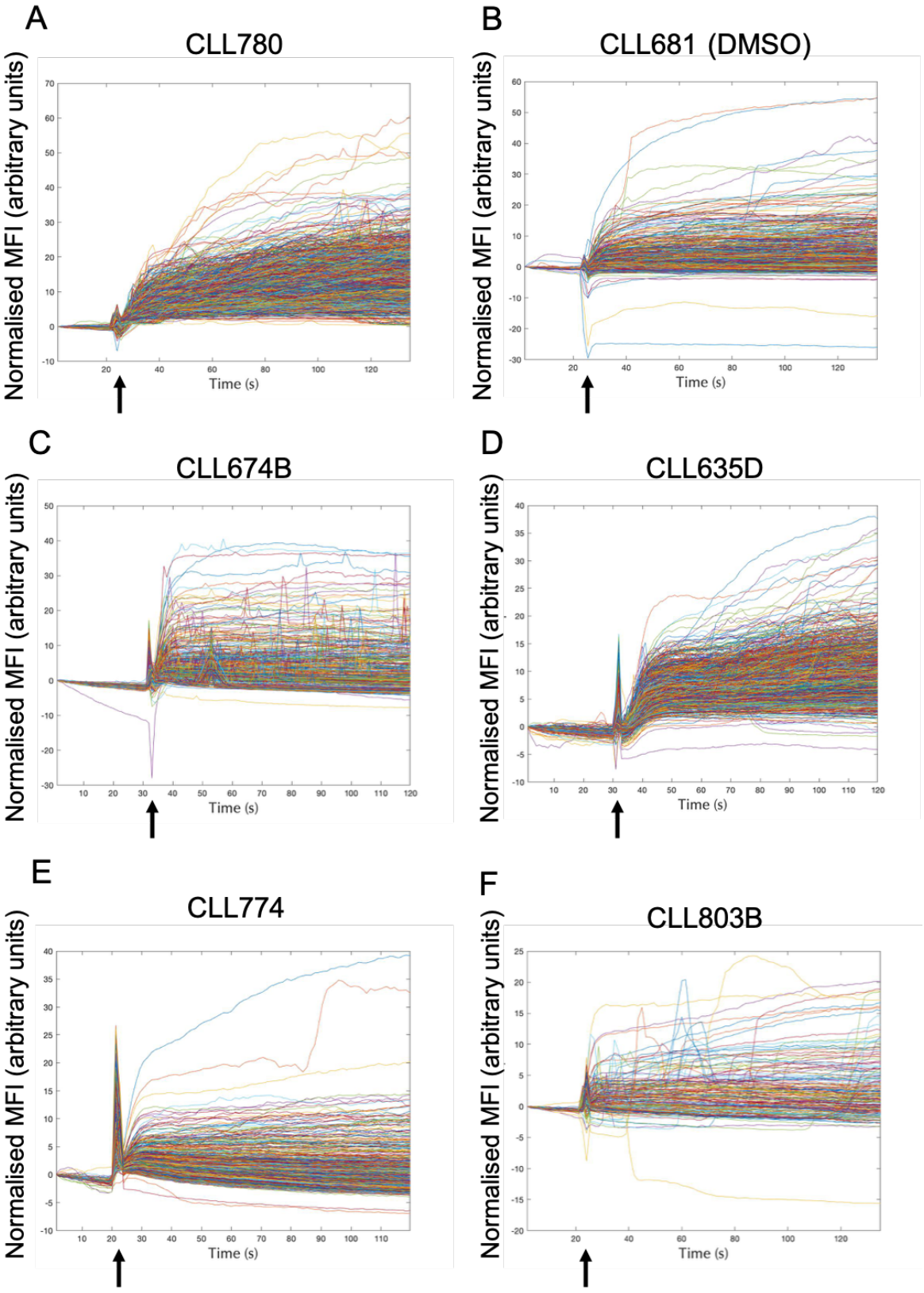
A
CLL780
Normalised MFI (arbitrary units)
Time (s)
B
CLL681 (DMSO)
Normalised MFI (arbitrary units)
Time (s)
C
CLL674B
Normalised MFI (arbitrary units)
Time (s)
D
CLL635D
Normalised MFI (arbitrary units)
Time (s)
E
CLL774
Normalised MFI (arbitrary units)
Time (s)
F
CLL803B
Normalised MFI (arbitrary units)
Time (s)

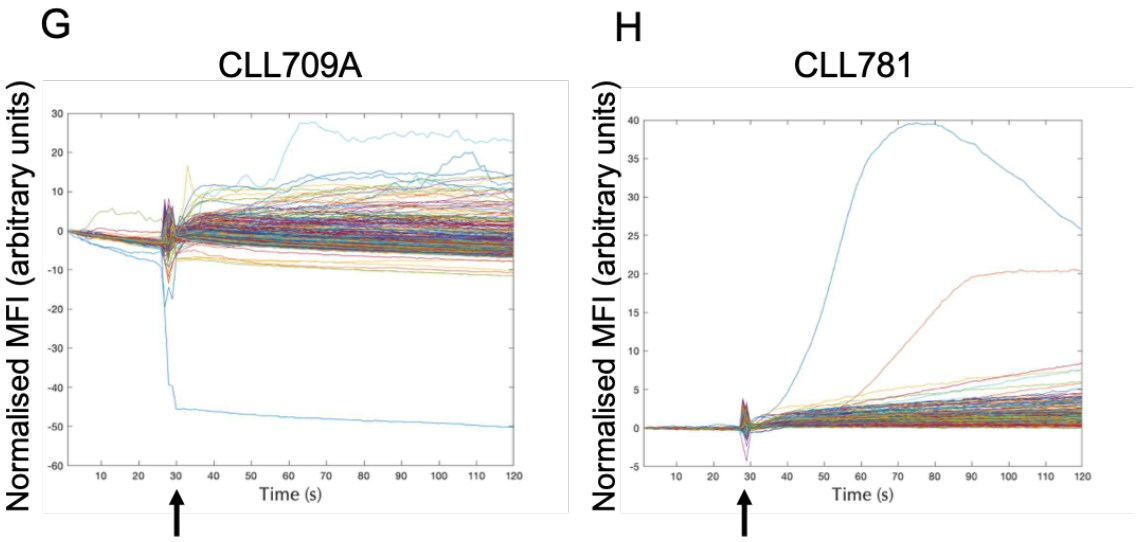

FIGURE 5-15: CA^{2+} MOBILIZATION ANALYSIS IN RESPONSE TO IONOMYCIN ADDITION IN PRIMARY CLL SAMPLES TRAPPED IN MICROWELL ARRAYS.

Untreated cells, with the exception of CLL681 **(B)** which had been pretreated with DMSO, were stimulated with ionomycin, indicated by the arrow on the x axis of each graph, following 30 seconds of baseline data collection and images were captured until 2 minutes.

5.7.2 Reponse to anti-IgM

I next investigated the response of each sample to anti-IgM (**Figure 5-16**). In each pair of graphs, the addition of control antibody is shown on the left-hand graph and the addition of anti-IgM is shown on the right-hand graph. In general, addition of control antibody had very little effect on iCa^{2+} release. The sharp peaks in **Figure 5-16A, 5-16F and 5-16G** are caused by cells being displaced from the microwells.

Overall, the response to anti-IgM stimulation was very weak and the experiment did not reliably detect anti-IgM responses. Potential anti-IgM-induced iCa^{2+} release was only detected in 3 of the 8 samples analysed, i.e. CLL 780 (**Figure 5-16A**), CLL 681 (**Figure 5-16B**) and CLL 674B (**Figure 5-16C**), whereas the remaining samples seemed unaffected by anti-IgM stimulation (**Figure 5-16D – 5-16H**). Again, the sharp peaks observed in **Figure 5-16D – 5-16G** represent cells that have been displaced from the microwells and were moving across the array; this makes analysis and interpretation of results somewhat challenging.

Overall, the samples that did respond to anti-IgM stimulation appeared to be less sensitive than when measured by flow cytometry. CLL 780 (**Figure 5-16A**) was reported to have a signalling capacity of 81% by flow cytometric analysis but in this experiment the cells appeared to have very modest responses with a substantial proportion of the cells not responding at all. There also appeared to be a delay of 10-20 seconds before an increase in fluorescence is observed following addition of anti-IgM.

CLL 681 (**Figure 5-16B**) was reported to have a signalling capacity of 60% by flow cytometric analysis, but the data presented here suggested that the majority of the population do not respond to anti-IgM stimulation but a small proportion of the cells exhibited a response with a greater magnitude, but overall the responses were still relatively weak.

CLL 674B (**Figure 5-16C**) was reported to have a signalling capacity of 89% by flow cytometric analysis, whereas the data presented here suggested only a small proportion of the cells exhibited relatively weak responses to anti-IgM stimulation. Interestingly in this sample, as with CLL 780,

there is a delay of 10-20 seconds between addition of anti-IgM and an increase in detection of fluorescence.

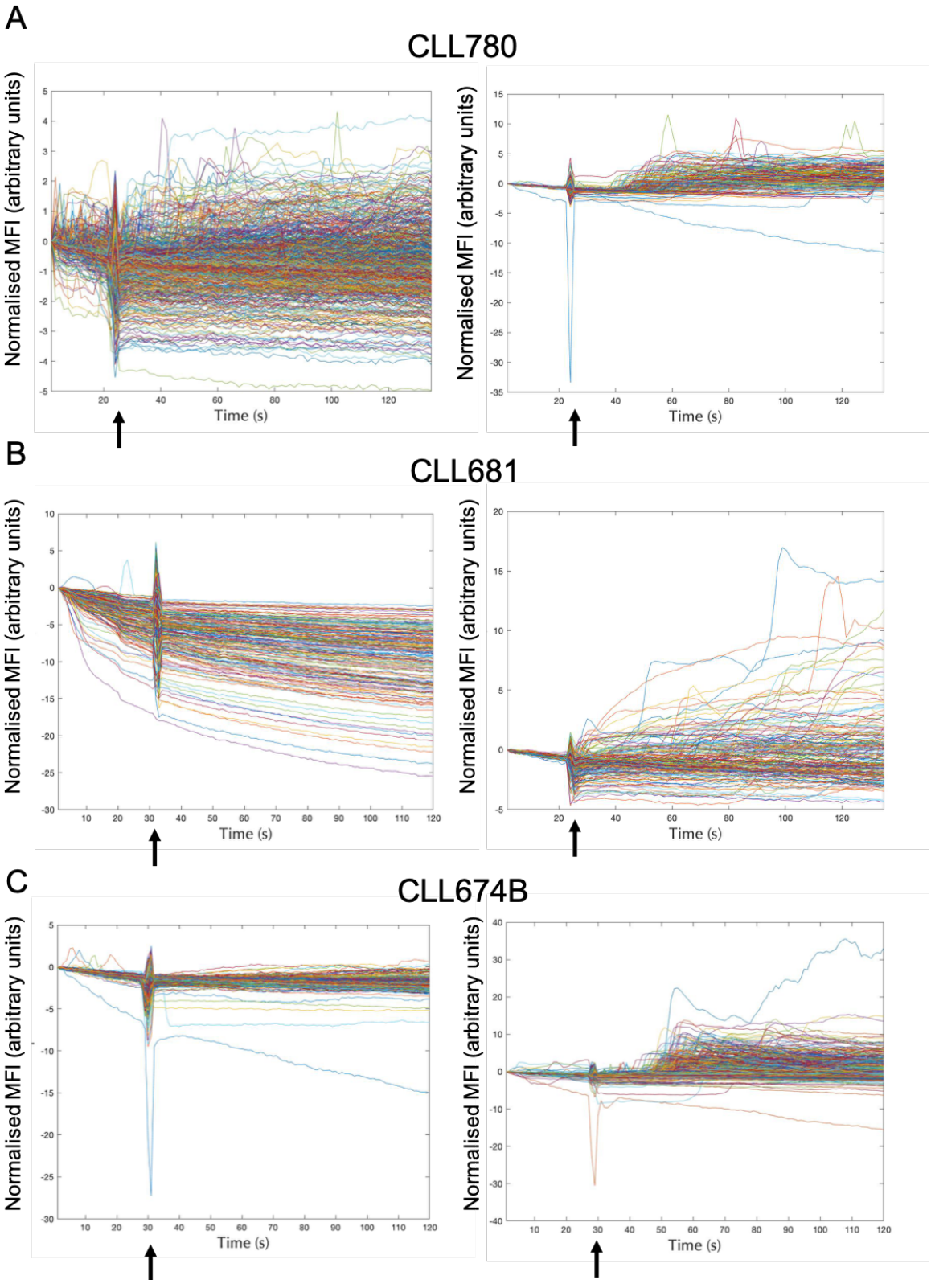
A
CLL780
Normalised MFI (arbitrary units)
Time (s)
B
CLL681
Normalised MFI (arbitrary units)
Time (s)
C
CLL674B
Normalised MFI (arbitrary units)
Time (s)

D

CLL635

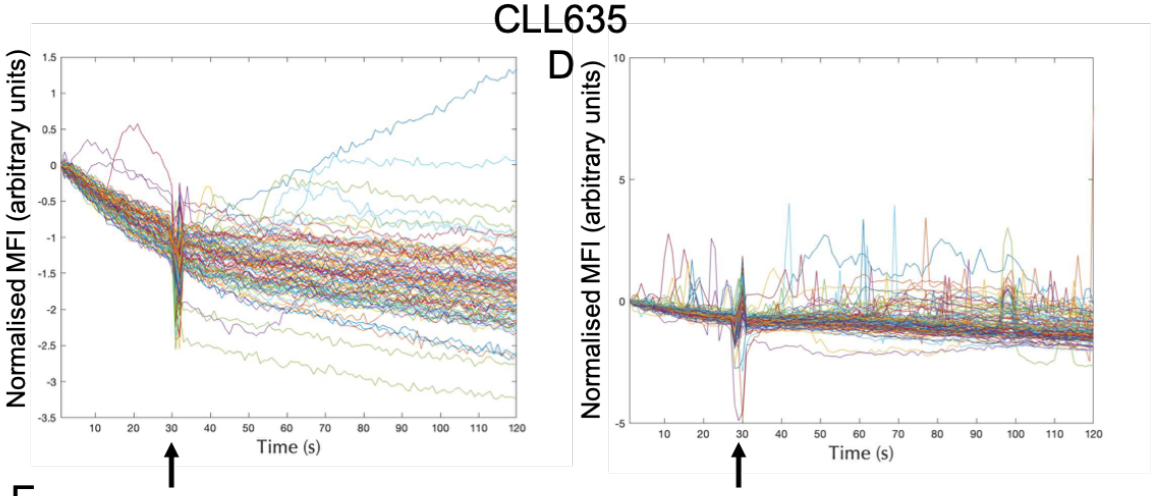

E

CLL774

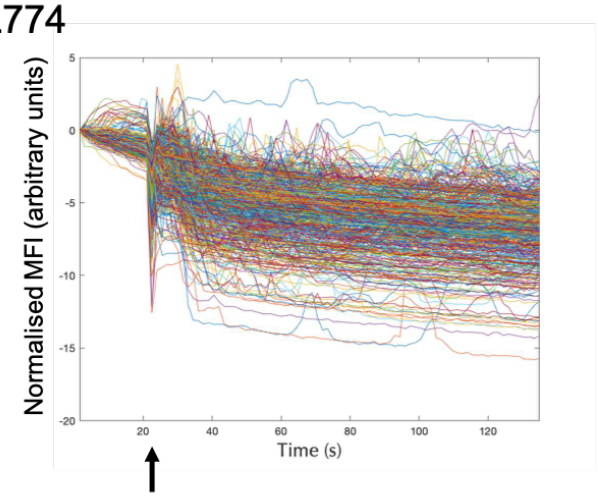

F

CLL803B

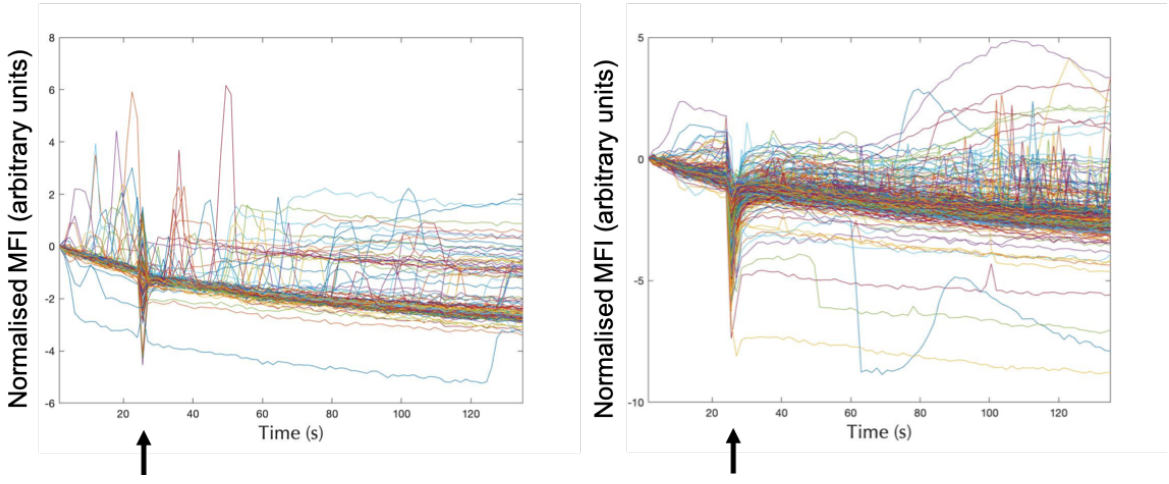

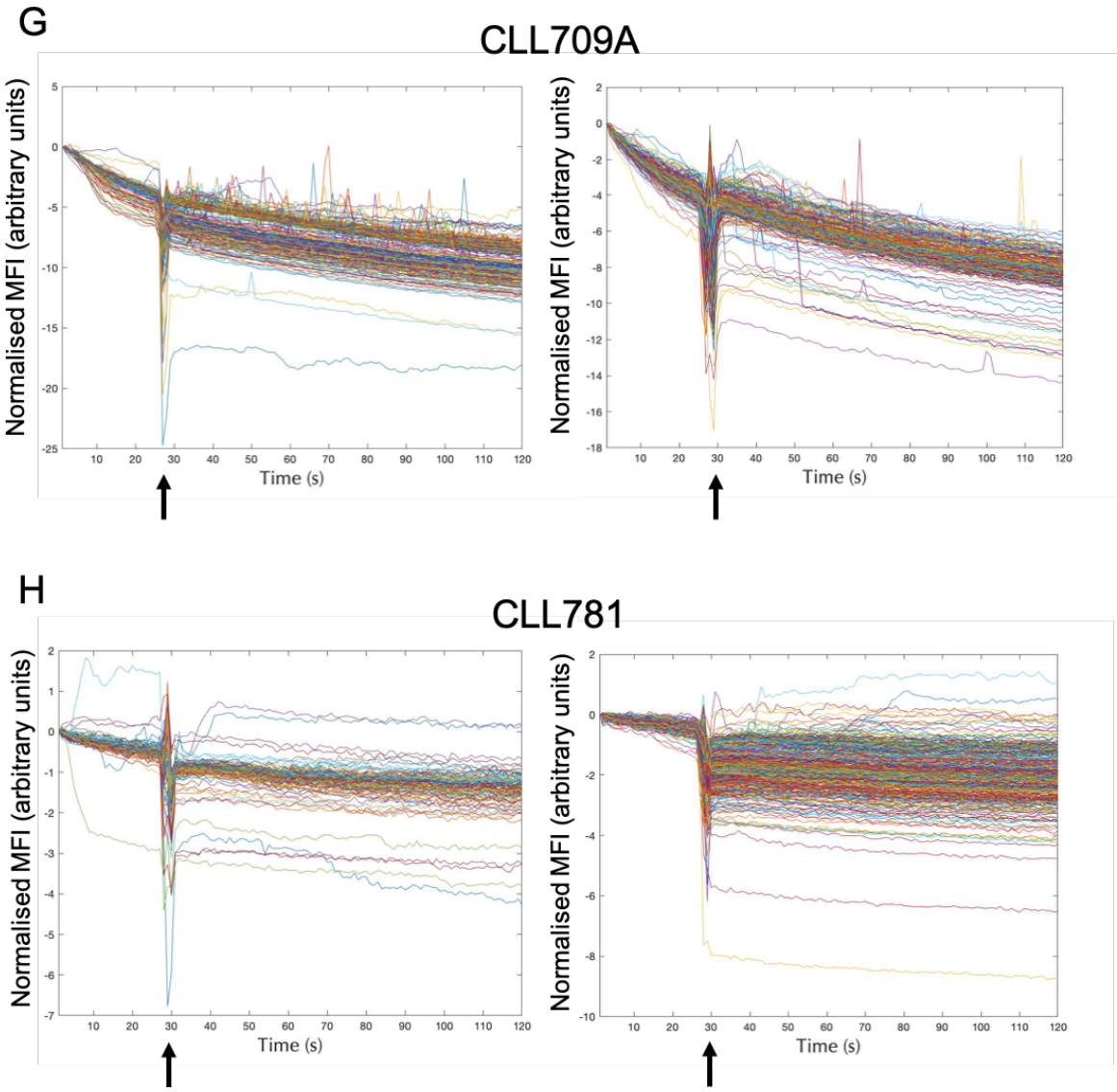

FIGURE 5-16: ANTI-IGM-INDUCED iCA^{2+} MOBILIZATION ANALYSIS IN PRIMARY CLL SAMPLES TRAPPED IN MICROWELL ARRAYS.

Untreated cells, with the exception of CLL 681 **(B)** which had been pretreated with DMSO prior to anti-IgM stimulation, were stimulated with either control antibody (left hand graph of each pair) or anti-IgM (right hand graph of each pair) following ~30 seconds of baseline data collection (indicated by the arrow on the x axis of each graph) and images were captured until 2 minutes. Data could for CLL 774 **(E)** following addition of control antibody could not be analysed because the array moved during data acquisition.

5.7.3 Anti-IgM responses following pretreatment with kinase inhibitors

Each sample was pretreated with 1 μM ibrutinib, 1 μM acalabrutinib, 10 μM R406 or DMSO alone for 1 hour prior to staining with Fluo-8 AM. The data presented in this section shows the results for the 3 CLL samples where a response to anti-IgM could be detected (the data for all samples is included in **Supplementary Figures 12 - 19**).

For each of these samples the results following ionomycin addition and anti-IgM (or control antibody) stimulation have been shown previously (**Figure 5-15** and **Figure 5-16**), but are included in the following figures for completeness but will not be discussed in detail again.

5.7.3.1 CLL 780

Pretreatment with DMSO as a control was investigated and the majority of the cells pretreated with DMSO alone showed a small but clear increase in response to anti-IgM stimulation (**Figure 5-17D**). Pretreatment with kinase inhibitors was generally very effective at inhibiting any response observed, with R406 being particularly effective (**Figure 5-17E**). Although there were very few ibrutinib-pretreated cells trapped in the array, there was very little response to anti-IgM stimulation observed (**Figure 5-17F**). Similarly, with acalabrutinib-pretreated cells there has only minimal responses observed in a small proportion of cells towards the end of the time course but otherwise acalabrutinib appeared to inhibit signalling responses (**Figure 5-17G**).

5.7.3.2 CLL 681

Pretreatment with kinase inhibitors was generally very effective at inhibiting any response observed, with R406 being particularly effective (**Figure 5-18D**) although there was a large movement of cells creating an artefact which makes interpretation of the results more challenging. There were relatively few cells trapped in the arrays for both ibrutinib- or acalabrutinib-pretreated cells but in each case there was very little response to anti-IgM stimulation observed, with a few notable cells that appeared to retain some signalling capacity but which showed a delay in their response to anti-IgM stimulation (**Figure 5-18E and 5-18F**, respectively).

5.7.3.3 CLL 674B

The majority of the cells pretreated with DMSO alone showed very little response to anti-IgM stimulation with a small proportion of cells exhibiting larger responses (**Figure 5-19D**), however in this case, there was a large movement of cells creating an artefact which makes interpretation of the results difficult. Pretreatment with kinase inhibitors was generally very effective at inhibiting any response observed, with R406 being particularly effective with the exception of one notable cell that presented an increased response to anti-IgM stimulation (**Figure 5-19E**). Similarly, both ibrutinib or acalabrutinib pretreatment reduced the number of cells responding to anti-IgM stimulation (**Figure 5-19F and 5-19G**, respectively), however in both cases there were a few cells which appear to retain their signalling ability despite inhibitor treatment. Interestingly in acalabrutinib-pretreated cells, there appeared to be a delay in the responses seen (**Figure 5-19G**).

5.7.3.4 Summary

In summary, there is some promising evidence that iCa^{2+} responses can be observed in CLL cells using microwell arrays. Ionomycin responses are clear although show much more variability than expected. This could be an interesting finding if proven to be a biological response and not a technical issue. Although anti-IgM responses were not consistently detected, they were validated by effective inhibition with kinase inhibitors, which also showed a very small population of cells that appeared to maintain signalling capacity and might represent 'atypical' responses.

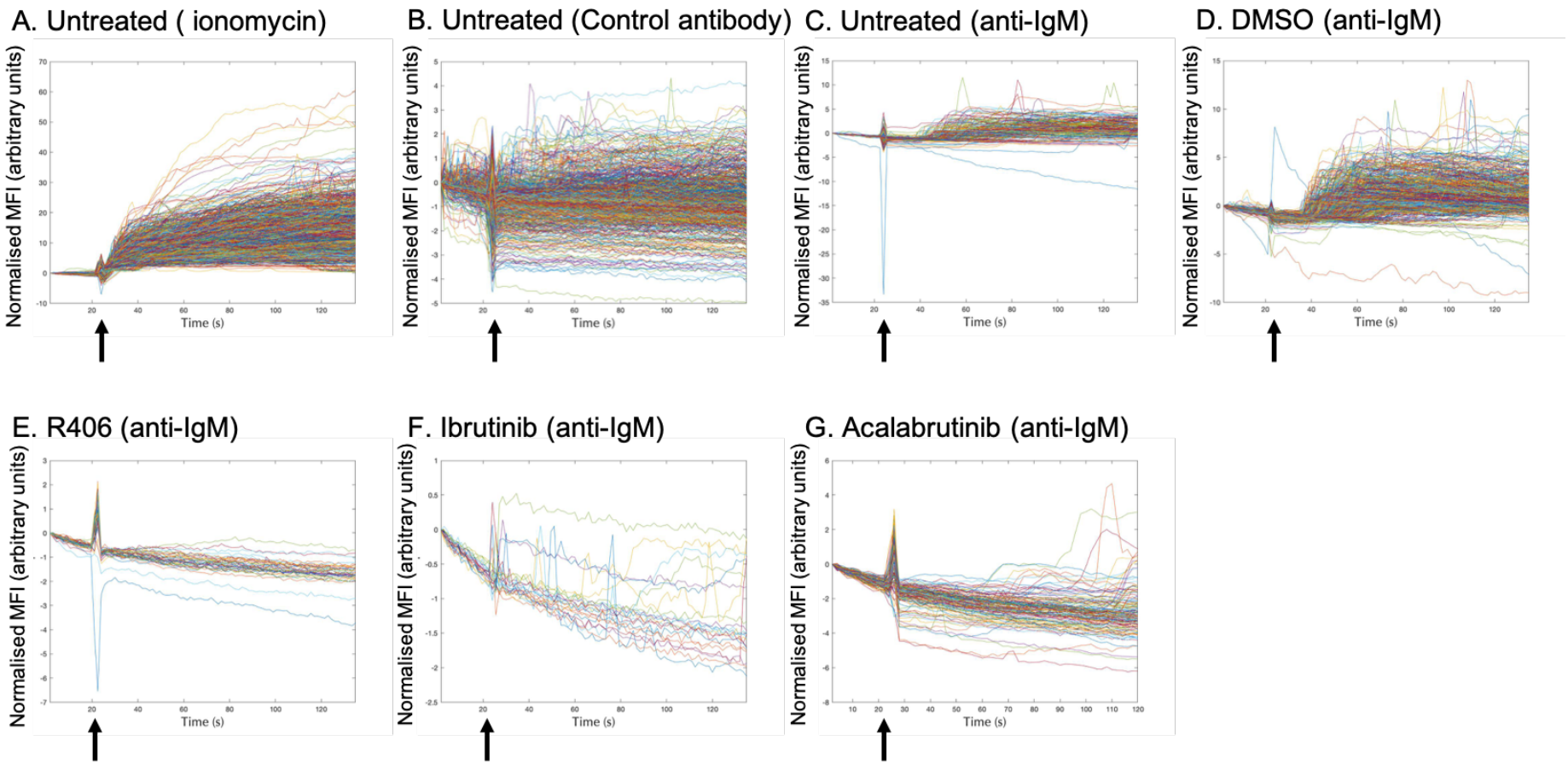

FIGURE 5-17: ANTI-IGM-INDUCED ICA^{2+} MOBILIZATION ANALYSIS IN CLL 780 TRAPPED IN MICROWELL ARRAYS.

Following collection of ~30 seconds of baseline data, untreated cells were stimulated with ionomycin **(A)**, control antibody **(B)** or anti-IgM **(C)** before data acquisition until 2 minutes. Baseline data for cells pretreated with DMSO **(D)**, R406 **(E)**, ibrutinib **(F)** or acalabrutinib **(G)** was collected for 30 seconds before stimulation with anti-IgM and data was acquired until 2 minutes. The arrows on the x axis of each graph indicate time of addition of ligand.

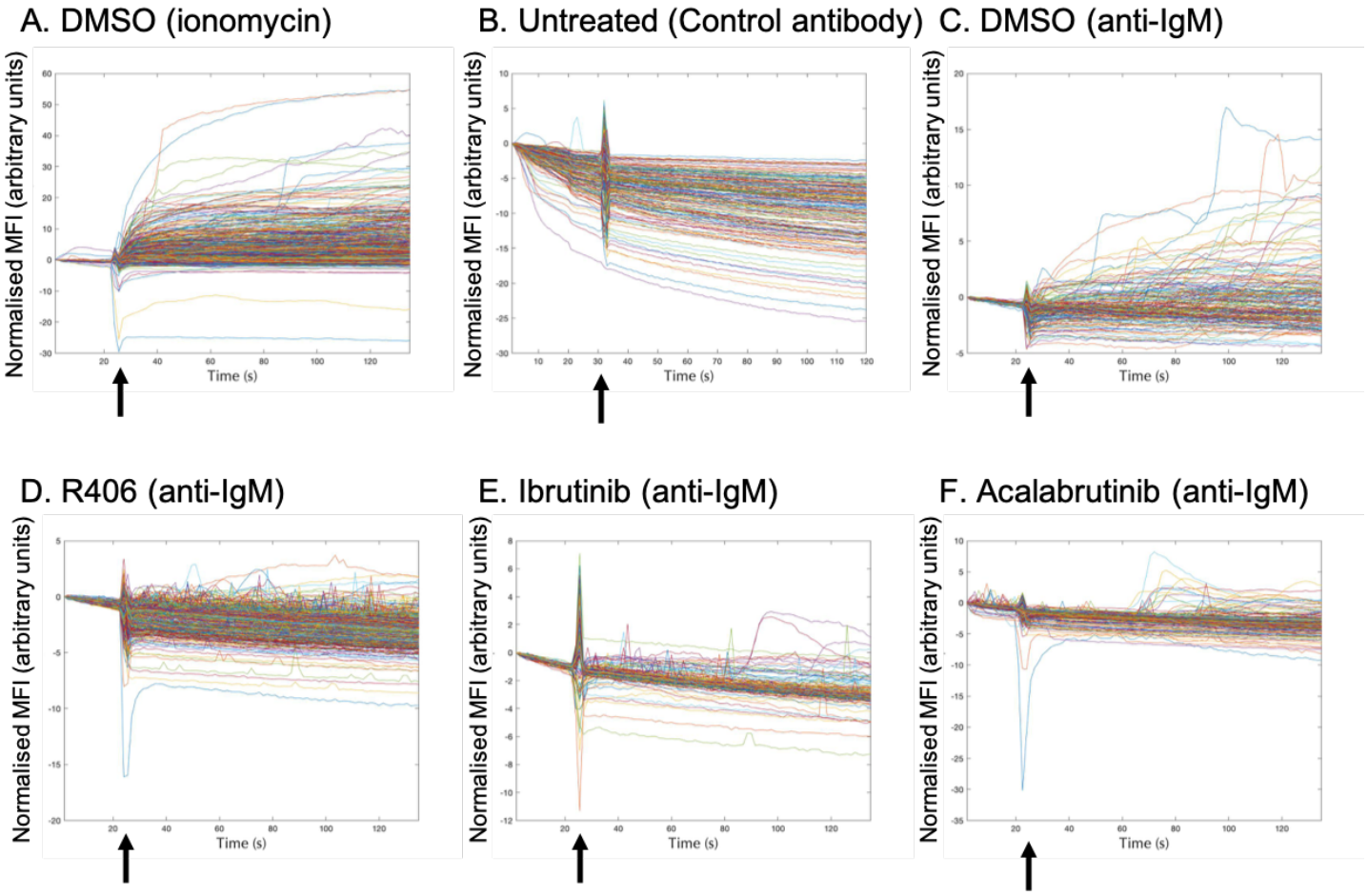

FIGURE 5-18: ANTI-IGM-INDUCED ICA^{2+} MOBILIZATION ANALYSIS IN CLL 681 TRAPPED IN MICROWELL ARRAYS.

Following collection of 30 seconds of baseline data, DMSO-pretreated cells were stimulated with ionomycin **(A)** or anti-IgM **(C)** and untreated cells were stimulated with control antibody **(B)** and data was acquired until 2 minutes. Baseline data for cells pretreated with R406 **(D)**, ibrutinib **(E)** or acalabrutinib **(F)** was collected for 30 seconds before stimulation with anti-IgM and data was acquired until 2 minutes. The arrows on the x axis of each graph indicate time of addition of ligand.

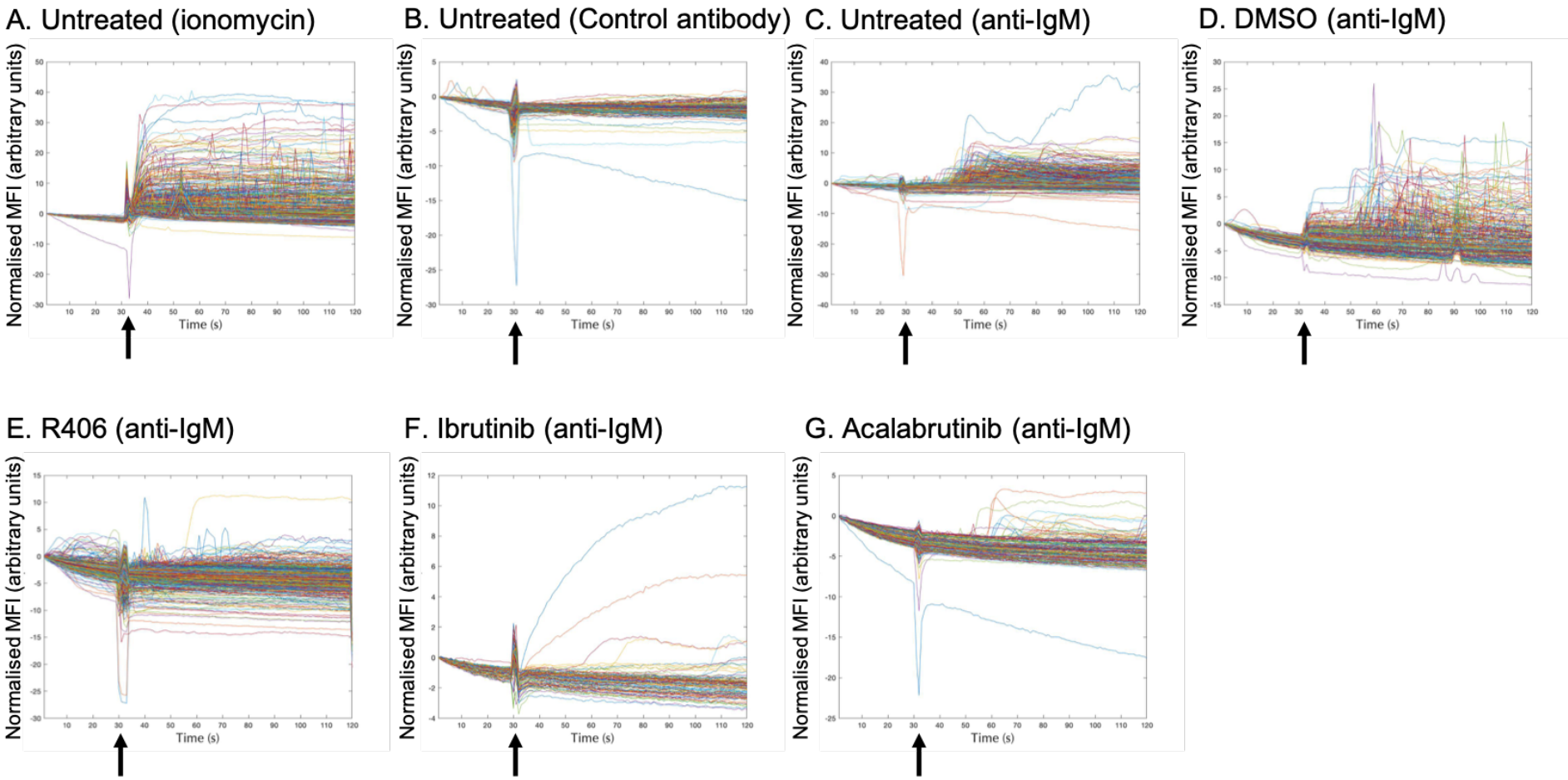

FIGURE 5-19: ANTI-IGM-INDUCED iCa^{2+} MOBILIZATION ANALYSIS IN CLL 674B TRAPPED IN MICROWELL ARRAYS.

Following collection of 30 seconds of baseline data, untreated cells were stimulated with ionomycin **(A)**, control antibody **(B)** or anti-IgM **(C)** before data acquisition until 2 minutes. Baseline data for cells pretreated with DMSO **(D)**, R406 **(E)**, ibrutinib **(F)** or acalabrutinib **(G)** was collected for 30 seconds before stimulation with anti-IgM and data was acquired until 2 minutes. The arrows on the x axis of each graph indicate time of addition of ligand.

5.8 Discussion

There is good evidence of an association between signalling capacity and clinical outcome whereby "high-signallers" have a poorer median survival than "low-signallers" (D'Avola et al., 2016)(D'Avola et al., 2016), which could be caused by a small subset of malignant cells that are able to evade treatment contributing to a disease-resistant subclone which promotes disease relapse or progression. The current method of flow cytometry for analysing signalling capacity has one primary limitation that we want to address: the inability to study time-resolved responses of single-cells, allowing the identification and further analysis of cells with 'atypical' signalling responses.

The overall goal of the experiments in this chapter were to allow fabrication of a suitable device and optimisation of the device for use with primary CLL cells. The devices were then used to analyse iCa^{2+} mobilisation in primary CLL samples. As an additional aim, the experiments were also designed to investigate whether the method could be extended to other B-cell malignancies by using OCI-Ly7 cells, a DLBCL cell line. To achieve this, I addressed four specific aims:

1. Perform exploratory experiments using existing arrays to determine approximate suitable microwell sizes and proof of concept for data collection, including the comparison of Ca^{2+} indicator dyes.
2. Design and fabricate wafers with a range of microwell diameters and heights.
3. Identify optimal microwell size and cell seeding conditions for primary CLL samples.
4. Quantify single-cell anti-IgM-induced iCa^{2+} signalling responses (including pre-treatment with kinase inhibitors) in CLL samples.

Summary of main findings:

- Fluo-8 AM Ca^{2+} indicator dye is brighter, allowing a reduced exposure time to be used when acquiring images, and therefore is more suitable for the microwell array assay, to reduce the effects of photobleaching.
- The optimal microwell size and cell seeding conditions selected for 'trapping' CLL cells is 11 μm diameter and a cell seeding ratio of 50 to 1 cells per microwell.

- For successful fabrication of a wafer with features as small as 10 μm, the exposure parameters required are 100 mJ/cm^2.
- There is some evidence that arrays can be used to assess iCa^{2+} flux and inhibitor responses, but at present it remains a rather insensitive method to study iCa^{2+} responses and it could not reliably detect an anti-IgM response.
- Interestingly, there is some indication of a small number of cells that respond differently to the main population, which might be masked in flow cytometry analysis.
- Overall, there are substantial technical challenges that would need to be solved, particularly method of ligand addition and the general low sensitivity, before robust results can be obtained.

The results presented in this chapter show that, at present, the use of microwell arrays for analysing iCa^{2+} mobilisation is not a sufficiently robust method, but does hold some promise if the technical challenges can be addressed. In light of the drawbacks and limitations, interpretation of biological findings made to date are tentative and should be considered with caution.

5.8.1 Technical drawbacks of microwell arrays

There are three key limitations of the microwell arrays, introduced at the beginning of this chapter, which require addressing and further optimisation to improve this method for analysing iCa^{2+} release. These include the cell seeding procedure, addition of reagents and the general sensitivity of the assay (including photobleaching of cellular dyes).

The aim for cell seeding is to 'trap' ≥1000 cells in each array to increase chances of detecting 'atypical' responders which could be rare in the population. With the current design which includes 1250 microwells in each array that means a single-cell occupancy of ≥80% is required. Currently, the method relies on sedimentation of cells which, whilst an easy and straightforward method, has not allowed for consistent or reproducible results for high single-cell occupancy (**Figure 5-13**). A simple way to overcome this is to re-seed the array. An array would initially be seeded with the optimal cell seeding density, in this case 50 to 1 cells per microwell, and left for 30 minutes for sedimentation to occur. The array would be rinsed and cells reapplied to the surface of the array and given time for sedimentation. This should increase the likelihood of any given microwell to contain a cell, but would require further investigation to ensure that the

number of microwells with multiple cells per microwell did not also increase. Since this would lead to a longer time delay between preparation of cells and image capture, cell viability in the microwell arrays should be assessed to investigate whether there are any effects on signalling ability caused by this extended time period. Alternative methods for trapping single CLL cells for iCa^{2+} flux analysis will be discussed in **Section 6.7.**

The method for addition of reagents also requires further optimisation. As mentioned in **Section 5.1,** preliminary experiments using OCI-Ly7 cell line showed that the simplest, more reproducible method for adding the ligand to the array was to pipette it directly onto the surface of the array (**Supplementary Figure 11**), but this was still not completely consistent. The key problems with this method included the movement of the array under the microscope if the pipette tip touched the array, this led to the results either being significantly reduced because fewer cells were captured in all frames or meant that the data captured could not be used at all. This could be improved by constructing a holder for the array. Another drawback of this method of ligand addition is the artefact created by the addition of ligand if/when the pipette tip passes between the array and the microscope. Whilst this can be excluded from the analysis it can create large artefacts which impact the scale of the *y* axis, presenting fluorescence intensity, making it more difficult to distinguish smaller, biologically relevant responses. The artefact might also obscure the initial iCa^{2+} response immediately following addition of ligand. The final limitation with this method is the time taken for the ligand to spread over the array after addition because the time it takes to spread across the array and make contact with the cells can vary within and between experiments. This could contribute to a delay in the response of a given cell that could be misinterpreted as a biologically relevant 'atypical' signaller. In general, the arrays are small enough that the ligand should flood the array quickly, but this is not always the case and is not necessarily consistent between experiments. The alternative method investigated in the preliminary work used a coverslip placed on top of the array to allow the ligand to be pipetted at the edge of the array and transported across the surface by capillary action. This method was less likely to wash cells out of the microwells, however movement under the microscope was still an issue (although again, this could be resolved with a holder for the array). The main problem with this method was that following ligand addition the images became very blurry and therefore fluorescence intensity could not be measured accurately. It is possible that the microwell arrays could be coupled to microfluidic devices that deliver ligand more directly to the array being imaged without requiring a pipette to be near the surface of the array, reducing movement and the associated problems (discussed further in **Section 6.7**).

The general sensitivity of this assay also appeared quite low, and photobleaching of the Ca^{2+} indicator dye might also contribute to an apparent lack of sensitivity. This sensitivity could be addressed by increasing the concentration of ligand added to the array to ensure that there is sufficient ligand available to interact with the cells and initiate a response. The effect of photobleaching of the dyes can be corrected for in the data analysis. This would require the photobleaching effects to be analysed in unstimulated cells and if the level of photobleaching is consistent across multiple samples tested then the data could be corrected for the level of photobleaching expected to occur, reducing this effect on the data analysed and preventing the likelihood of misidentified biological effects.

5.8.2 Possible biological signatures and patterns of signalling behaviour

As already highlighted, the current method used for analysing iCa^{2+} mobilisation in cells trapped in the microwell array is not sufficiently robust due to the technical challenges raised and discussed. This, along with the relatively small number of CLL samples analysed with this approach, means that interpretation of biological findings made to date are tentative and should be considered with caution. Whilst some conclusions will be tentatively speculated and discussed it is important to note that at this stage, a somewhat superficial analysis was conducted to demonstrate how the microwell arrays could be used in the future and to present a proof of principle and highlight the need for time-resolved single-cell analysis over time as well as requirement for optimisation of the technique.

However, in general, samples, or at least proportions of samples, responded to ionomycin (**Figure 5-15**) and anti-IgM-induced iCa^{2+} responses were seen in some samples (**Figure 5-16**) which were validated by the ability of kinase inhibitors to suppress the responses observed (**Figure 5-17 - Figure 5-19**). The responses to anti-IgM stimulation were quite varied within and between samples which could be an interesting phenomenon to investigate further if these results could be confirmed with more samples analysed. To further support the validation of these results, it was clear that pretreatment with R406 more effectively inhibited anti-IgM-induced iCa^{2+} release in these cells than BTKi pretreatment, as seen in flow cytometry data (**Figure 4-2**), with the exception of one notable cell in CLL674B (**Figure 5-19**) that appears to retain its signalling ability despite R406 treatment. Interestingly, in all three samples where an anti-IgM-induced iCa^{2+}

response was observed, pretreatment with ibrutinib or acalabrutinib did not fully inhibit all cells. In each case, there was always a very small population of cells that appeared to retain some signalling ability, compared with the level of inhibition achieved in the rest of the population, despite BTKi treatment. In most cases, the responses observed were delayed from the time of anti-IgM stimulation although at this stage it is hard to be sure whether this is a biological effect or part of the technical limitations to be addressed. The interesting point here though, is that these samples were selected based on their flow cytometric analysis classifying them as "high-signallers", and BTKi pretreatment only resulted in a partial inhibition of iCa^{2+} signalling, which is in agreement with the results from **Chapter 3** whereby "high-signallers" were generally only partially inhibited by BTKi.

Considering that the samples were selected to be relatively high signallers to ensure the best possible chance that responses would be seen using the arrays there were surprisingly weak signals observed in some samples and an anti-IgM-induced signal could not reliably be detected. There was also a considerable level of variation in the ionomycin responses, both within and between samples. The key question is whether this variation is driven by technical limitations or whether it reveals something interesting regarding the biology of signalling behaviour or suggests differences in iCa^{2+} stores and subsequent release into the cytoplasm.

Despite the overall weak signals observed and perhaps the lack of sensitivity of the assay using microwell arrays, there were cells with atypical signalling and/or inhibitor responses clearly observed (most notably in CLL681 and CLL674B, **Figure 5-18 and Figure 5-19**, respectively) and it would be interesting to investigate this further, both by determining whether these atypical responses were seen in other samples, whether they were reliably detected in repeat experiments using the same sample and also whether they are the result of technical drawbacks. It is possible that these cells are 'cells of interest' that might lead to confirmation of the hypothesis that a small subset of cells, which have an 'atypical' signalling and/or inhibitor response, contribute to treatment resistance and the subsequent disease relapse/progression observed in patients. It would be important to first clarify whether these are in fact CLL cells and not normal B cells, although all samples chosen had a tumour population of ≥85%. In future analyses, CD19 and CD5 staining could be included in the preparation of samples to ensure that any cells identified as 'atypical' responders can confidently be identified as CLL cells.

Finally, the data was normalised to set the baseline iCa^{2+} fluorescence intensity to zero, allowing comparisons to be made between cells in the same sample, and also allowing tentative comparisons between samples. Whilst this provides some advantages for data analysis by reducing variation to allow comparisons to be made, the reduction in variation of basal iCa^{2+} loses information that could be useful or interesting. For example, cells with high basal iCa^{2+} flux might not exhibit an anti-IgM-induced increase in iCa^{2+} release because they are anergised.

Overall, these results show some evidence for utilising microwell arrays for analysing iCa^{2+} flux in CLL cells but, at present, they do not provide a sufficiently robust method, and require several technical challenges to be addressed.

Chapter Six

Final Discussion

6 Final Discussion

6.1 Hypotheses

This thesis addressed two important challenges centred on activation of the BCR-associated signalling pathway leading to BTK and PLCγ2 activation, and the subsequent release of Ca^{2+} from intracellular stores in malignant B-cells. This is an important area of study because the signalling capacity of the BCR, measured by iCa^{2+} flux assay, directly correlates with outcome, suggesting that this parameter could be used as a disease biomarker. Moreover, this pathway is a key target for drug therapy, and ibrutinib, the first clinically approved BTK inhibitor, has revolutionised the treatment of patients with CLL. However, some patients experience resistance to ibrutinib therapy and new approaches to target this pathway may be beneficial.

The first part of this thesis addressed a potential BTK "by-pass" signalling pathway identified in the laboratory, whereby PLCγ2 is activated downstream of the BCR in CLL cells despite full BTK inhibition. By understanding this "by-pass", it may be possible to more effectively inhibit activation of signalling to iCa^{2+} mobilisation in patients. The second part of this thesis focussed on development of new techniques to quantify time-resolved, single-cell iCa^{2+} flux. Although these studies were at a very early stage, the longer-term potential is that such an approach could improve the potential prognostic value of iCa^{2+} mobilisation analysis, perhaps by identifying small numbers of cells within the malignant clone with 'atypical' signalling behaviour.

The specific hypotheses were:

1. The inhibitory effects of BTKi on anti-IgM-induced iCa^{2+} fluxes are variable between CLL samples, reflecting the action of a BTK "by-pass" mechanism whereby activation of PLCγ2 and subsequent iCa^{2+} release occurs independently of BTK.

2. Microwell arrays are a suitable platform for analysis of single-cell, time-resolved analysis of iCa^{2+} signalling in malignant B cells.

6.2 Summary of main findings

The key findings related to the first hypothesis (addressed in **Chapters 3 and 4**) were:

- Ibrutinib and acalabrutinib variably, but generally only partially, inhibited anti-IgM-induced iCa^{2+} fluxes in CLL samples. Therefore, "by-pass" is a drug class effect and not an ibrutinib specific effect.
- Partial inhibition by BTK inhibitors was associated with strong sIgM signalling capacity.
- Analysis of a BTK-degrading PROTAC demonstrated that "by-pass" was not mediated by a kinase-independent function of BTK.
- BTK "by-pass" signalling was not specific for CLL cells and was also observed in DLBCL cell lines.
- In CLL and DLBCL cell lines, BTK "by-pass" was associated with retained anti-IgM-induced phosphorylation of PLCγ2 on Tyr^{753} and Tyr^{759} (but not Tyr^{1197} and Tyr^{1217}).

The key findings related to the second hypothesis (addressed in **Chapter 1**) were:

- There is some evidence that arrays can be used to assess iCa^{2+} flux and inhibitor responses. However, at present it remains a rather insensitive method to study iCa^{2+} responses and it could not reliably detect an anti-IgM response.
- There was some indication of a small number of cells that respond differently to the main population, which might be masked in flow cytometry analysis.
- There are substantial technical challenges that would need to be solved, particularly method of ligand addition and the general low sensitivity, before robust results can be obtained.

Overall, the data presented in this thesis supports the hypothesis that a BTK "by-pass" mechanism exists whereby PLCγ2 is activated independently of BTK in a subset of CLL samples. The association between operation of this "by-pass" and signal capacity indicates that it is acquisition of "by-pass" which actually mediates strong signal. The data presented also provides evidence to tentatively support the hypothesis that microwell arrays can be used to assess iCa^{2+} flux in

malignant B cells, but the technique is currently not able to provide substantial evidence due to technical challenges that need to be resolved.

6.3 BTK "by-pass" signalling

A key conclusion from this thesis is that the anti-IgM-induced iCa^{2+} response of "high-signallers" can only be partially inhibited by BTKi (**Figure 3-1, Figure 3-2, Figure 4-1, and Figure 4-2**) revealing the presence of BTK "by-pass" signalling to PLCγ2 activation (**Figure 4-15 and Figure 4-16**). The results presented here suggest that it is likely that canonical BCR signalling (i.e. SYK→BTK→PLCγ2) with the addition of this BTK-independent pathway causes the high-signalling seen in some samples, whereas samples termed "low-signallers" rely solely on canonical BCR signalling. **Figure 6-1** summarises this proposed model, and describes how inhibition of BTK will either partially or fully inhibit iCa^{2+} signalling in high- or low-signallers respectively and this also influences downstream transcription responses and survival.

The most likely explanation for the engagement of a "by-pass" pathway in addition to the canonical signalling pathway in a subset of samples is that the "by-pass" pathway has a higher threshold for activation than the canonical pathway. Although the nature of the "by-pass" pathway has not been fully revealed, it is clear from previous work that distinct arms of the BCR response are not necessarily always engaged in unison, but are sensitive to signal strength and can therefore be activated selectively. For example, Healy *et al*. (Healy et al., 1997) showed that antigen exposure of naïve B cells stimulated a biphasic Ca^{2+} response that leads to activation of nuclear signals via NFAT, NF-κB, JNK and ERK, whereas the same ligand has a negative effect in self-reactive B cells which exhibit a much smaller Ca^{2+} response leading to activation of NFAT and ERK only. Similarly, Berry *et al*. (Berry et al., 2020) showed weak BCR engagement led to apoptosis by the lack of NF-κB survival signals, but stronger BCR engagement promoted NF-κB survival and also enhanced cell cycle entry and proliferation through activation of NFAT, mTORC1 and MYC. Benson *et al*. (Benson et al., 2007) provide evidence that the affinity of the BCR, and therefore the signal strength mediated by the BCR, along with other environmental stimuli, determine the fate of GC B cells. The authors suggest that an initial high-affinity drives the B cell towards plasma cell differentiation whereas initial lower affinity drives the B cell towards long-lived plasma cell and memory cell formation.

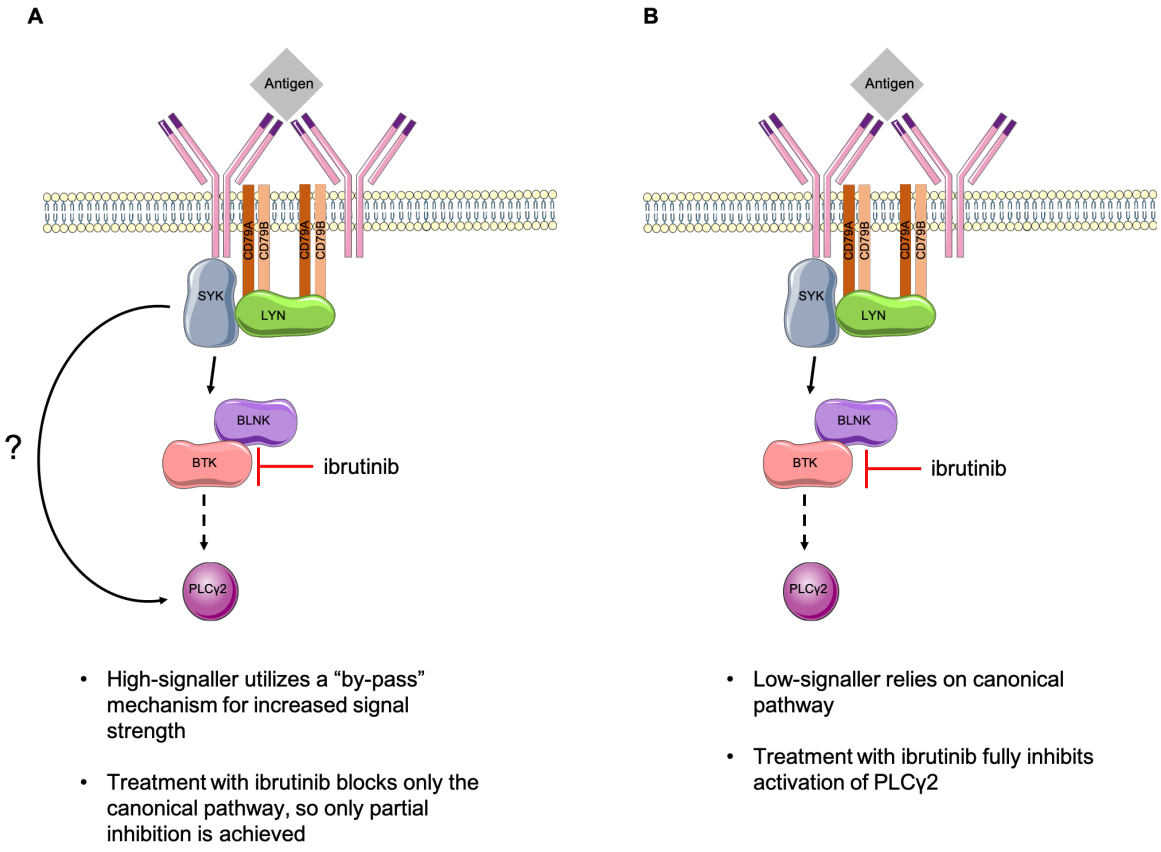

- High-signaller utilizes a "by-pass" mechanism for increased signal strength
- Treatment with ibrutinib blocks only the canonical pathway, so only partial inhibition is achieved

- Low-signaller relies on canonical pathway
- Treatment with ibrutinib fully inhibits activation of PLCγ2

FIGURE 6-1: PROPOSED MODEL OF ENGAGEMENT OF BTK "BY-PASS" PATHWAY AND THE EFFECT OF BTK INHIBITION.

A. Canonical BCR signalling (SYK→BTK→PLCγ2) and "by-pass" signalling operate together in samples classified as "high-signallers". Pretreatment with BTKi only block canonical BCR signalling and therefore only partial inhibition of downstream signalling occurs. **B.** "Low-signallers" rely on canonical BCR signalling, and therefore the pathway can be fully inhibited by BTKi.

A key question surrounding the potential BTK "by-pass" mechanism was whether the mechanism was entirely BTK-independent or whether it relied on kinase-independent functions of BTK, e.g. scaffolding functions (Saito et al., 2003; Roman-garcia et al., 2018; Buggy and Elias, 2012). This was investigated using a BTK-specific PROTAC to target BTK for proteasomal degradation. The data shows that the BTK "by-pass" mechanism is largely BTK independent since BTK degradation had no further inhibitory effects on anti-IgM-induced iCa^{2+} mobilisation (**Figure 3-9**). This was supported by other experiments from the laboratory, which investigated the effect of idelalisib, a PI3K inhibitor, on iCa^{2+} flux in primary CLL. As described in **Section 1.3.3**, the PI3K pathway is one of the major BTK kinase-independent pathways downstream of the BCR with some evidence of interaction and activation of PLCγ2 (Hippen et al., 1997; Mette Buhl and Cambier, 1999; Kim et al., 2004). Experiments performed in the laboratory showed that pretreatment with idelalisib alone was not as effective at inhibiting iCa^{2+} flux as ibrutinib alone, and when used in combination with ibrutinib there was no substantial additional inhibitory effects compared with ibrutinib treatment alone (B. Valle-Argos, personal communication). This supports the conclusion that BTK "by-pass" does not rely on kinase-independent functions of BTK. Although there was no evidence in my study for an advantage of using PROTACs over ibrutinib (at least for iCa^{2+} signalling), they still remain of outstanding interest for further investigation, and potential treatment, including of cases with mutant BTK, for which they are much more effective against than ibrutinib (Arthur et al., 2020).

Based on my results, there were three main hypotheses to explain BTK-independent "by-pass" signalling via PLCγ2 activation (**Figure 6-2**), although it should be noted that these are not mutually exclusive and more than one might contribute to the mechanism.

1. Retained (BTK-independent) phosphorylation of PLCγ2 on $Tyr^{753/759}$ is sufficient for activation and IP_3 generation.

Evidence from mutation studies in B cells, described in detail in **Section 1.3.4**, supports the hypothesis that phosphorylation of Tyr^{753} and Tyr^{759} are sufficient for, at least partial, activation of PLCγ2. Watanabe *et al*. (Watanabe et al., 2001) showed that individual mutation of each of the four key phosphorylation sites reduced iCa^{2+} flux, but simultaneous mutation of all four sites was required for full ablation of PLCγ2 activity. Thus, retention of Tyr^{753} and Tyr^{759} phosphorylation is associated with some retained PLCγ2 activity. This was confirmed by studies from Humphries *et*

al. (Humphries et al., 2004). Rodriguez *et al*. (Rodriguez et al., 2001) demonstrated full ablation of anti-IgM-induced iCa^{2+} flux after mutations in both Tyr^{753} and Tyr^{759}. This evidence points to $Tyr^{753/759}$ as major sites of phosphorylation required for PLCγ2 activation.

One key question is what kinase(s) may be capable of phosphorylating PLCγ2 Tyr^{753} and Tyr^{759} in the presence of BTK inhibitors. Kim *et al*. (Kim et al., 2004) used RNAi to deplete SYK in Ramos cells and showed reduced phosphorylation of Tyr^{753}, Tyr^{759} and Tyr^{1217}. This was consistent with studies by Takata *et al*. (1994) in DT40 cells suggesting an essential role for SYK upstream of PLCγ2. The data presented in this thesis also supports the hypothesis for SYK directly phosphorylating and activating PLCγ2 whereby full inhibition of iCa^{2+} flux and all downstream signalling molecules, including phosphorylation of PLCγ2, following treatment with R406, a SYK inhibitor, is observed. In addition, kinases responsible for BTK-independent phosphorylation of PLCγ2 need to be 100-fold less sensitive to ibrutinib than BTK (**Section 4.7.2**), and the data from Honigberg *et al*. (2010) is consistent with the idea that SYK may be a likely candidate. Therefore, I speculate that SYK directly phosphorylates PLCγ2, although at this stage other kinases contributing to this activation cannot be ruled out. SYK inhibition has been, and is still being, explored with promising results in CLL (ten Hacken and Burger, 2016), and will be discussed further in **Section 6.4**.

2. Phosphorylation-independent activation of PLCγ2.

The second hypothesis is phosphorylation-independent activation of PLCγ2. PLCγ2 exists in an autoinhibited state mediated by the SH2 domain and maintained by the split PH domain in the absence of tyrosine phosphorylation (Koss et al., 2014). Phosphorylation of the tyrosine residues within PLCγ2, specifically those in the SH2-SH3 linker region (Tyr^{753} and Tyr^{759}), cause conformational changes allowing PLCγ2 to move from an autoinhibited state to an "open" confirmation whereby the active site, located in the TIM barrel, becomes available and catalysis can proceed (Koss et al., 2014). Whilst this activation is based on tyrosine phosphorylation, there is evidence for phosphorylation-independent activation of PLCγ by various lipid-derived second messengers, including phosphatidic acid, PIP_3, and arachidonic acid (reviewed in (Sekiya et al., 1999)). More recently, studies have found BCR-mediated activation of Vav/Rac directly activates PLCγ2 (Piechulek et al., 2005; Bunney et al., 2009), introduced in **Section 1.3.6.**

BCR engagement induces SYK- and LYN-dependent formation of "microsignalosomes" comprised of BTK, BLNK, Vav and PLCγ2 (Weber et al., 2008). SYK-dependent activation of Vav subsequently activates Rac, which selectively activates PLCγ2 through direct protein-protein interactions (Piechulek et al., 2005; Walliser et al., 2015). Interestingly, two of the most common PLCγ2 mutants found in CLL (R665W and L845F), are hypersensitive to Rac2 activation, which might explain the ibrutinib-resistance observed in these patients (Walliser et al., 2016). This might also provide novel strategies to overcome treatment-resistance with CLL patients with *PLCG2* mutations (Walliser et al., 2016).

Experiments carried out in the host laboratory used EHT-1864, an inhibitor of Rac (demonstrated by Walliser *et al*., 2016), in combination with ibrutinib to investigate whether iCa^{2+} mobilisation could be inhibited to a greater extent in primary CLL than ibrutinib treatment alone. Results did not show any additional inhibitory effects with the use of EHT-1864 (B. Valle-Argos, personal communication) suggesting that BTK "by-pass" pathway does not occur through Vav/Rac-mediated activation of PLCγ2. These results do not exclude the possibility that retained phosphorylation on PLCγ2 is not relevant, and that there is an alternative mechanism for phosphorylation-independent activation.

3. A role for PLCγ1.

The final hypothesis is retained phosphorylation of PLCγ1, which has the same enzymatic activity as PLCγ2. BCR-induced activation of PLCγ1, by phosphorylation of Tyr^{783}, can occur directly via SYK (Law et al., 1996) but is also BTK-dependent in some human B-cell lines (Humphries et al., 2004).

The results presented in this thesis show that in DLBCL cell lines, BTKi pretreatment reduces the level of phosphorylation of Tyr^{783} in a concentration-dependent manner, although full inhibition is not generally achieved at BTKi concentrations known to completely inhibit BTK **(Figure 4-7 - Figure 4-10**). However, in CLL phospho-PLCγ1 Tyr^{783} is generally very difficult to detect, even following IL-4 stimulation, suggesting that it does not play a major role in the BCR-associated signalling cascade (**Figure 4-15 and Figure 4-16**). In CLL, SYK inhibition with R406 variably but seemingly only partially inhibited phosphorylation of Tyr^{783} suggesting that SYK-dependent phosphorylation might contribute to activation of PLCγ1 in this setting, although further

investigation would be required. Overall, the contribution of PLCγ1 to iCa^{2+} mobilisation appears to be relatively low and is unlikely to be the sole mechanism for BTK "by-pass" but might be a contributing factor.

Finally, whilst the majority of my work focussed on primary CLL I did also extend analysis to DLBCL cell lines which is of interest clinically, as a different B-cell malignancy, but also biologically through distinct modes of BCR signalling and function. This is most interesting in those lines expressing the My-T-BCR (e.g. TMD8), which promotes ibrutinib-responsiveness, suggesting a greater reliance on BCR-associated signalling for survival (Phelan et al., 2018) and therefore opens opportunities for improved therapies. Both DLBCL cell lines used in this thesis (OCI-Ly7 and TMD8) retained features of "by-pass" suggesting that this mechanism is not CLL specific and might be occurring more widely in B-cell malignancies. However, as discussed above, it is important to note that BTKi predominantly influences the magnitude of the peak response in CLL cells, whereas these drugs accelerate the decline in iCa^{2+} levels after the peak in cell lines. This points to distinct roles of BTK in the two models whereby BTK is at least partly responsible for determining the magnitude of the initial release of iCa^{2+} in CLL cells, but seems to play a more prominent role in determining the kinetics of the response in the lymphoma cell lines. However, the observation that the initial magnitude of the response is at most partly inhibited by BTKi in CLL cells and the cell lines validates the cell lines as potential models to be used in the future into transfections studies to investigate operating mechanisms in much greater detail using genetic manipulation (e.g. RNAi, CRISPR-Cas9).

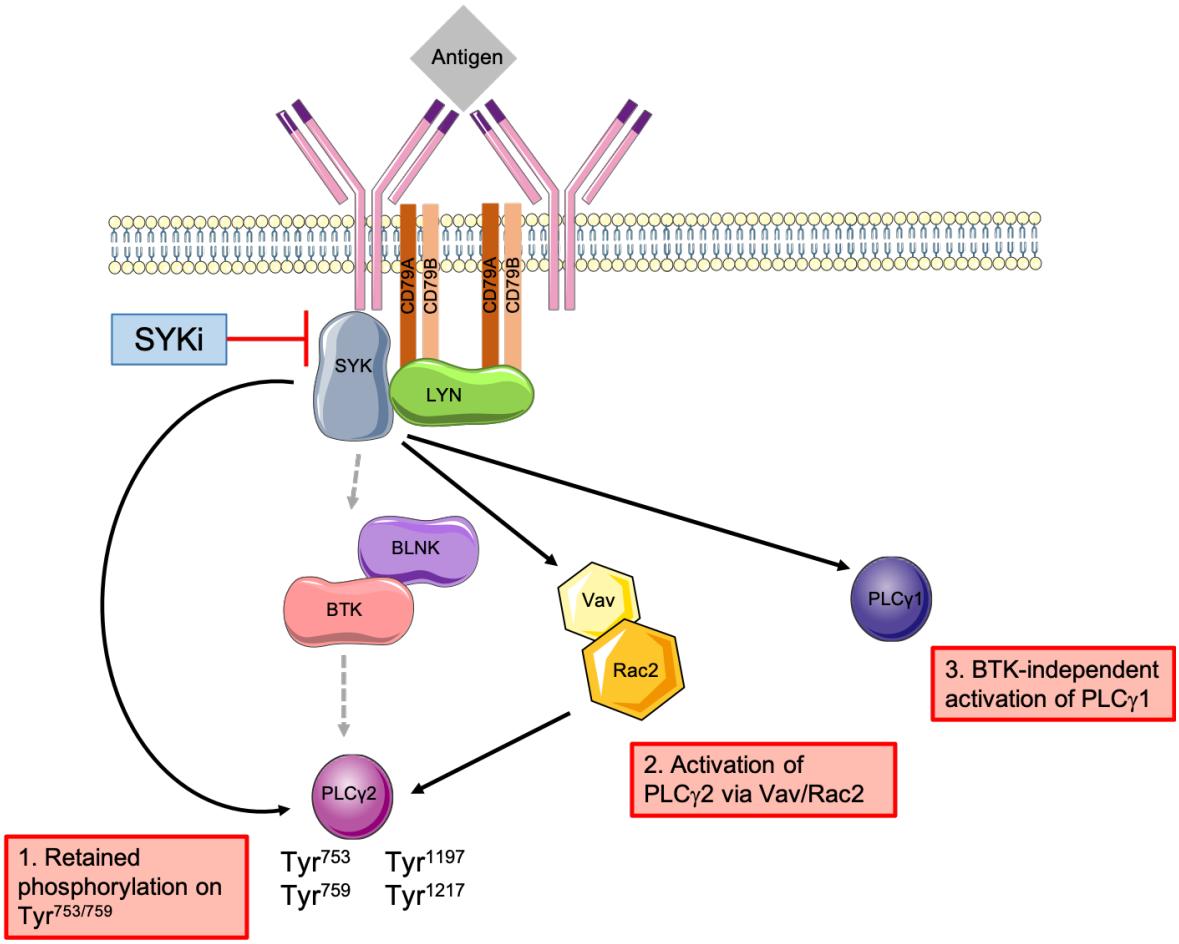

FIGURE 6-2: SUMMARY OF THE BTK "BY-PASS" PATHWAY HYPOTHESES.

Canonical BCR signaling (SYK→BTK→PLCγ2) is shown by the dotted grey arrows with each of the three "by-pass" hypotheses indicated by black arrows. 1. Direct phosphorylation of PLCγ2 by SYK to retain phosphorylation of $Tyr^{753/759}$. 2. Phosphorylation-independent activation of PLCγ2 via SYK-dependent Vav/Rac activation. 3. BTK-independent activation of PLCγ1 leading to iCa^{2+} mobilisation. SYK inhibition (SYKi) is indicated on the figure as a proposed intervention to prevent canonical and BTK "by-pass" signalling.

6.4 Clinical significance of BTK "by-pass" mechanism

Since BTK "by-pass" mechanism is a feature that has been revealed in *in vitro* experiments, its clinical significance remains unclear. However, based on the evidence presented showing that BTK inhibition is less effective in samples termed "high-signallers" and therefore more likely to be activating "by-pass" pathways, along with the evidence that signalling capacity correlates with clinical outcome (D'Avola et al., 2016), it is possible that engagement of BTK "by-pass" pathways could influence efficacy of BTKi treatment and/or emergence of resistance. Mutations (e.g. within BTK and PLCγ2) appear to mediate resistance in a proportion of cases, and it is possible that "by-pass" might influence resistance that emerges either with or without these mutations.

One possibility is that "by-pass" engagement provides a window of opportunity whereby malignant cells are less effected by BTKi and hence have a greater opportunity of accumulating BTKi-resistant associated gene mutations (or other changes that cause BTKi resistance). In CLL, many cells are driven from tissues into the circulation following BTKi treatment (Herman et al., 2014b), but a fraction may be retained in the tissues where they could continue to receive antigen stimulation. Here, operation of "by-pass" signalling in the presence of BTKi treatment, may allow continued low-level engagement of survival/proliferation promoting BCR responses, thereby increasing chances for acquisition of mutations. Alternatively, activation of "by-pass" signalling in a subset of cases may influence the nature of the pathway which leads to subsequent clinical resistance. It is interesting to note that PLCγ2 mutations associated with ibrutinib resistance have a similar characteristic to "by-pass" signalling in that they render PLCγ2 less dependent on BTK for activation, either by increased sensitivity to Rac activation (Walliser et al., 2016) or hypersensitivity to BTK (Wist et al., 2020). It may be possible that cases with capacity for "by-pass" signalling are more susceptible to acquisition of these mutations.

My work on the nature of "by-pass" signalling suggests two potential strategies to improve drug responses. First, more proximal targeting should avoid "by-pass" by blocking responses upstream of the bifurcation of canonical signalling (SYK→BTK→PLCγ2) and "by-pass" pathways (**Figure 6-2**). This is revealed most clearly in my work by studies on SYK inhibition, which completely blocks iCa^{2+} responses in all samples, and in both DLBCL cell lines studied. SYK inhibition has been explored in the clinic with promising results seen in patients with relapsed or refractory CLL using fostamatinib (Friedberg et al., 2010) and entospletinib (Sharman et al., 2015). Buchner *et al*. (Buchner et al., 2009) showed that, despite increased expression of SYK in CLL cells compared

with normal B cells, a combination of fludarabine with R406 increases cytotoxicity compared with fludarabine alone, and the authors suggest that this has the potential to be useful in patients with poor prognosis. Second, it may be possible to combine BTKi with a second inhibitor selectively targeted at the "by-pass" mechanism. Clearly, this would require further work to understand whether "by-pass" is mediated via a direct effect of SYK on PLCγ2 or whether another intermediate enzyme is involved.

Although many of my studies were performed using relatively high concentrations of BTKi (to ensure full target inhibition), I also performed detailed dose-response experiments to probe effects of differing concentration of BTKi. These showed that concentrations of ~10 nM ibrutinib and acalabrutinib were required to effectively block BTK activity measured using analysis of BTK autophosphorylation as a surrogate for kinase activity. Although the number of experiments performed was more limited, this was consistent with results from analysis with MIBs, which directly measures occupancy of the BTK active site, which showed full binding at 50 nM ibrutinib. This also compares well with the effects of BTKi on iCa^{2+} mobilisation where a concentration of 10 nM acalabrutinib was sufficient for the maximal inhibitory effects of this drug. As the concentrations of ibrutinib were raised, additional off-target effects were observed and "by-pass" signalling was overcome, potentially by inhibition of SYK. However, it is important to note that a recent study by Chen *et al*. (Chen et al., 2018), which performed parallel analysis of plasma and intracellular concentrations of ibrutinib, and BTK occupancy, demonstrated that with standard dosing (420 mg/d) there was a mean intracellular concentration of ~20 nM ibrutinib and this was associated with full BTK occupancy. Thus, intracellular ibrutinib concentrations in treated patients are not so high that they would be expected to circumvent "by-pass".

At these concentrations (i.e. ≤100 nM), both ibrutinib and acalabrutinib are relatively selective for BTK but as the concentration is raised increased off-target effects are more likely to occur (e.g. binding and inhibiting SYK, observed most notably for ibrutinib in the data presented in this thesis). Both inhibitors potently inhibit BTK, with ibrutinib being more potent than acalabrutinib, but selectivity is somewhat harder to rigorously assess because it is important to consider both steps of kinase inhibition (compound interacting with kinase, driven by affinity, and kinase inactivation) (Hopper et al., 2020). It is important to remember that physiologically relevant exposures for acalabrutinib are 5-fold higher than for ibrutinib (Byrd et al., 2013, 2016) so using an arbitrary concentration for comparing the two inhibitors is not necessarily informative. Hopper

et al. (Hopper et al., 2020) performed experiments with physiologic relevant concentrations in a cellular context and concluded that ibrutinib and acalabrutinib have similar selectivity for BTK.

6.5 Suggestions for future work to investigate BTK "by-pass" mechanisms

To fully resolve the BTK "by-pass" pathway it would be important to understand the functional role of each of the four canonical phosphorylation sites of PLCγ2 (Tyr^{753}, Tyr^{759}, Tyr^{1197} and Tyr^{1217}) and the effect that each one has within the BCR-associated signalling pathway. The DLBCL cell lines used in this thesis could be used as model systems representing B-cell malignancies (particularly DLBCL and CLL, since this thesis has presented similar results in the cell lines and primary CLL), but the TMD8 cell line expressing the My-T-BCR would be particularly interesting to use. There is also the possibility of using CLL 'lines' (e.g. MEC1), if these could be validated to use a similar mechanism. CRISPR-Cas9 could either be used to introduce specific mutations into endogenous *PLCG2* or to remove endogenous *PLCG2* before overexpressing wildtype or mutant PLCγ2 expression plasmids to investigate each phosphorylation site individually or combinations of phosphorylation sites both loss-of function mutations and constitutively active mutations to fully manipulate the pathway. Immunoblotting and iCa^{2+} flux assay by flow cytometry could be used to assess the functional consequence of manipulating each of the PLCγ2 phosphorylation sites. Inhibitor experiments could also be used to clarify the kinase-dependent phosphorylation sites of both BTK and SYK. This would allow the pathway to be more fully resolved. RNAi or CRISPR-Cas9 could also be used to knock-out PLCγ1 to confirm whether or not this has a significant role in iCa^{2+} mobilisation in malignant B-cells.

Investigation into improving drug therapy is also valuable. One approach is to identify whether combinations of drugs, to work alongside ibrutinib, can be used to achieve full inhibition of the signalling pathways. An unbiased screening of a chemical library could be carried out to identify appropriate candidates to take forward, and an affinity capture technique, similar to that presented in the MIBs assay, used to identify any unknown drug targets. A simple method of achieving this in primary CLL would be to develop a calcium assay using 96 well plates that can be read using a plate reader following injection of anti-IgM (e.g. PBX Calcium Assay Kit, BD), as a medium/high-throughput platform for drug-screening. This would provide valuable data for the kinetic phases of iCa^{2+} mobilisation to select the most appropriate candidates to take forward.

To further understand the clinical relevance of the “by-pass” mechanism, early analysis of emerging ibrutinib resistance in patients prior to accumulation of mutations would be very important. Access to samples could prove difficult since we cannot predict which patients will become resistant or when, however samples collected at regular intervals from patients receiving ibrutinib therapy could prove useful. Each patient could be monitored over the course of their therapy to identify if “by-pass” is in place prior to treatment, if it occurs during treatment, or if it occurs after disease progression/relapse. This could help answer the question of whether “by-pass” is a precursor to resistance. Additionally, if “by-pass” does correlate with ibrutinib resistance, studying a series of samples from patients over the course of their treatment might help to improve predictions on who will become resistant, and possibly how quickly resistance could occur. Finally, it would be very interesting to investigate whether “by-pass”, and its potential correlation with ibrutinib resistance, could be used to determine which pathway of resistance emerges i.e. mutations in BTK or PLCγ2. This knowledge, especially if it could be used as a predictive tool, would allow the selection of a better combination of therapies, possibly targeting alternative kinases or pathways leading to iCa^{2+} mobilisation, to improve patient survival and reduce the chance of disease relapse/progression.

6.6 Single-cell time-resolved analysis of iCa^{2+} signalling

Single-cell investigation is becoming more prevalent as technology advances. One of the major benefits is the opportunity to investigate “outliers” in greater detail which are often masked in bulk population analysis. The devices used in this thesis are simple microwell arrays, which trap cells by sedimentation, and receive stimulation by supplying the ligand to the surface of the array, and these types of device have been used for a variety of applications including monitoring reactive oxygen species generation, intracellular enzymatic activity, dynamics of cell killing by cytotoxic T cells and iCa^{2+} flux (Schiffenbauer et al., 2009). They also have applications in studying cell:cell interactions, where stimulation is achieved by bringing cells into contact with one another (Desalvo et al., 2020; Rothbauer et al., 2017), and stimulation can also be achieved using microfluidic components to deliver more complex cell stimulation (Chung et al., 2011). Therefore, this technology could be applied to studying time-resolved iCa^{2+} flux in single B cells to determine whether we can improve on the current technique of flow cytometry to obtain more information of the activity of cells at the single-cell level.

The aim of this part of the project was to develop and optimise microwell arrays for use with B-cell lines and primary CLL samples, using simple devices to trap cells and couple with fluorescence microscopy for analysis. Whilst there is some evidence to suggest that microwell arrays can be used to assess iCa^{2+} flux in malignant B cells there are substantial technical challenges that remain to be resolved.

The fabrication of wafers, consisting of micropillars that will imprint the agarose to form the microwell arrays, was performed using photolithography techniques with SU8-3025 photoresist (see **Figure 2-4**). This photoresist is designed to create a thickness of 25 μm when applied with a spin speed of 3000 rpm, the spin speed can be increased to reduce the thickness of the photoresist, but to obtain a consistent thickness across the wafer the limit is 4000 rpm creating a thickness of ~20 μm. The thickness achieved in fabrication attempts varied quite substantially, considering the size of the cells which are required to be trapped in the arrays, and ranged from ~15 μm to ~20 μm. This can be caused by variable room temperature (which should be controlled in the facility) affecting the viscosity of the photoresist and the age of the photoresist can also impact its quality. The height of the features created, which correspond to the depth of the microwells, is important because the aim is to achieve one cell per microwell and the larger the size the more likely cells will be able to stack on top of one another. Another key step in the fabrication process is the exposure of the photoresist-covered wafer to UV light to allow crosslinking to occur. The exposure energy range suitable for the thickness of photoresist is provided on the photoresist data sheet and is 150 – 250 mJ/cm^2 for this design. To calculate the exposure time required to achieve this intensity, the dose required is divided by the intensity of the machine which was calibrated and measured at regular, but infrequent, intervals throughout the year. The combination of the range of suitable exposure energy with the uncertainty of the exact calibration measurement of the intensity of the mask aligner introduced variables that affected the ability to consistently fabricate wafers. In addition to these challenges, CLL cells are very small (~6 - 7 μm) requiring small feature dimensions, and this might be at the limit for the photoresist and equipment being used. It would be important to investigate other photoresists in the future, to identify whether a more suitable photoresist could be found that was designed for smaller features. Following fabrication of the wafer, it was important to determine the most suitable microwell dimensions and the cell seeding conditions to achieve a high single-cell occupancy of the microwell array, but this was a time-consuming process. Optimisation is a time-consuming process for any new model because the technique relies heavily on the specificity for each cell type used. **Chapter 1** presents some optimisation for CLL, but additional optimisation is

still required, for example the method of ligand addition could be improved and will be discussed in **Section 6.7**.

Despite the technical issues, preliminary biological data was collected and is presented in **Chapter 1** and shows some indication that microwell arrays can be used to assess iCa^{2+} flux and inhibitor responses in CLL. Although in general it was rather insensitive and could not reliably detect anti-IgM responses, there was some indication that a small number of cells respond differently to the main population which could be masked by flow cytometry. This was validated by the use of kinase inhibitors which effectively inhibited iCa^{2+} flux. Interestingly, Schiffenbauer *et al*. (Schiffenbauer et al., 2009) also observed variations in responses even in clonal populations which would remain undetected in bulk population analysis. Overall, CLL appears to be particularly challenging because the signalling responses are known to be relatively weak, reflecting the low level of sIgM expression compared with normal cells (Damle et al., 2002). It would be interesting to test normal B cells, which have a much higher sIgM expression, however the challenge would then be to isolate the sIgM expressing B cells from a PBMC population since B-cell numbers would be relatively low and only a proportion would express sIgM as others would have undergone class-switching.

Overall, there is potential for the microwell arrays to be used as hypothesised, which could still be very useful in understanding pathways in greater detail. There is also the potential that they could be useful for diseases like DLBCL and follicular lymphoma where patient samples are less readily available since the devices work well with small volumes of cells.

6.7 Suggestions for future work to investigate and optimise single-cell time-resolved analysis of iCa^{2+} signalling

Future work needs to begin with the continued optimisation of the devices to overcome the technical issues described. This major next step is the optimisation of the addition of ligand, to ensure reproducibility between experiments. Several studies use the method of pipetting ligand directly onto the surface of the array (e.g. (Desalvo et al., 2020; Schiffenbauer et al., 2009)), but use of additional equipment would improve this method, for example a scaffold for holding the agarose microwell array would prevent movement if the pipette touched the array. Alternatively,

microfluidic components could be included in the design of the cell trapping device to allow microfluidic control of addition of ligand. Chung *et al*. (Chung et al., 2011) demonstrated a high-throughput capture and imaging technique of cells trapped in microwells along a channel system which could be stimulated by injection of ligand into the channel. The authors observed heterogeneity in calcium oscillatory behaviour in genetically identical Jurkat cells, highlighting the sensitivity of the method. Alternative methods of cell trapping could also be investigated, for example Zhang *et al*. (Zhang et al., 2006) took advantage of the chemical reaction between the glass surface and silanisation reagent which allows amino groups to be linked to the silicon atoms of the glass creating a positively charged surface. This promoted adhesion of negatively charged cells to the glass surface of the cell trap chamber and ligand could be applied to the cells through a microfluidic inlet. The authors demonstrated the ability of this device to visualise iCa^{2+} flux in CHO cells.

Improvement to single-cell capture could also be investigated through use of magnetic cell traps, which work by labelling the cells of interest with magnetic nanoparticles. Huang, Hwong and Lai (Huang et al., 2018b) demonstrated successful trapping of immunomagnetic-labelled THP-1 cells within 10 minutes by using a device consisting of a microwell array with a permanent magnet next to it, above a microfluidic channel into which the cells could be injected. The cells of interest were drawn up to the array by the magnet. The microfluidic channel could then be used to provide stimulation to the cells of interest through injection of soluble ligand.

Once the technical issues are resolved, the technique has significant biological and clinical application. There was some indication that a small number of cells respond differently to the main population and these have the potential to be “outliers” with atypical responses and might be of interest to analyse further. There are several techniques described in the literature for removal of cells of interest from microwell arrays with the most commonly described being use of a micromanipulator (Yamamura et al., 2005; Hosokawa et al., 2009; Kinoshita et al., 2009; Tokimitsu et al., 2007), which essentially uses a motorised micropipette to locate and remove specific cells. Alternatively, Kim, Devarenne and Han (Kim et al., 2015) designed a device where each individual cell trap could be opened or closed, controlled with microfluidics, with the application of a backflow to release cells of interest. Both of these techniques remove cells from the array and further investigation such as genomic sequencing could be carried out on these cells.

Alternatively, in-well analyses have also been described, and were introduced in **Section 1.8.3**, and could be carried out to provide further characterisation of the cells. These include single-cell western blotting, described by Kang *et al*. (Kang et al., 2014), which could be used to investigate autophosphorylation of BTK and phosphorylation of PLCγ2 as measures of the effectiveness of BTK inhibitor treatment and determine which cells are utilising the BTK "by-pass" pathway. RNA sequencing of trapped single-cells has also been described (Ke et al., 2013) and could be used to investigate NFAT and NF-κB target genes downstream of iCa^{2+} flux.

Both in-well analyses, including iCa^{2+} mobilisation and the techniques mentioned above, along with further analysis upon cell retrieval all point towards the use of these devices for assisting with clinical decisions on a per patient basis. Wang *et al*. (Wang et al., 2015) applied this technology to screen anti-cancer drugs and reliably calculated IC_{50} values for five clinically established chemotherapy agents highlighting the potential for these devices to be used to identify optimal therapies for patients in a personalised approach to treatment (Wang et al., 2014).

Supplementary Figures

Supplementary Figure 1 relates to **Section 3.7.1** of the main thesis.

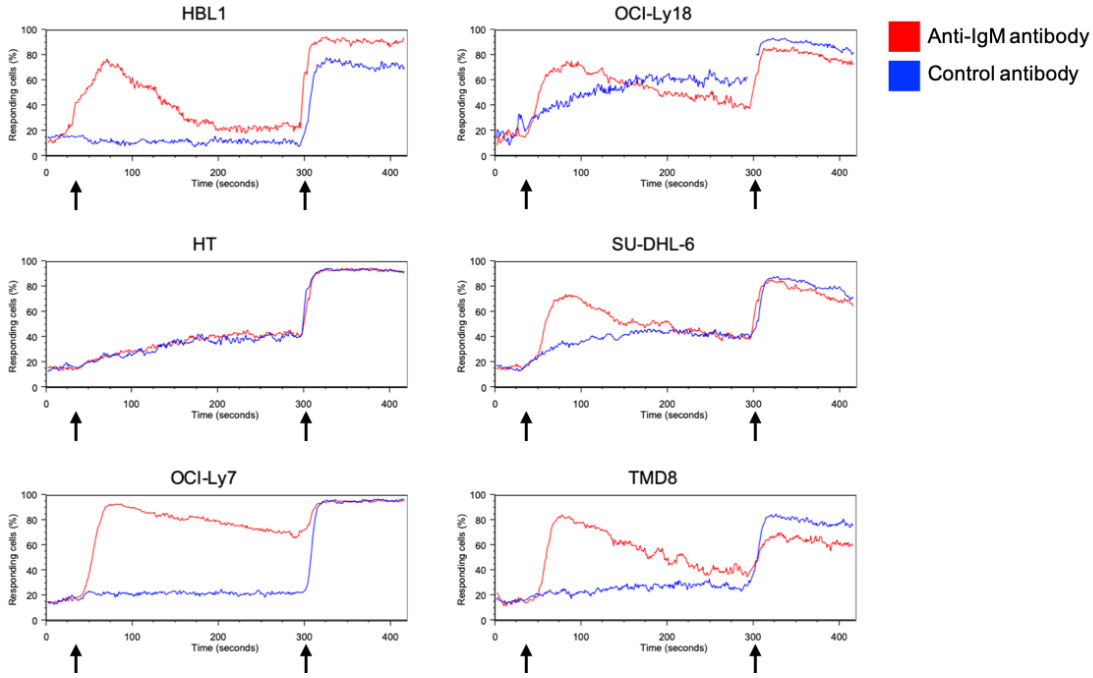

SUPPLEMENTARY FIGURE 1: ANALYSIS OF ANTI-IGM-INDUCED iCa^{2+} FLUX IN DLBCL CELL LINES.

iCa^{2+} fluxes were analysed in the indicated cell lines following addition of control antibody (blue) or anti-IgM (red). The first arrow shows time of addition of antibody following baseline data recording for 30 seconds. The second arrow shows time of addition of ionomycin as a positive control. The experiment was performed once for each cell line.

Supplementary Figure 2 relates to **Section 0** of the main thesis.

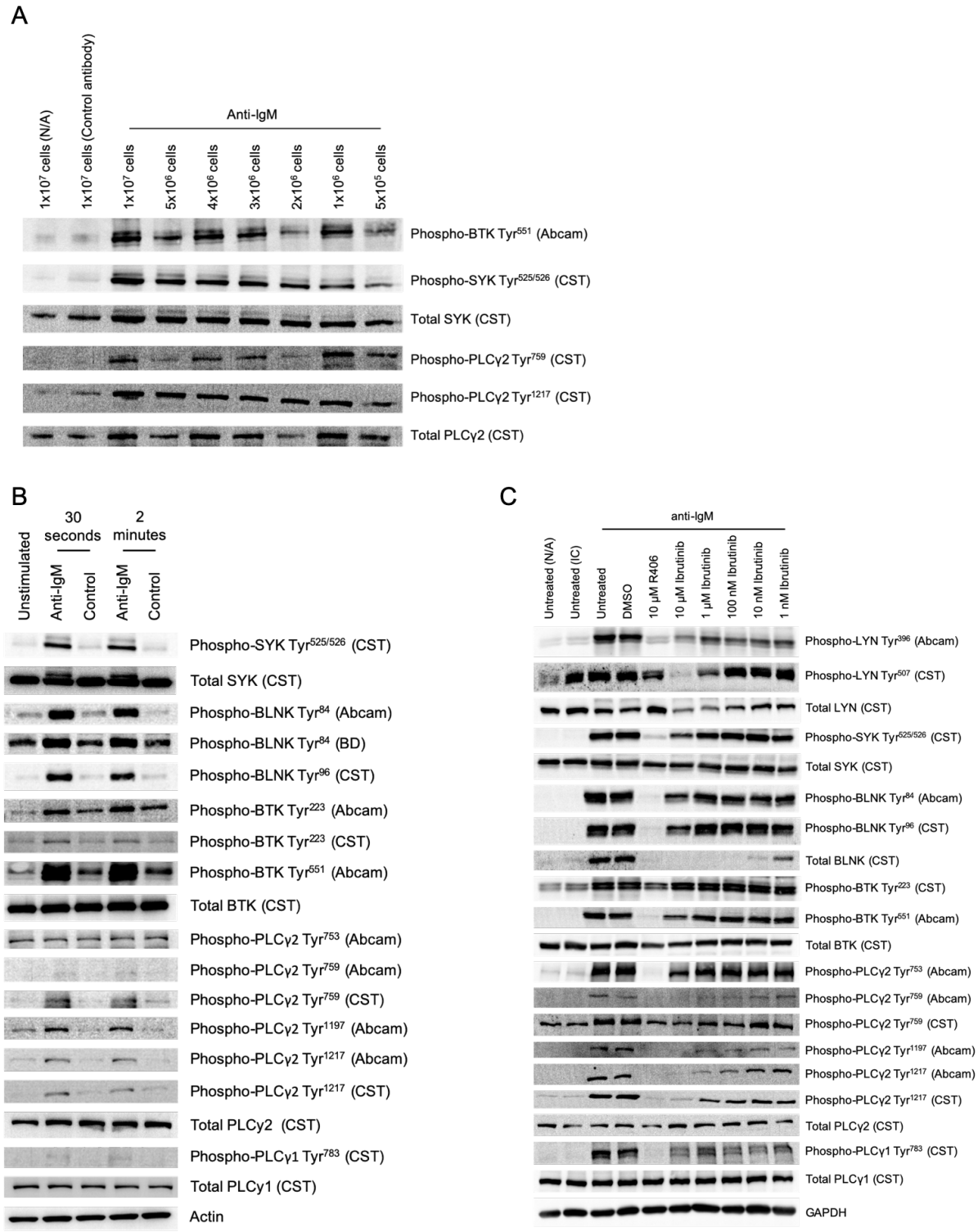

SUPPLEMENTARY FIGURE 2: ANTIBODY SELECTION AND OPTIMIZATION FOR BCR-ASSOCIATED SIGNALING PATHWAY ANALYSIS.

A. The number of OCI-Ly7 cells as indicated on the figure were treated with anti-IgM or control antibody for 2 minutes. As an additional control, some cells were left untreated for the duration of the experiment (N/A). Expression of a small number of phosphorylated and total proteins as indicated on the figure were analysed by immunoblotting. **B.** $5x10^6$ OCI-Ly7 cells per condition were treated with anti-IgM or control

antibody for 30 seconds or 2 minutes as indicated on the figure. As an additional control, some cells were left untreated for the duration of the experiment (Unstimulated). Expression of phosphorylated and total proteins as indicated on the figure, along with Actin as a loading control, were analysed by immunoblotting. **C.** $5x10^6$ OCI-Ly7 cells per condition were pretreated with 10 μM, 1 μM, 100 nM, 10 nM or 1 nM ibrutinib, 10 μM R406, DMSO (as a vehicle control), or left untreated as a control for 1 hour before treatment with anti-IgM or control antibody [Untreated (IC)]. As an additional control, some cells were left untreated for the duration of the experiment [Untreated (N/A)]. Cells were collected after 30 seconds of anti-IgM treatment and expression of phosphorylated and total proteins as indicated on the figure, along with GAPDH as a loading control, were analysed by immunoblotting. The company from which the antibody was purchased is indicated on the figure (CST: Cell Signaling Technology). Multiple antibodies for various phospho-sites were used to select the ones with with good detection following stimulation and with low background.

Supplementary Figures

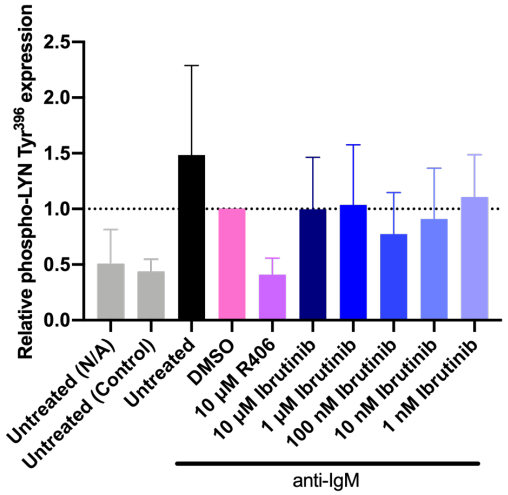

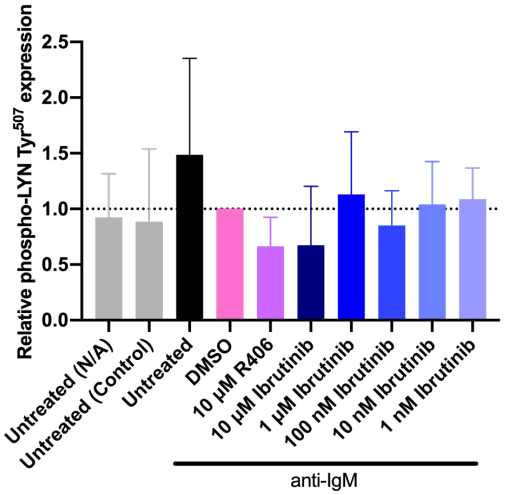

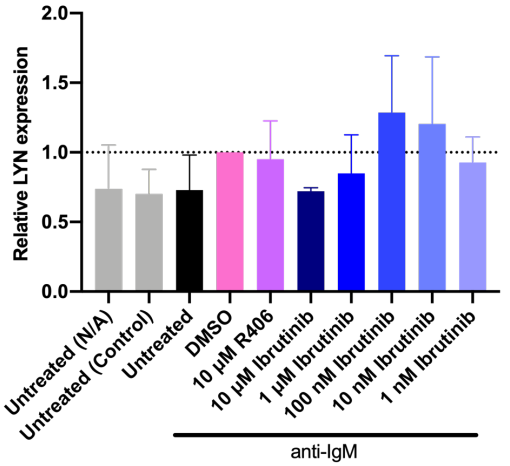

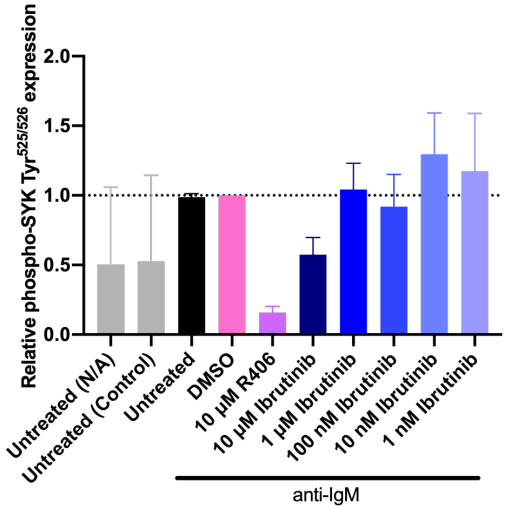

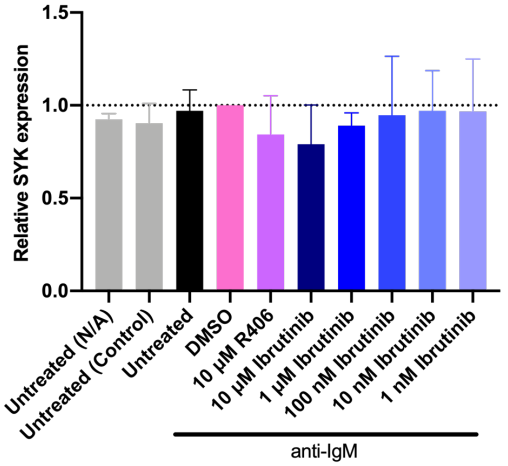

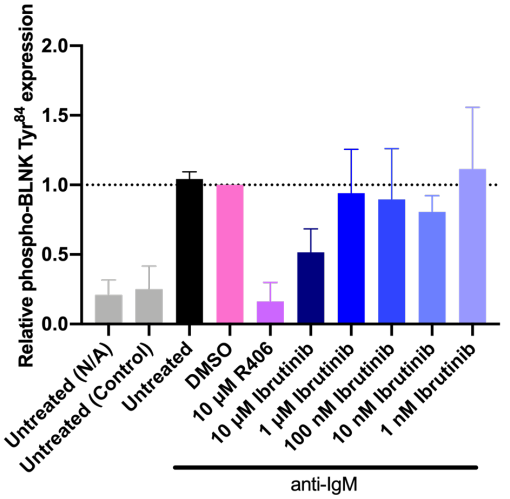

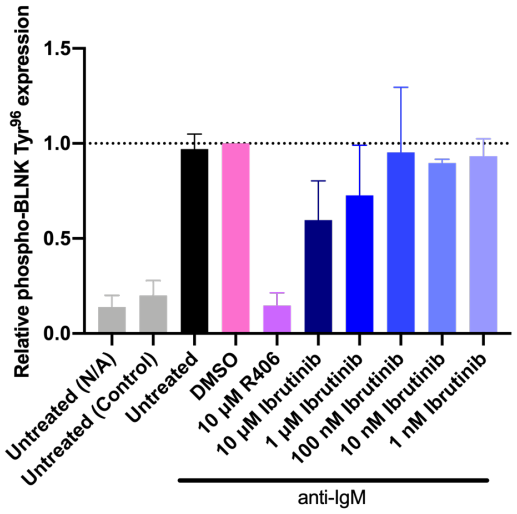
Relative phospho-BLNK Tyr96 expression
1.5
1.0
0.5
0.0
Untreated (N/A)
Untreated (Control)
Untreated
DMSO
10 μM R406
10 μM Ibrutinib
1 μM Ibrutinib
100 nM Ibrutinib
10 nM Ibrutinib
1 nM Ibrutinib
anti-IgM

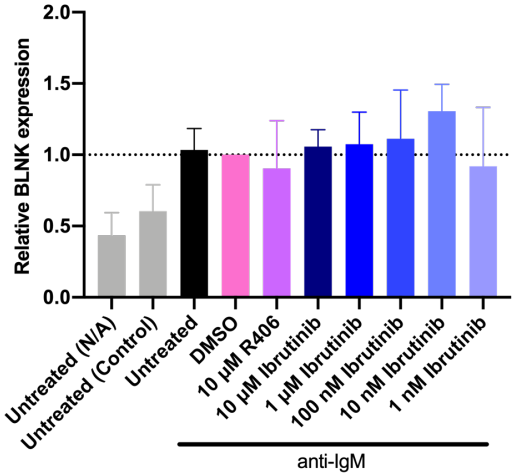
Relative BLNK expression
2.0
1.5
1.0
0.5
0.0
Untreated (N/A)
Untreated (Control)
Untreated
DMSO
10 μM R406
10 μM Ibrutinib
1 μM Ibrutinib
100 nM Ibrutinib
10 nM Ibrutinib
1 nM Ibrutinib
anti-IgM

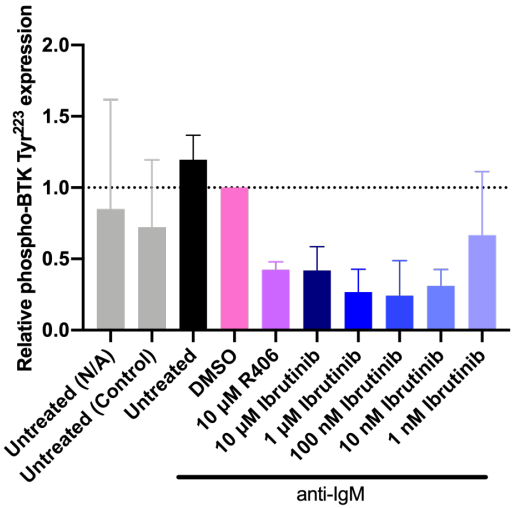
Relative phospho-BTK Tyr223 expression
2.0
1.5
1.0
0.5
0.0
Untreated (N/A)
Untreated (Control)
Untreated
DMSO
10 μM R406
10 μM Ibrutinib
1 μM Ibrutinib
100 nM Ibrutinib
10 nM Ibrutinib
1 nM Ibrutinib
anti-IgM

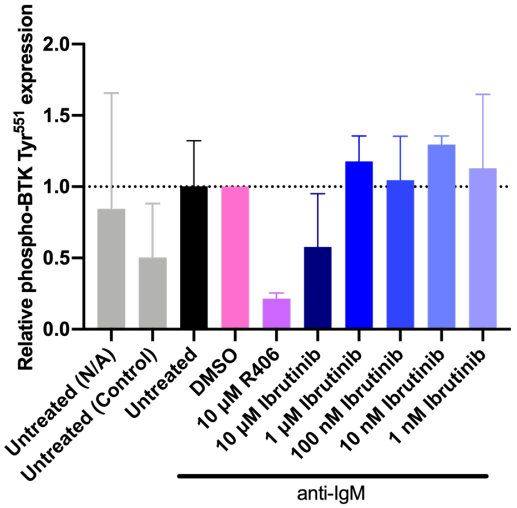
Relative phospho-BTK Tyr551 expression
2.0
1.5
1.0
0.5
0.0
Untreated (N/A)
Untreated (Control)
Untreated
DMSO
10 μM R406
10 μM Ibrutinib
1 μM Ibrutinib
100 nM Ibrutinib
10 nM Ibrutinib
1 nM Ibrutinib
anti-IgM

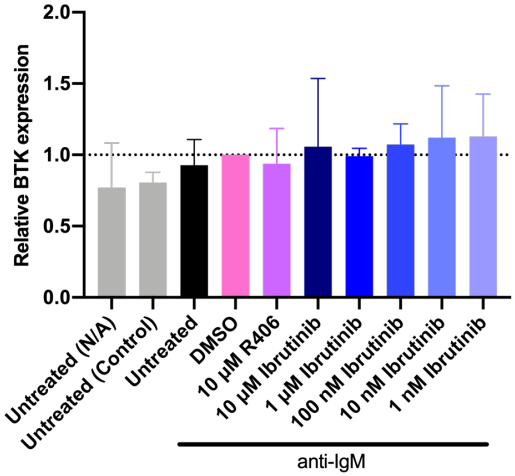
Relative BTK expression
2.0
1.5
1.0
0.5
0.0
Untreated (N/A)
Untreated (Control)
Untreated
DMSO
10 μM R406
10 μM Ibrutinib
1 μM Ibrutinib
100 nM Ibrutinib
10 nM Ibrutinib
1 nM Ibrutinib
anti-IgM

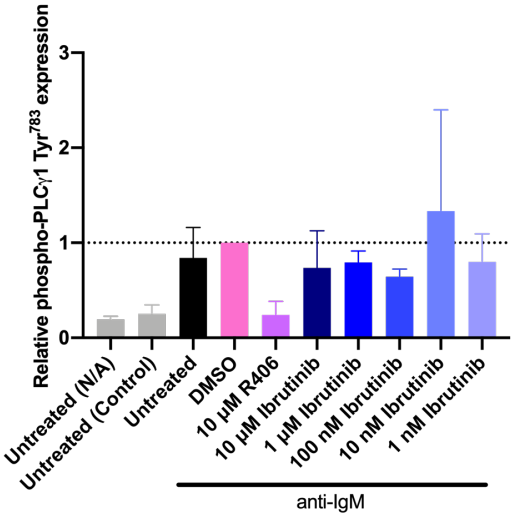
Relative phospho-PLCγ1 Tyr783 expression
3
2
1
0
Untreated (N/A)
Untreated (Control)
Untreated
DMSO
10 μM R406
10 μM Ibrutinib
1 μM Ibrutinib
100 nM Ibrutinib
10 nM Ibrutinib
1 nM Ibrutinib
anti-IgM

Supplementary Figures

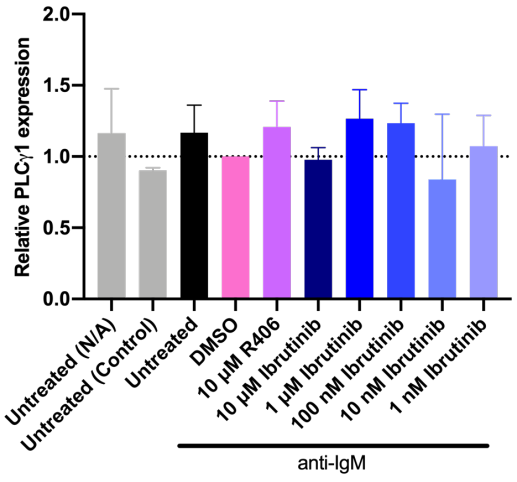

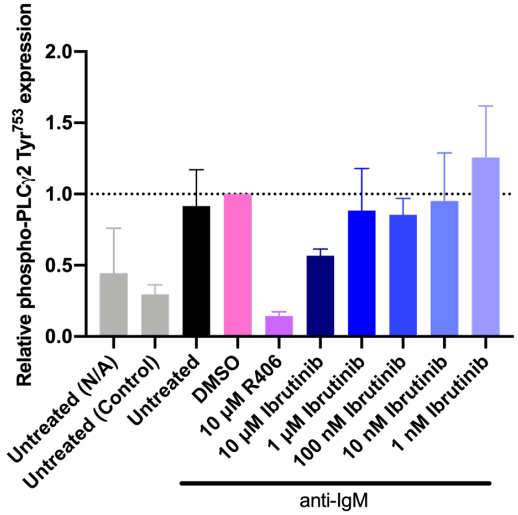

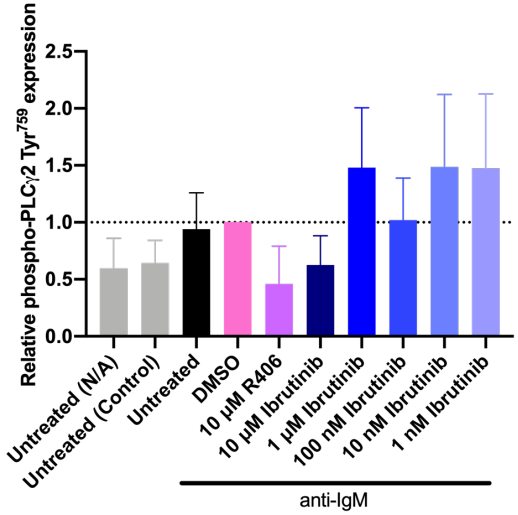

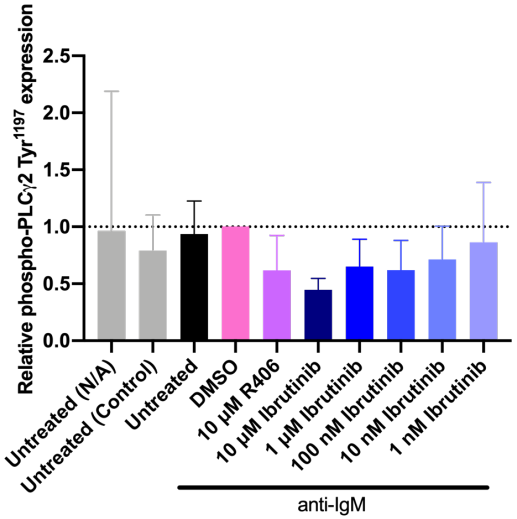

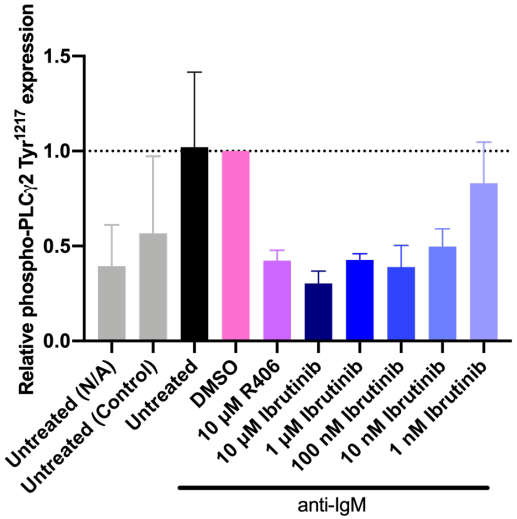

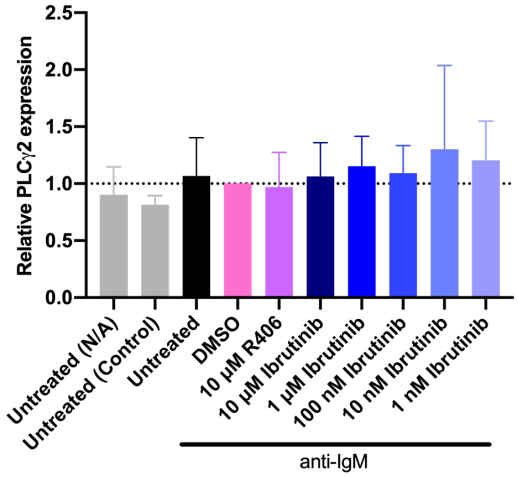

SUPPLEMENTARY FIGURE 3: SUMMARY OF THE EFFECT OF IBRUTINIB ON ANTI-IGM-INDUCED PHOSPHORYLATION OF BCR-ASSOCIATED SIGNALLING PROTEINS IN OCI-LY7 CELLS.

OCI-Ly7 cells were pretreated with 10 μM, 1 μM, 100 nM, 10 nM or 1 nM ibrutinib, 10 μM R406, DMSO (as a vehicle control), or left untreated as a control for 1 hour before treatment with anti-IgM or control antibody [Untreated (Control)]. As an additional control, some cells were left untreated for the duration of the experiment [Untreated (N/A)]. Cells were collected after 30 seconds of anti-IgM treatment and expression of phosphorylated proteins as indicated on the figure, along with GAPDH as a loading control, were analysed by immunoblotting. Figure shows quantification for all samples analysed, calculated as relative protein expression, where the bars represent mean and standard deviation of n=3. The values for the DMSO-treated cells are set to 1.0.

Supplementary Figure 3 relates to **Section 4.4.1** of the main thesis.

Supplementary Figures

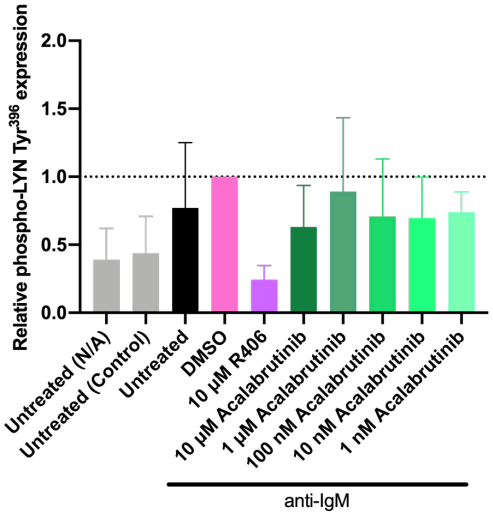

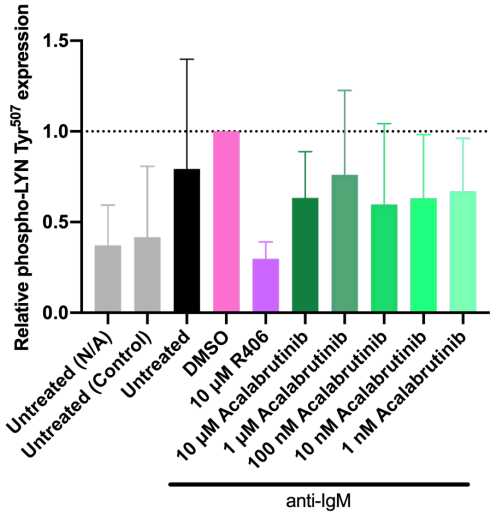

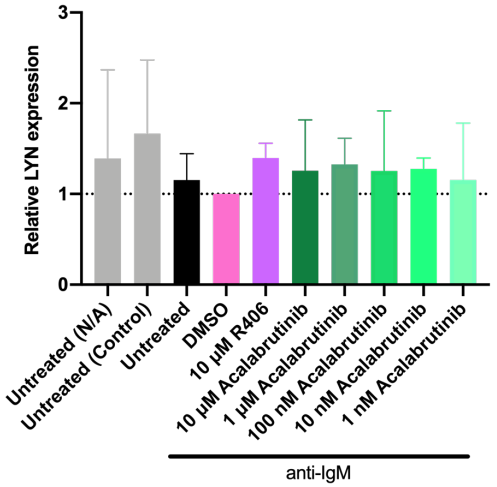

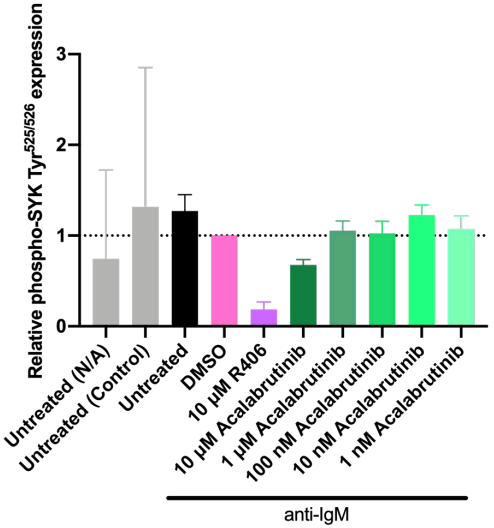

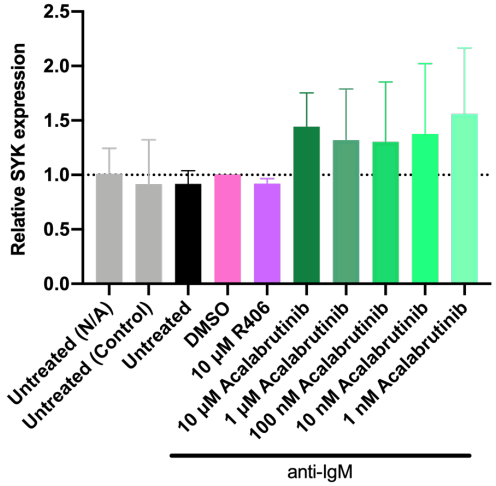

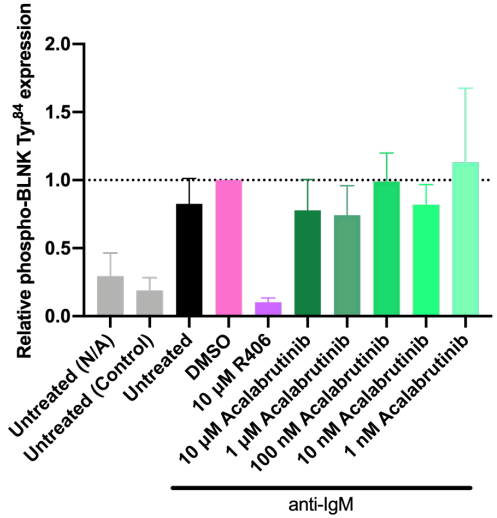

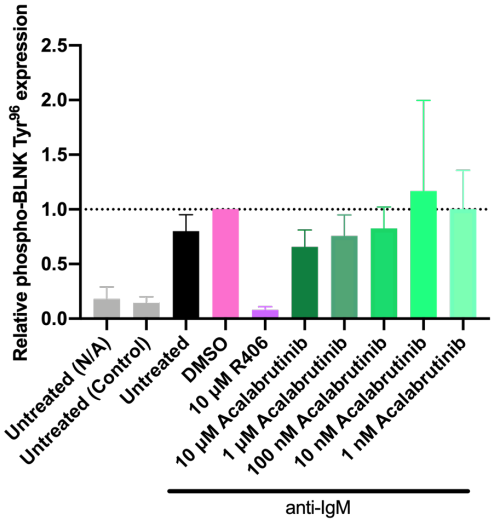
Relative phospho-BLNK Tyr96 expression
2.5
2.0
1.5
1.0
0.5
0.0
Untreated (N/A)
Untreated (Control)
Untreated
DMSO
10 μM R406
10 μM Acalabrutinib
1 μM Acalabrutinib
100 nM Acalabrutinib
10 nM Acalabrutinib
1 nM Acalabrutinib
anti-IgM

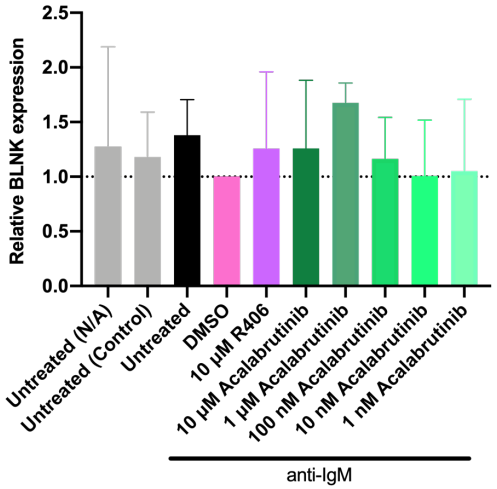
Relative BLNK expression
2.5
2.0
1.5
1.0
0.5
0.0
Untreated (N/A)
Untreated (Control)
Untreated
DMSO
10 μM R406
10 μM Acalabrutinib
1 μM Acalabrutinib
100 nM Acalabrutinib
10 nM Acalabrutinib
1 nM Acalabrutinib
anti-IgM

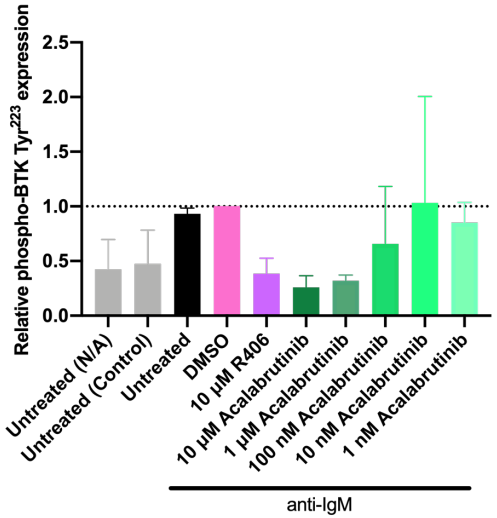
Relative phospho-BTK Tyr223 expression
2.5
2.0
1.5
1.0
0.5
0.0
Untreated (N/A)
Untreated (Control)
Untreated
DMSO
10 μM R406
10 μM Acalabrutinib
1 μM Acalabrutinib
100 nM Acalabrutinib
10 nM Acalabrutinib
1 nM Acalabrutinib
anti-IgM

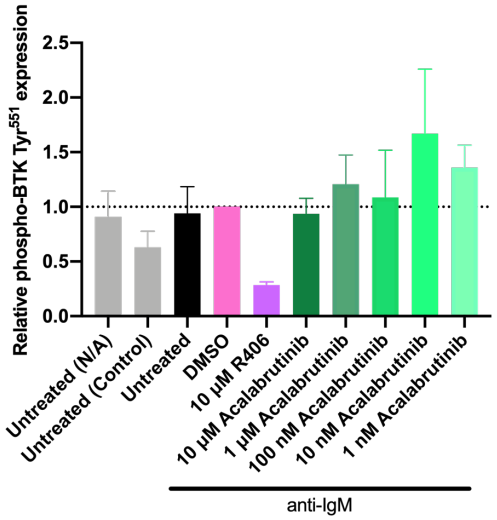
Relative phospho-BTK Tyr551 expression
2.5
2.0
1.5
1.0
0.5
0.0
Untreated (N/A)
Untreated (Control)
Untreated
DMSO
10 μM R406
10 μM Acalabrutinib
1 μM Acalabrutinib
100 nM Acalabrutinib
10 nM Acalabrutinib
1 nM Acalabrutinib
anti-IgM

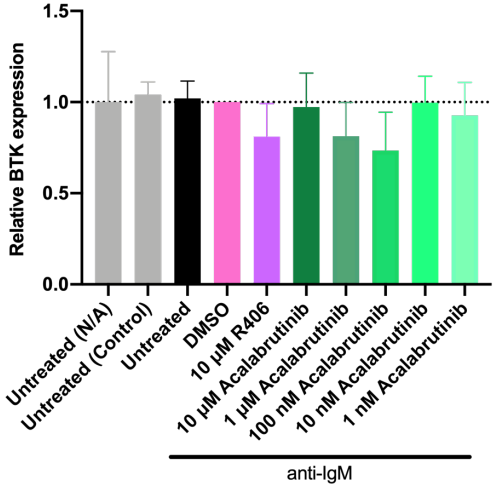
Relative BTK expression
1.5
1.0
0.5
0.0
Untreated (N/A)
Untreated (Control)
Untreated
DMSO
10 μM R406
10 μM Acalabrutinib
1 μM Acalabrutinib
100 nM Acalabrutinib
10 nM Acalabrutinib
1 nM Acalabrutinib
anti-IgM

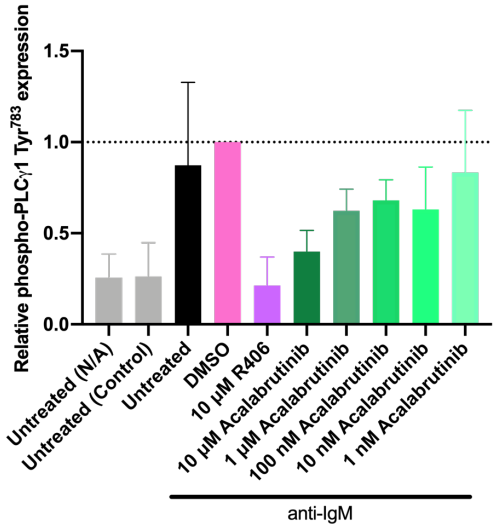
Relative phospho-PLCγ1 Tyr783 expression
1.5
1.0
0.5
0.0
Untreated (N/A)
Untreated (Control)
Untreated
DMSO
10 μM R406
10 μM Acalabrutinib
1 μM Acalabrutinib
100 nM Acalabrutinib
10 nM Acalabrutinib
1 nM Acalabrutinib
anti-IgM

Supplementary Figures

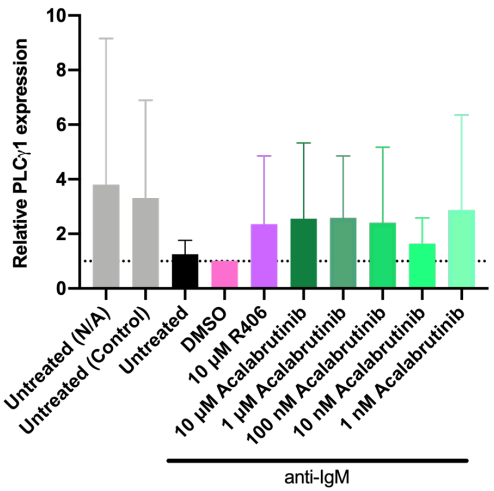

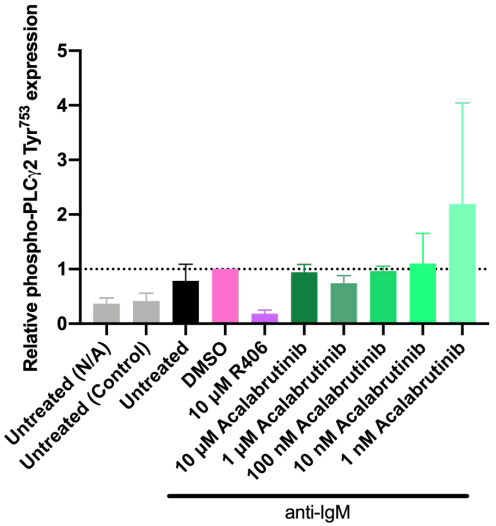

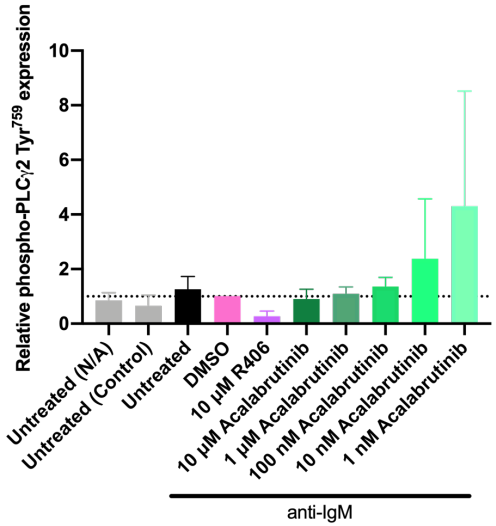

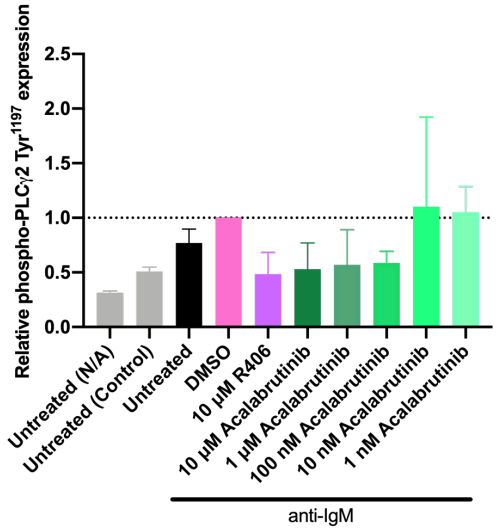

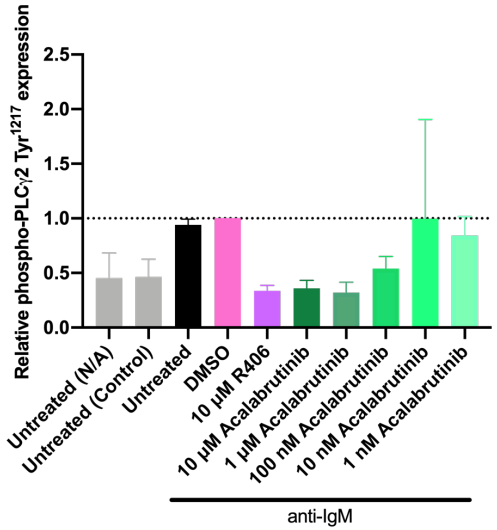

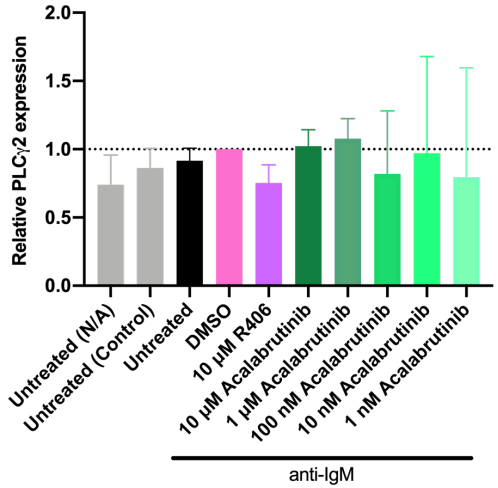

SUPPLEMENTARY FIGURE 4: SUMMARY OF THE EFFECT OF ACALABRUTINIB ON ANTI-IGM-INDUCED PHOSPHORYLATION OF BCR-ASSOCIATED SIGNALLING PROTEINS IN OCI-LY7 CELLS.

OCI-Ly7 cells were pretreated with 10 μM, 1 μM, 100 nM, 10 nM or 1 nM acalabrutinib, 10 μM R406, DMSO (as a vehicle control), or left untreated as a control for 1 hour before treatment with anti-IgM or control antibody [Untreated (Control)]. As an additional control, some cells were left untreated for the duration of the experiment [Untreated (N/A)]. Cells were collected after 30 seconds of anti-IgM treatment and expression of phosphorylated proteins as indicated on the figure, along with GAPDH as a loading control, were analysed by immunoblotting. Figure shows quantification for all samples analysed, calculated as relative protein expression, where the bars represent mean and standard deviation of n=3. The values for the DMSO-treated cells are set to 1.0.

Supplementary Figure 4 relates to **Section 4.4.1** of the main thesis.

Supplementary Figures

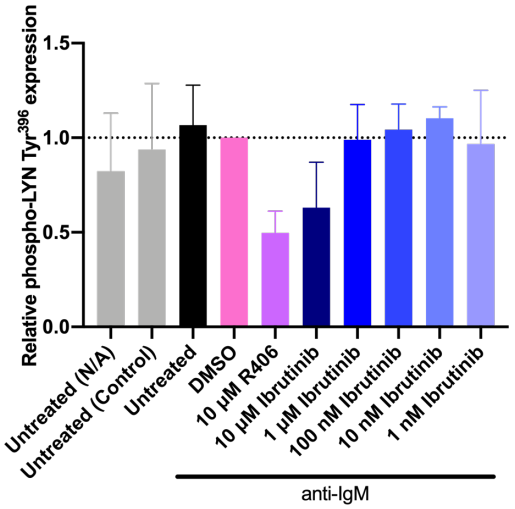

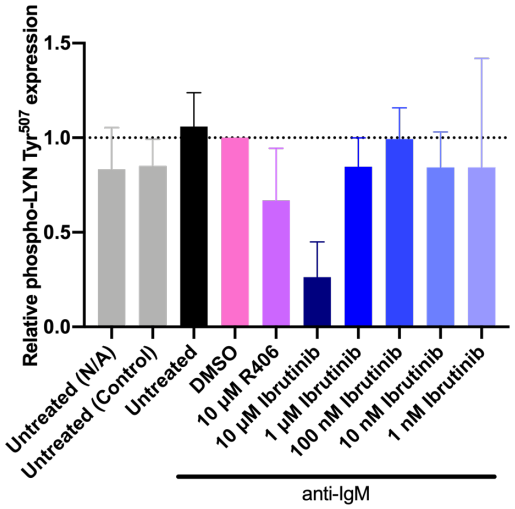

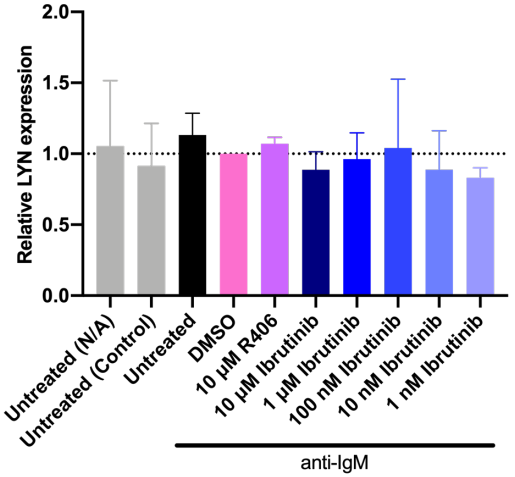

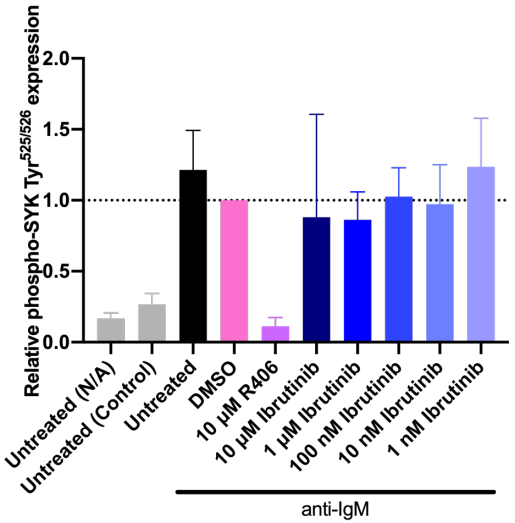

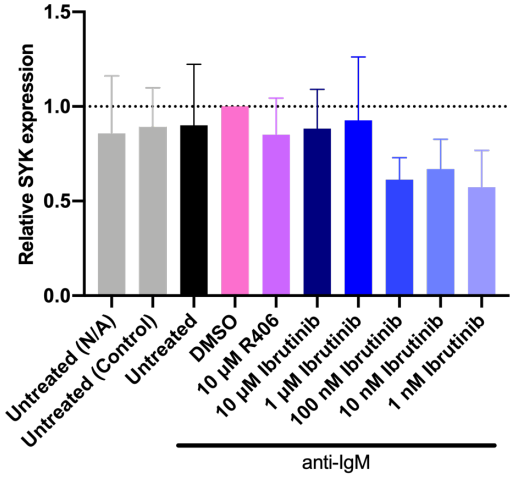

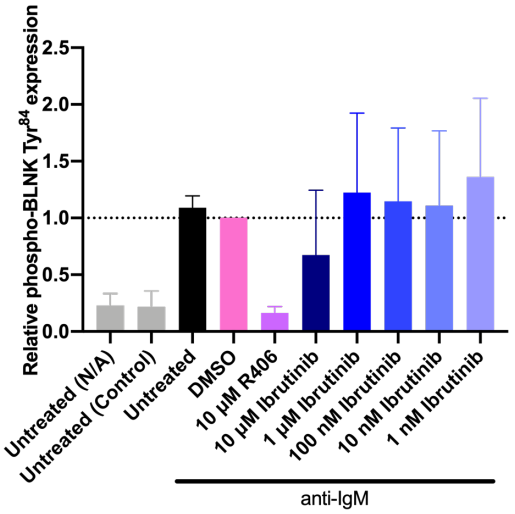

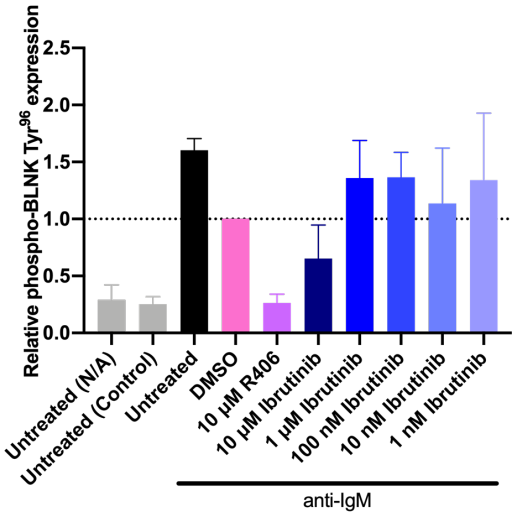
Relative phospho-BLNK Tyr96 expression
2.5
2.0
1.5
1.0
0.5
0.0
Untreated (N/A)
Untreated (Control)
Untreated
DMSO
10 μM R406
10 μM Ibrutinib
1 μM Ibrutinib
100 nM Ibrutinib
10 nM Ibrutinib
1 nM Ibrutinib
anti-IgM

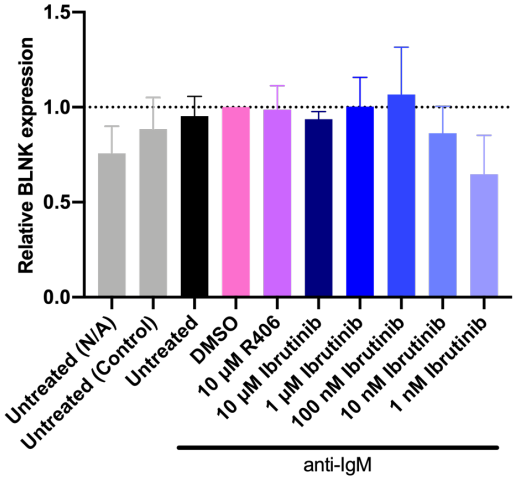
Relative BLNK expression
1.5
1.0
0.5
0.0
Untreated (N/A)
Untreated (Control)
Untreated
DMSO
10 μM R406
10 μM Ibrutinib
1 μM Ibrutinib
100 nM Ibrutinib
10 nM Ibrutinib
1 nM Ibrutinib
anti-IgM

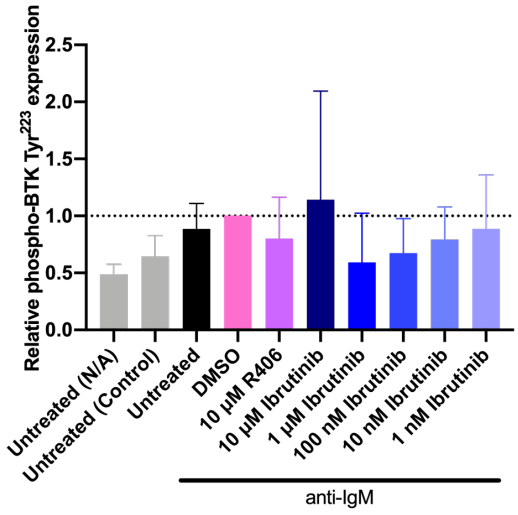
Relative phospho-BTK Tyr223 expression
2.5
2.0
1.5
1.0
0.5
0.0
Untreated (N/A)
Untreated (Control)
Untreated
DMSO
10 μM R406
10 μM Ibrutinib
1 μM Ibrutinib
100 nM Ibrutinib
10 nM Ibrutinib
1 nM Ibrutinib
anti-IgM

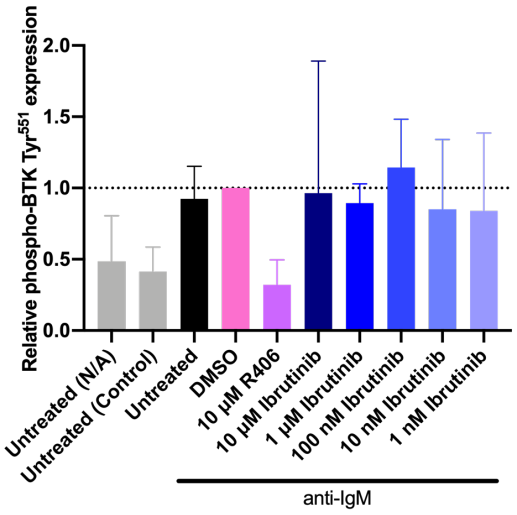
Relative phospho-BTK Tyr551 expression
2.0
1.5
1.0
0.5
0.0
Untreated (N/A)
Untreated (Control)
Untreated
DMSO
10 μM R406
10 μM Ibrutinib
1 μM Ibrutinib
100 nM Ibrutinib
10 nM Ibrutinib
1 nM Ibrutinib
anti-IgM

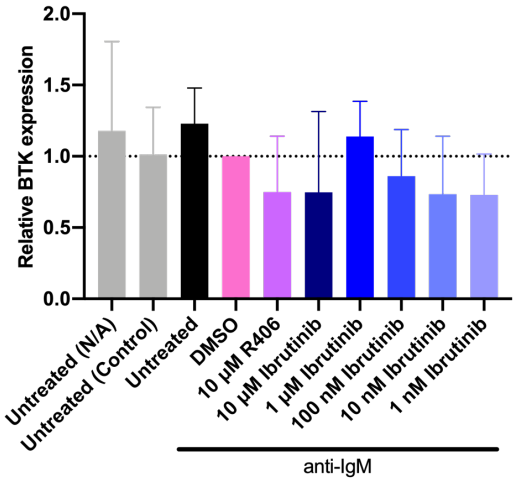
Relative BTK expression
2.0
1.5
1.0
0.5
0.0
Untreated (N/A)
Untreated (Control)
Untreated
DMSO
10 μM R406
10 μM Ibrutinib
1 μM Ibrutinib
100 nM Ibrutinib
10 nM Ibrutinib
1 nM Ibrutinib
anti-IgM

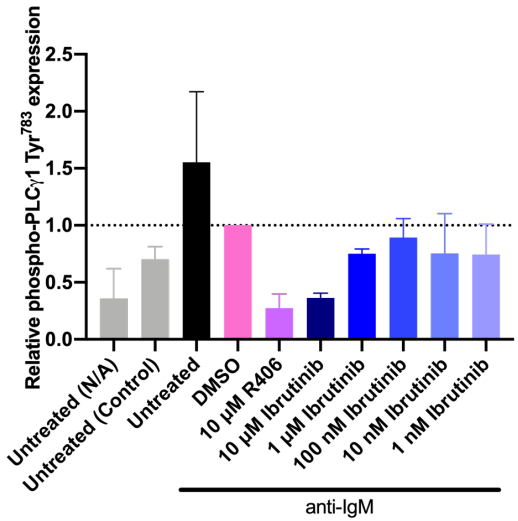
Relative phospho-PLCγ1 Tyr783 expression
2.5
2.0
1.5
1.0
0.5
0.0
Untreated (N/A)
Untreated (Control)
Untreated
DMSO
10 μM R406
10 μM Ibrutinib
1 μM Ibrutinib
100 nM Ibrutinib
10 nM Ibrutinib
1 nM Ibrutinib
anti-IgM

Supplementary Figures

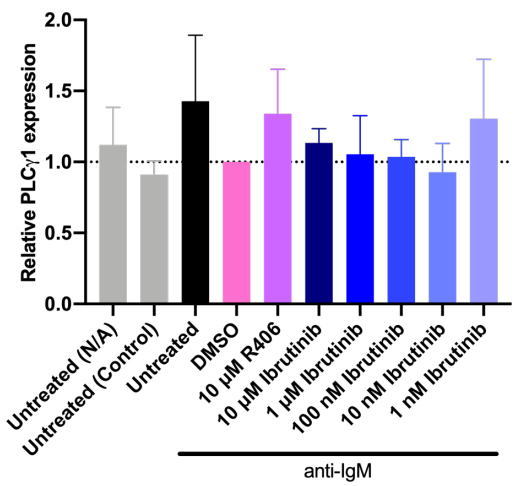

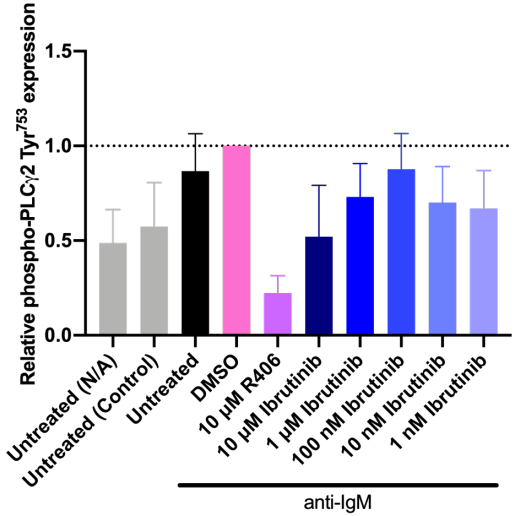

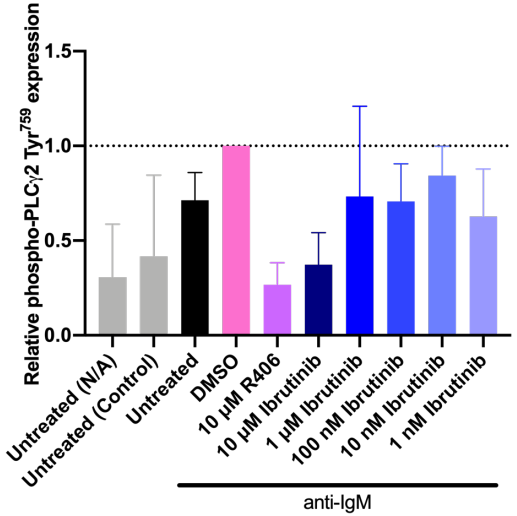

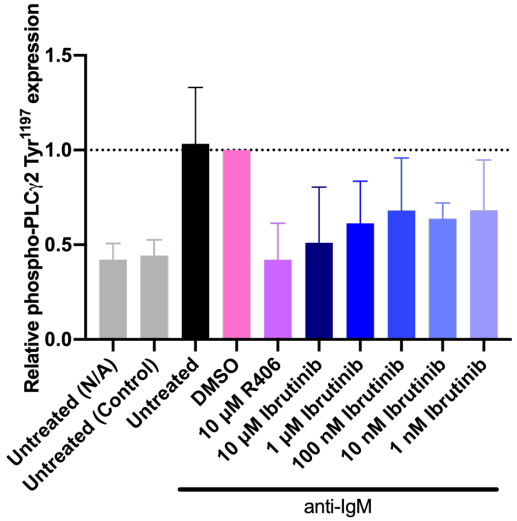

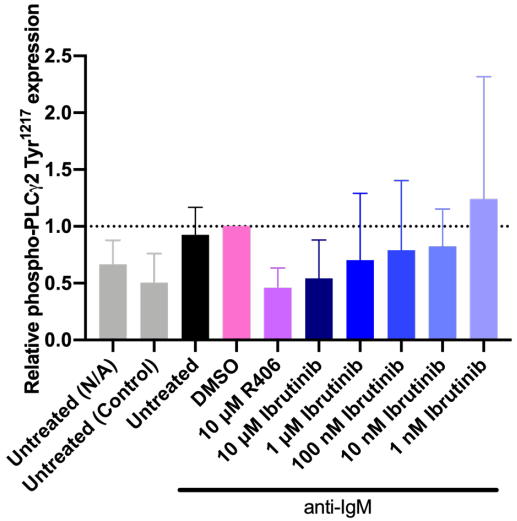

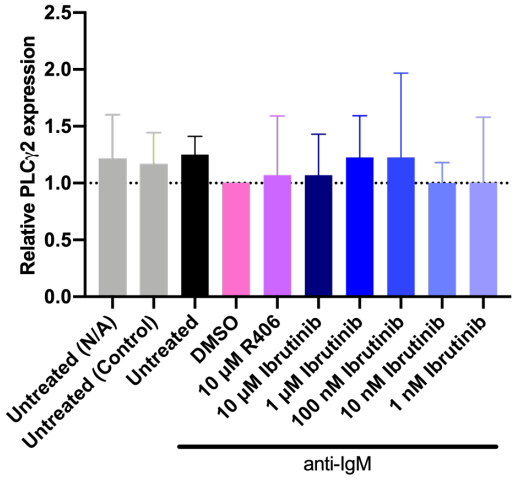

SUPPLEMENTARY FIGURE 5: SUMMARY OF THE EFFECT OF IBRUTINIB ON ANTI-IGM-INDUCED PHOSPHORYLATION OF BCR-ASSOCIATED SIGNALLING PROTEINS IN TMD8 CELLS.

TMD8 cells were pretreated with 10 μM, 1 μM, 100 nM, 10 nM or 1 nM ibrutinib, 10 μM R406, DMSO (as a vehicle control), or left untreated as a control for 1 hour before treatment with anti-IgM or control antibody [Untreated (Control)]. As an additional control, some cells were left untreated for the duration of the experiment [Untreated (N/A)]. Cells were collected after 30 seconds of anti-IgM treatment and expression of phosphorylated proteins as indicated on the figure, along with GAPDH as a loading control, were analysed by immunoblotting. Figure shows quantification for all samples analysed, calculated as relative protein expression, where the bars represent mean and standard deviation of n=3. The values for the DMSO-treated cells are set to 1.0.

Supplementary Figure 5 relates to **Section 4.4.2** of the main thesis.

Supplementary Figures

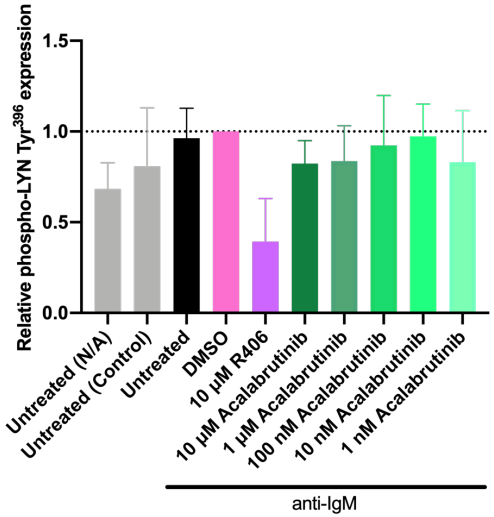

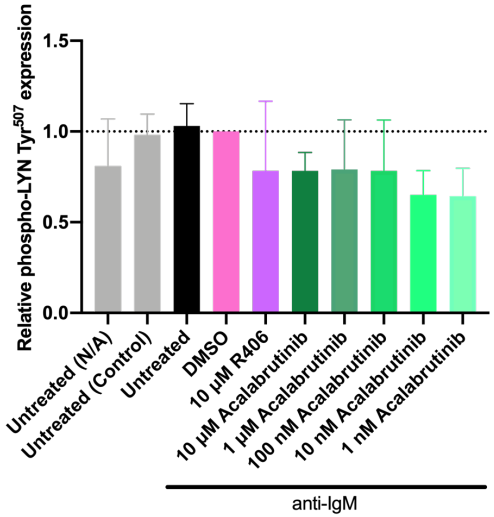

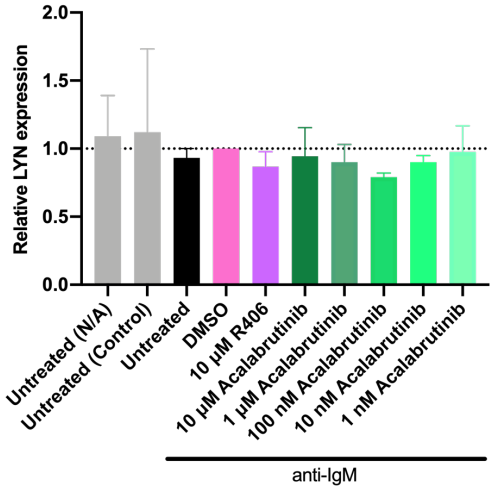

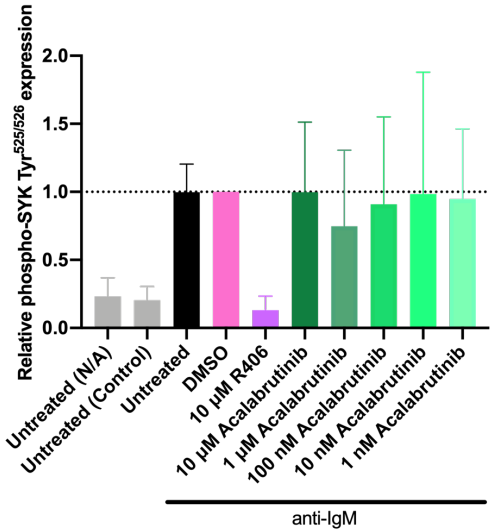

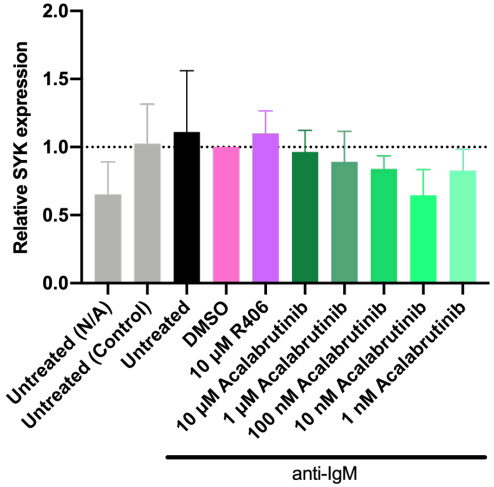

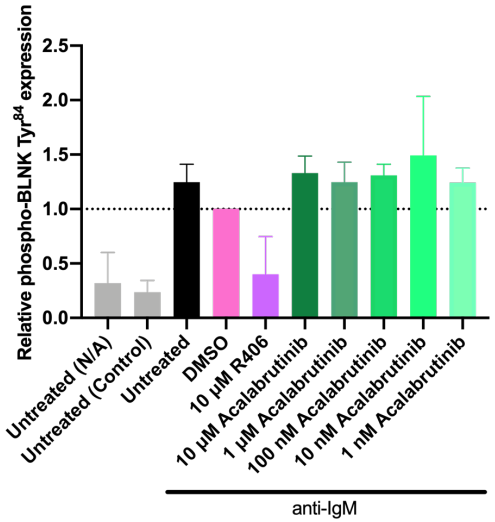

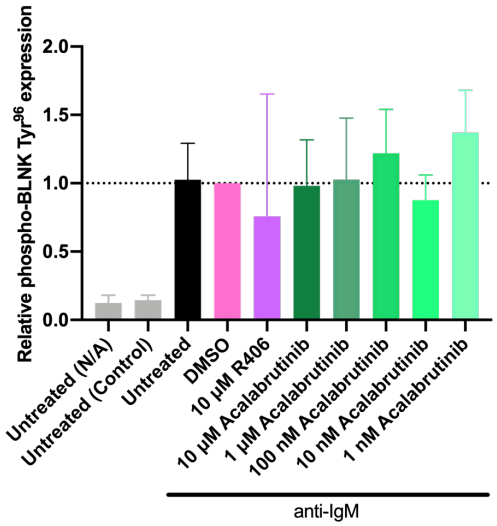
Relative phospho-BLNK Tyr96 expression
2.0
1.5
1.0
0.5
0.0
Untreated (N/A)
Untreated (Control)
Untreated
DMSO
10 μM R406
10 μM Acalabrutinib
1 μM Acalabrutinib
100 nM Acalabrutinib
10 nM Acalabrutinib
1 nM Acalabrutinib
anti-IgM

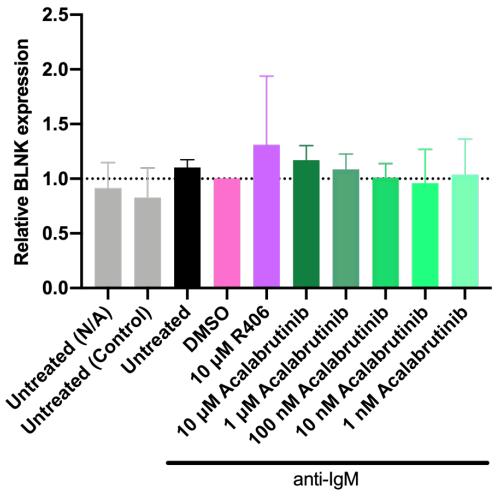
Relative BLNK expression
2.5
2.0
1.5
1.0
0.5
0.0
Untreated (N/A)
Untreated (Control)
Untreated
DMSO
10 μM R406
10 μM Acalabrutinib
1 μM Acalabrutinib
100 nM Acalabrutinib
10 nM Acalabrutinib
1 nM Acalabrutinib
anti-IgM

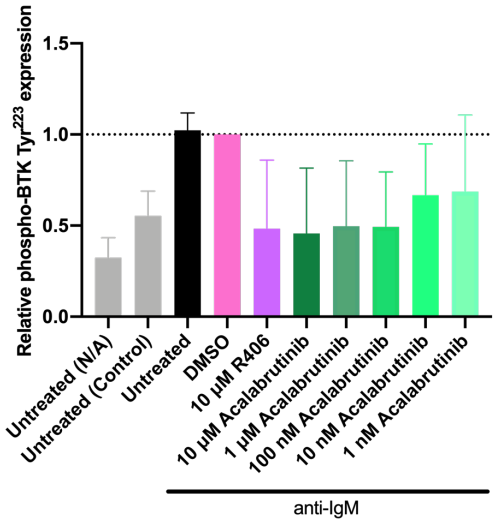
Relative phospho-BTK Tyr223 expression
1.5
1.0
0.5
0.0
Untreated (N/A)
Untreated (Control)
Untreated
DMSO
10 μM R406
10 μM Acalabrutinib
1 μM Acalabrutinib
100 nM Acalabrutinib
10 nM Acalabrutinib
1 nM Acalabrutinib
anti-IgM

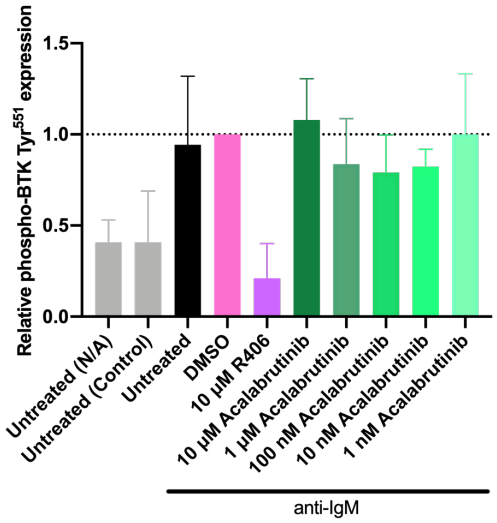
Relative phospho-BTK Tyr551 expression
1.5
1.0
0.5
0.0
Untreated (N/A)
Untreated (Control)
Untreated
DMSO
10 μM R406
10 μM Acalabrutinib
1 μM Acalabrutinib
100 nM Acalabrutinib
10 nM Acalabrutinib
1 nM Acalabrutinib
anti-IgM

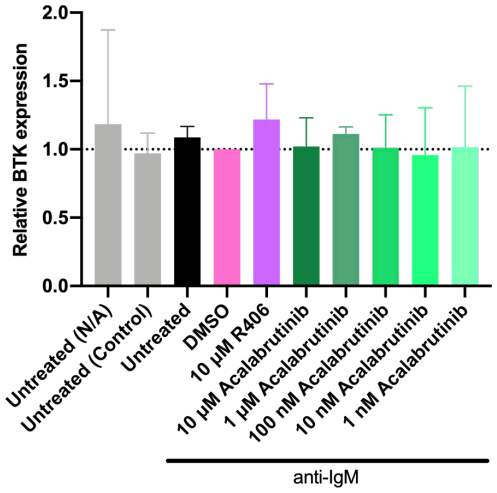
Relative BTK expression
2.0
1.5
1.0
0.5
0.0
Untreated (N/A)
Untreated (Control)
Untreated
DMSO
10 μM R406
10 μM Acalabrutinib
1 μM Acalabrutinib
100 nM Acalabrutinib
10 nM Acalabrutinib
1 nM Acalabrutinib
anti-IgM

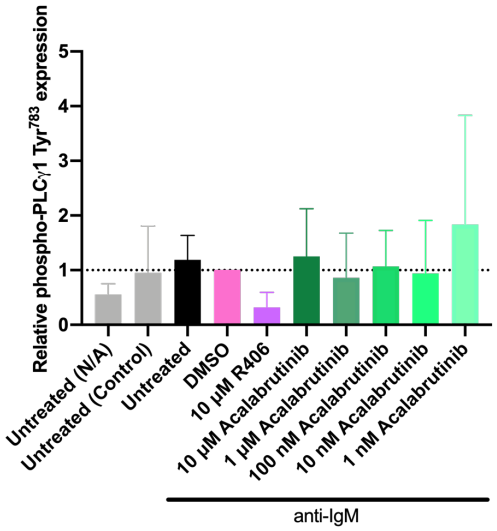
Relative phospho-PLCγ1 Tyr783 expression
5
4
3
2
1
0
Untreated (N/A)
Untreated (Control)
Untreated
DMSO
10 μM R406
10 μM Acalabrutinib
1 μM Acalabrutinib
100 nM Acalabrutinib
10 nM Acalabrutinib
1 nM Acalabrutinib
anti-IgM

Supplementary Figures

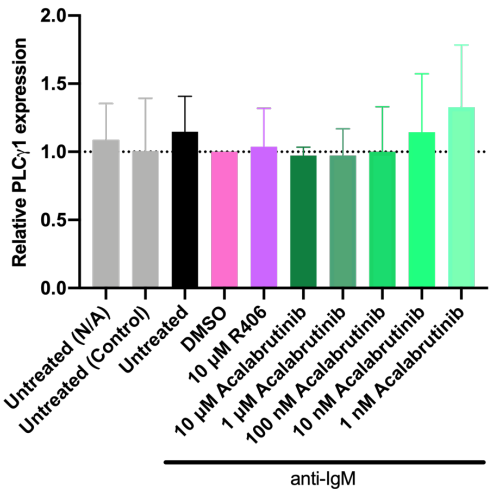

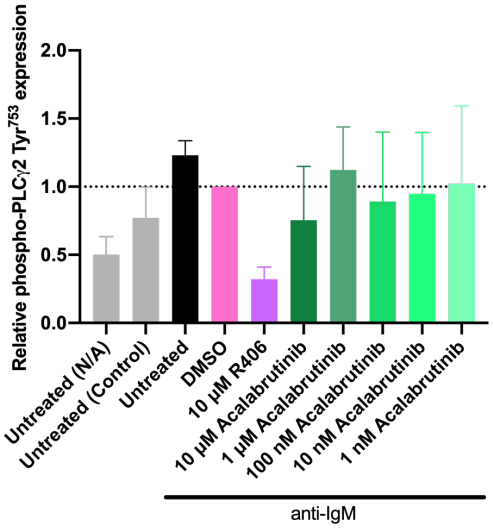

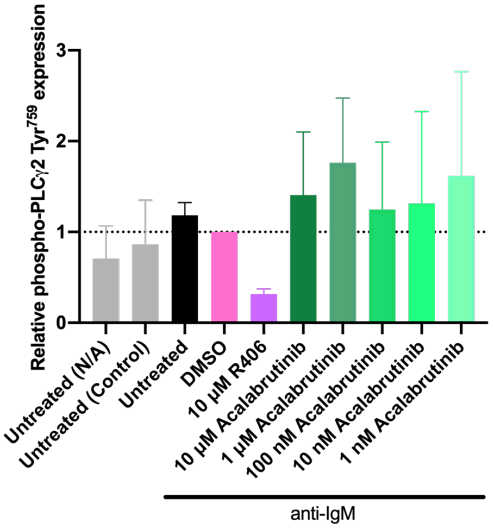

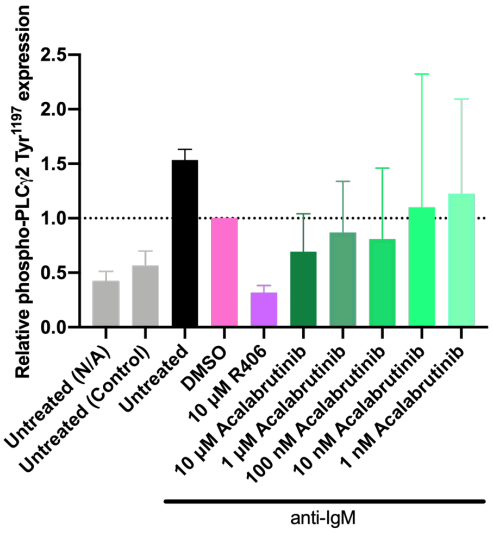

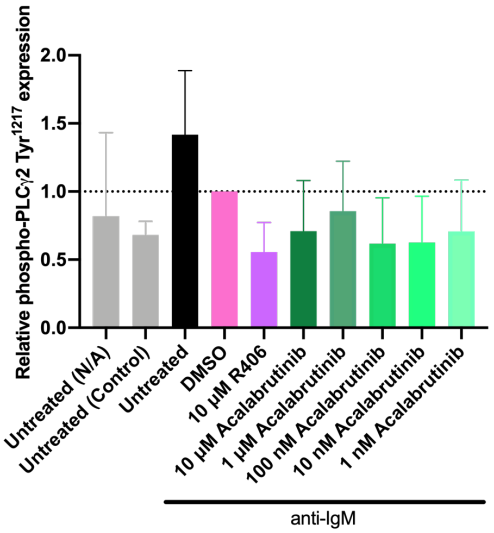

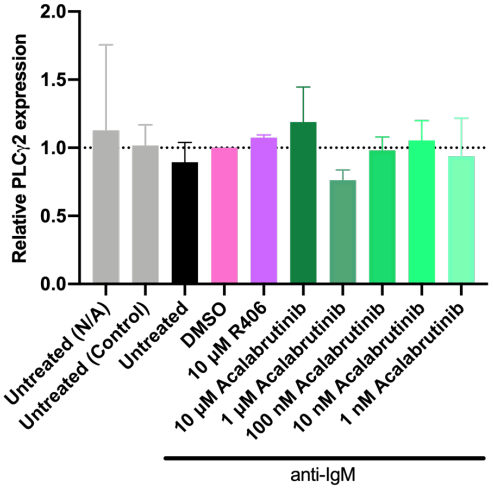

SUPPLEMENTARY FIGURE 6: SUMMARY OF THE EFFECT OF ACALABRUTINIB ON ANTI-IGM-INDUCED PHOSPHORYLATION OF BCR-ASSOCIATED SIGNALLING PROTEINS IN TMD8 CELLS.

TMD8 cells were pretreated with 10 μM, 1 μM, 100 nM, 10 nM or 1 nM acalabrutinib, 10 μM R406, DMSO (as a vehicle control), or left untreated as a control for 1 hour before treatment with anti-IgM or control antibody [Untreated (Control)]. As an additional control, some cells were left untreated for the duration of the experiment [Untreated (N/A)]. Cells were collected after 30 seconds of anti-IgM treatment and expression of phosphorylated proteins as indicated on the figure, along with GAPDH as a loading control, were analysed by immunoblotting. Figure shows quantification for all samples analysed, calculated as relative protein expression, where the bars represent mean and standard deviation of n=3. The values for the DMSO-treated cells are set to 1.0.

Supplementary Figure 6 relates to **Section 4.4.2** of the main thesis.

Supplementary Figure 7 referes to **Section 4.5.1** of the main thesis.

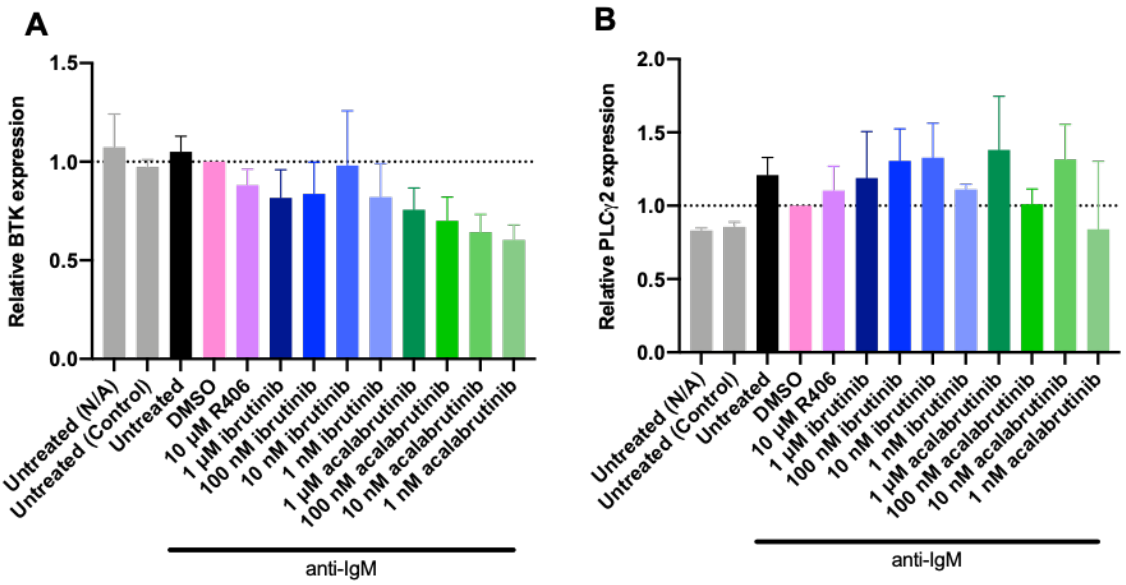

SUPPLEMENTARY FIGURE 7: SUMMARY OF THE EFFECT OF BTK INHIBITION ON ANTI-IGM-INDUCED PHOSPHORYLATION OF BCR-ASSOCIATED SIGNALLING PROTEINS IN PRIMARY CLL SAMPLES.

CLL samples were pretreated with 1 μM, 100 nM, 10 nM or 1 nM ibrutinib or 1 μM, 100 nM, 10 nM or 1 nM acalabrutinib, 10 μM R406, DMSO (as a vehicle control), or left untreated as a control for 1 hour before treatment with anti-IgM or control antibody [Untreated (Control)]. As an additional control, some cells were left untreated for the duration of the experiment [Untreated (N/A)]. Cells were collected after 30 seconds of anti-IgM treatment and expression of phosphorylated and total proteins as indicated on the figure, along with GAPDH as a loading control, were analysed by immunoblotting. Figure shows quantification for all samples analysed, calculated as relative protein expression, with each bar representing the mean and standard deviation of n=3 . The values for the DMSO-treated cells are set to 1.0. Statistical significance, determined by paired t test, of the difference between DMSO and each condition is indicated on the graph.

Supplementary Figure 8 relates to **Section 0** of the main thesis.

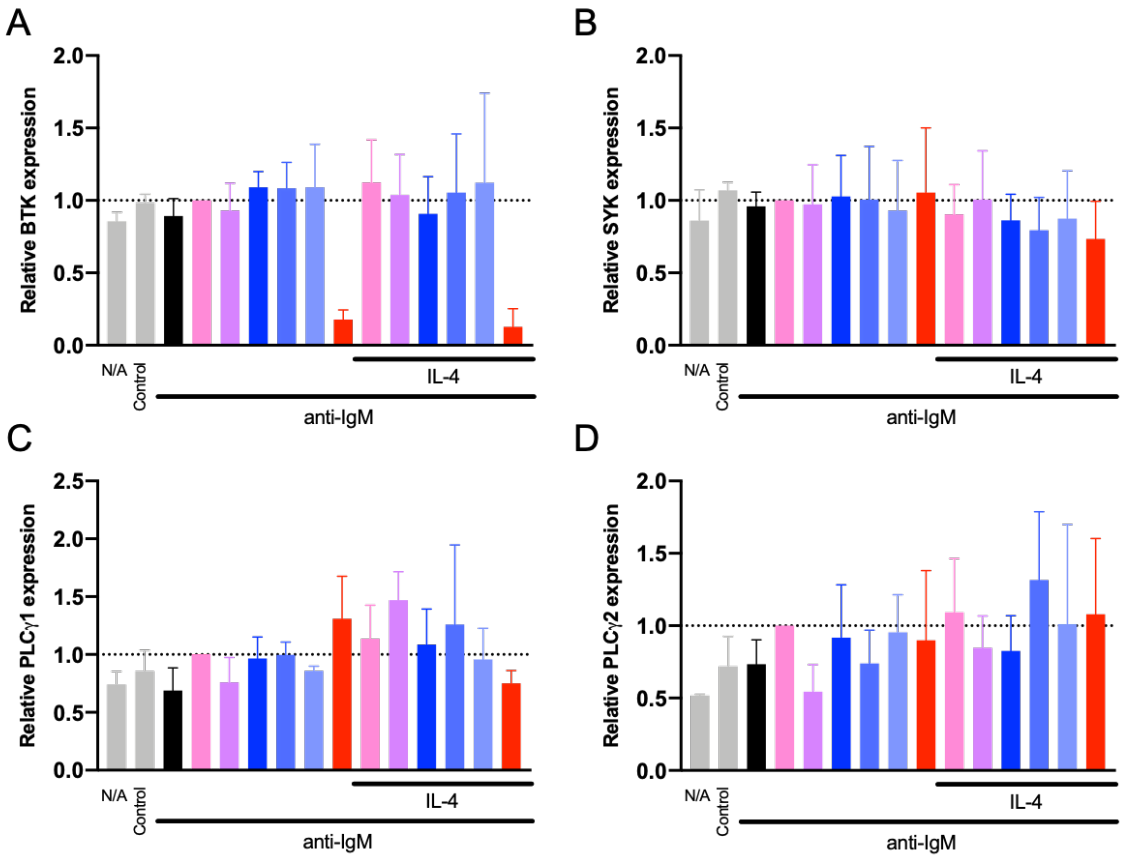

Key
Untreated (Control or N/A)
Untreated (with anti-IgM)
DMSO
R406
100 nM ibrutinib
10 nM ibrutinib
1 nM ibrutinib
500 nM MT-802

SUPPLEMENTARY FIGURE 8: SUMMARY OF THE EFFECT OF BTK INHIBITION ON ANTI-IGM-INDUCED PHOSPHORYLATION OF BCR-ASSOCIATED SIGNALLING PROTEINS IN PRIMARY CLL SAMPLES FOLLOWING IL-4 STIMULATION.

CLL samples (n=5) were left untreated or treated with IL-4 for a total of 24 hours with the addition of 500 nM MT-802 (n=3), or DMSO for 4 hours, or with 100 nM, 10 nM or 1 nM ibrutinib, 10 μM R406, or left untreated as an additional control for 1 hour before treatment with anti-IgM or control antibody. Cells were collected after 30 seconds of anti-IgM (or control antibody) treatment and expression of phosphorylated and total proteins, along with GAPDH as a loading control, were analysed by immunoblotting. Figure shows quantification for all samples analysed, calculated as relative protein expression, with each square representing the mean of n=5 (except MT-802 treated cells where n=3). The values for the DMSO-treated cells (without IL-4 pretreatment) are set to 1.0.

Supplementary Figure 9 relates to **Section 4.7.1** of the main thesis.

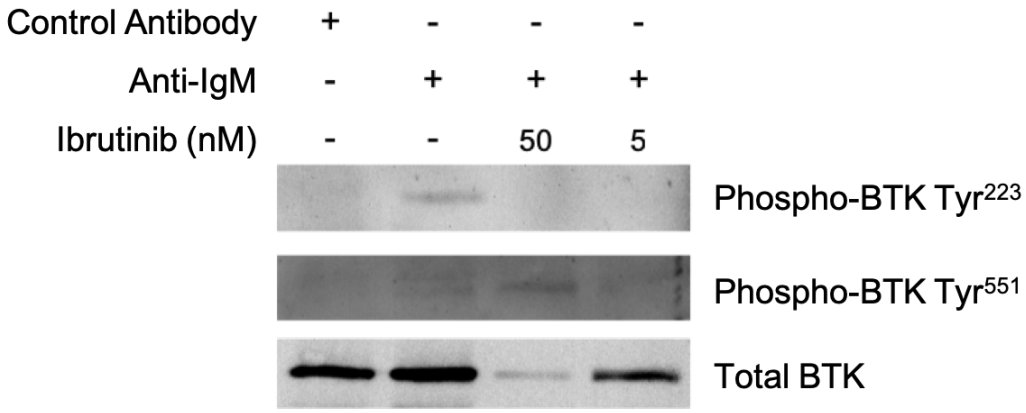

SUPPLEMENTARY FIGURE 9: EFFECT OF IBRUTINIB TREATMENT ON THE OCCUPANCY OF THE BTK ACTIVE SITE AND ACTIVATION OF THE KINASE.

OCI-Ly7 cells were pretreated with 50 nM or 5 nM ibrutinib or left untreated for 1 hour prior to treatment with anti-IgM or control antibody. Cells were collected after 30 seconds of anti-IgM treatment and protein lysates were passed through multi-inhibitor beads to capture kinases with available active sites and the bead-bound fraction with eluted and collected. Protein expression was analysed by immunoblotting where phospho-BTK Tyr223 was detectable in 1 repeat and phospho-BTK Tyr551 was detectable in 2 repeats. Figure shows representative immunoblots for phospho-BTK Tyr551 and total BTK (n=3).

Supplementary Figure 10 relates to **Section 4.6.1** of the main thesis.

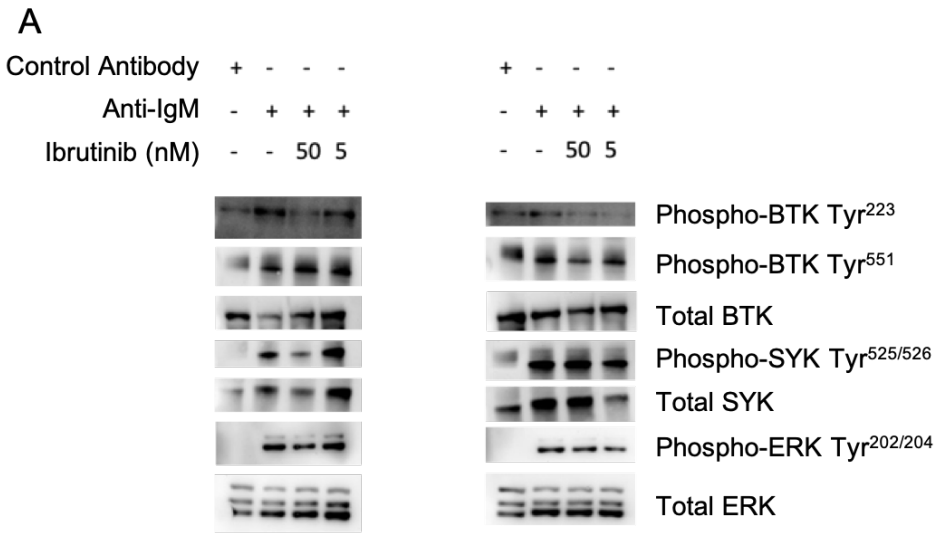

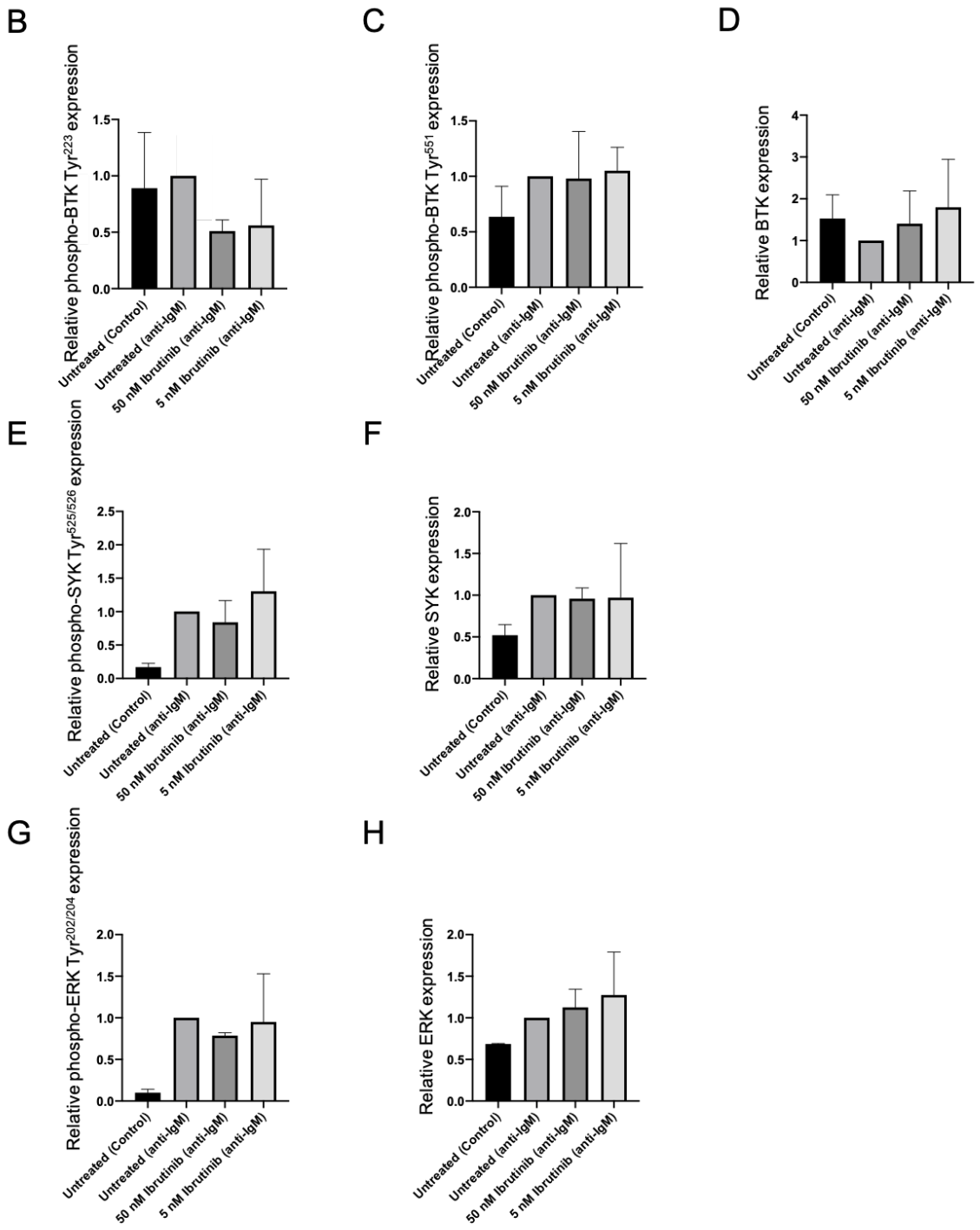

SUPPLEMENTARY FIGURE 10: EFFECT OF IBRUTINIB TREATMENT ON ANTI-IGM-INDUCED PHOSPHORYLATION OF BCR-ASSOCIATED SIGNALLING PROTEINS.

OCI-Ly7 cells were pretreated with 50 nM or 5 nM ibrutinib before treatment with anti-IgM or control antibody. Cells were collected after 30 seconds of anti-IgM treatment and protein lysates were either used for the MIBs assay (**Figure 4-17 and 4-18**) or were anlaysed by immunoblotting, shown here. Expression of phosphorylated and total proteins as indicated on the figure were analysed by immunoblotting. Matched lysates from the MIBs assay were available for 2 of the repeats (**A**) and each protein was quantified. Summary of the quantification of relative protein expression (**B-H**) is indicated with each bar representing the mean and standard deviation of n=2. The untreated cells stimulated with anti-IgM is set to 1.0.

Supplementary Figure 11 relates to **Section 5.1** of the main thesis.

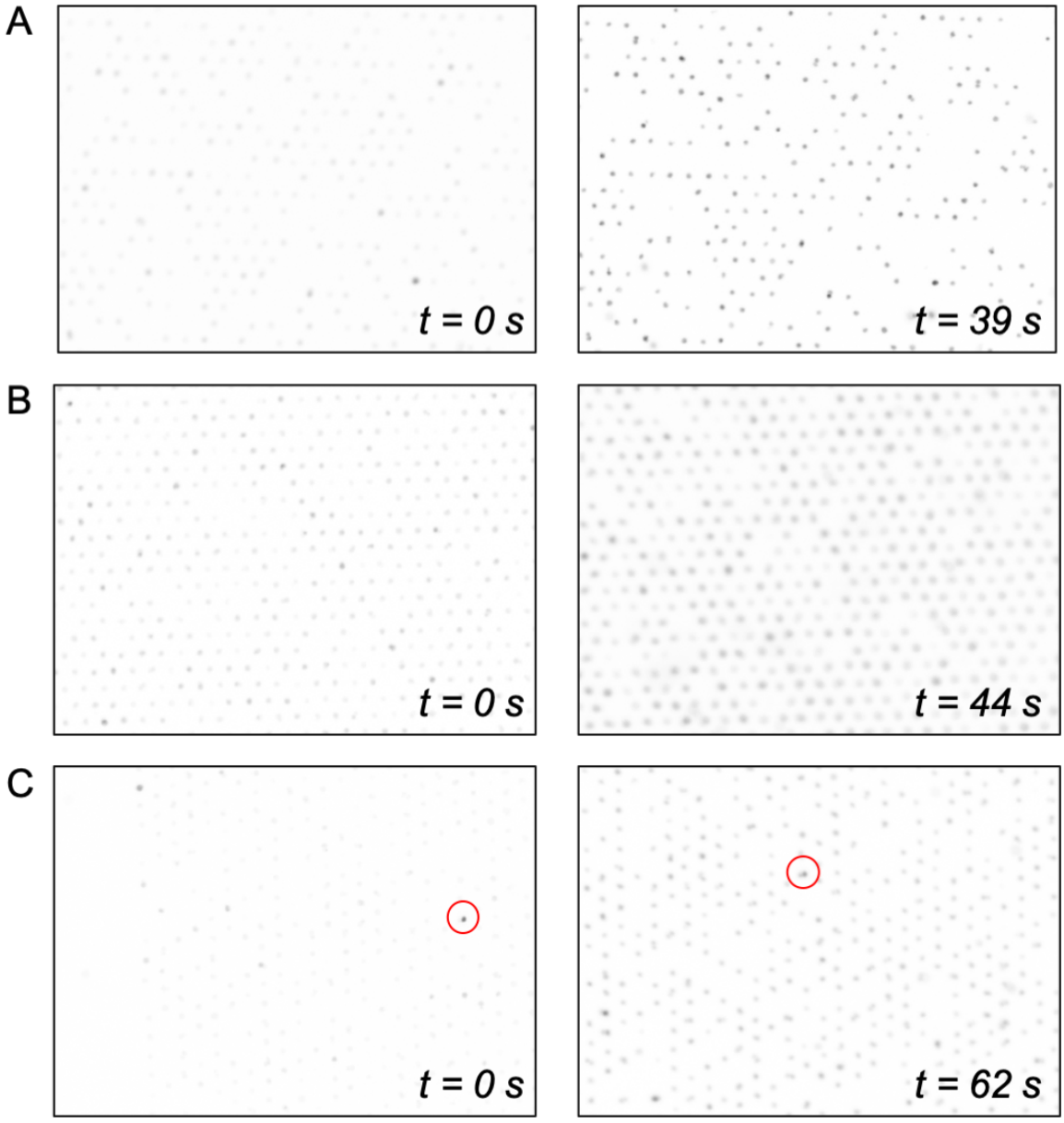

SUPPLEMENTARY FIGURE 11: COMPARISON OF METHOD OF LIGAND DELIVERY TO OCI-LY7 CELLS TRAPPED IN THE MICROWELL ARRAYS.

OCI-Ly7 cells stained with Fluo-8 AM Ca^{2+} indicator dye were loaded into the microwell arrays. Images were captured at 500 ms intervals with an exposure time of 100 ms and 10 frames were collected as baseline fluorescence; a representative image is shown on the left. Ionomycin was added either by directly pipetting on to the surface of the array **(A)**, or by pipetting at the edge of a coverslip placed on the array prior to imaging (**B and C**). The images on the right are representative of the response seen following ionomycin addition. The cell highlighted in the red circle in both images of part **C** is the same cell and indicates movement of the array under the microscope.

Supplementary Figure 12 relates to **Section 5.3** of the main thesis.

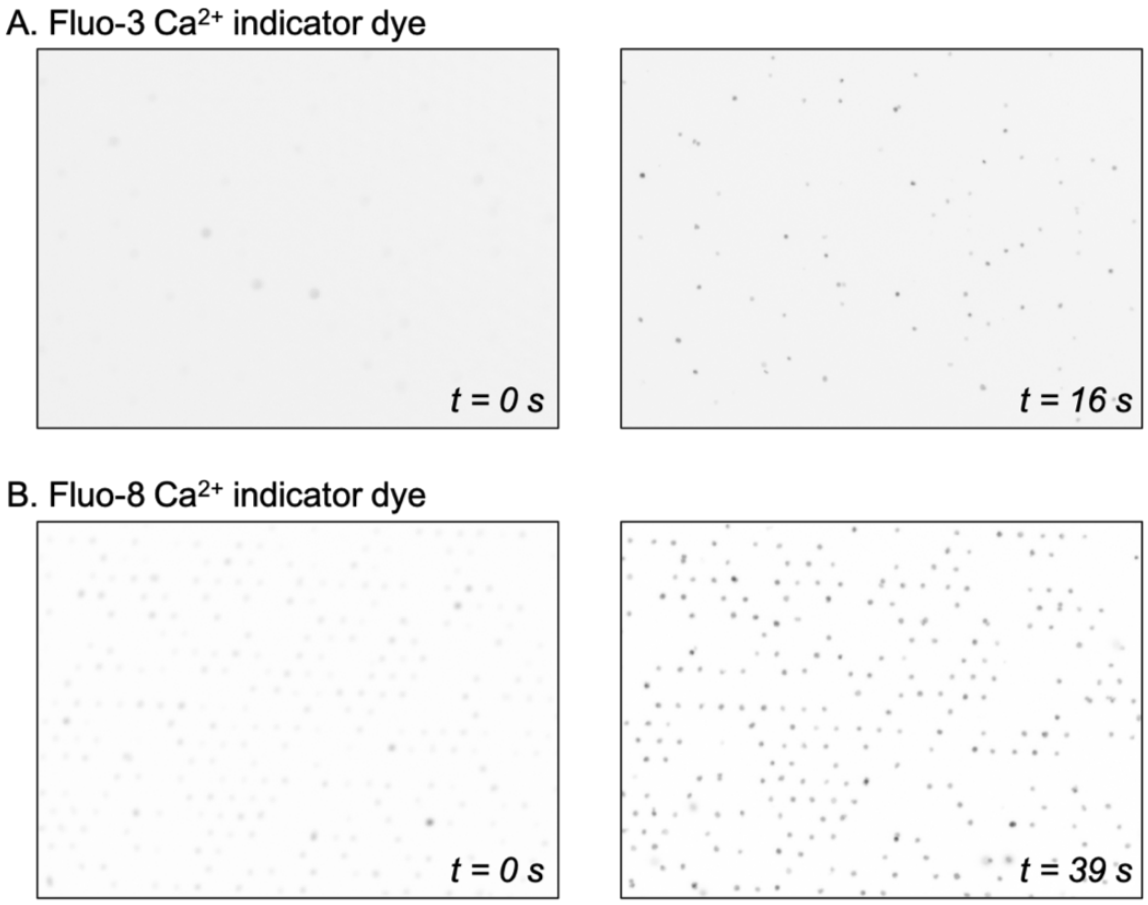

SUPPLEMENTARY FIGURE 12: COMPARISON OF CA^{2+} INDICATOR DYES USING OCI-LY7 CELLS TRAPPED IN MICROWELL ARRAYS.

OCI-Ly7 cells were stained with Fluo-3 AM **(A)** or Fluo-8 AM **(B)** prior to seeding in the arrays. Images were captured at 500 ms intervals. Arrays containing Fluo-3 AM-stained cells were imaged with an exposure time of 300 ms, whereas arrays containing Fluo-8 AM-stained cells were imaged with an exposure time of 100 ms. 10 frames were acquired before the addition of ionomycin. Images on the left represent baseline fluorescence and images on the right represent the brightest fluorescence observed following the addition of ionomycin.

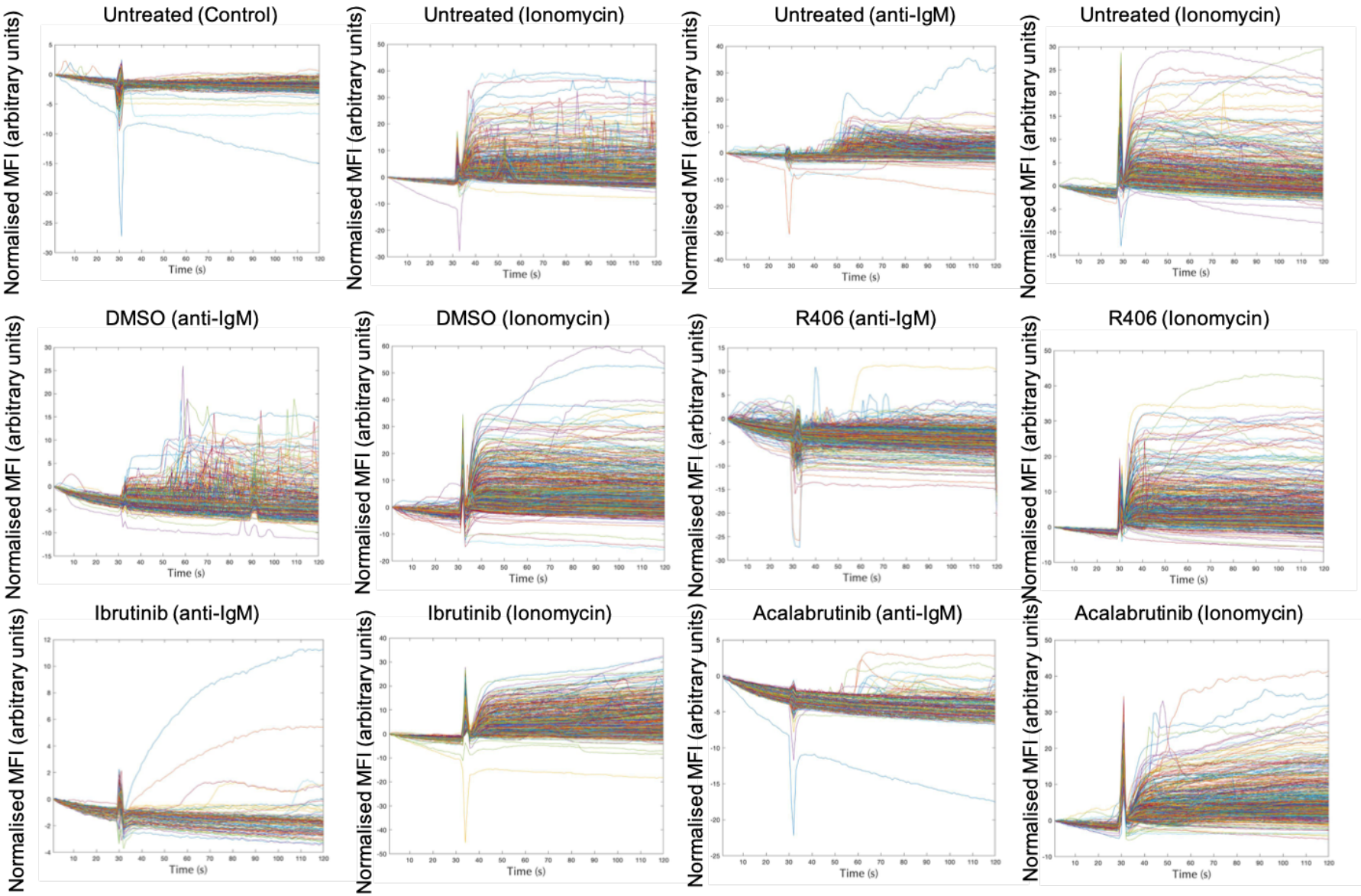
Untreated (Control)
Untreated (Ionomycin)
Untreated (anti-IgM)
Untreated (Ionomycin)
DMSO (anti-IgM)
DMSO (Ionomycin)
R406 (anti-IgM)
R406 (Ionomycin)
Ibrutinib (anti-IgM)
Ibrutinib (Ionomycin)
Acalabrutinib (anti-IgM)
Acalabrutinib (Ionomycin)
Normalised MFI (arbitrary units)
Time (s)

SUPPLEMENTARY FIGURE 13: CA^{2+} MOBILIZATION ANALYSIS IN CLL 674B TRAPPED IN MICROWELL ARRAYS.

Baseline data was captured for ~30 seconds for all conditions. The response to addition of control antibody or anti-IgM was collected using untreated cells, as indicated on the figure. The response to anti-IgM stimulation was recorded in cells pretreated with kinase inhibitors or DMSO, as a vehicle control. All conditions were treated with ionomycin as a control.

Supplementary Figure 13 relates to **Section 5.7** of the main thesis.

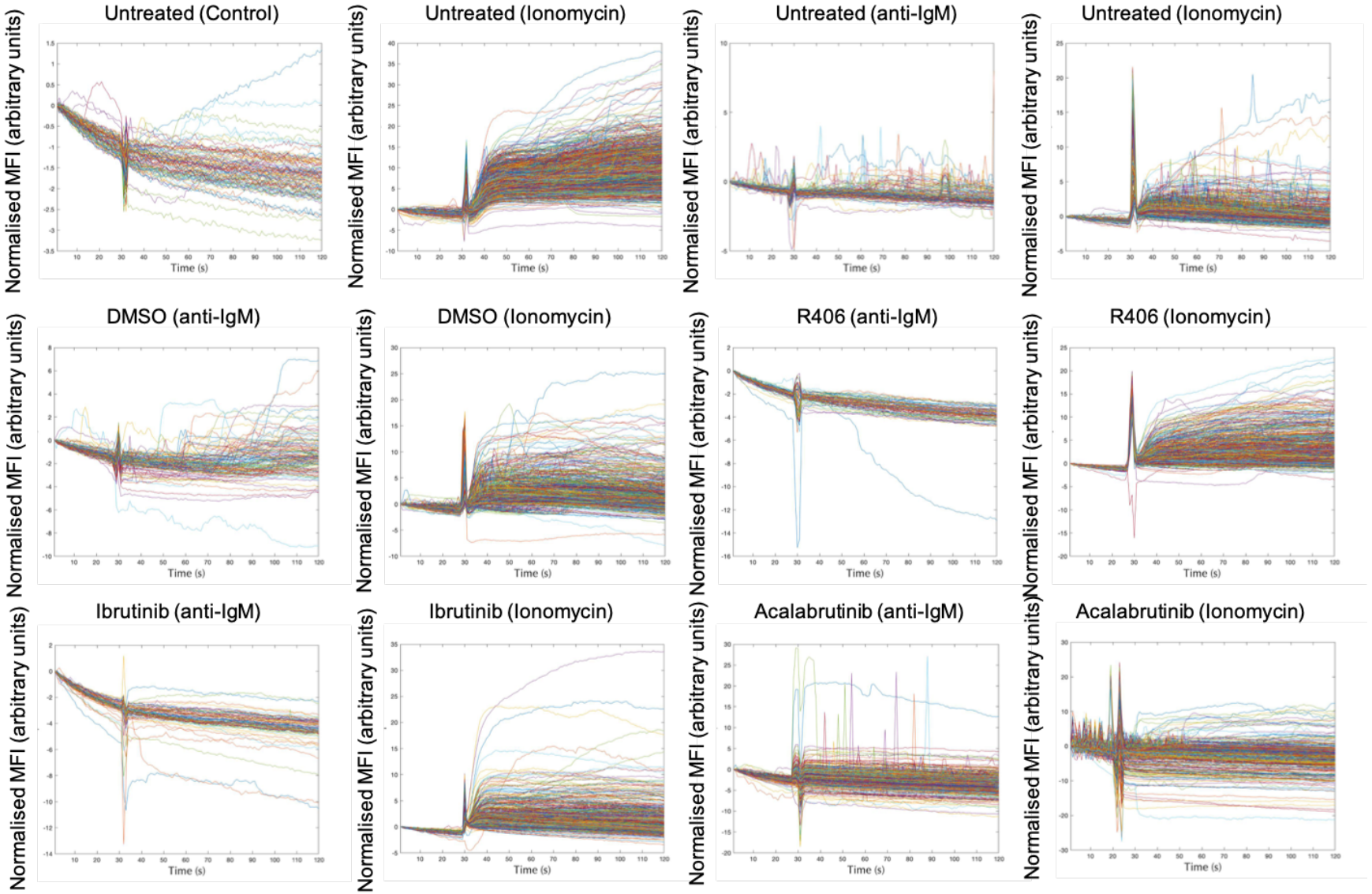
Untreated (Control)
Untreated (Ionomycin)
Untreated (anti-IgM)
Untreated (Ionomycin)
DMSO (anti-IgM)
DMSO (Ionomycin)
R406 (anti-IgM)
R406 (Ionomycin)
Ibrutinib (anti-IgM)
Ibrutinib (Ionomycin)
Acalabrutinib (anti-IgM)
Acalabrutinib (Ionomycin)
Normalised MFI (arbitrary units)
Time (s)

SUPPLEMENTARY FIGURE 14: CA^{2+} MOBILIZATION ANALYSIS IN CLL 635D TRAPPED IN MICROWELL ARRAYS.

Baseline data was captured for ~30 seconds for all conditions. The response to addition of control antibody or anti-IgM was collected using untreated cells, as indicated on the figure. The response to anti-IgM stimulation was recorded in cells pretreated with kinase inhibitors or DMSO, as a vehicle control. All conditions were treated with ionomycin as a control.

Supplementary Figure 14 relates to **Section 5.7** of the main thesis.

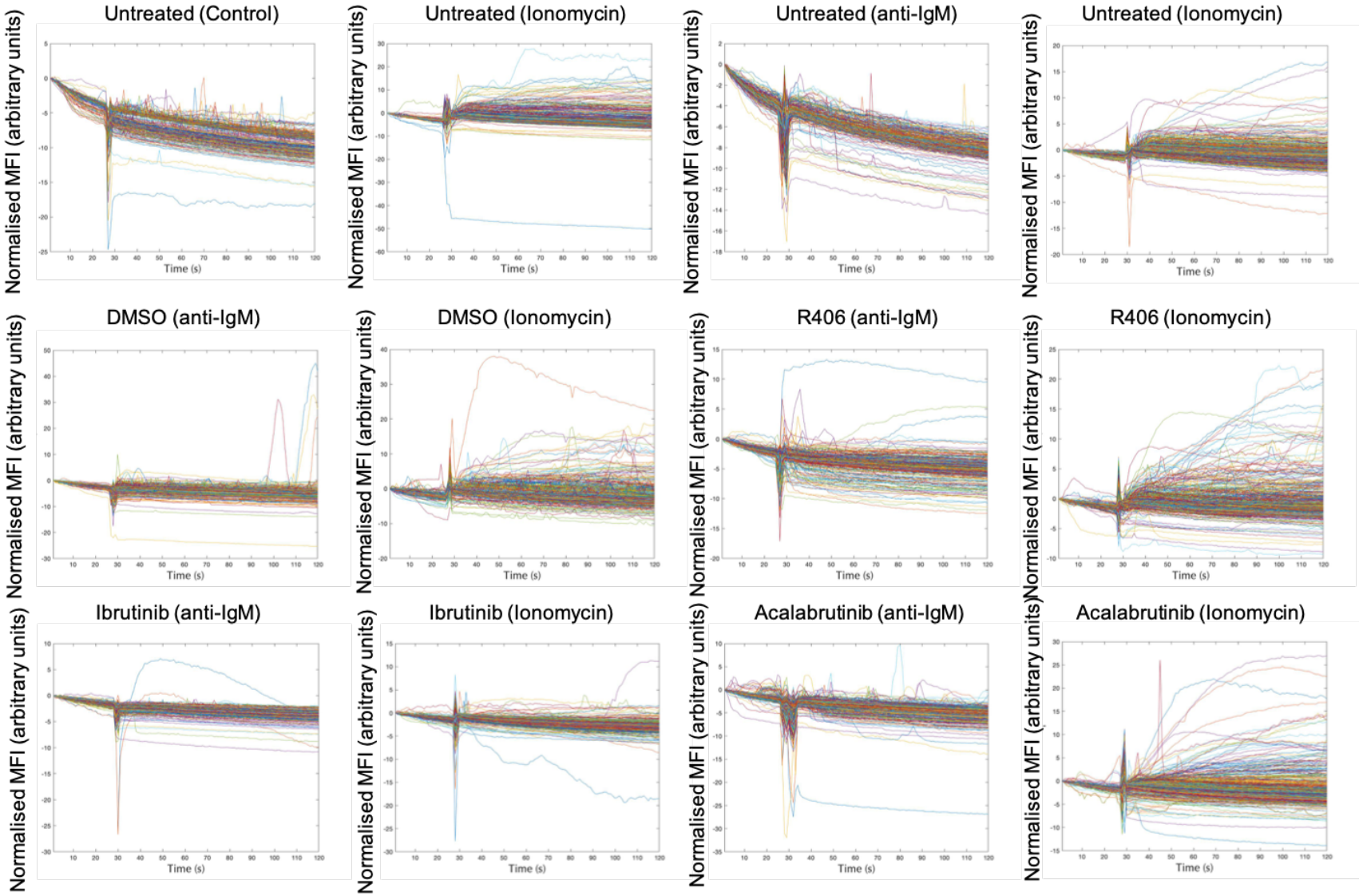
Untreated (Control)
Untreated (Ionomycin)
Untreated (anti-IgM)
Untreated (Ionomycin)
DMSO (anti-IgM)
DMSO (Ionomycin)
R406 (anti-IgM)
R406 (Ionomycin)
Ibrutinib (anti-IgM)
Ibrutinib (Ionomycin)
Acalabrutinib (anti-IgM)
Acalabrutinib (Ionomycin)
Normalised MFI (arbitrary units)
Time (s)

SUPPLEMENTARY FIGURE 15: CA^{2+} MOBILIZATION ANALYSIS IN CLL 709A TRAPPED IN MICROWELL ARRAYS.

Baseline data was captured for ~30 seconds for all conditions. The response to addition of control antibody or anti-IgM was collected using untreated cells, as indicated on the figure. The response to anti-IgM stimulation was recorded in cells pretreated with kinase inhibitors or DMSO, as a vehicle control. All conditions were treated with ionomycin as a control.

Supplementary Figure 15 relates to **Section 5.7** of the main thesis.

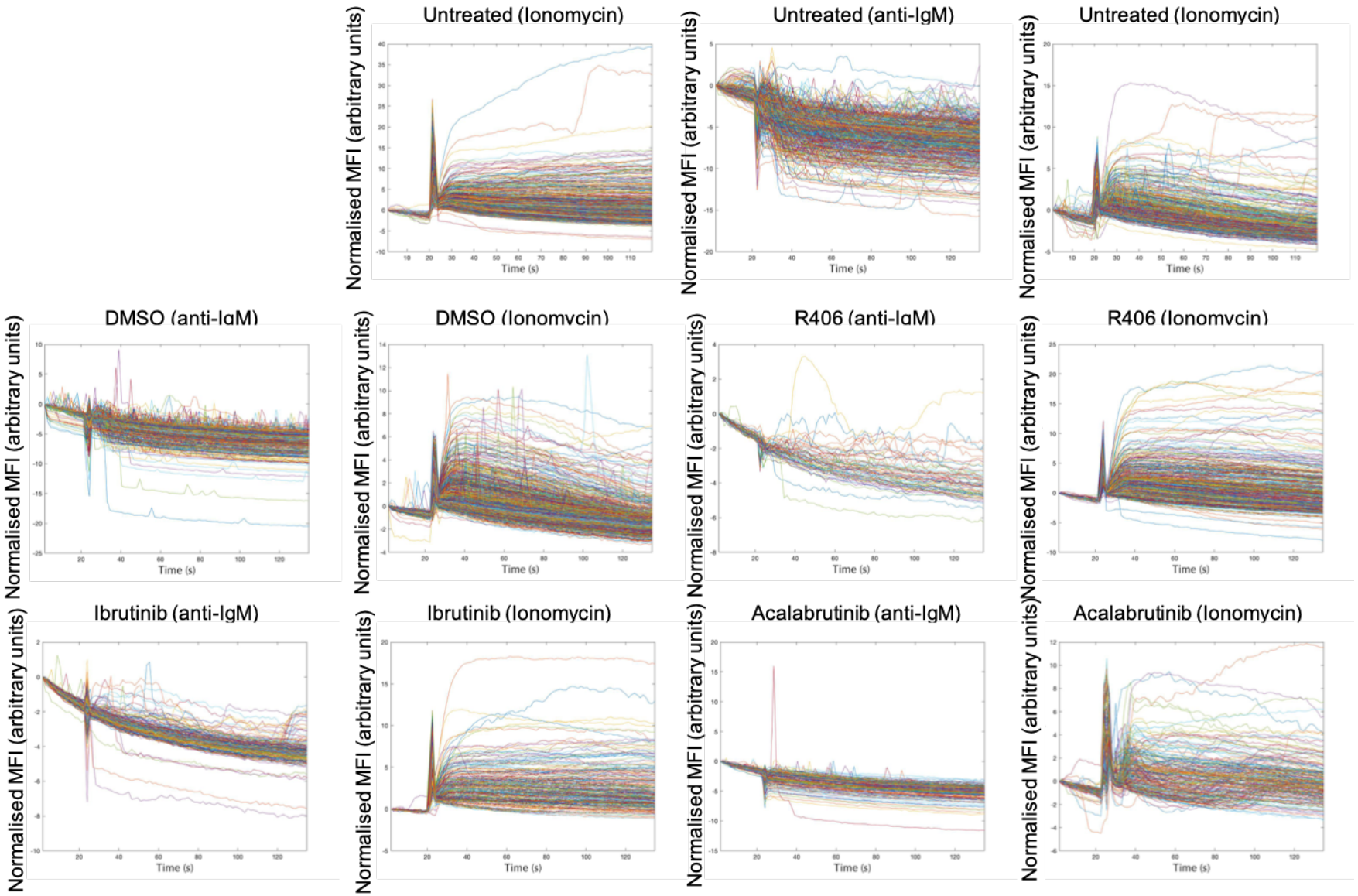
Untreated (Ionomycin)
Untreated (anti-IgM)
Untreated (Ionomycin)
DMSO (anti-IgM)
DMSO (Ionomycin)
R406 (anti-IgM)
R406 (Ionomycin)
Ibrutinib (anti-IgM)
Ibrutinib (Ionomycin)
Acalabrutinib (anti-IgM)
Acalabrutinib (Ionomycin)
Normalised MFI (arbitrary units)
Time (s)

SUPPLEMENTARY FIGURE 16: CA^{2+} MOBILIZATION ANALYSIS IN CLL 774 TRAPPED IN MICROWELL ARRAYS.

Baseline data was captured for ~30 seconds for all conditions. The response to addition of anti-IgM was collected using untreated cells, as indicated on the figure. The response to anti-IgM stimulation was recorded in cells pretreated with kinase inhibitors or DMSO, as a vehicle control. All conditions were treated with ionomycin as a control. The response to control antibody in untreated cells could not be analysed due to array movement following ligand addition.

Supplementary Figure 16 relates to **Section 5.7** of the main thesis.

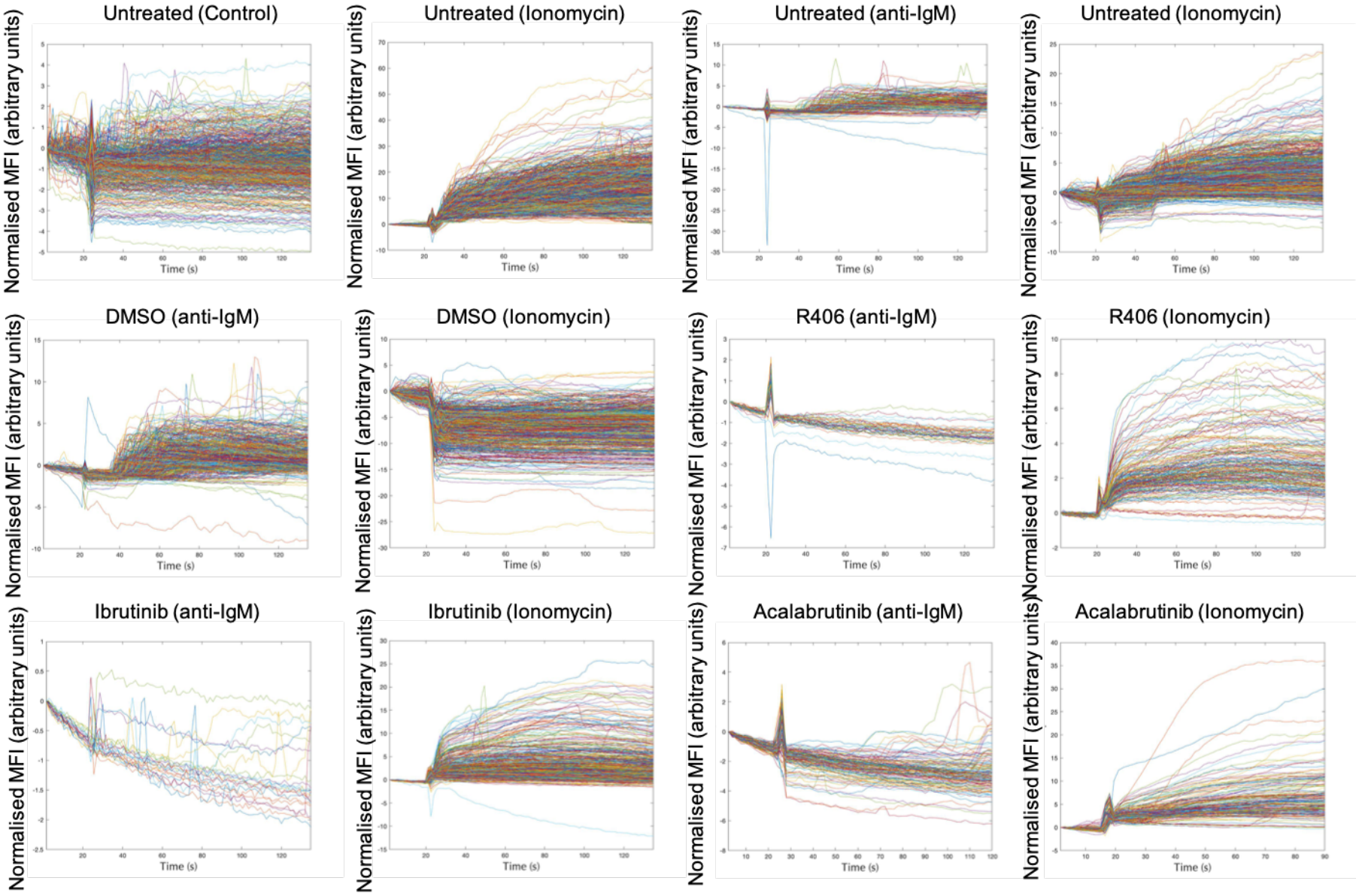
Untreated (Control)
Untreated (Ionomycin)
Untreated (anti-IgM)
Untreated (Ionomycin)
DMSO (anti-IgM)
DMSO (Ionomycin)
R406 (anti-IgM)
R406 (Ionomycin)
Ibrutinib (anti-IgM)
Ibrutinib (Ionomycin)
Acalabrutinib (anti-IgM)
Acalabrutinib (Ionomycin)
Normalised MFI (arbitrary units)
Time (s)

SUPPLEMENTARY FIGURE 17: CA^{2+} MOBILIZATION ANALYSIS IN CLL 780 TRAPPED IN MICROWELL ARRAYS.

Baseline data was captured for ~30 seconds for all conditions. The response to addition of control antibody or anti-IgM was collected using untreated cells, as indicated on the figure. The response to anti-IgM stimulation was recorded in cells pretreated with kinase inhibitors or DMSO, as a vehicle control. All conditions were treated with ionomycin as a control.

Supplementary Figure 17 relates to **Section 5.7** of the main thesis.

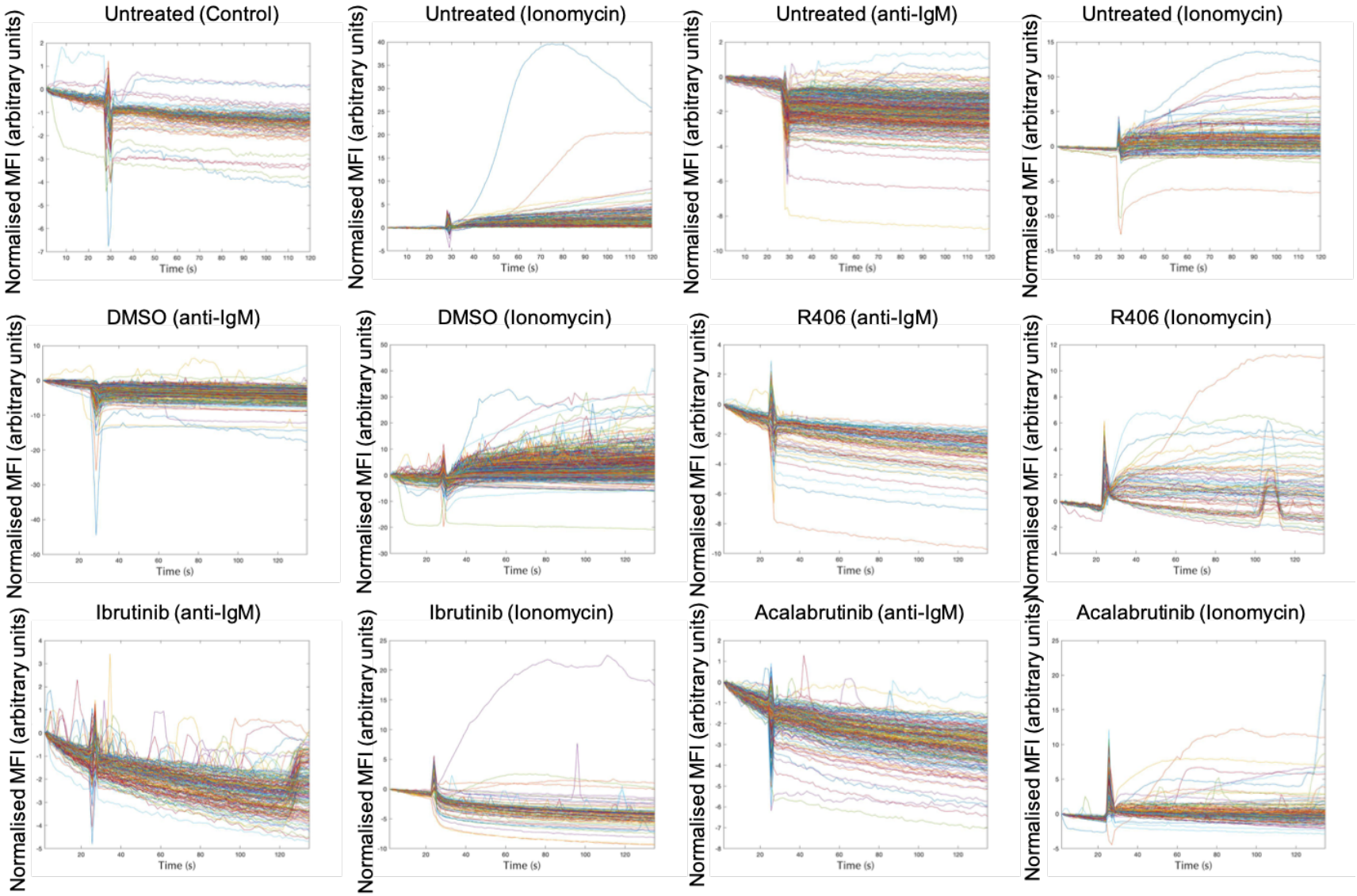
Untreated (Control)
Untreated (Ionomycin)
Untreated (anti-IgM)
Untreated (Ionomycin)
DMSO (anti-IgM)
DMSO (Ionomycin)
R406 (anti-IgM)
R406 (Ionomycin)
Ibrutinib (anti-IgM)
Ibrutinib (Ionomycin)
Acalabrutinib (anti-IgM)
Acalabrutinib (Ionomycin)
Normalised MFI (arbitrary units)
Time (s)

SUPPLEMENTARY FIGURE 18: CA^{2+} MOBILIZATION ANALYSIS IN CLL 781 TRAPPED IN MICROWELL ARRAYS.

Baseline data was captured for ~30 seconds for all conditions. The response to addition of control antibody or anti-IgM was collected using untreated cells, as indicated on the figure. The response to anti-IgM stimulation was recorded in cells pretreated with kinase inhibitors or DMSO, as a vehicle control. All conditions were treated with ionomycin as a control.

Supplementary Figure 18 relates to **Section 5.7** of the main thesis.

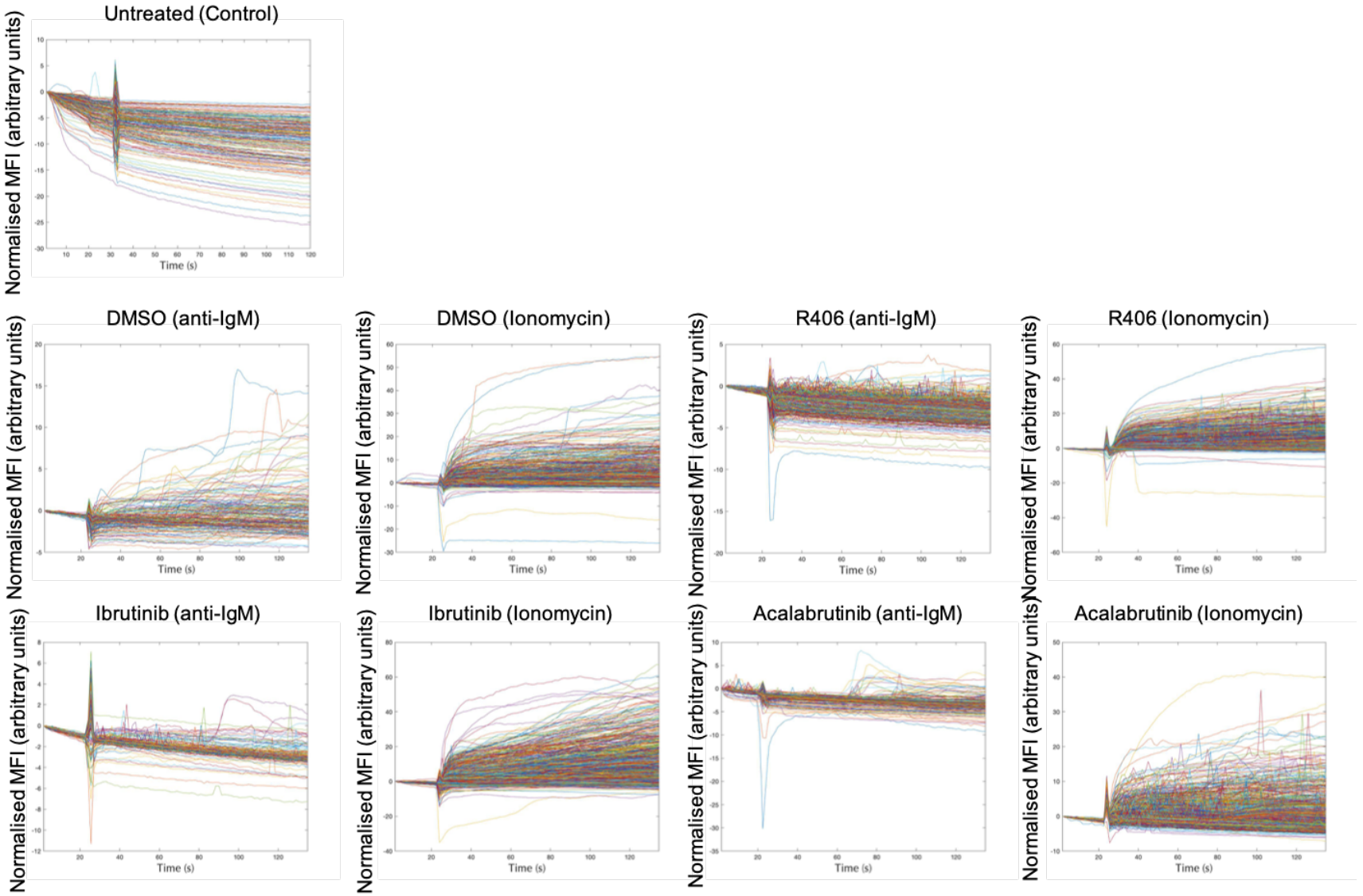
Untreated (Control)
DMSO (anti-IgM)
DMSO (Ionomycin)
R406 (anti-IgM)
R406 (Ionomycin)
Ibrutinib (anti-IgM)
Ibrutinib (Ionomycin)
Acalabrutinib (anti-IgM)
Acalabrutinib (Ionomycin)
Normalised MFI (arbitrary units)
Time (s)

SUPPLEMENTARY FIGURE 19: CA^{2+} MOBILIZATION ANALYSIS IN CLL 681 TRAPPED IN MICROWELL ARRAYS.

Baseline data was captured for ~30 seconds for all conditions. The response to addition of control antibody was collected using untreated cells, as indicated on the figure. The response to anti-IgM stimulation was recorded in cells pretreated with kinase inhibitors or DMSO, as a vehicle control. All conditions were treated with ionomycin as a control. The reponse of untreated cells to anti-IgM or ionomycin addition could not be analysed fue to movement of the array upon ligand addition.

Supplementary Figure 19 relates to **Section 5.7** of the main thesis.

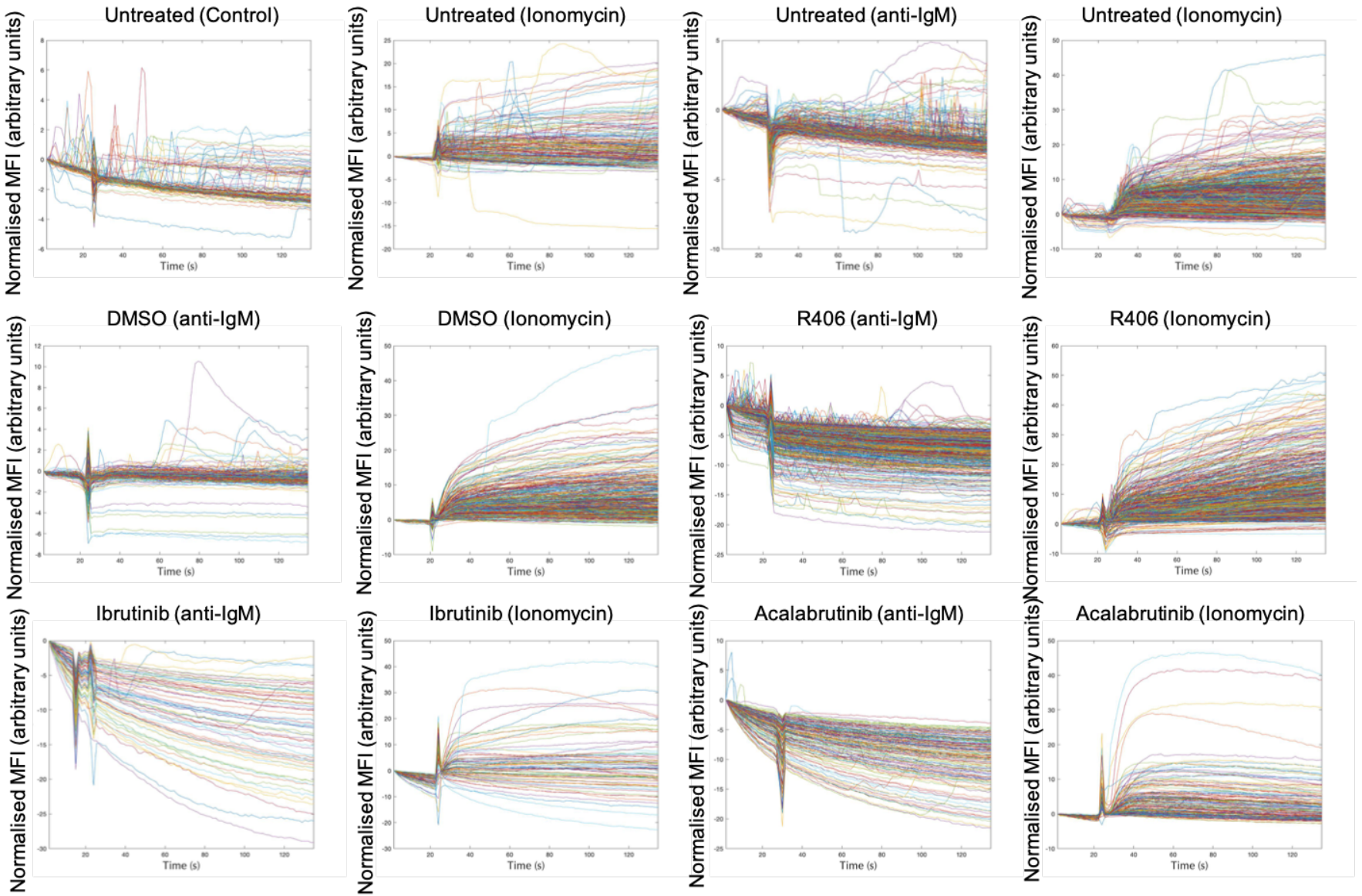
Untreated (Control)
Untreated (Ionomycin)
Untreated (anti-IgM)
Untreated (Ionomycin)
DMSO (anti-IgM)
DMSO (Ionomycin)
R406 (anti-IgM)
R406 (Ionomycin)
Ibrutinib (anti-IgM)
Ibrutinib (Ionomycin)
Acalabrutinib (anti-IgM)
Acalabrutinib (Ionomycin)
Normalised MFI (arbitrary units)
Time (s)

SUPPLEMENTARY FIGURE 20: CA^{2+} MOBILIZATION ANALYSIS IN CLL 803B TRAPPED IN MICROWELL ARRAYS.

Baseline data was captured for ~30 seconds for all conditions. The response to addition of control antibody or anti-IgM was collected using untreated cells, as indicated on the figure. The response to anti-IgM stimulation was recorded in cells pretreated with kinase inhibitors or DMSO, as a vehicle control. All conditions were treated with ionomycin as a control.

Supplementary Figure 20 relates to **Section 5.7** of the main thesis.

List of References

Abe, M., Y. Nozawa, H. Wakasa, H. Ohno, and S. Fukuhara. 1988. Characterization and comparison of two newly established Epstein-Barr virus-negative lymphoma B-cell lines: Surface markers, growth characteristics, cytogenetics, and transplantability. Cancer. 61:483–490. doi:10.1002/1097-0142(19880201)61:3<483::AID-CNCR2820610313>3.0.CO;2-L.

Aguilar-Hernandez, M.M., M.D. Blunt, R. Dobson, A. Yeomans, S. Thirdborough, M. Larrayoz, L.D. Smith, A. Linley, J.C. Strefford, A. Davies, P.M.W. Johnson, N. Savelyeva, M.S. Cragg, F. Forconi, G. Packham, F.K. Stevenson, and A.J. Steele. 2016. IL-4 enhances expression and function of surface IgM in CLL cells. Blood. 127:3015–3025. doi:10.1182/blood-2015-11-682906.

Alexandrov, L.B., S. Nik-Zainal, D.C. Wedge, S.A.J.R. Aparicio, S. Behjati, A. Biankin, G. Bignell, N. Bolli, A. Borg, A.-L. Borresen-Dale, S. Boyault, B. Burkhardt, A. Butler, C. Caldas, H. Davies, C. Desmedt, R. Eils, J. Eyfjord, J. Foekens, M. Greaves, F. Hosoda, B. Hutter, T. Ilicic, S. Imbeaud, M. Imielink, N. Jager, D. Jones, D. Jones, S. Knappskog, M. Kool, S. Lakhani, C. Lopez-Otin, S. Martin, N. Munshi, H. Nakamura, P. Northcott, M. Pajic, E. Papaemmanuil, A. Paradiso, J. Pearson, X. Puente, K. Raine, M. Ramakrishna, A. Richardson, J. Richter, P. Rosenstiel, M. Schlesner, T. Schumacher, P. Span, J. Teague, Y. Totoki, A. Tutt, R. Valdes-Mas, M. van Buuren, L. van 't Veer, A. Vincent-Salomon, N. Waddell, L. Yates, J. Zucman-Rossi, P. Futreal, U. McDermott, P. Lichter, M. Meyerson, S. Grimmond, R. Siebert, E. Campo, T. Shibata, S. Pfister, P. Campbell, and M. Stratton. 2013. Signatures of mutational processes in human cancer. Nature. 500:415–421. doi:10.1038/nature12477.Signatures.

Allen, C.D.C., K.M. Ansel, C. Low, R. Lesley, H. Tamamura, N. Fujii, and J.G. Cyster. 2004. Germinal center dark and light zone organization is mediated by CXCR4 and CXCR5. Nat. Immunol. 5:943–952. doi:10.1038/ni1100.

Alt, F.W., T.K. Blackwell, and G.D. Yancopoulos. 1987. Development of the Primary Antibody Repertoire. Science. 238:1079–1087.

Amé-Thomas, P., S. Hoeller, C. Artchounin, J. Misiak, M.S. Braza, R. Jean, J. Le Priol, C. Monvoisin, N. Martin, P. Gaulard, and K. Tarte. 2015. CD10 delineates a subset of human IL-4 producing follicular helper T cells involved in the survival of follicular lymphoma B cells. Blood. 125:2381–2385. doi:10.1182/blood-2015-02-625152.

Arnson, J.E. and J. Brown. 2017. Targeting B cell signaling in chronic lymphocytic leukemia. Curr. Oncol. Rep. 19:61. doi:10.1007/s11912-107-0620-7.

Arthur, R., B. Beatriz Valle-Argos, A.J. Steele, and G. Packham. 2020. Development of PROTACs to address clinical limitations associated with BTK-targeted kinase inhibitors. Explor. Target. Anti-tumor Ther. 1:131–152. doi:10.37349/etat.2020.00009.

Atkinson, B.T., W. Ellmeier, and S.P. Watson. 2003. Tec regulates platelet activation by GPVI in the absence of Btk. Blood. 102:3592–3599. doi:10.1182/blood-2003-04-1142.

Autore, F., P. Strati, I. Innocenti, F. Corrente, L. Trentin, A. Cortelezzi, C. Visco, M. Coscia, A. Cuneo, A. Gozzetti, F.R. Mauro, A.M. Frustaci, M. Gentile, F. Morabito, S. Molica, P. Falcucci, G. D'Arena, R. Murru, D. Vincelli, D.G. Efremov, A. Ferretti, G.M. Rigolin, C. Vitale, M.C. Tisi, G. Reda, A. Visentin, S. Sica, R. Foà, A. Ferrajoli, and L. Laurenti. 2019. Elevated lactate dehydrogenase has prognostic relevance in treatment-naïve patients affected by chronic lymphocytic leukemia with trisomy 12. Cancers. 11(7):1–12. doi:10.3390/cancers11070896.

Avalos, A.M., and H.L. Ploegh. 2014. Early BCR events and antigen capture, processing, and loading on MHC class II on B cells. Front. Immunol. 5:1–5. doi:10.3389/fimmu.2014.00092.

Baba, Y., and T. Kurosaki. 2011. Impact of Ca^{2+} signaling on B cell function. Trends Immunol. 32:589–594. doi:10.1016/j.it.2011.09.004.

Baba, Y., M. Matsumoto, and T. Kurosaki. 2014. Calcium signaling in B cells: Regulation of cytosolic Ca^{2+} increase and its sensor molecules, STIM1 and STIM2. Mol. Immunol. 62:339–343. doi:10.1016/j.molimm.2013.10.006.

Banér, J., M. Nilsson, M. Mendel-Hartvig, and U. Landegren. 1998. Signal amplification of padlock probes by rolling circle replication. Nucleic Acids Res. 26:5073–5078. doi:10.1093/nar/26.22.5073.

Barf, T., T. Covey, R. Izumi, B. Van De Kar, M. Gulrajani, B. Van Lith, M. Van Hoek, E. De Zwart, D. Mittag, D. Demont, S. Verkaik, F. Krantz, P.G. Pearson, R. Ulrich, and A. Kaptein. 2017. Acalabrutinib (ACP-196): A covalent Bruton tyrosine kinase inhibitor with a differentiated selectivity and in vivo potency profile. J. Pharmacol. Exp. Ther. 363:240–252. doi:10.1124/jpet.117.242909.

Beckwith, M., D.L. Longo, C.D. O'Connell, C.M. Moratz, and W.J. Urba. 1990. Phorbol ester-induced, cell-cycle-specific, growth inhibition of human B-lymphoma cell lines. J. Natl. Cancer Inst. 82:501–509. doi:10.1093/jnci/82.6.501.

Benson, M.J., L.D. Erickson, M.W. Gleeson, and R.J. Noelle. 2007. Affinity of antigen encounter and other early B-cell signals determine B-cell fate. Curr. Opin. Immunol. 19:275–280. doi:10.1016/j.coi.2007.04.009.Affinity.

Berry, C.T., X. Liu, A. Myles, C.J. Lengner, M.J. May, B.D. Freedman, C.T. Berry, X. Liu, A. Myles, S. Nandi, Y.H. Chen, U. Hershberg, and I.E. Brodsky. 2020. Survival , Metabolic Reprogramming , and Proliferation of Naive B Cells Article Tune Survival , Metabolic Reprogramming , and Proliferation of Naive B Cells. Cell Reports. 31:107474. doi:10.1016/j.celrep.2020.03.038.

Binet, J.L., A. Auqier, G. Dighiero, C. Chastang, H. Piguet, J. Goasguen, G. Vaugier, G. Potron, P. Colona, F. Oberling, M. Thomas, G. Tchernia, C. Jacquillat, P. Bovin, C. Lesty, M.T. Duault, M. Monconduit, S. Belabbes, and F. Gremy. 1981. A new prognostic classification of chronic lymphocytic leukaemia derived from a multivariate survival analysis. Cancer. 48:198-206. doi: 10.1002/1097-0142(19810701)48:1<198::aid-cncr2820480131>3.0.co;2-v.

Bond, D.A., and J. Woyach. 2019. Targeting BTK in CLL: Beyond ibrutinib. Curr. Hematol. Malig. Rep. 14:197-205. doi: 10.1007/s11899-019-00512-0.

Bondeson, D.P., A. Mares, I.E.D. Smith, E. Ko, S. Campos, A.H. Miah, K.E. Mulholland, N. Routly, D.L. Buckley, J.L. Gustafson, N. Zinn, P. Grandi, S. Shimamura, G. Bergamini, M. Faelth-Savitski, M. Bantscheff, C. Cox, D.A. Gordon, R.R. Willard, J.J. Flanagan, L.N. Casillas, B.J. Votta, W. Den Besten, K. Famm, L. Kruidenier, P.S. Carter, J.D. Harling, I. Churcher, and C.M. Crews. 2015. Catalytic in vivo protein knockdown by small-molecule PROTACs. Nat. Chem. Biol. 11:611–617. doi:10.1038/nchembio.1858.

Brown, J.R., J. Moslehi, S. O'Brien, P. Ghia, P. Hillmen, F. Cymbalista, T.D. Shanafelt, G. Fraser, S. Rule, T.J. Kipps, S. Coutre, M.S. Dilhuydy, P. Cramer, A. Tedeschi, U. Jaeger, M. Dreyling, J.C. Byrd, A. Howes, M. Todd, J. Vermeulen, D.F. James, F. Clow, L. Styles, R. Valentino, M. Wildgust, M. Mahler, and J.A. Burger. 2017. Characterization of atrial fibrillation adverse events reported in ibrutinib randomized controlled registration trials. Haematologica. 102:1796–1805.

doi:10.3324/haematol.2017.171041.

Buchner, M., S. Fuchs, G. Prinz, D. Pfeifer, K. Bartholome, M. Burger, N. Chevalier, L. Vallat, J. Timmer, J.G. Gribben, H. Jumaa, H. Veelken, C. Dierks, and K. Zirlik. 2009. Spleen Tyrosine Kinase Is Overexpressed and Represents a Potential Therapeutic Target in Chronic Lymphocytic Leukemia. Cancer Res. 69:5424–5433. doi:10.1158/0008-5472.CAN-08-4252.

Buggy, J.J., and L. Elias. 2012. Bruton Tyrosine Kinase (BTK) and Its Role in B-cell Malignancy. Int. Rev. Immunol. 31:119-132. doi:10.3109/08830185.2012.664797.

Buhimschi, A.D., H.A. Armstrong, M. Toure, S. Jaime-Figueroa, T.L. Chen, A.M. Lehman, J.A. Woyach, A.J. Johnson, J.C. Byrd, and C.M. Crews. 2018. Targeting the C481S Ibrutinib-Resistance Mutation in Bruton's Tyrosine Kinase using PROTAC-mediated Degradation. Biochemistry. 57:3564–3575. doi:10.1021/acs.biochem.8b00391.

Bunney, T.D., O. Opaleye, S.M. Roe, P. Vatter, R.W. Baxendale, C. Walliser, K.L. Everett, M.B. Josephs, C. Christow, F. Rodrigues-lima, P. Gierschik, L.H. Pearl, and M. Katan. 2009. Structural Insights into Formation of an Active Signaling Complex between Rac and Phospholipase C Gamma 2. Mol. Cell. 34:223–233. doi:10.1016/j.molcel.2009.02.023.

Burger, J.A., and N. Chiorazzi. 2013. B cell receptor signaling in chronic lymphocytic leukemia. Trends Immunol. 34:592–601. doi:10.1016/j.it.2013.07.002.

Byrd, J.C., R.R. Furman, S.E. Coutre, I.W. Flinn, J.A. Burger, K.A. Blum, B. Grant, J.P. Sharman, M. Coleman, W.G. Wierda, J.A. Jones, W. Zhao, N.A. Heerema, A.J. Johnson, J. Sukbuntherng, B.Y. Chang, F. Clow, E. Hedrick, J.J. Buggy, D.F. James, and S. O'Brien. 2013. Targeting BTK with ibrutinib in relapsed chronic lymphocytic leukemia. N. Engl. J. Med. 369:32–42. doi:10.1056/NEJMoa1215637.

Byrd, J.C., B. Harrington, S. O'Brien, J. a. Jones, A. Schuh, S. Devereux, J. Chaves, W.G. Wierda, F.T. Awan, J.R. Brown, P. Hillmen, D.M. Stephens, P. Ghia, J.C. Barrientos, J.M. Pagel, J. Woyach, D. Johnson, J. Huang, X. Wang, A. Kaptein, B.J. Lannutti, T. Covey, M. Fardis, J. McGreivy, A. Hamdy, W. Rothbaum, R. Izumi, T.G. Diacovo, A.J. Johnson, and R.R. Furman. 2016. Acalabrutinib (ACP-196) in Relapsed Chronic Lymphocytic Leukemia. N. Engl. J. Med. 374:323–332. doi:10.1056/NEJMoa1509981.

Calin, G.A., C.D. Dumitru, M. Shimizu, R. Bichi, S. Zupo, E. Noch, H. Aldler, S. Rattan, M. Keating, K. Rai, L. Rassenti, T. Kipps, M. Negrini, F. Bullrich, and C.M. Croce. 2002. Frequent deletions and down-regulation of micro-RNA genes miR15 and miR16 at 13q14 in chronic lymphocytic leukemia. Proc. Natl. Acad. Sci. U. S. A. 99:15524–15529. doi:10.1073/pnas.242606799.

Calissano, C., R.N. Damle, S. Marsilio, X.J. Yan, S. Yancopoulos, G. Hayes, C. Emson, E.J. Murphy, M.K. Hellerstein, C. Sison, M.S. Kaufman, J.E. Kolitz, S.L. Allen, K.R. Rai, I. Ivanovic, I.M. Dozmorov, S. Roa, M.D. Scharff, W. Li, and N. Chiorazzi. 2011. Intraclonal complexity in chronic lymphocytic leukemia: Fractions enriched in recently born/divided and older/quiescent cells. Mol. Med. 17:1374–1382. doi:10.2119/molmed.2011.00360.

Cambier, J.C., S.B. Gauld, K.T. Merrell, and B.J. Vilen. 2007. B-cell anergy: from transgenic models to naturally occurring anergic B cells? Nat Rev Immunol. 7:633–643. doi:10.1038/nri2133.B-cell.

Catovsky, D., J. Fooks, and S. Richards. 1989. Prognostic factors in chronic lymphocytic leukaemia: the importance of age, sex and response to treatment in survival. British J. Heam. 72:141-149.

Chang, H., J.A. Blondal, S. Benchimol, M.D. Minden, and H.A. Messner. 1995. p53 mutations, c-

myc and bcl-2 rearrangements in human non-Hodgkin's lymphoma cell lines. Leuk. Lymphoma. 19:165–171. doi:10.3109/10428199509059672.

Chang, H., H.A. Messner, X.-H. Wang, C. Yee, L. Addy, J. Meharchand, and M.D. Minden. 1992. A Human Lymphoma Cell Line with Multiple Immunoglobulin Rearrangements. J. Clin. Invest. 89:1014–1020.

Chen, J., T. Kinoshita, J. Sukbuntherng, B.Y. Chang, and L. Elias. 2016. Ibrutinib Inhibits ERBB Receptor Tyrosine Kinases and HER2-Amplified Breast Cancer Cell Growth. Mol. Cancer Ther. 15:2835–2844. doi:10.1158/1535-7163.MCT-15-0923.

Chen, L.S., P. Bose, N.D. Cruz, Y. Jiang, Q. Wu, P.A. Thompson, S. Feng, M.H. Kroll, W. Qiao, X. Huang, N. Jain, W.G. Wierda, M.J. Keating, and V. Gandhi. 2018. A pilot study of lower doses of ibrutinib in patients with chronic lymphocytic leukemia. Blood. 132:2249–2259. doi:10.1182/blood-2018-06-860593.

Chung, K., C.A. Rivet, M.L. Kemp, and H. Lu. 2011. Imaging single-cell signaling dynamics with a deterministic high-density single-cell trap array. Anal. Chem. 83:7044–7052. doi:10.1021/ac2011153.

Clark, M.R., K.S. Campbell, A. Kazlauskas, S.A. Johnson, T.A. Potter, C. Pleiman, J.C. Cambier, R. Clark, S. Campbell, and A. Potter. 1992. The B Cell Antigen Receptor Complex: Association of lg-α and lg-β with Distinct Cytoplasmic Effectors. Science. 258:123–126.

Cornall, R.J., and C.C. Goodnow. 1998. B cell antigen receptor signalling in the balance of tolerance and immunity. Novartis Found. Symp. 215:21–40. doi:10.1002/9780470515525.ch3.

D'Avola, A., S. Drennan, I. Tracy, I. Henderson, L. Chiecchio, M. Larrayoz, M. Rose-Zerilli, J. Strefford, C. Plass, P.W. Johnson, A.J. Steele, G. Packham, F.K. Stevenson, C.C. Oakes, and F. Forconi. 2016. Surface IgM expression and function are associated with clinical behavior, genetic abnormalities, and DNA methylation in CLL. Blood. 128:816–827. doi:10.1182/blood-2016-03-707786.

Dai, X., Y. Chen, J. Schuman, Z. Hua, J.W. Adamson, R. Wen, and D. Wang. 2006. Distinct Roles of Phosphoinositide-3 Kinase and Phospholipase Cγ2 in B-Cell Receptor-Mediated Signal Transduction. Mol. Cell. Biol. 26:88–99. doi:10.1128/MCB.26.1.88-99.2006.

Damle, R.N., F. Ghiotto, A. Valetto, E. Albesiano, F. Fais, X. Yan, C.P. Sison, S.L. Allen, J. Kolitz, P. Schulman, V.P. Vinciguerra, P. Budde, J. Frey, K.R. Rai, M. Ferrarini, and N. Chiorazzi. 2002. B-cell chronic lymphocytic leukemia cells express a surface membrane phenotype of activated, antigen-experienced B lymphocytes. Blood. 99:4087–4094.

Damle, R.N., T. Wasil, F. Fais, F. Ghiotto, A. Valetto, S.L. Allen, A. Buchbinder, D. Budman, K. Dittmar, J. Kolitz, S.M. Lichtman, P. Schulman, V.P. Vinciguerra, K.R. Rai, M. Ferrarini, and N. Chiorazzi. 1999. Ig V gene mutation status and CD38 expression as novel prognostic indicators in chronic lymphocytic leukemia. Blood. 94:1840–1847.

Debant, M., P. Hemon, C. Brigaudeau, Y. Renaudineau, and O. Mignen. 2015. Calcium signaling and cell fate: how can Ca^{2+} signals contribute to wrong decisions for Chronic Lymphocytic Leukemic B lymphocyte outcome? Int. J. Dev. Biol. 59:379–389. doi:10.1387/ijdb.150204om.

Desalvo, A. 2019. Real-time activation profiles of a single T cell arrays following controlled interaction with antigen-presenting cells. University of Southampton, Doctoral Thesis, 243pp.

Desalvo, A., F. Bateman, E. James, H. Morgan, and T. Elliott. 2020. Time-resolved microwell cell-pairing array reveals multiple T cell activation profiles. Lab on a Chip. 20:3772–3783. doi:10.1039/d0lc00628a.

Dicker, F., H. Herholz, S. Schnittger, A. Nakao, N. Patten, L. Wu, W. Kern, T. Haferlach, and C. Haferlach. 2009. The detection of TP53 mutations in chronic lymphocytic leukemia independently predicts rapid disease progression and is highly correlated with a complex aberrant karyotype. Leukemia. 23:117–124. doi:10.1038/leu.2008.274.

Dikic, I. 2017. Proteasomal and autophagic degradation systems. Annu. Rev. Biochem. 86:193-224.

Dolmetsch, R.E., R.S. Lewis, C.C. Goodnow, and J.I. Healy. 1997. Differential activation of transcription factors induced by Ca response amplitude and duration. Nature. 386:855–858.

Dolmetsch, R.E., K. Xu, and R.S. Lewis. 1998. Calcium oscillations increase the efficiency and specificity of gene expression. Nature. 392:933–936.

Dubovsky, J.A., K.A. Beckwith, G. Natarajan, J.A. Woyach, S. Jaglowski, Y. Zhong, J.D. Hessler, T.M. Liu, B.Y. Chang, K.M. Larkin, M.R. Stefanovski, D.L. Chappell, F.W. Frissora, L.L. Smith, K.A. Smucker, J.M. Flynn, J.A. Jones, L.A. Andritsos, K. Maddocks, A.M. Lehman, R. Furman, J. Sharman, A. Mishra, M.A. Caligiuri, A.R. Satoskar, J.J. Buggy, N. Muthusamy, A.J. Johnson, and J.C. Byrd. 2013. Ibrutinib is an irreversible molecular inhibitor of ITK driving a Th1-selective pressure in T lymphocytes. Blood. 122:2539–2549. doi:10.1182/blood-2013-06-507947.

Dunleavy, K., T. Erdmann, and G. Lenz. 2018. Targeting the B-cell receptor pathway in diffuse large B-cell lymphoma. Cancer Treat. Rev. 65:41–46. doi:10.1016/j.ctrv.2018.01.002.

Duyao, M.P., A.J. Buckler, and G.E. Sonenshein. 1990. Interaction of an NF-κB-like factor with a site upstream of the c-myc promoter. Proc. Natl. Acad. Sci. U. S. A. 87:4727–4731. doi:10.1073/pnas.87.12.4727.

Epstein, A.L., R. Levy, H. Kim, W. Henle, G. Henle, and H.S. Kaplan. 1978. Biology of the human malignant lymphomas. IV. Functional characterisation of ten diffuse histiocytic lymphoma cell lines. Cancer. 42:2379–2391.

Fluckiger, A.-C., Z. Li, R.M. Kato, M.I. Wahl, H.D. Ochs, R. Longnecker, J.-P. Kinet, O.N. Witte, A.M. Scharenberg, and D.J. Rawlings. 1998. Btk/Tec kinases regulate sustained increases in intracellular Ca^{2+} following B-cell receptor activation. EMBO J. 17:1973–1985.

Friedberg, J.W., J. Sharman, J. Sweetenham, P.B. Johnston, J.M. Vose, A. Lacasce, J. Schaefer-cutillo, S. De Vos, R. Sinha, J.P. Leonard, L.D. Cripe, S.A. Gregory, M.P. Sterba, A.M. Lowe, R. Levy, and M.A. Shipp. 2010. Inhibition of Syk with fostamatinib disodium has significant clinical activity in non-Hodgkin lymphoma and chronic lymphocytic leukemia. Blood. 115:2578–2585. doi:10.1182/blood-2009-08-236471.An.

Fu, C., C.W. Turck, T. Kurosaki, and A.C. Chan. 1998. BLNK: A central linker protein in B cell activation. Immunity. 9:93–103. doi:10.1016/S1074-7613(00)80591-9.

Gaidano, G., and D. Rossi. 2017. The mutational landscape of chronic lymphocytic leukemia and its impact on prognosis and treatment. Hematology. 2017:329–337. doi:10.1182/asheducation-2017.1.329.

Gao, W., M. Wang, L. Wang, H. Lu, S. Wu, B. Dai, Z. Ou, L. Zhang, J. V. Heymach, K.A. Gold, J. Minna, J.A. Roth, W.L. Hofstetter, S.G. Swisher, and B. Fang. 2014. Selective antitumor activity of

ibrutinib in EGFR-mutant non-small cell lung cancer cells. J. Natl. Cancer Inst. 106:1–4. doi:10.1093/jnci/dju204.

Goldmann, L., R. Duan, T. Kragh, G. Wittmann, C. Weber, R. Lorenz, P. von Hundelshausen, M. Spannagl, and W. Siess. 2019. Oral Bruton tyrosine kinase inhibitors block activation of the platelet Fc receptor CD32a (FcγRIIA): A new option in HIT? Blood Adv. 3:4021–4033. doi:10.1182/bloodadvances.2019000617.

Golkowski, M., R.S.R. Vidadala, C.K. Lombard, H.W. Suh, D.J. Maly, and S.E. Ong. 2017. Kinobead and Single-Shot LC-MS Profiling Identifies Selective PKD Inhibitors. J. Proteome Res. 16:1216–1227. doi:10.1021/acs.jproteome.6b00817.

Gonzalez, D., P. Martinez, R. Wade, S. Hockley, D. Oscier, E. Matutes, C.E. Dearden, S.M. Richards, D. Catovsky, and G.J. Morgan. 2011. Mutational status of the TP53 gene as a predictor of response and survival in patients with chronic lymphocytic leukemia: Results from the LRF CLL4 trial. J. Clin. Oncol. 29:2223–2229. doi:10.1200/JCO.2010.32.0838.

de Gorter, D.J.J., E.A. Beuling, R. Kersseboom, S. Middendorp, J.M. van Gils, R.W. Hendriks, S.T. Pals, and M. Spaargaren. 2007. Bruton's Tyrosine Kinase and Phospholipase Cγ2 Mediate Chemokine-Controlled B Cell Migration and Homing. Immunity. 26:93–104. doi:10.1016/j.immuni.2006.11.012.

Guinamard, B.R., N. Signoret, M. Ishiai, M. Marsh, T. Kurosaki, and J. V Ravetch. 1999. Protein Kinase C (PKC)-induced Internalization of CXCR4. J Ex Med. 189:0–5.

ten Hacken, E., and J.A. Burger. 2016. Microenvironment interactions and B-cell receptor signaling in chronic lymphocytic leukemia: implications for disease pathogensis and treatment. Biochim Biophys Acta. 1863:401–413. doi:10.1016/j.bbamcr.2015.07.009.Microenvironment.

Hamblin, T.J., Z. Davis, A. Gardiner, D.G. Oscier, and F.K. Stevenson. 1999. Unmutated Ig VH genes are associated with a more aggressive form of chronic lymphocytic leukemia. Blood. 94:1848–1854.

Hashimoto, S., A. Iwamatsu, M. Ishiai, K. Okawa, T. Yamadori, M. Matsushita, Y. Baba, T. Kishimoto, T. Kurosaki, and S. Tsukada. 1999. Identification of the SH2 domain binding protein of Bruton's tyrosine kinase as BLNK - Functional significance of Btk-SH2 domain in B-cell antigen receptor-coupled calcium signaling. Blood. 94:2357–2364. doi:10.1182/blood.v94.7.2357.419k40_2357_2364.

Havranek, O., J. Xu, K. Stefan, Z. Wang, L. Becker, J.M. Comer, J. Henderson, W. Ma, J. Man, C. Ma, J.R. Westin, D. Ghosh, N. Shinners, L. Sun, A.F. Yi, A.R. Karri, J.A. Burger, T. Zal, and R.E. Davis. 2017. Tonic B-cell receptor signaling in diffuse large B-cell lymphoma. Blood. 130:995–1007. doi:10.1182/blood-2016-10-747303.The.

Healy, J.I., R.E. Dolmetsch, L.A. Timmerman, J.G. Cyster, M.L. Thomas, G.R. Crabtree, R.S. Lewis, and C.C. Goodnow. 1997. Different Nuclear Signals Are Activated by the B Cell Receptor during Positive Versus Negative Signaling. Immunity. 6:419–428.

Herishanu, Y., P. Pérez-Galán, D. Liu, A. Biancotto, S. Pittaluga, B. Vire, F. Gibellini, N. Njuguna, E. Lee, L. Stennett, N. Raghavachari, P. Liu, J.P. McCoy, M. Raffeld, M. Stetler-Stevenson, C. Yuan, R. Sherry, D.C. Arthur, I. Maric, T. White, G.E. Marti, P. Munson, W.H. Wilson, and A. Wiestner. 2011. The lymph node microenvironment promotes B-cell receptor signaling, NF-κB activation, and tumor proliferation in chronic lymphocytic leukemia. Blood. 117:563–574. doi:10.1182/blood-2010-05-284984.

Herman, S.E.M., R.Z. Mustafa, J. a Gyamfi, S. Pittaluga, S. Chang, B. Chang, M. Farooqui, and A. Wiestner. 2014. Ibrutinib inhibits BCR and NF-κB signaling and reduces tumor proliferation in tissue-resident cells of patients with CLL. Blood. 123:3286–3295. doi:10.1182/blood-2014-02-548610.

Herman, S.E.M, C.U. Niemann1, M. Farooqui, J. Jones, R.Z. Mustafa, A. Lipsky, N. Saba, S. Martyr, S. Soto, J. Valdez, J.A. Gyamfi, I. Maric, K.R. Calvo, L.B. Pedersen, C.H. Geisler, D. Liu, G.E. Marti, G. Aue, and A. Wiestner. 2014. Ibrutinib-induced lymphocytosis in patients with chronic lymphocytic leukemia: correlative analyses from a phase II study. Leukemia. 28(11):2188–2196. doi:10.1038/leu.2014.122.

Hikida, M., S. Johmura, A. Hashimoto, M. Takezaki, and T. Kurosaki. 2003. Coupling between B cell receptor and phospholipase C-γ2 is essential for mature B cell development. J. Exp. Med. 198:581–589. doi:10.1084/jem.20030280.

Hippen, K.L., A.M. Buhl, D. D'Ambrosio, K. Nakamura, C. Persin, and J.C. Cambier. 1997. FcγRIIB1 inhibition of BCR-mediated phosphoinositide hydrolysis and Ca^{2+} mobilization is integrated by CD19 dephosphorylation. Immunity. 7:49–58. doi:10.1016/S1074-7613(00)80509-9.

Hogan, P.G., and A. Rao. 2015. Store-operated calcium entry: Mechanisms and modulation. Biochem. Biophys. Res. Commun. 460:40–49. doi:10.1016/j.bbrc.2015.02.110.

Holmes D., and B.L.J. Webb. 2012 Electrical Impedance Cytometry. Encyclopedia of Nanotechnology. Springer, Dordrecht. https://doi.org/10.1007/978-90-481-9751-4_122).

Honigberg, L.A., A.M. Smith, M. Sirisawad, E. Verner, D. Loury, B. Chang, S. Li, Z. Pan, D.H. Thamm, R.A. Miller, and J.J. Buggy. 2010. The Bruton tyrosine kinase inhibitor PCI-32765 blocks B-cell activation and is efficacious in models of autoimmune disease and B-cell malignancy. Proc. Natl. Acad. Sci. 107:13075–13080. doi:10.1073/pnas.1004594107.

Hopper, M., T. Gururaja, T. Kinoshita, J.P. Dean, R.J. Hill, and A. Mongan. 2020. Relative Selectivity of Covalent Inhibitors Requires Assessment of Inactivation Kinetics and Cellular Occupancy : A Case Study of Ibrutinib and Acalabrutinib. J. Pharmacol. Exp. Ther. 372:331-338.

Hosokawa, M., A. Arakaki, M. Takahashi, T. Mori, H. Takeyama, and T. Matsunaga. 2009. High-density microcavity array for cell detection: Single-cell analysis of hematopoietic stem cells in peripheral blood mononuclear cells. Anal. Chem. 81:5308–5313. doi:10.1021/ac900535h.

Hou, J., U. Schindler, W.J. Henzel, T.C. Ho, M. Brasseur, and S.L. Mcknight. 1994. An Interleukin-4-Induced Transcription Factor : IL-4 Stat. Science. 265:1701-1706.

Huang, H.T., D. Dobrovolsky, J. Paulk, G. Yang, E.L. Weisberg, Z.M. Doctor, D.L. Buckley, J.H. Cho, E. Ko, J. Jang, K. Shi, H.G. Choi, J.D. Griffin, Y. Li, S.P. Treon, E.S. Fischer, J.E. Bradner, L. Tan, and N.S. Gray. 2018a. A Chemoproteomic Approach to Query the Degradable Kinome Using a Multi-kinase Degrader. Cell Chem. Biol. 25:88-99.e6. doi:10.1016/j.chembiol.2017.10.005.

Huang, N.-T., Y.-J. Hwong, and R.L. Lai. 2018b. A microfluidic microwell device for immunomagnetic single-cell trapping. Microfluid. Nanofluidics. 22:16. doi:10.1007/s10404-018-2040-x.

Huang, X., W. Yue, D. Liu, J. Yue, J. Li, D. Sun, M. Yang, and Z. Wang. 2016. Monitoring the intracellular calcium response to a dynamic hypertonic environment. Sci. Rep. 6:23591. doi:10.1038/srep23591.

Humphries, L.A., C. Dangelmaier, K. Sommer, K. Kipp, R.M. Kato, N. Griffith, I. Bakman, C.W. Turk, J.L. Daniel, and D.J. Rawlings. 2004. Tec kinases mediate sustained calcium influx via site-specific tyrosine phosphorylation of the phospholipase Cγ Src homology 2-Src homology 3 linker. J. Biol. Chem. 279:37651–37661. doi:10.1074/jbc.M311985200.

Iwanaga, R., E. Ozono, J. Fujisawa, M.A. Ikeda, N. Okamura, Y. Huang, and K. Ohtani. 2008. Activation of the cyclin D2 and cdk6 genes through NF-κB is critical for cell-cycle progression induced by HTLV-I Tax. Oncogene. 27:5635–5642. doi:10.1038/onc.2008.174.

Jaime-Figueroa, S., A.D. Buhimschi, M. Toure, J. Hines, and C.M. Crews. 2020. Design, synthesis and biological evaluation of Proteolysis Targeting Chimeras (PROTACs) as a BTK degraders with improved pharmacokinetic properties. Bioorganic Med. Chem. Lett. 30:126877. doi:10.1016/j.bmcl.2019.126877.

Jain, N., and S. O'Brien. 2016. BCR inhibitor failure in CLL: An unmet need. Blood. 128:2193–2194. doi:10.1182/blood-2016-09-739664.

Jefferies, C.A., S. Doyle, C. Brunner, A. Dunne, E. Brin, C. Wietek, E. Walch, T. Wirth, and L.A.J. O'Neill. 2003. Bruton's tyrosine kinase is a Toll/interleukin-1 receptor domain-binding protein that participates in nuclear factor κB activation by toll-like receptor 4. J. Biol. Chem. 278:26258–26264. doi:10.1074/jbc.M301484200.

Joseph, R.E., T.E. Wales, D.B. Fulton, J.R. Engen, and A.H. Andreotti. 2017. Achieving a Graded Immune Response: BTK Adopts a Range of Active/Inactive Conformations Dictated by Multiple Interdomain Contacts. Cell Press Structure. 25:1481-1494.e4. doi:10.1016/j.str.2017.07.014.

Junek, S., M. Engelke, D. Schild, and J. Wienands. 2012. Spatiotemporal resolution of Ca2+ signaling events by real time imaging of single B cells. FEBS Lett. 586:1452–1458. doi:10.1016/j.febslet.2012.03.057.

Kamel, S., L. Horton, L. Ysebaert, M. Levade, K. Burbury, S. Tan, M. Cole-Sinclair, J. Reynolds, R. Filshie, S. Schischka, A. Khot, S. Sandhu, M.J. Keating, H. Nandurkar, and C.S. Tam. 2015. Ibrutinib inhibits collagen-mediated but not ADP-mediated platelet aggregation. Leukemia. 29:783–787. doi:10.1038/leu.2014.247.

Kang, C.C., J.M.G. Lin, Z. Xu, S. Kumar, and A.E. Herr. 2014. Single-cell western blotting after whole-cell imaging to assess cancer chemotherapeutic response. Anal. Chem. 86:10429–10436. doi:10.1021/ac502932t.

Kay, N.E., L. Han, N. Bone, and G. Williams. 2001. Interleukin 4 content in chronic lymphocytic leukaemia (CLL) B cells and blood CD8 + T cells from B-CLL patients: Impact on clonal B-cell apoptosis. Br. J. Haematol. 112:760–767. doi:10.1046/j.1365-2141.2001.02605.x.

Ke, R., M. Mignardi, A. Pacureanu, J. Svedlund, J. Botling, C. Wählby, and M. Nilsson. 2013. In situ sequencing for RNA analysis in preserved tissue and cells. Nat. Methods. 10:857–860. doi:10.1038/nmeth.2563.

Kim, H.S., T.P. Devarenne, and A. Han. 2015. A high-throughput microfluidic single-cell screening platform capable of selective cell extraction. Lab Chip. 15:2467–2475. doi:10.1039/C4LC01316F.

Kim, Y.J., F. Sekiya, B. Poulin, Y.S. Bae, and S.G. Rhee. 2004. Mechanism of B-Cell Receptor-Induced Phosphorylation and Activation of Phospholipase C-γ2. Mol. Cell. Biol. 24:9986–9999. doi:10.1128/MCB.24.22.9986.

Kindt, T.J., R.A. Goldsby and B.A. Osborne. Kuby Immunology, 6th Edition. W.H. Freeman and Company, New York.

Kinoshita, K., T. Ozawa, K. Tajiri, S. Kadowaki, H. Kishi, and A. Muraguchi. 2009. Identification of antigen-specific B cells by concurrent monitoring of intracellular Ca^{2+} mobilization and antigen binding with microwell array chip system equipped with a CCD imager. Cytom. Part A. 75:682–687. doi:10.1002/cyto.a.20758.

Kipps, T.J., F.K. Stevenson, C.J. Wu, C.M. Croce, G. Packham, W.G. Wierda, S. O'Brien, J. Gribben, and K. Rai. 2017. Chronic lymphocytic leukaemia. Nat. Rev. Dis. Prim. 3:1–21. doi:10.1038/nrdp.2016.96.

Konstantinidou, M., J. Li, B. Zhang, Z. Wang, S. Shaabani, F. Ter Brake, K. Essa, and A. Dömling. 2019. PROTACs– a game-changing technology. Expert Opin. Drug Discov. 14:1255–1268. doi:10.1080/17460441.2019.1659242.

Koss, H., T.D. Bunney, S. Behjati, and M. Katan. 2014. Dysfunction of phospholipase Cγ in immune disorders and cancer. Trends Biochem. Sci. 39:603–611. doi:10.1016/j.tibs.2014.09.004.

Koues, O.I., E.M. Oltz, and J.E. Payton. 2015. Short-Circuiting Gene Regulatory Networks: Origins of B Cell Lymphoma. Trends Genet. 31:720–731. doi:10.1016/j.tig.2015.09.006.

Krysov, S., S. Dias, A. Paterson, C.I. Mockridge, K.N. Potter, K.-A. Smith, M. Ashton-Key, F.K. Stevenson, and G. Packham. 2012. Surface IgM stimulation induces MEK1/2-dependent MYC expression in chronic lymphocytic leukemia cells. Blood. 119:170–179. doi:10.1182/blood-2011-07-370403.

Kurosaki, T., and M. Kurosaki. 1997. Transphosphorylation of Bruton's tyrosine kinase on tyrosine 551 is critical for B cell antigen receptor function. J.Biol.Chem. 272:15595–15598.

Kurosaki, T., A. Maeda, M. Ishiai, A. Hashimoto, K. Inabe, and M. Takata. 2000. Regulation of the phospholipase C-γ2 pathway in B cells. Immunol Rev. 176:19–29. doi:10.1034/j.1600-065X.2000.00605.x.

Kurosaki, T., and S. Tsukada. 2000. BLNK: connecting Syk and Btk to calcium signals. Immunity. 12:1–5. doi:10.1016/S1074-7613(00)80153-3.

Kuse, R., S. Schuster, S., H. Schubbe, S. Dix, and K. Hausmann. 1985. Blood lymphocyte volumes and diameters in patients with chronic lymphocytic leukaemia and normal controls. Blut. 50:243-248.

Lam, K.-P., R. Kühn, and K. Rajewsky. 1997. In vivo ablation of surface immunoglobulin on mature B cells by inducible gene targeting results in rapid cell death. Cell. 90:1073–1083. doi:10.1016/S0092-8674(00)80373-6.

Landau, D.A., E. Tausch, A.N. Taylor-Weiner, C. Stewart, J.G. Reiter, J. Bahlo, S. Kluth, I. Bozic, M. Lawrence, S. Böttcher, S.L. Carter, K. Cibulskis, D. Mertens, C.L. Sougnez, M. Rosenberg, J.M. Hess, J. Edelmann, S. Kless, M. Kneba, M. Ritgen, A. Fink, K. Fischer, S. Gabriel, E.S. Lander, M.A. Nowak, H. Döhner, M. Hallek, D. Neuberg, G. Getz, S. Stilgenbauer, and C.J. Wu. 2015. Mutations driving CLL and their evolution in progression and relapse. Nature. 526:525–530. doi:10.1038/nature15395.

Law, C.L., K.A. Chandran, S.P. Sidorenko, and E.A. Clark. 1996. Phospholipase C-γ1 interacts with

conserved phosphotyrosyl residues in the linker region of Syk and is a substrate for Syk. Mol. Cell. Biol. 16:1305–1315. doi:10.1128/mcb.16.4.1305.

Lebien, T.W., and T.F. Tedder. 2008. B lymphocytes : how they develop and function. Blodd, 112:1570–1580. doi:10.1182/blood-2008-02-078071.

Lee, W.C., S. Rigante, A.P. Pisano, and F.A. Kuypers. 2010. Large-scale arrays of picolitre chambers for single-cell analysis of large cell populations. Lab Chip. 10:2952–2958. doi:10.1039/c0lc00139b.

Lenz, G., G.W. Wright, N.C.T. Emre, H. Kohlhammer, S.S. Dave, R.E. Davis, S. Carty, L.T. Lam, A.L. Shaffer, W. Xiao, J. Powell, A. Rosenwald, G. Ott, H.K. Muller-Hermelink, R.D. Gascoyne, J.M. Connors, E. Campo, E.S. Jaffe, J. Delabie, E.B. Smeland, L.M. Rimsza, R.I. Fisher, D.D. Weisenburger, W.C. Chan, and L.M. Staudt. 2008. Molecular subtypes of diffuse large B-cell lymphoma arise by distinct genetic pathways. Proc. Natl. Acad. Sci. 105:13520–13525. doi:10.1073/pnas.0804295105.

Levade, M., E. David, C. Garcia, P.A. Laurent, S. Cadot, A.S. Michallet, J.C. Bordet, C. Tam, P. Sié, L. Ysebaert, and B. Payrastre. 2014. Ibrutinib treatment affects collagen and von Willebrand factor-dependent platelet functions. Blood. 124:3991–3995. doi:10.1182/blood-2014-06-583294.

Li, S., K.H. Young, and L.J. Medeiros. 2018. Diffuse large B-cell lymphoma. Pathology. 50:74–87. doi:10.1016/j.pathol.2017.09.006.

Linley, A.J., R. Griffin, S. Cicconi, A. D'Avola, D.J. MacEwan, A.R. Pettit, N. Kalakonda, G. Packham, I.A. Prior, and J.R. Slupsky. 2020. Kinobead profiling reveals reprogramming of B-cell receptor signaling in response to therapy within primary CLL cells. BioRXiv. doi: https://doi.org/10.1101/841312

Liu, T.-M., J. A. Woyach, Y. Zhong, A. Lozanski, G. Lozanski, S. Dong, E. Strattan, A. Lehman, X. Zhang, J. A. Jones, J. Flynn, L. A. Andritsos, K. Maddocks, S.M. Jaglowski, K. A. Blum, J.C. Byrd, J. A. Dubovsky, and A. J. Johnson. 2015. Hypermorphic mutation of phospholipase C, γ2 acquired in ibrutinib resistant CLL confers BTK independency upon BCR activation. Blood. 126:61–68. doi:10.1182/blood-2015-02-626846.

Liu, X., Z. Zhan, D. Li, L. Xu, F. Ma, P. Zhang, H. Yao, and X. Cao. 2011. Intracellular MHC class II molecules promote TLR-triggered innate immune responses by maintaining activation of the kinase Btk. Nat. Immunol. 12:416–424. doi:10.1038/ni.2015.

Long, M., K. Beckwith, P. Do, B.L. Mundy, A. Gordon, A.M. Lehman, K.J. Maddocks, C. Cheney, J.A. Jones, J.M. Flynn, L.A. Andritsos, F. Awan, J.A. Fraietta, C.H. June, M. V. Maus, J.A. Woyach, M.A. Caligiuri, A.J. Johnson, N. Muthusamy, and J.C. Byrd. 2017. Ibrutinib treatment improves T cell number and function in CLL patients. J. Clin. Invest. 127:3052–3064. doi:10.1172/JCI89756.

Maddocks, K.J., A.S. Ruppert, G. Lozanski, N.A. Heerema, W. Zhao, L. Abruzzo, A. Lozanski, M. Davis, A. Gordon, L.L. Smith, R. Mantel, J.A. Jones, J.M. Flynn, S.M. Jaglowski, L.A. Andritsos, F. Awan, K.A. Blum, M.R. Grever, A.J. Johnson, J.C. Byrd, and J.A. Woyach. 2015. Etiology of ibrutinib therapy discontinuation and outcomes in patients with chronic lymphocytic leukemia. JAMA Oncol. 1:80–87. doi:10.1001/jamaoncol.2014.218.

Marshall, A.J., H. Niiro, T.J. Yun, and E.A. Clark. 2000. Regulation of B-cell activation and differentiation by the phosphatidylinositol 3-kinase and phospholipase Cγ pathways. Immunol. Rev. 176:30–46. doi:10.1034/j.1600-065X.2000.00611.x.

Mato, A.R., C. Nabhan, P.M. Barr, C.S. Ujjani, B.T. Hill, N. Lamanna, A.P. Skarbnik, C. Howlett, J.J.

Pu, A.R. Sehgal, L.E. Strelec, A. Vandegrift, D.M. Fitzpatrick, C.S. Zent, T. Feldman, A. Goy, D.F. Claxton, S. Henick Bachow, G. Kaur, J. Svoboda, S. Dwivedy Nasta, D. Porter, D.J. Landsburg, S.J. Schuster, B.D. Cheson, P. Kiselev, and A.M. Evens. 2016. Outcomes of CLL patients treated with 1 sequential kinase inhibitor therapy: A real world experience. Blood. 128:2199–2206. doi:10.1182/blood-2016-05-716977.

McBlane, J.F., D.C. van Gent, D.A. Ramsden, C. Romeo, C.A. Cuomo, M. Gellert, and M.A. Oettinger. 1995. Cleavage at a V(D)J recombination signal requires only RAG1 and RAG2 proteins and occurs in two steps. Cell. 83:387-395. doi:10.1016/0092-8674(95)90116-7.

McMullen, J.R., and E.J.H. Boey. 2014. Ibrutinib increases the risk of atrial fibrillation, potentially through inhibition of cardiac PI3K-Akt signaling. Blood. 124:3829–3831.

Médard, G., F. Pachl, B. Ruprecht, S. Klaeger, S. Heinzlmeir, D. Helm, H. Qiao, X. Ku, M. Wilhelm, T. Kuehne, Z. Wu, A. Dittmann, C. Hopf, K. Kramer, and B. Kuster. 2015. Optimized chemical proteomics assay for kinase inhibitor profiling. J. Proteome Res. 14:1574–1586. doi:10.1021/pr5012608.

Merron, B., and A. Davies. 2018. Double hit lymphoma : How do we define it and how do we treat it? Best Practice and Research Clinical Haematology. 31:233–240. doi:10.1016/j.beha.2018.07.012.

Mette Buhl, A., and J.C. Cambier. 1999. Phosphorylation of CD19 Y484 and Y515, and Linked Activation of Phosphatidylinositol 3-Kinase, Are Required for B Cell Antigen Receptor-Mediated Activation of Bruton's Tyrosine Kinase. J. Immunol. 162:4438–4446. doi:10.4049/jimmunol.1500386.

Middendorp, S., G.M. Dingjan, A. Maas, K. Dahlenborg, and R.W. Hendriks. 2003. Function of Bruton's Tyrosine Kinase during B Cell Development Is Partially Independent of Its Catalytic Activity. J. Immunol. 171:5988–5996. doi:10.4049/jimmunol.171.11.5988.

Mockridge, C.I., K.N. Potter, I. Wheatley, L.A. Neville, G. Packham, and F.K. Stevenson. 2007. Reversible anergy of sIgM-mediated signaling in the two subsets of CLL defined by VH-gene mutational status. Blood. 109:4424–4431. doi:10.1182/blood-2006-11-056648.

Nilsson, M., H. Malmgren, M. Samiotaki, M. Kwiatkowski, B. Chowdhary, and U. Landegren. 1994. Padlock probes: circularizing oligonucleotides for localized DNA detection. Science. 265:2085–2088. doi:10.1126/science.7522346.

Nishibe, S., M.I. Wahl, S.M.T. Hernández-Sotomayor, N.K. Tonks, S.G. Rhee, and G. Carpenter. 1990. Increase of the catalytic activity of phospholipase C-γ1 by tyrosine phosphorylation. Science. 250:1253–1256. doi:10.1126/science.1700866.

Nozawa, Y., M. Abe, H. Wakasa, H. Ohno, S. Fukuhara, T. Kinoshita, and T. Osato. 1988. Establishment and Characterization of an Epstein-Barr Virus Negative B-Cell Lymphoma Cell Line and Successful Heterotransplantation. J. Exp. Med. 156:319–330.

Oettinger, M.A., D.G. Schatz, C. Gorka, and D. Baltimore. 1990. RAG-1 and RAG-2, Adjacent Genes That Synergistically Activate V(D)J Recombination. Science. 248:1517–1523.

Oprea, M. and A.S. Perelson. 1997. Somatic mutation leads to efficient affinity maturation when centrocytes recycle back to centroblasts. J. Immunol. 158(11): 5155-5162.

Ozawa, T., K. Kinoshita, S. Kadowaki, K. Tajiri, S. Kondo, R. Honda, M. Ikemoto, L. Piao, A.

Morisato, K. Fukurotani, H. Kishi, and A. Muraguchi. 2009. MAC-CCD system: a novel lymphocyte microwell-array chip system equipped with CCD scanner to generate human monoclonal antibodies against influenza virus. Lab Chip. 9:158–163. doi:10.1039/b810438g.

Ozdener, F., C. Dangelmaier, B. Ashyby, S.P. Kunapuli, and J.L. Daniel. 2002. Activation of phospholipase Cγ2 by tyrosine phosphorylation. Mol. Pharmacol. 62:672-679.

Packham, G., S. Krysov, A. Allen, N. Savelyeva, A.J. Steele, F. Forconi, and F.K. Stevenson. 2014. The outcome of B-cell receptor signaling in chronic lymphocytic leukemia: proliferation or anergy. Haematologica. 99:1138–1148. doi:10.3324/haematol.2013.098384.

Pahl, H.L. 1999. Activators and target genes of Rel/NF-κB transcription factors. Oncogene. 18:6853–6866. doi:10.1038/sj.onc.1203239.

Paiva, S.L., and C.M. Crews. 2019. Targeted protein degradation: elements of PROTAC design. Curr. Opin. Chem. Biol. 50:111–119. doi:10.1016/j.cbpa.2019.02.022.

Pangault, C., P. Amé-Thomas, P. Ruminy, D. Rossille, G. Caron, M. Baia, J. De Vos, M. Roussel, C. Monvoisin, T. Lamy, H. Tilly, P. Gaulard, K. Tarte, and T. Fest. 2010. Follicular lymphoma cell niche: Identification of a preeminent IL-4-dependent TFH-B cell axis. Leukemia. 24:2080–2089. doi:10.1038/leu.2010.223.

Patel, V., K. Balakrishnan, E. Bibikova, M. Ayres, M.J. Keating, W.G. Wierda, and V. Gandhi. 2017. Comparison of acalabrutinib, a selective Bruton tyrosine kinase inhibitor, with ibrutinib in chronic lymphocytic leukemia cells. Clin. Cancer Res. 23:3734–3743. doi:10.1158/1078-0432.CCR-16-1446.

Pekarsky, Y., V. Balatti, and C.M. Croce. 2018. BCL2 and miR-15/16: From gene discovery to treatment. Cell Death Differ. 25:21–26. doi:10.1038/cdd.2017.159.

Petlickovski, A., L. Laurenti, X. Li, S. Marietti, P. Chiusolo, S. Sica, G. Leone, and D.G. Efremov. 2005. Sustained signaling through the B-cell receptor induces Mcl-1 and promotes survival of chronic lymphocytic leukemia B cells. Blood. 105:4820–4827. doi:10.1182/blood-2004-07-2669.

Phelan, J.D., R.M. Young, D.E. Webster, S. Roulland, G.W. Wright, M. Kasbekar, A.L. Shaffer, M. Ceribelli, J.Q. Wang, R. Schmitz, M. Nakagawa, E. Bachy, D.W. Huang, Y. Ji, L. Chen, Y. Yang, H. Zhao, X. Yu, W. Xu, M.M. Palisoc, R.R. Valadez, T. Davies-Hill, W.H. Wilson, W.C. Chan, E.S. Jaffe, R.D. Gascoyne, E. Campo, A. Rosenwald, G. Ott, J. Delabie, L.M. Rimsza, F.J. Rodriguez, F. Estephan, M. Holdhoff, M.J. Kruhlak, S.M. Hewitt, C.J. Thomas, S. Pittaluga, T. Oellerich, and L.M. Staudt. 2018. A multiprotein supercomplex controlling oncogenic signalling in lymphoma. Nature. 560:387–391. doi:10.1038/s41586-018-0290-0.

Piechulek, T., T. Rehlen, C. Walliser, P. Vatter, B. Moepps, and P. Gierschik. 2005. Isozyme-specific stimulation of phospholipase C-γ2 by Rac GTPases. J. Biol. Chem. 280:38923–38931. doi:10.1074/jbc.M509396200.

Ponader, S., S.S. Chen, J.J. Buggy, K. Balakrishnan, V. Gandhi, W.G. Wierda, M.J. Keating, S. O'Brien, N. Chiorazzi, and J.A. Burger. 2012. The Bruton tyrosine kinase inhibitor PCI-32765 thwarts chronic lymphocytic leukemia cell survival and tissue homing in vitro and in vivo. Blood. 119:1182–1189. doi:10.1182/blood-2011-10-386417.

te Raa, G.D., and A.P. Kater. 2016. TP53 dysfunction in CLL: Implications for prognosis and treatment. Best Pract. Res. Clin. Haematol. 29:90–99. doi:10.1016/j.beha.2016.08.002.

Rai, K.R., A. Sawitsky, E.P. Cronkite, A.D. Chanana, R.N. Levy, and B.S. Pasternack. 1975. Clinical

staging of chronic lymphocytic leukaemia. Blood. 46:219-234.

Rawlings, D.J. 1999. Bruton's tyrosine kinase controls a sustained calcium signal essential for B lineage development and function. Clin. Immunol. 91:243–253. doi:10.1006/clim.1999.4732.

Rawlings, D.J., D.C. Saffran, S. Tsukada, D.A. Largaespada, J.C. Grimaldi, L. Cohen, R.N. Mohr, J.F. Bazan, M. Howard, N.G. Copeland, N.A. Jenkins, and O.N. Witte. 1993. Mutation of unique region of Bruton's tyrosine kinase in immunodeficient XID mice. Science. 261:358–361. doi:10.1126/science.8332901.

Redondo-Muñoz, J., A. García-Pardo, and J. Teixidó. 2019. Molecular players in hematologic tumor cell trafficking. Front. Immunol. 10:1–18. doi:10.3389/fimmu.2019.00156.

Reiff, S.D., R. Mantel, L.L. Smith, J. Greene, E. Muhowski, C.A. Fabian, V.M. Goettl, M. Tran, B.K. Harrington, K.A. Rogers, F.T. Awan, K. Maddocks, L.A. Andritsos, A.M. Lehman, D. Sampath, R. Lapalombella, S. Eathiraj, G. Abbadessa, B. Schwartz, A.J. Johnson, J.C. Byrd, and J.A. Woyach. 2018. The BTK inhibitor ARQ 531 targets ibrutinib resistant CLL and Richter's transformation. Cancer Discov. 8:1300-1315. doi:10.1158/2159-8290.CD-17-1409.The.

Ren, L., A. Campbell, H. Fang, S. Gautam, S. Elavazhagan, K. Fatehchand, P. Mehta, A. Stiff, B.F. Reader, X. Mo, J.C. Byrd, W.E. Carson, J.P. Butchar, and S. Tridandapani. 2016. Analysis of the Effects of the Bruton's tyrosine kinase (Btk) Inhibitor Ibrutinib on Monocyte Fcγ Receptor (FcγR) Function. J. Biol. Chem. 291:3043–3052. doi:10.1074/jbc.M115.687251.

Rettig, J.R., and A. Folch. 2005. Large-scale single-cell trapping and imaging using microwell arrays. Anal. Chem. 77:5628–5634. doi:10.1021/ac0505977.

Rickert, R.C. 2013. New insights into pre-BCR and BCR signalling with relevance to B cell malignancies. Nat. Rev. Immunol. 13:578–591. doi:10.1038/nri3487.

Rodriguez, R., M. Matsuda, O. Perisic, J. Bravo, A. Paul, N.P. Jones, Y. Light, K. Swann, R.L. Williams, and M. Katan. 2001. Tyrosine Residues in Phospholipase Cγ2 Essential for the Enzyme Function in B-cell Signaling. J. Biol. Chem. 276:47982–47992. doi:10.1074/jbc.M107577200.

Roman-Garcia, S., S. V Merino-Cortes, S.R. Gardeta, M.J.W. De Bruijn, R.W. Hendriks, and Y.R. Carrasco. 2018. Distinct Roles for Bruton's Tyrosine Kinase in B Cell Immune Synapse Formation. Front. Immunol. 9:1–16. doi:10.3389/fimmu.2018.02027.

De Rooij, M.F.M., A. Kuil, C.R. Geest, E. Eldering, B.Y. Chang, J.J. Buggy, S.T. Pals, and M. Spaargaren. 2012. The clinically active BTK inhibitor PCI-32765 targets B-cell receptor- and chemokine-controlled adhesion and migration in chronic lymphocytic leukemia. Blood. 119:2590–2594. doi:10.1182/blood-2011-11-390989.

Roskoski (Jr.), R. 2016. Classification of small molecule protein kinase inhibitors based upon the structures of their drug-enzyme complexes. Pharmacol. Res. 103:26–48. doi:10.1016/j.phrs.2015.10.021.

Rossi, D., M. Cerri, C. Deambrogi, E. Sozzi, S. Cresta, S. Rasi, L. De Paoli, V. Spina, V. Gattei, D. Capello, F. Forconi, F. Lauria, and G. Gaidano. 2009. The prognostic value of TP53 mutations in chronic lymphocytic leukemia is independent of Del17p13: Implications for overall survival and chemorefractoriness. Clin. Cancer Res. 15:995–1004. doi:10.1158/1078-0432.CCR-08-1630.

Rossmann, E.D., N. Lewin, M. Jeddi-Tehrani, A. Österborg, and H. Mellstedt. 2002. Intracellular T cell cytokines in patients with B cell chronic lymphocytic leukaemia (B-CLL). Eur. J. Haematol.

68:299–306. doi:10.1034/j.1600-0609.2002.01612.x.

Roth, D.B. 2014. V(D)J Recombination: Mechanism, Errors and Fidelity. Microbiol. Spectr. 2. doi:10.1128/microbiolspec.MDNA3-0041-2014.f1.

Rothbauer, M., H. Zirath, and P. Ertl. 2017. Recent advances in microfluidic technologies for cell-to-cell interaction studies. Lab Chip. 18:249–270. doi:10.1039/C7LC00815E.

Le Roy, C., P.A. Deglesne, N. Chevallier, T. Beitar, V. Eclache, M. Quettier, M. Boubaya, R. Letestu, V. Lévy, F. Ajchenbaum-Cymbalista, and N. Varin-Blank. 2012. The degree of BCR and NFAT activation predicts clinical outcomes in chronic lymphocytic leukemia. Blood. 120:356–365. doi:10.1182/blood-2011-12-397158.

Rush, J.S., and P.D. Hodgkin. 2001. B cells activated via CD40 and IL-4 undergo a division burst but require continued stimulation to maintain division, survival and differentiation. Eur. J. Immunol. 31:1150–1159. doi:10.1002/1521-4141(200104)31:4<1150::AID-IMMU1150>3.0.CO;2-V.

Saito, K., K.F. Tolias, A. Saci, H.B. Koon, L.A. Humphries, A. Scharenberg, D.J. Rawlings, J.P. Kinet, and C.L. Carpenter. 2003. BTK regulates PtdIns-4,5-P2 synthesis: Importance for calcium signaling and PI3K activity. Immunity. 19:669–677. doi:10.1016/S1074-7613(03)00297-8.

Salim, K., M.J. Bottomley, E. Querfurth, M.J. Zvelebil, I. Gout, R. Scaife, R.L. Margolis, R. Gigg, C.I.E. Smith, P.C. Driscoll, M.D. Waterfield, and G. Panayotou. 1996. Distinct specificity in the recognition of phosphoinositides by the pleckstrin homology domains of dynamin and Bruton's tyrosine kinase. EMBO J. 15:6241–6250. doi:10.1002/j.1460-2075.1996.tb01014.x.

Sambrook, J., E.F. Fritsch, and T. Maniatis. 1989. Molecular cloning: a laboratory manual. Vol2. Cold Spring Harbor Laboratory Press, New York.

Scharenberg, A.M., O. El-Hillal, D.A. Fruman, L.O. Beitz, Z. Li, S. Lin, I. Gout, L.C. Cantley, D.J. Rawlings, and J.-P. Kinet. 1998. Phosphatidylinositol-3,4,5-trisphosphate (PtdIns-3,4,5-P3)/Tec kinase-dependent calcium signaling pathway: a target for SHIP-mediated inhibitory signals. EMBO J. 17:1961–1972. doi:10.1073/PNAS.91.19.9175.

Scharenberg, A.M., L.A. Humphries, and D.J. Rawlings. 2007. Calcium signalling and cell-fate choice in B cells. Nat. Rev. Immunol. 7:778–789. doi:10.1038/nri2172.Calcium.

Scharenberg, A.M., and J.-P. Kinet. 1998. PtdIns-3,4,5-P3: A regulatory nexus between tyrosine kinases and sustained calcium signals. Cell. 94:5–8. doi:10.1016/s0092-8674(00)81214-3.

Schieber, M., and S. Ma. 2019. The expanding role of venetoclax in chronic lymphocytic leukemia and small lymphocytic lymphoma. Blood Lymphat. Cancer Targets Ther. Volume 9:9–17. doi:10.2147/blctt.s177009.

Schiffenbauer, Y.S., Y. Kalma, E. Trubniykov, O. Gal-Garber, L. Weisz, A. Halamish, M. Sister, and G. Berke. 2009. A cell chip for sequential imaging of individual non-adherent live cells reveals transients and oscillations. Lab Chip. 9:2965–72. doi:10.1039/b904778f.

Sekiya, F., Y.S. Bae, and S.G. Rhee. 1999. Regulation of phospholipase C isozymes : activation of phospholipase C- γ in the absence of tyrosine-phosphorylation. Chem. Phys. Lipids. 98:3–11.

Senis, Y.A., A. Mazharian, and J. Mori. 2014. Src family kinases: At the forefront of platelet activation. Blood. 124:2013–2024. doi:10.1182/blood-2014-01-453134.

Sharman, J., M. Hawkins, K. Kolibaba, M. Boxer, L. Klein, M. Wu, J. Hu, S. Abella, and C. Yasenchak. 2015. An open-label phase 2 trial of entospletinib (GS-9973), a selective spleen tyrosine kinase inhibitor , in chronic lymphocytic leukemia. Blood. 125:2336–2343. doi:10.1182/blood-2014-08-595934.The.

Smyth, J.T., S.Y. Hwang, T. Tomita, W.I. DeHaven, J.C. Mercer, and J.W. Putney. 2010. Activation and regulation of store-operated calcium entry. J. Cell. Mol. Med. 14:2337–2349. doi:10.1111/j.1582-4934.2010.01168.x.

Spaargaren, M., E.A. Beuling, M.L. Rurup, H.P. Meijer, M.D. Klok, S. Middendorp, R.W. Hendriks, and S.T. Pals. 2003. The B Cell Antigen Receptor Controls Integrin Activity through Btk and PLCγ2. J. Exp. Med. 198:1539–1550. doi:10.1084/jem.20011866.

Stevenson, F.K., and F. Caligaris-Cappio. 2004. Chronic lymphocytic leukemia: revelations from the B-cell receptor. Blood. 103:4389–4396. doi:10.1182/blood-2003-12-4312.Supported.

Stevenson, F.K.F., S. Krysov, A.J. Davies, A.J. Steele, and G. Packham. 2011. B-cell receptor signaling in chronic lymphocytic leukemia. Blood. 118:4313–4320. doi:10.1182/blood-2011-06-338855.

Stokoe, D., L.R. Stephens, T. Copeland, P.R.J. Gaffney, C.B. Reese, G.F. Painter, A.B. Holmes, F. McCormick, and P.T. Hawkins. 1997. Dual role of phosphatidylinositol-3,4,5-trisphosphate in the activation of protein kinase B. Science. 277:567–570. doi:10.1126/science.277.5325.567.

Su, Y.W., Y. Zhang, J. Schwelkert, G.A. Koretzky, M. Reth, and J. Wienands. 1999. Interaction of SLP adaptors with the SH2 domain of Tec family kinases. Eur. J. Immunol. 29:3702–3711. doi:10.1002/(SICI)1521-4141(199911)29:11<3702::AID-IMMU3702>3.0.CO;2-R.

Sun, T., D. Holmes, S. Gawad, N.G. Green, and H. Morgan. 2007. High speed multi-frequency impedance analysis of single particles in a microfluidic cytometer using maximum length sequences. Lab Chip. 7:1034–40. doi:10.1039/b703546b.

Sun, Y., N. Ding, Y. Song, Z. Yang, W. Liu, J. Zhu, and Y. Rao. 2019. Degradation of Bruton's tyrosine kinase mutants by PROTACs for potential treatment of ibrutinib-resistant non-Hodgkin lymphomas. Leukemia. 33:2105–2110.

Takata, M., and T. Kurosaki. 1996. A Role for Bruton's Tyrosine Kinase in B Cell Antigen Receptor-mediated Activation of Phospholipase C-γ2. J. Exp. Med. 184:31–40.

Takata, M., H. Sabe, A. Hata, T. Inazu, Y. Homma, T. Nukada, H. Yamamura, and T. Kurosaki. 1994. Tyrosine kinases Lyn and Syk regulate B cell receptor-coupled Ca^{2+} mobilization through distinct pathways. EMBO J. 13:1341–1349.

Thomas, J.D., P. Sideras, C.I.E. Smith, I. Vořechovský, V. Chapman, and W.E. Paul. 1993. Colocalization of X-linked agammaglobulinemia and X-linked immunodeficiency genes. Science. 261:355–358. doi:10.1126/science.8332900.

Tinworth, C.P., H. Lithgow, L. Dittus, Z.I. Bassi, S.E. Hughes, M.Muelbaier, H. Dai, I.E.D. Smith, W.J. Kerr, G.A. Burley, M. Bantscheff, and J.D. Harling. 2019. PROTAC-mediated degradation of Bruton's tyrosine kinase is inhibited by covalent binding. ACS Chem. Biol. 14:342-347.

Tohda, S., T. Sato, H. Kogoshi, L. Fu, S. Sakano, and N. Nara. 2006. Establishment of a novel B-cell lymphoma cell line with suppressed growth by gamma-secretase inhibitors. Leuk. Res. 30:1385–1390. doi:10.1016/j.leukres.2006.05.003.

Tokimitsu, Y., H. Kishi, S. Kondo, R. Honda, K. Tajiri, K. Motoki, T. Ozawa, S. Kadowaki, T. Obata, S. Fujiki, C. Tateno, H. Takaishi, K. Chayama, K. Yoshizato, E. Tamiya, T. Sugiyama, and A. Muraguchi. 2007. Single lymphocyte analysis with a microwell array chip. Cytom. Part A. 71:1003–1010. doi:10.1002/cyto.a.20478.

Tomlinson, M.G., D.B. Woods, M. McMahon, M.I. Wahl, O.N. Witte, T. Kurosaki, J.B. Bolen, and J.A. Johnston. 2001. A conditional form of Bruton's tyrosine kinase is sufficient to activate multiple downstream signaling pathways via PLCγ2 in B cells. BMC Immunol. 2. doi:10.1186/1471-2172-2-4.

Tonegawa, S. 1983. Somatic generation of antibody diversity. Nature. 302:575–581. doi:10.1038/302575a0.

Tsukada, S., D.C. Saffran, D.J. Rawlings, O. Parolini, R.C. Allen, I. Klisak, R.S. Sparkes, H. Kubagawa, T. Mohandas, S. Quan, J.W. Belmont, M.D. Cooper, M.E. Conley, and O.N. Witte. 1993. Deficient expression of a B cell cytoplasmic tyrosine kinase in human X-linked agammaglobulinemia. Cell. 72:279–290. doi:10.1016/0092-8674(93)90667-F.

Tweeddale, M., N. Jamal, A. Nguyen, X.H. Wang, M.D. Minden, and H.A. Messner. 1989. Production of Growth Factors by Malignant Lymphoma Cell Lines. Blodd. 74:572–578. doi:10.1037/11919-024.

Tweeddale, M.E., B. Lim, N. Jamal, J. Robinson, J. Zalcberg, G. Lockwood, D.M. Minden, and H.A. Messner. 1987. The Presence of Clonogenic Cells in High-Grade Malignant Lymphoma: A Prognostic Factor. Blood. 69:1307–1315.

Uhlén, P., and N. Fritz. 2010. Biochemistry of calcium oscillations. Biochem. Biophys. Res. Commun. 396:28–32. doi:10.1016/j.bbrc.2010.02.117.

Vetrie, D., I. Vořechovský, P. Sideras, J. Holland, A. Davies, F. Flinter, L. Hammarström, C. Kinnon, R. Levinsky, M. Bobrow, C.I.E. Smith, and D.R. Bentley. 1993. The gene involved in X-linked agammaglobulinaemia is a member of the src family of protein-tyrosine kinases. Nature. 361:226–233. doi:10.1038/361226a0.

Vogler, M. 2012. BCL2A1: The underdog in the BCL2 family. Cell Death Differ. 19:67–74. doi:10.1038/cdd.2011.158.

Wahl, M.I., S. Nishibe, P.G. Suh, S.G. Rhee, and G. Carpenter. 1989. Epidermal growth factor stimulates tyrosine phosphorylation of phospholipase C-II independently of receptor internalization and extracellular calcium. Proc. Natl. Acad. Sci. U. S. A. 86:1568–1572. doi:10.1073/pnas.86.5.1568.

Walliser, C., E. Hermkes, A. Schade, S. Wiese, J. Deinzer, M. Zapatka, L. Désiré, D. Mertens, S. Stilgenbauer, and P. Gierschik. 2016. The phospholipase Cγ2 mutants R665W and L845F identified in ibrutinib-resistant chronic lymphocytic leukemia patients are hypersensitive to the Rho GTPase Rac2 protein. J. Biol. Chem. 291:22136–22148. doi:10.1074/jbc.M116.746842.

Walliser, C., K. Tron, K. Clauss, O. Gutman, A.Y. Kobitski, M. Retlich, A. Schade, C. Röcker, Y.I. Henis, G.U. Nienhaus, and P. Gierschik. 2015. Rac-mediated stimulation of phospholipase Cγ2 amplifies B cell receptor-induced calcium signaling. J. Biol. Chem. 290:17056–17072. doi:10.1074/jbc.M115.645739.

Wang, M.S., Z. Luo, and N. Nitin. 2014. Rapid assessment of drug response in cancer cells using

microwell array and molecular imaging. Anal. Bioanal. Chem. 406:4195–4206. doi:10.1007/s00216-014-7759-y.

Wang, Y., X. Tang, X. Feng, C. Liu, P. Chen, D. Chen, and B.F. Liu. 2015. A microfluidic digital single-cell assay for the evaluation of anticancer drugs. Anal. Bioanal. Chem. 407:1139–1148. doi:10.1007/s00216-014-8325-3.

Watanabe, D., S. Hashimoto, M. Ishiai, M. Matsushita, Y. Baba, T. Kishimoto, T. Kurosaki, and S. Tsukada. 2001. Four Tyrosine Residues in Phospholipase C-γ2, Identified as Btk-dependent Phosphorylation Sites, Are Required for B Cell Antigen Receptor-coupled Calcium Signaling. J. Biol. Chem. 276:38595–38601. doi:10.1074/jbc.M103675200.

Weber, M., B. Treanor, D. Depoil, H. Shinohara, N.E. Harwood, M. Hikida, T. Kurosaki, and F.D. Batista. 2008. Phospholipase C-γ2 and Vav cooperate within signaling microclusters to propagate B cell spreading in response to membrane-bound antigen. J. Exp. Med. 205:853–868. doi:10.1084/jem.20072619.

Westin, J., L.J. Nastoupil, L. Fayad, F.B. Hagemeister, Y. Oki, F. Turturro, S. Ahmed, M.A. Rodriguez, H.J. Lee, R. Steiner, R. Nair, S. Parmar, K.H. Young, T. McDonnell, H. Chuang, M.R. Green, S.S. Neelapu, and R.E. Davis. 2019. Smart start: Final results of rituximab, lenalidomide, and ibrutinib lead in prior to combination with chemotherapy for patients with newly diagnosed diffuse large B-cell lymphoma. J. Clin. Oncol. 37(7508).

Winding, P., and M.W. Berchtold. 2001. The chicken B cell line DT40: A novel tool for gene disruption experiments. J. Immunol. Methods. 249:1–16. doi:10.1016/S0022-1759(00)00333-1.

Winter, J.N., D. Variakojis, and A.L. Epstein. 1984. Phenotypic analysis of established diffuse histiocytic lymphoma cell lines utilizing monoclonal antibodies and cytochemical techniques. Blood. 63:140–146.

Wist, M., L. Meier, O. Gutman, J. Haas, S. Endres, Y. Zhou, R. Rösler, S. Wiese, S. Stilgenbauer, E. Hobeika, Y.I. Henis, X.P. Gierschik, and C. Walliser. 2020. Noncatalytic Bruton's tyrosine kinase activates PLCγ2 variants mediating ibrutinib resistance in human chronic lymphocytic leukemia cells. J. Biol. Chem. 295:5717–5736. doi:10.1074/jbc.RA119.011946.

Wood, D.K., D.M. Weingeist, S.N. Bhatia, and B.P. Engelward. 2010. Single cell trapping and DNA damage analysis using microwell arrays. Proc. Natl. Acad. Sci. U. S. A. 107:10008–10013. doi:10.1073/pnas.1004056107.

Woyach, J.A., R.R. Furman, T.-M. Liu, H.G. Ozer, M. Zapatka, A.S. Ruppert, L. Xue, D.H.-H. Li, S.M. Steggerda, M. Versele, S.S. Dave, J. Zhang, A.S. Yilmaz, S.M. Jaglowski, K.A. Blum, A. Lozanski, G. Lozanski, D.F. James, J.C. Barrientos, P. Lichter, S. Stilgenbauer, J.J. Buggy, B.Y. Chang, A.J. Johnson, and J.C. Byrd. 2014. Resistance Mechanisms for the Bruton's Tyrosine Kinase Inhibitor Ibrutinib. N. Engl. J. Med. 370:2286–2294. doi:10.1056/NEJMoa1400029.

Xue, G., J. Chen, L. Liu, D. Zhou, Y. Zuo, T. Fu, and Z. Pan. 2020. Protein degradation through covalent inhibitor-based PROTACs. Chem. Commun. 56:1521–1524. doi:10.1039/c9cc08238g.

Yamamura, S., H. Kishi, Y. Tokimitsu, S. Kondo, R. Honda, S. Ramachandra Rao, M. Omori, E. Tamiya, and A. Muraguchi. 2005. Single-cell microarray for analyzing cellular response. Anal. Chem. 77:8050–8056. doi:10.1021/ac0515632.

Yamanashi, Y., T. Kakiuchi, J. Mizuguchi, T. Yamamoto, and K. Toyoshima. 1991. Association of B cell antigen receptor with protein tyrosine kinase Lyn. Science. 251:192–194.

Yarkoni, Y., A. Getahun, and J.C. Cambier. 2010. Molecular underpinning of B-cell anergy. Immunol. Rev. 237:249–263. doi:10.1111/j.1600-065X.2010.00936.x.

Yeomans, A., S.M. Thirdborough, B. Valle-Argos, A. Linley, S. Krysov, M.S. Hidalgo, E. Leonard, M. Ishfaq, S.D. Wagner, A.E. Willis, A.J. Steele, F.K. Stevenson, F. Forconi, M.J. Coldwell, and G. Packham. 2016. Engagement of the B-cell receptor of chronic lymphocytic leukemia cells drives global and MYC-specific mRNA translation. Blood. 127:449–457. doi:10.1182/blood-2015-07-660969.

Yoon, S.E., S.J. Kim, D.H. Yoon, Y. Koh, Y-C. Mun, Y.R. Do, Y.S. Choi, D.H. Yang, M.K. Kim, G-W. Lee, C. Suh, Y.H. Ko, and W.S. Kim. 2020. A phase II study of ibrutinib in combination with rituximab-cyclophosphamide-doxorubicin hydrochloride-vincristine sulfate-prednisone therapy in Epstein-Barr virus-positive, diffuse large B cell lymphoma (54179060LYM2003: IVORY study): results of the final analysis. Ann Hematol. 99:1283-1291. doi: 10.1007/s00277-020-04005-6.

Younes, A., L.H. Sehn, P. Johnson, P.L. Zinzani, X, Hong, J. Zhu, O. Samoilova, C. Suh, I. Matsumura, A. Lopez-Hernandez, U. Duhrsen, C. Thieblemont, J. Carey, G. Liu, S.M. Shreeve, S. Sun, J. Vermeulen, L.M. Staudt, and W.H. Wilson. 2018. A Global, Randomized, Placebo-Controlled, Phase 3 Study of Ibrutinib Plus Rituximab, Cyclophosphamide, Doxorubicin, Vincristine, and Prednisone (RCHOP) in Patients with Previously Untreated Non-Germinal Center B-Cell-like (GCB) Diffuse Large B-Cell Lymphoma (DLBCL). Blood. 132 (Supplement 1):784

Young, R.M., J.D. Phelan, W.H. Wilson, and L.M. Staudt. 2019. Pathogenic B-cell receptor signaling in lymphoid malignancies: New insights to improve treatment. Immunol. Rev. 291:190–213. doi:10.1111/imr.12792.

Zhang, J., V. Grubor, C.L. Love, A. Banerjee, K.L. Richards, P.A. Mieczkowski, C. Dunphy, W. Choi, W. Yan Au, G. Srivastava, P.L. Lugar, D.A. Rizzieri, A.S. Lagoo, L. Bernal-Mizrachi, K.P. Mann, C. Flowers, K. Naresh, A. Evens, L.I. Gordon, M. Czader, J.I. Gill, E.D. Hsi, Q. Liu, A. Fan, K. Walsh, D. Jima, L.L. Smith, A.J. Johnson, J.C. Byrd, M.A. Luftig, T. Ni, J. Zhu, A. Chadburn, S. Levy, D. Dunson, and S.S. Dave. 2013a. Genetic heterogeneity of diffuse large B-cell lymphoma. Proc. Natl. Acad. Sci. 110:1398–1403. doi:10.1038/sj.thj.6200441.

Zhang, L., I.P. Holmes, F. Hochgra, S.R. Walker, N.A. Ali, E.S. Humphrey, J. Wu, M. De Silva, W.J.A. Kersten, T. Connor, H. Falk, L. Allan, I.P. Street, J.D. Bentley, P.A. Pilling, B.J. Monahan, T.S. Peat, and R.J. Daly. 2013b. Characterization of the Novel Broad-Spectrum Kinase Inhibitor CTx- 0294885 As an Affinity Reagent for Mass Spectrometry-Based Kinome Profiling. J. Proteome Res. 12:3104-3116. doi:10.1021/pr3008495.

Zhang, X., H. Yin, J.M. Cooper, and S.J. Haswell. 2006. A microfluidic-based system for analysis of single cells based on Ca^{2+} flux. Electrophoresis. 27:5093–5100. doi:10.1002/elps.200600390.

Zorba, A., C. Nguyen, Y. Xu, J. Starr, K. Borzilleri, J. Smith, H. Zhu, K.A. Farley, W.D. Ding, J. Schiemer, X. Feng, J.S. Chang, D.P. Uccello, J.A. Young, C.N. Garcia-Irrizary, L. Czabaniuk, B. Schuff, R. Oliver, J. Montgomery, M.M. Hayward, J. Coe, J. Chen, M. Niosi, S. Luthra, J.C. Shah, A. El-Kattan, X. Qiu, G.M. West, M.C. Noe, V. Shanmugasundaram, A.M. Gilbert, M.F. Brown, and M.F. Calabrese. 2018. Delineating the role of cooperativity in the design of potent PROTACs for BTK. Proc. Natl. Acad. Sci. U. S. A. 115:E7285–E7292. doi:10.1073/pnas.1803662115.

Appendix 1

Table A1-1: Summary information of primary CLL samples used for analysis of the effect of ibrutinib on anti-IgM-induced iCa^{2+} flux. Related to Figure 3-1.

CLL Sample Number	CD19 CD5 coexpressing cells (%)	sIgM MFI	Cells responding to anti-IgM[1] (%)	IGHV gene mutation status[2]
471B	96	77	81	M
523H	92	45	39	M
564B	92	1700	83	M
604F	87	54	79	M
609C	94	53	79	M
635C	90	78	89	U
674D	85	314	88	U
681	97	212	60	M
684A	92	31	14	M
684C	92	25	13	M
739	98	99	76	U
758	80	90	84	M
774	97	80	27	U
775	83	65	57	U
780A	99	81	81	U
791A	88	47	28	M
803B	93	38	20	U
816B	89	43	70	U
908	92	144	NK	ND
960	96	76	NK	U

Table A1-2: Summary information of primary CLL samples used for analysis of the effect of acalabrutinib on anti-IgM-induced iCa^{2+} flux. Related to Figure 3-2.

CLL Sample Number	CD19 CD5 coexpressing cells (%)	sIgM MFI	Cells responding to anti-IgM[1] (%)	IGHV gene mutation status[2]
471B	96	77	81	M
523H	92	45	39	M
604F	87	54	79	M
609C	94	53	79	M
674A	88	331	89	U
674D	85	314	88	U
681	97	212	60	M
684A	92	31	14	M
684C	92	25	13	M
687B	72	252	81	U
747B	83	184	40	U
758	80	90	84	M
774	97	80	27	U
775	83	65	57	U
780A	99	81	81	U
791A	88	47	28	M
803B	93	38	20	U
816B	89	43	70	U

Table A1-3: Summary information of primary CLL samples used by Alex Wathan, added to my analysis for correlations between clinical and biological characteristics and signalling capacity and inhibitor responses. Related to Figure 3-4, 3-5 and 3-6.

CLL Sample Number	CD19 CD5 coexpressing cells (%)	sIgM MFI	Cells responding to anti-IgM[1] (%)	IGHV gene mutation status[2]
368D	97	52	35	M
500C	92	60	12	U
523B	94	26	14	M
523D	95	48	65	M
595D	95	36	20	U
643	92	25	26	M
674A	88	331	89	U
705	96	70	16	M
739A	97	83	75	U
755	91	72	81	U

Table A1-4: Summary information of primary CLL samples used for analysis of the effect of different concentrations of BTK-targeted PROTAC, MT-802, on BTK expression in CLL cells. Related to Figure 3-7.

CLL Sample Number	CD19 CD5 coexpressing cells (%)	sIgM MFI	Cells responding to anti-IgM[1] (%)	IGHV gene mutation status[2]
681	97	212	60	M
780	99	65	81	U
782A	87	155	69	M
803A	94	33	31	U

Appendix 1

Table A1-5: Summary information of primary CLL samples used for analysis of the effect of BTK-targeted PROTAC, MT-802, on BTK expression in CLL cells over time. Related to Figure 3-8.

CLL Sample Number	CD19 CD5 coexpressing cells (%)	sIgM MFI	Cells responding to anti-IgM[1] (%)	IGHV gene mutation status[2]
635D	95	50	78	U
739	98	99	76	U
791A	88	47	28	M

Table A1-6: Summary information of primary CLL samples used for analysis of the effect of MT-802 and ibrutinib on anti-IgM-induced Ca^{2+} flux. Related to Figure 3-9.

CLL Sample Number	CD19 CD5 coexpressing cells (%)	sIgM MFI	Cells responding to anti-IgM[1] (%)	IGHV gene mutation status[2]
564B	92	1700	83	M
635C	90	78	89	U
635D	95	50	78	U
681A	98	185	31	M
803C	95	30	31	U

Table A1-7: Summary information of primary CLL samples used for analysis of the effect of MT-802 and ibrutinib on expression and anti-IgM-induced phosphorylation of BCR-associated signalling proteins. Related to Figure 3-11.

CLL Sample Number	CD19 CD5 coexpressing cells (%)	sIgM MFI	Cells responding to anti-IgM[1] (%)	IGHV gene mutation status[2]
564B	92	1700	83	M
635D	95	50	78	U
681A	98	185	31	M
803C	95	30	31	U

Table A1-8: Summary information of primary CLL samples used for analysis of the effect of BTK inhibition on anti-IgM-induced iCa^{2+} mobilisation and phosphorylation of BCR-associated signalling proteins. Related to Figure 4-2 and 4-12.

CLL Sample Number	CD19 CD5 coexpressing cells (%)	sIgM MFI	Cells responding to anti-IgM[1] (%)	IGHV gene mutation status[2]
523H	92	45	39	M
674D	85	314	88	U
780A	99	81	81	U

Table A1-9: Summary information of primary CLL samples used for validation of the effect of IL-4 on surface IgM expression. Related to Figure 4-13.

CLL Sample Number	CD19 CD5 coexpressing cells (%)	sIgM MFI	Cells responding to anti-IgM[1] (%)	IGHV gene mutation status[2]
409C	73	112	60	U
480	86	50	32	M
523F	97	31	25	M
564B	92	1700	83	M
575B	97	87	64	M
604C	86	61	60	M
621B	93	49	49	M
681A	98	185	31	M
681B	98	116	27	M
803	96	33	30	U
803A	94	33	31	U
815	84	55	32	M
842A	94	91	49	U
960A	98	61	58	U

Appendix 1

Table A1-10: Summary information of primary CLL samples used for validation of the effect of IL-4 on iCa^{2+} flux. Related to 4-13.

CLL Sample Number	CD19 CD5 coexpressing cells (%)	sIgM MFI	Cells responding to anti-IgM[1] (%)	IGHV gene mutation status[2]
523F	97	31	25	M
564B	92	1700	83	M
575B	97	87	64	M
604C	86	61	60	M
621B	93	49	49	M
681A	98	185	31	M
803A	94	33	31	U
842A	94	91	49	U
960A	98	61	58	U

Table A1-11: Summary information of primary CLL samples used for analysis of the effect of IL-4 on iCa^{2+} flux in primary CLL samples pretreated with ibrutinib or MT-802. Related to Figure 4-14.

CLL Sample Number	CD19 CD5 coexpressing cells (%)	sIgM MFI	Cells responding to anti-IgM[1] (%)	IGHV gene mutation status[2]
409C	73	112	60	U
480	86	50	32	M
604C	86	61	60	M
681B	98	116	27	M
960A	98	61	58	U

Table A1-12: Summary information of primary CLL samples used for analysis of the effect of BTK inhibition on anti-IgM-induced phosphorylation of BCR-associated signalling proteins in primary CLL samples following IL-4 stimulation. Related to Figure 4-16.

CLL Sample Number	CD19 CD5 coexpressing cells (%)	sIgM MFI	Cells responding to anti-IgM[1] (%)	IGHV gene mutation status[2]
409C	73	112	60	U
480	86	50	32	M
803A	94	33	31	U
842A	94	91	49	U
960A	98	61	58	U

Table A1-13: Summary information of primary CLL samples used for analysis of occupied microwells using different cell seeding ratios. Related to Figure 5-13.

CLL Sample Number	CD19 CD5 coexpressing cells (%)	sIgM MFI	Cells responding to anti-IgM[1] (%)	IGHV gene mutation status[2]
803D	NK	NK	NK	ND
816D	NK	NK	NK	ND
895A	NK	NK	NK	ND
900A	NK	NK	NK	ND

[1] Measurement of intracellular Ca^{2+} flux as described by Mockridge et al., 2007. Analysis performed by research technicians.
[2] Sequencing carried out by Isla Henderson. U: unmutated, M: mutated, ND: not determined.
NK: not known.
N.B. The sample numbers (without letter) represent the first sample collected from a patient; a letter after the number denotes a subsequent sample from the same patient.